High-Index-Contrast Electromechanical Optical Switches

by

Reginald Eugene Bryant

Submitted to the Department of Electrical Engineering and Computer Science
in partial fulfillment of the requirements for the degree of

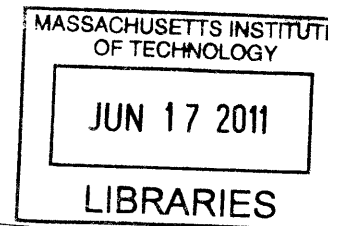Doctor of Philosophy in Electrical Engineering and Computer Science

at the

MASSACHUSETTS INSTITUTE OF TECHNOLOGY

June 2011

©Massachusetts Institute of Technology. All rights reserved.

Author _

L $\slash$ Department of Electrical Engineering and Computer Science
May 20 2011

Certified by _____   _____

Leslie A. Kolodziejski
Professor
Thesis Supervisor

Accepted by _____   _____

Terry P. Orlando
Chairman, Department Committee on Graduate Students

"If you don't have time to do it right you must have time to do it over. "

Anonymous

High-Index-Contrast Electromechanical Optical Switches

by

Reginald Eugene Bryant

Submitted to the Department of Electrical Engineering and Computer Science
in partial fulfillment of the requirements for the degree of

Doctor of Philosophy in Electrical Engineering and Computer Science

Abstract

System developers are looking to replace protocol-dependent, bandwidth-limited optical networks with intelligent optically-transparent integrated photonic networks. Several electromechanical optical switches are explored with the intent of being utilized as optical switching elements in transparent, integrated photonic networks. The electromechanical optical switches are based on high-index-contrast waveguide optics that is integrated with electrostatic parallel plate actuators on submicron scales. High-index-contrast waveguides are attractive due to their reduced bending radius and low in-plane scattering and optical loss. These qualities of high-index-contrast waveguides make them uniquely suited for low-cost, large-scale integration. The parallel plate actuators are used to control the waveguide light switching by mechanically establishing and terminating light pathways on time scales well below $100s$ of microseconds. Investigations of light pathway coupling schemes and parallel plate actuator configurations led to the development of several device structures that are categorized in three distinct device generations. Design premiums were placed upon device footprint minimization, polarization independence, high extinction ratios, and operational robustness.

Thesis Supervisor: Leslie A. Kolodziejski
Title: Professor

Acknowledgements

Contents

List of Figures

List of Tables

Chapter 1

Introduction

1.1 Motivation

In 1962, three engineering groups at General Electric [1] [2], IBM [3] [4] and MIT Lincoln Laboratory [5] each experimentally demonstrated the operation of a gallium arsenide (GaAs) semiconductor laser diode. Shortly following, in 1970, engineers at Corning Glass Works announced the world's first doped-silica optical fiber with 20dB/km loss [6]. After that, research interest blossomed around the idea of developing optimized semiconductor photodiodes to complete the source, medium, and detector triad for high-speed, large-bandwidth telecommunication networks [7]. Eventually, two decades of technological developments gave millions of people the ability to transmit large amounts of data at gigabit-per-second speeds from all across the planet. However, the progress to date seems to be unable to satisfy the need for increasingly larger data transfers at faster transfer rates from more locations around the globe. Unfortunately, presently deployed telecommunication systems will not be able to meet the insatiable need for data, speed, and ubiquity while simultaneously reducing the cost and raising the reliability of future networks [8],[9]. For example, modulated data on optical signals is typically routed from location to location by first photodetecting the optical signal, then electronically processing the data bit-by-bit, and finally retransmitting the data on an optical signal. The optical conversion process is termed an optical-electrical-optical (OEO) signal conversion. In general, current telecommunication systems rely on OEO signal conversions in order to manage, monitor, and manipulate optical signals [9]. As telecommunication networks grow to meet the insatiable needs of its users, OEO signal processing

1

will reach a throughput bottleneck, become increasingly expensive to deploy, and will have to be continuously upgraded in order to accommodate the constantly evolving bit-rate transmission schemes. Therefore, instead of relying solely on electronics to handle optical signal manipulation, newly developed optical components will begin to be commissioned to handle more of the signal manipulation, thus leveraging all of the available bandwidth of fiber optic systems and reducing the number of costly OEO signal conversions in fiber optic telecommunication systems. Furthermore, future proof networks can be realized since signal manipulation in optical-optical-optical (OOO) networks is performed only on the carrier signal; OOO network operation is independent of bit-rate protocols that are superimposed on the carrier optical signal. Consequently, in order to realize OOO networks, integrated, scalable and low cost solutions are required. Naturally, in order to create integrated, scalable and low cost OOO networking solutions, fashioning monolithic photonic microsystems on a common substrate has become the dominate method that is used to accomplish this objective. Specifically, two levels of integrated photonic circuitry are being considered: photonic integrated circuit (PIC) technology and photoelectronic integrated circuit (PEIC) technology. PIC technology features interconnected photonic devices that function primarily to manipulate, route and modulate light signals, whereas PEIC technology, while featuring the same functionality of PIC technology, also features the increased functionality of light creation and detection, the transduction of information between the photonic and electronic energy domains. In essence, PIC and PEIC technology can be differentiate by the fact that PEICs incorporate photoelectronic devices (e.g., lasers and detectors) on a single *optical platform*[1] while PICs do not.

Several competing material systems have been identified as viable candidate substrates for monolithic photonic integration. Namely, glass fibers, silica-on-silicon (SOS), silicon-on-insulator (SOI), silicon oxynitride (SiON), polymers, lithium niobate (LiNbO$_3$), sol-gels, indium phosphide (InP), and gallium arsenide (GaAs) material systems have been demonstrated to support at least four different optical device types [10]. Although glass fiber devices are well established and can be easily interfaced to glass fiber transmission lines, substrate-based material systems (i.e., SOS, SOI, SiON, sol-gels, polymers, LiNbO$_3$, InP, and GaAs material systems) have the advantage of being compact, low-cost, scalable and more accommodative to multiple monolithically integrated devices.

---

[1]Note that an optical platform is not strictly defined as a single substrate material.

To date, lasers, amplifiers, modulators, arrayed waveguides and detectors can only be reliably fabricated with compound semiconductor (i.e., GaAs and InP) material systems due to the atomic crystalline structure resulting in a direct energy bandgap. Reliable fabrication of lasers, amplifiers and detectors in compound semiconductor material systems positions GaAs PIC and InP PIC technologies with a unique functional advantage over SOS PIC, SOI PIC, SiON PIC, polymer PIC, and LiNbO$_3$ PIC technologies.

The extensive use of InP substrates for long wavelength lasers ($1.00\mu m$-$1.70\mu m$ wavelengths) should make InP the premiere choice material system for monolithic integration. However, there are several reasons why GaAs can be considered a comparable and more practical alternative compound semiconductor material system for monolithic photonic integration. From a production vantage point, GaAs is (less costly) (GaAs substrates are approximate in price to SOI substrates), available in larger wafer sizes (up to 8 inch), and are more durable when compared to InP [11]. Additionally, GaAs electronics are more mature than InP electronics. In fact, GaAs detection electronics are preferred over silicon detection electronics for stringent bit-rate requirements [12]. Moreover, GaAs electronics are well suited for high-speed, low-voltage signal modulation [13]. From an optical perspective, propagation loss in GaAs (0.5dB/cm)[10] is much lower than the propagation loss in InP (3dB/cm) [10]. Consequently, GaAs is the better choice for realizing large scale integration of many waveguide-based devices. However, fabrication of active devices in the $1000nm-1600nm$ wavelength long haul telecommunication window is most easily accomplished in the InP material system. While that may be true, there is interest in developing $1000nm-1600nm$ wavelength lasers in the more cost effective and well established GaAs material system due to the attractive aforementioned attributes of GaAs. As a result, one decade of investigative study has led to promising results of using GaAs as an alternative material system that can support monolithic integration of $1000nm-1600nm$ wavelength active devices [14]. In short, the combination of material properties, low-loss light propagation and the development of active devices within the $1000nm-1600nm$ wavelength window present a strong argument in favor of GaAs PIC/ GaAs PEIC technology as a monolithic solution for meeting the needs of a demanding telecommunication network.

The investigated electromechanical high-index-contrast (NEM HIC) devices were developed with the express purpose of increasing the functionality and flexibility of GaAs-on-insulator-based photonic integrated circuits (GaAs on insulator PICs) and ultimately

GaAs on insulator-based photoelectric integrated circuits (GaAs on insulator PEICs). To explain, the GaAs on insulator material system is composed of a bottom layer of aluminum oxide (Al_xO_y) which is the bottom low-index insulator material that supports one or many layer(s) of $Al_{1-x}Ga_xAs$/GaAs thin films which are used for photonic, electrical, and/or photoelectrical functionality. Either sapphire or a GaAs wafer can be used as the growth substrate for the GaAs on insulator material system. Typically, a GaAs substrate is used for the GaAs on insulator material system by initially growing an oxidizable high-aluminum content $Al_{1-x}Ga_xAs$ layer which serves as the low-index insulator material. GaAs on insulator PIC/GaAs on insulator PEIC technology differs from GaAs PIC/GaAs PEIC technology only in fabrication processing, and thus retains all of the attributes which makes GaAs PIC/GaAs PEIC a competitive technology for implement OOO telecommunication networking.

This thesis focuses on novel implementations of transparent optical switches that are designed for compatibility with the GaAs-on-insulator material system. Specifically, the optical switch devices establish lightpaths with butt-coupling (BC) and directional-coupling (DC) mechanisms. Moreover, the optical switch devices are mechanically toggled on and off with the use of electromechanical actuation. Consequently, the optical switch devices are termed nanoelectromechanical high-index-contrast (NEM HIC) devices which denotes both the type of materials that are used for light guidance as well as the type of mechanism that is used for light switching. Seven NEM HIC switch designs, or generations, are presented. Each of the seven NEM HIC switches are intended to served as primary photonic components to increase the functionality of GaAs-on-insulator PICs and ultimately GaAs on insulator PEICs. The NEM HIC switch designs are based on preliminary fabrication work in conjunction with a variety of simulation methods to understand their performance, advantages and disadvantages.

The coupled effects of mechanical, electrical and optical operation of the NEM HIC switch inspire a different type of device classification paradigm which can aptly classify candidate devices for monolithic integration in a GaAs on insulator PEIC. Mechanical, electrical and optical device operation is classified as being either active or passive.

TABLE 1.1: Several monolithic photonic devices. Each device is categorized in terms of mechanical (MECH), electrical (ELEC) and optical (OPTI), and activeness (ACT) / passiveness (PASS).

Type	Device	MECH	ELEC	OPTI	GaAs-on-Oxide Device	Ref.
I	Y-splitters, Bends, Crossings, V-Grooves, Stand-Off Bumpers, Pedestal Aligners.	PASS	PASS	PASS	Photonic Bandgap (PBG) High-Index-Contrast (HIC) GaAs Nanostructures, Wet-Etched GaAs, GaAs PIC mounted on Anisotropic-Etched Silicon.	[15], [15], [16], [17].
II	Optical-Optical Switches.	PASS	PASS	ACT	PBG HIC GaAs Nanostructures.	[18].
III	Scanning Probe Cantilevers	ACT	PASS	PASS		[?]
IV	Emitters, Detectors.	PASS	ACT	ACT	$GaAs_{1-x}N_x/$ $GaAs_{1-x}Sb_x/$ $InGaAsN$ Lasers and Detectors $(1.3 - 1.5\mu m)$.	[19], [20], [21], [22].
V	Electromechanical Optical Switches.	ACT	ACT	PASS	Discussed in Thesis.	
VI	MEMS Emitters, Receivers.	ACT	ACT	ACT	MEMS Tunable LED/ Photodetector $(1.52\mu m)$.	[23]

Table (1.1) is a list of PIC building block devices that are classified with the proposed classification paradigm. A mechanical active device utilizes micromachined thin film structures to facilitate an optical operation. An electrical active device utilizes electric fields and/or moving charges to control optical signals. An optically-active device is capable of modulating, creating, or detecting light with energy transitions (e.g., electronic energy transitions) within a material.

1.2 Thesis Structure

Seven electromechanical optical switches will be discussed. The seven optical switches were designed sequentially. The first six optical switch devices are representative of design evolutions in electromechanical and/or optical operation which ultimately lead to the creation of the final (seventh) optical switch.

"Chapter 2: Theoretical Modeling" is divided into two sections: (1) "Optical Operation" and (2) "Electromechanical Operation". "Optical Operation" starts with a review of electromagnetic wave propagation through dielectric waveguides and finishes with a discussion of the three optical simulation methods that are used to model the guided wave phenomenon that the optical switches relies upon. "Electromechanical Operation" starts with a review of vibrating beam theory that is based on the Euler-Bernoulli formulation and finishes with a discussion of the two electromechanical simulation methods that are used to model quasi-static and dynamic electromechanical operation of the optical switches.

"Chapter 3: Integrated Structures" begins with a general introduction of all seven optical switch designs. This introduction will briefly cover all seven devices as well as describe the general design strategy that was used to create these optical switches. Seven of the ten sections in "Chapter 3: Integrated Structures" will be dedicated to each optical switch, providing a physical description of the optical switch structure, an explanation of the operation of the optical switch, and a performance summary of the optical switch.

Additionally, the design specifics that are used to create the optical switch will be exemplified with a section that is dedicated to the Device 04 optical switch. Moreover, specific aspects of the optical switch structures will have dedicated sections. Specifically, two of the electromechanical structures that are used in the designs of Device 05, 06 and 07 will have dedicated sections and the optical waveguide structure that is used in the design of Device 07 will have a dedicated section.

"Chapter 4: Fabrication" will discuss a proposed fabrication sequence that can be used to realize all seven optical switches. The preliminary results from several fabricated structures will be discussed.

"Chapter 5: Summary and Future Directions" summarizes the thesis. In particular, design and fabrication results will be linked; critical fabrication issues will be addressed; and suggestions for improvement will be provided.

Chapter 2

Theoretical Modeling

This chapter provides a two-part analysis on how the electromechanical high-index-contrast optical switches are modeled and simulated.

Section 2.1: Optical Operation. Section 2.1 examines the fundamental equations that describe light propagation in semiconductor waveguides that operate under the principle of total internal reflection (TIR). Specifically, three optical simulation methods are discussed: (1) the three-dimensional Fast Fourier Transform Beam Propagation Method (FFT BPM), (2) the three-dimensional Finite-Difference Beam Propagation Method (FD BPM), and (3) the two-dimensional Bi-Directional Eigenmode Propagation Method (BEPM).

Section 2.2: Electromechanical Operation. Section 2.2 examines the fundamental equations that describe the quasi-static and dynamic mechanical behavior of vibrating beams actuated by external loads. Specifically, two electromechanical simulation methods are discussed: (1) the three-dimensional Finite Element Method (FEM), and (2) the one-dimensional Finite Difference Method (FDM).

2.1   Optical Operation

A stripe waveguide is the canonical photonic optical element, serving not only as an optical routing "wire" for light signals (analogous to the electrical wire for electronics) but also as a building block for more sophisticated waveguide-based photonic devices (e.g., lasers, modulators, detectors). Typically, two or more materials with contrasting refractive indices concertedly trap, or confine, light as it propagates along the waveguide. As a result, TIR light guidance is achieved. By convention, stripe waveguides can be classified by both the way light is guided by the waveguide as well as the method in which the waveguide is created. Consequently, light can be guided in four distinct ways with four distinct type of waveguides configurations:

1. The Ridge Waveguide

2. The Rib Waveguide

3. The Strip-Loaded Waveguide

4. The Dilute Waveguide

Accordingly, there are four standard ways to create stripe waveguides:

1. Etching

2. Ion-Implantation

3. Oxidation

4. Diffusion

The isometric schematics in Figures (2.1) and (2.2) represent the four types of stripe waveguides. Each of these stripe waveguides are overlaid with the confined light mode profiles which are shown as concentric white outlines; the sketched mode profiles illustrates how light is confined to each of the waveguide types.
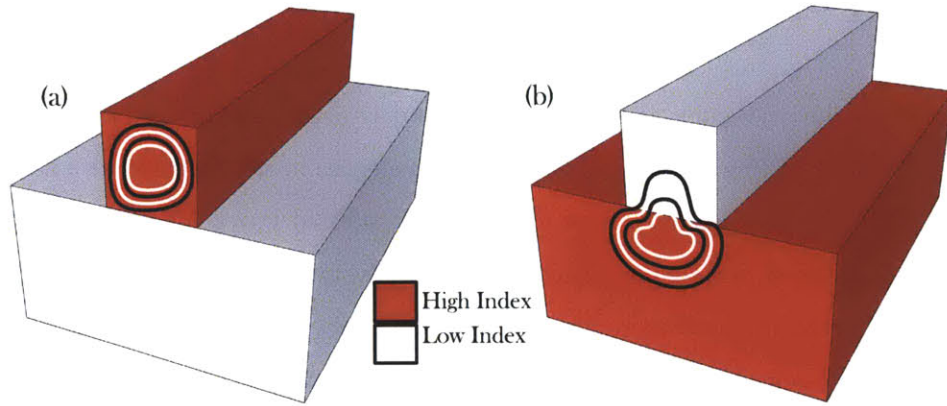
FIGURE 2.1: Schematic representation of the (a) ridge waveguide and (b) the rib waveguide.
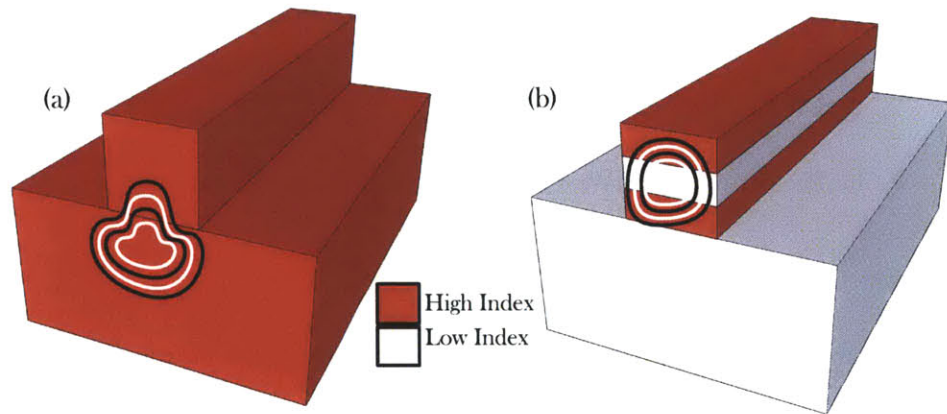
FIGURE 2.2: Schematic representation of the (a) strip-loaded waveguide and (b) the dilute waveguide.

In Figures (2.1a) and (2.2b) , the ridge and dilute ridge waveguides are shown to confine light to the cross-section of high index core material in an elliptical concentric pattern. Indeed, the ridge and dilute waveguides can be easily designed to support a symmetric circular modal profile. Although the ridge and dilute ridge waveguides confine light in a similar manner, the ridge waveguide has three degrees of freedom for controlling the propagation speed of the guided light (i) refractive index (ii) thickness and (iii) width of the core while the dilute waveguide has a variety of degrees of freedom for controlling the propagation speed of the guided light (i) thickness of one or all of the core layers,

(ii) refractive indices of one or all the core layers, (iii) width of the total core, and (iv) thickness of the total core. In Figure (2.1b) and (2.2a), the rib and strip-loaded waveguides are shown to confine light to pear-shaped modal profiles. As a result, designing a rib or strip-loaded waveguide to support a symmetric modal profile is difficult.

Ridge and dilute waveguides have the greatest potential for large-scale photonic integration due in part to their tight confinement of light. Tightly confined light allows waveguides to be fabricated in close proximity without the threat of interference, or crosstalk, between waveguides. As a result, more real estate on a photonic chip can be used for waveguides and waveguide-based devices. Moreover, optical transitions like waveguide tapers, coupling lengths, and curves can be fabricated on micron-order length-scales without compromising the adiabaticity of light propagation modal transitions. In contrast, rib and strip-loaded waveguides can be easily fabricated to be low loss and have a longer legacy of use and development. In fact, there are a variety of simulation methods and models as well as commercial software packages which can be used to reliably and accurately predict the behavior of (low-index-contrast) rib and strip-loaded waveguides. In spite of the extensive infrastructure enjoyed by rib and strip-loaded waveguide-based photonic devices, the electromechanical optical switches are created from ridge waveguides.

Waveguides that are based on total internal reflection can be fabricated using a variety of index contrast systems ranging from low-index-contrast systems to high-index-contrast systems. Low-index-contrast waveguide devices can be created to have low-loss with lenient fabrication tolerances at the expense of poor light confinement which directly affects the packing density (scale-level of integration). Comparatively, high-index-contrast waveguide devices demand stringent fabrication tolerances in order to be low-loss. However, medium- to large-scale integrated photonic circuits can be created with photonic devices that are based on a high-index-contrast waveguide material system. An abundance of accurate simulation techniques, models, and empirical data exist for conventional low-index-contrast waveguide devices, while high-index-contrast waveguides are currently evolving to an equivalent stage of development [24], [25], [26], [27]. Moreover,

alternative optical simulations are required to not only model light propagation in high-index-contrast waveguides, but to also accurately identify and model light propagation effects that are specific to high-index-contrast waveguides. Photonic devices that are based on high-index-contrast ridge waveguides boast many advantages that come at the expense of challenging fabrication requirements [28] [29].

In summary, the electromechanical optical switches that are discussed here are composed of high-index-contrast etched ridge waveguides which are well suited for medium-to large-scale photonic integration. In addition, the lack of systematic scaling laws for refractive index, size, and structure makes designing and modeling optical devices that are comprised of high-index-contrast waveguides especially challenging [30]. Nevertheless, for the very reason that the field of high-index-contrast photonics do not have universally applicable rules, metrics and/or scaling laws, elegant design solutions and assiduous experimental characterizations are likely to lead to the development of novel photonic devices.

2.1.1   Modeling Light Propagation in Dielectric Waveguides

Light propagation, light-material interaction, light creation, and light absorption are all associated by Maxwell's equations which provides a fundamental description of the electromagnetic nature of light.

$$\nabla \times \mathbf{E} = \frac{\partial \mathbf{B}}{\partial t} \tag{2.1a}$$

$$\nabla \times \mathbf{H} = \frac{\partial \mathbf{D}}{\partial t} + \mathbf{J} \tag{2.1b}$$

$$\nabla \cdot \mathbf{D} = \rho \tag{2.1c}$$

$$\nabla \cdot \mathbf{B} = 0 \tag{2.1d}$$

Equations (2.1a), (2.1b), (2.1c) and (2.1d) are Maxwell's four equations which describe electromagnetic light propagation in terms of a magnetic field (H) and an electric field

(**E**) of the light, an electric displacement field (**D**) and a magnetic displacement field (**B**) of the material, and the charge density (ρ) and current density (J) within the material.

$$\nabla \cdot \mathbf{J} = -\frac{\partial \rho}{\partial t} \tag{2.2}$$

In addition to Maxwell's equations, the continuity equation in Equation (2.2) relates the charge density (ρ) to the current density (**J**). A decrease in a time rate of change in charge density gives rise to an increased spatial change in the current density.

Following this further, the light-guiding dielectric materials are defined to have a linear reaction to incident light fields. That is to say, the magnetic displacement field (**B**) and electric displacement field (**D**) of the dielectric material will only have a linear dependence on magnetic fields (**H**) and electric fields (**E**), respectively.

$$\mathbf{D} = \epsilon_0 \cdot \epsilon_r \cdot \mathbf{E} \tag{2.3a}$$

$$\mathbf{B} = \epsilon_0 \cdot \epsilon_r \cdot \mathbf{H} \tag{2.3b}$$

where ϵ_0 is the permittivity in a vacuum, ϵ_r is the relative permittivity of a material, μ_0 is the permeability in a vacuum, and μ_r is the relative permeability of a material.

$$n = \sqrt{\epsilon_r \mu_r} \tag{2.4}$$

The refractive index of a material (n) is defined as the square root of the product of a material's relative permittivity and relative permeability. Since all of the materials used for the optical switches are not magnetic, ($\mu_r = 1$) and (n=$\sqrt{\epsilon_r}$).

The investigated NEM-HIC devices will have no charge-density sources ($\rho = 0$). Also, the waveguiding dielectrics are considered to be perfect dielectric materials with negligible conductivity ($\sigma = 0$), so that the current density (**J**) that is produced by the light

waves E-field is zero ($\sigma\mathbf{E} = \mathbf{J} = 0$). Negligible conductivity is indicative of a dielectric material devoid of charge. However, the waveguide core material will be doped in order to facilitate electromechanical actuation. The loss associated with this charge will be captured in a complex refractive index instead of being explicitly defined by a charge density or current density. As a result of ($\frac{d\rho}{dt} = 0$) and ($\nabla \cdot J = 0$), Maxwell's equations reduce to:

$$\nabla \times \mathbf{E} = \frac{d\mathbf{B}}{dt} \tag{2.5a}$$

$$\nabla \times \mathbf{H} = \frac{d\mathbf{D}}{dt} + \mathbf{J} \tag{2.5b}$$

$$\nabla \cdot \mathbf{D} = 0 \tag{2.5c}$$

$$\nabla \cdot \mathbf{B} = 0 \tag{2.5d}$$

Next, the magnetic fields and the electric fields are expressed in phasor form [Equation (2.6)]; the electromagnetic (EM) field oscillates at a single frequency (angular frequency: ω_0).

$$\mathbf{E}\,(\mathbf{r}, t) = Re\{\mathbf{E}\,(\mathbf{r}) \cdot exp\,(j\omega_0 t)\} \tag{2.6a}$$

$$\mathbf{H}\,(\mathbf{r}, t) = Re\{\mathbf{H}\,(\mathbf{r}) \cdot exp\,(j\omega_0 t)\} \tag{2.6b}$$

$$\mathbf{D}\,(\mathbf{r}, t) = Re\{\mathbf{D}\,(\mathbf{r}) \cdot exp\,(j\omega_0 t)\} \tag{2.6c}$$

$$\mathbf{B}\,(\mathbf{r}, t) = Re\{\mathbf{B}\,(\mathbf{r}) \cdot exp\,(j\omega_0 t)\} \tag{2.6d}$$

Incidentally, the wave vector (k_o), the refractive index of a material (n), angular frequency (ω_0), and wavelength (λ_0) are related by:

$$\left(\frac{\omega_0}{\sqrt{\epsilon_0 \cdot \mu_0}}\right) \cdot (\sqrt{\epsilon_r \cdot \mu_r}) = \left(\frac{\omega_0}{c}\right) \cdot (\sqrt{\epsilon_r \cdot \mu_r}) = \left(\frac{2\pi}{\lambda_0} \cdot \sqrt{\epsilon_r \cdot \mu_r}\right) \cdot (\sqrt{\epsilon_r \cdot \mu_r}) = k_0 \cdot n \tag{2.7}$$

where c is the speed of light and λ_o is the wavelength of the guided light in air/vacuum and is equal to 1550 nm unless otherwise denoted.

To summarize, the light guiding dielectric materials that are used in the electrome-chanical optical switches are free of fixed and mobile charges (i.e., $\mathbf{J} = 0$, $\rho = 0$), and have linear magnetic and electric displacement fields. As a result, the two coupled EM equations which describe light propagation in the investigated NEM-HIC devices can be formulated as:

$$\nabla \times \mathbf{E} = -j\omega_0 \cdot \mu_0 \cdot \mathbf{H} \tag{2.8a}$$

$$\nabla \times \mathbf{H} = -j\omega_0 \cdot \epsilon_0 \cdot n^2 \cdot \mathbf{E} \tag{2.8b}$$

Pursuing this further, the two coupled Hamiltonian functions in Equation (2.8) can be separated into two Hamiltonian functions that are dependent on a single optical wave.

$$\nabla \times \nabla \times \mathbf{E} = -j\omega_0 \cdot \mu_0 \cdot \left(-j\omega_0 \cdot \epsilon_0 \cdot n^2 \cdot \mathbf{E} \right) \tag{2.9a}$$

$$\nabla \times \nabla \times \mathbf{H} = j\omega_0 \cdot \epsilon_0 \cdot \left[\nabla n^2 \times \left(\frac{1}{j\omega_0 \cdot \epsilon_0 \cdot n^2} \cdot \nabla \times \mathbf{H} \right) + n^2 \cdot \left(-j\omega_0 \cdot \mu_0 \cdot \mathbf{H} \right) \right] \tag{2.9b}$$

Using the vectorial formula $\nabla \times (\nabla \times \mathbf{A}) = \nabla (\nabla \times \mathbf{A}) - \nabla^2 \mathbf{A}$ where $\mathbf{A}$ is an arbitrary vectorial quantity, Equations (2.9a) and (2.9b) can then be rewritten after some mathematical manipulation as:

$$\nabla \left(\frac{\nabla \cdot n^2}{n^2} \cdot \mathbf{E} \right) + \nabla^2 \mathbf{E} + k_0^2 \cdot n^2 \cdot \mathbf{E} = 0 \tag{2.10a}$$

$$\frac{\nabla \cdot n^2}{n^2} \times (\nabla \times \mathbf{H}) + \nabla^2 \mathbf{H} + k_0^2 \cdot n^2 \cdot \mathbf{H} = 0 \tag{2.10b}$$

Equation (2.10a) is the electric field Helmholtz formulation; Equation (2.10b) is the magnetic field Helmholtz formulation.

2.1.2 TE$_0$ and TM$_0$ Modes Vs. Quasi-TE$_{00}$(E$_{11}^x$) and Quasi-TM$_{00}$(E$_{11}^y$) Modes

The design of each of the optical switches involves the use of two- and three-dimensional optical structure simulations. As a result, guided light through these two different structures will be different.

Two-dimensional optical structures are defined to have only one transverse dimension which is on the order of the wavelength of the light that is guided; the other transverse dimension is treated as infinitely large. Consequently, light will propagate in either a transverse electric mode or a transverse magnetic mode. The transverse electric (TE) mode is defined to have one electric field component (E_y), which is oriented parallel with the waveguide surface and perpendicular to the direction of propagation, the z direction, and two magnetic field components (H_x and H_z). The transverse magnetic (TM) mode is defined to have one magnetic field component (H_y) and two electric field components (E_x and E_z), where E_x is oriented normal to the normal to the waveguide surface and the direction of propagation. For TE- and TM-polarized light, the E_z and the H_z components vanish, respectively. The modes for TE and TM polarizations are indexed sequentially by subscript n

$$TE_n$$

$$TM_n,$$

where n is defined as 0 for the fundamental TE and TM modes:

$$TE_0$$

$$TM_0.$$

Three-dimensional optical structures are defined to have two transverse dimensions that are on the order of the wavelength of the light that is guided. As a result of both dimensions being on the order of the wavelength, neither the E_z nor H_y components

vanish, except in special cases. Consequently, light will travel in hybrid modes. Representing these hybrid modes can be complicated. However, Goell [31] in his seminal, 1969 publication suggested an intuitive methodology for labeling hybrid modes for waveguide structures with small index differences as these particular waveguide structures establish strong transverse electric field components.[1] In Goell's scheme, a hybrid mode is labeled by the direction and distribution of the strong transverse electric field component

$$E_{pq}^x$$

$$E_{pq}^y.$$

The superscript of these hybrid modes denotes the direction of the major electric field distribution and the subscripts denotes the number of nulls in the electric field distribution, where the electric field distribution has $p-1$ nulls in the x-direction and $q-1$ nulls in the y-direction. Consequently, the fundamental hybrid modes are defined as:

$$E_{11}^x$$

$$E_{11}^y.$$

Incidently, The E_{pq}^x mode is similar to the TE_n mode and the E_{11}^y mode is similar to the TM_n mode. Consequently, the E_{pq}^x and the E_{11}^y modes are often referred to as quasi-TE and quasi-TM modes, respectively. This similarity in mode types will be used in order to support arguments asserted about the performance of a particular optical switch.

---

[1]While the optical switches are based on high-index-contrast (HIC) waveguide structures, the Goell scheme was found to still be useful due to the manner in which the HIC waveguide structures are simulated.
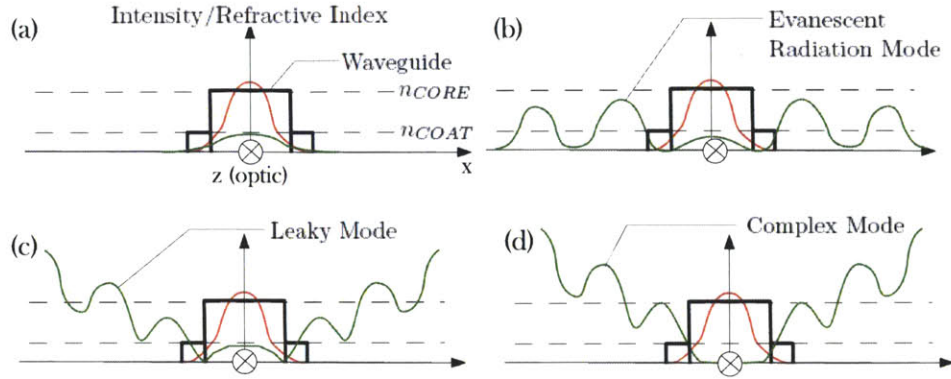
FIGURE 2.3: Schematic outlining simulated light confinement modal profiles for an unbounded channel dielectric waveguide. (a) An unbounded dielectric waveguide comprised of a core and a coat cladding materials defined by the refractive index n_{CORE} and n_{COAT}, respectively. Two guided modes (Guided Mode 01 and 02) are superimposed on the waveguide structure. (b) Guided Mode 01 and an evanescent radiation mode are superimposed on the waveguide structure. (c) Guided Mode 01 and a leaky mode are superimposed on the waveguide structure. (d) Guided Mode 01 and a complex mode are superimposed on the waveguide structure.

Figure (2.3) is a schematic of a planar waveguide with a superposition of four possible types of eigenvectors of electromagnetic energy: (1) the guided, (2) the evanescent radiation, (3) the leaky and (4) the complex modes. More specifically, the planar waveguide extends axially into the page and along the y-axis with a constant refractive index. The weighted superposition of the four eigenvectors are used to describe the light distribution in the presence of a waveguide with a refractive index of n_{core} in a background refractive index of air $n_{back} = n_{air}$. In essence, the light that is localized to the dielectric core of the planar waveguide can be spatially described by a superposition of the four modal types that correspond to an effective index of (n_{eff}). n_{eff} is related to the speed at which light propagates within the media. As displayed in Figure (2.3), the four modes are unconstrained and transversely extend to infinity. Generally, an unconstrained optical device is considered an open structure.

TABLE 2.1: Eight modal types that were represented by Figure (2.3b) for an open waveguide structure.

Mode Type	Effective Index Form		Effective Index Amplitude
Guided Mode	Forward Propagative $n_{eff} = n_{eff}^{re}$	Backward Propagative $n_{eff} = -n_{eff}^{re}$	$n_{clad} < \left\lvert n_{eff}^{re} \right\rvert < n_{guide}$
Radiation Mode	Forward/Backward Propagative $n_{eff} = \pm n_{eff}^{re}$	Forward/Backward Evanescent $n_{eff} = \pm j n_{eff}^{im}$	$\left\lvert n_{eff}^{re} \right\rvert \leq n_{clad}$
Leaky Mode	Forward/Backward Evanescent $n_{eff} = n_{eff}^{re} - j n_{eff}^{im}$	Forward/Backward Evanescent $n_{eff} = -n_{eff}^{re} + j n_{eff}^{im}$	$\left\lvert n_{eff}^{re} \right\rvert \leq n_{clad}$
Complex Mode[2]	E_{pq}^{x} and E_{pq}^{y} Modal Coupling $n_{eff} = \pm n_{eff}^{re} \pm j n_{eff}^{im}$, where $n_{eff}^{re} = n_{eff}^{im}$		$n_{clad} < \left\lvert n_{eff}^{re} \right\rvert < n_{guide}$ $n_{clad} < \left\lvert n_{eff}^{im} \right\rvert < n_{guide}$

Guided modes and radiation modes represent physical and observable mode types. By contrast, leaky modes, and complex modes are nonphysical modes that are used to describe intramodal coupling behavior [32]. Table (2.1) lists all of the permissible mode types and their respective effective index (n_{eff}) eigenvalue types for an open structure waveguide. In fact, the modal types in Table (2.1) are representative of all possible modal types that are associated with an arbitrarily defined waveguiding structure since the modes form a complete solution set of eigenvalues which satisfy the coupled electromagnetic equations in Equation (2.10).

Guided modes have eigenvalues that are bound by the index of the guiding material (n_{core}) and the index of the cladding material (n_{clad}). Moreover, guided modes are discrete modes that can be either forward propagative or backward propagative, which is indicative to the direction along the optical axis that the light propagates. In general, guided modes which have the characteristic of being either forward propagative or backward propagative are considered bi-directional guided modes. Incidentally, contingent on the method of simulation, a waveguide can have either bi-directional guided

---

[2]The Complex Mode is the only mode type to require all four terms to appear at the same time.

modes or forward propagative guided modes, which are simply referred to as guided modes. Secondly, radiation modes form a continuum of modes that act to transversely radiate light away from the waveguide. Moreover, radiation modes are characterized by —n_{eff}— with values equal to or less than n_{clad}. Furthermore, radiation modes can be either bi-directional propagative or bi-directional evanescent. In particular, real bi-directional propagative radiation modes travel along the waveguide conjointly with the guided modes and continuously remove light from the waveguide. Conversely, purely imaginary bi-directional evanescent radiation modes do not travel along the waveguide, but rather, decays as it propagates along the waveguide and contributes to waveguide light loss over a short distance.

A leaky mode is a nonphysical mode that is represented with a complex n_{eff} with a real effective index (n_{eff}^{re}) that is less than n_{clad} and with an unbound imaginary effective index (n_{eff}^{im}). Following this further, leaky modes grow exponentially in power as they transversely extend to infinity. Point in fact, only a few leaky modes are needed to simulate a continuum of radiative modes while a large number of radiative modes are needed to simulate a continuum of radiation modes [32]. A complex mode consists of four equal n_{eff} components that have values between n_{clad} and n_{guide}. Complex modes function only as a coupling mechanism to exchange energy between E_{pq}^{x}- and E_{pq}^{y}-polarized light.

2.1.3 Beam Propagation Method (FFT BPM)

Design of the optical switches begins with the specification of the *base* waveguide refractive index profiles and cross section dimensions. Particularly for this project, a range of refractive index profiles and cross-section dimensions are specified for strict single-mode light propagation. For a given refractive index profile, the cross-section dimensions are to be no smaller than the cross-section dimensions which can sufficiently guide single-mode light propagation without having appreciable light radiation. Moreover, for that same

refractive index profile, the cross-section dimensions are to be no larger than the cross-section dimensions which will start to support the next higher mode of light propagation.

To this end, the beam-propagation method (BPM) was used in order to precisely and accurately define the range of refractive index profiles and cross-section dimensions that were able to support single-mode light propagation as specified in the prior paragraph. Particularly, the imaginary-distance BPM was used as implemented by the commercially-available RSoft BeamPROP program[33].

In order to properly describe imaginary-distance BPM, consider the Helmholtz wave equation for a single-frequency wave, characterized by angular frequency ω_0:

$$\nabla^2 \mathbf{E} + k_0^2 \cdot n^2 \cdot \mathbf{E} = 0 \qquad (2.11)$$

where

$$k_0 = \frac{n_0 \omega_0}{c}.$$

Since waveguide structures are assumed for this project, the single-frequency wave (as specified by $\mathbf{E}$) can be considered as a wave which is governed by the slowly varying envelope approximation (SVEA), which allows $\mathbf{E}$ to be described as a product of a complex field amplitude $\phi_{\mathbf{E}}(x, y, z)$ and a carrier wave $exp\left(-jn_{eff}k_0 z\right)$, moving along a waveguide structure which extends along the z-axis (the optic axis).

$$\mathbf{E}(x, y, z, t) = \phi_{\mathbf{E}}(x, y, z) \, exp\left(-jn_{eff}k_0 z\right) \cdot exp\left(-j\omega_0 \cdot t\right) \qquad (2.12)$$

where n_{eff} is the effective index of the very fast oscillatory phase term. n_{eff} provides a measure of how fast the guided light travels in the presence of a given waveguide structure. Moreover, the complex field amplitude, $\phi_E(x, y, z)$ and the carrier wave, $exp(-jn_{eff}k_0 z)$, can be represented as a superposition of optical modes, index by n.

$$\phi_E\left(x, y, z\right) \exp(-jn_{eff}k_0 z) = \sum_n a_{E_n} \phi_{E_n} \exp\left(-jn_{eff_n}k_0 z\right) \qquad (2.13)$$

where a_{E_n} is the amount of optical energy carried in mode n and ϕ_{E_n} is the eigenfunction, the modal spatial distribution, of mode n. Thus, $\mathbf{E}\left(x, y, z, t\right)$ can be represented as

$$\mathbf{E}\left(x, y, z, t\right) = \sum_n a_{E_n} \phi_{E_n} \exp\left(-jn_{eff_n}k_0 z\right) \exp\left(-j\omega_0 t\right) \qquad (2.14)$$

Substituting Equation (2.12) into Equation (2.11) yields the Helmholtz formulation for light propagation under SVEA conditions:

$$\frac{\partial^2 \phi_E}{\partial z^2} - 2jk_0 n_{eff} \cdot \frac{\partial \phi_E}{\partial z} + \frac{\partial^2 \phi_E}{\partial y^2} + \frac{\partial^2 \phi_E}{\partial x^2} + k_0^2 \left(n_0^2 - n_{eff}^2\right) \phi_E = 0 \qquad (2.15)$$

Similarly, substituting Equation (2.14) into (2.11) yields:

$$\frac{\partial^2 \phi_{E_n}}{\partial z^2} - 2jk_0 \cdot n_{eff_n} \cdot \frac{\partial \phi_{E_n}}{\partial z} + \frac{\partial^2 \phi_{E_n}}{\partial y^2} + \frac{\partial^2 \phi_{E_n}}{\partial x^2} + k_0^2 \cdot \left(n_0^2 - n_{eff_n}^2\right) \cdot \phi_{E_n} = 0 \qquad (2.16)$$

By solving Equation (2.15), the light field distribution of an optical field (ϕ_E), characterized by the eigenvalue, n_{eff}, in the presence of a refractive index, n_0, can be determined; whereas, solving Equation (2.16) produces multiple eigenfunctions (ϕ_{E_n}) and eigenvalues (n_{eff_n}), indexed by n, the mode number.

Note that solving Equations (2.15) and (2.16) is computationally intensive for three-dimensional structures. As a result, Equation (2.15) and (2.16) can be further simplified by imposing another assumption on light propagation. If light is assumed to propagate primarily along the optic axis *and* is weakly guided by the waveguide structure, then

$$\left|\frac{\partial^2 \phi_E}{\partial z^2}\right| << 2k_0 n_{eff} \left|\frac{\phi_E}{\partial x}\right|. \qquad (2.17)$$

As a result, the $\frac{\partial^2 \phi_E^h}{\partial z^2}$ term in Equation (2.15) can be neglected. Consequently Equations (2.15) and (2.15) become

$$-2jk_0\tilde{n}_{eff}\frac{\partial \tilde{\phi}_{\mathbf{E}}}{\partial z} + \frac{\partial^2 \tilde{\phi}_{\mathbf{E}}}{\partial y^2} + \frac{\partial^2 \tilde{\phi}_{\mathbf{E}}}{\partial x^2} + k_0^2\left(n^2 - \tilde{n}_{eff}^2\right)\tilde{\phi}_{\mathbf{E}} = 0 \qquad (2.18)$$

and

$$-2jk_0\tilde{n}_{eff_n} \cdot \frac{\partial \tilde{\phi}_{\mathbf{E_n}}}{\partial z} + \frac{\partial^2 \tilde{\phi}_{\mathbf{E_n}}}{\partial y^2} + \frac{\partial^2 \tilde{\phi}_{\mathbf{E_n}}}{\partial x^2} + k_0^2\left(n^2 - \tilde{n}_{eff_n}^2\right)\tilde{\phi}_{\mathbf{E}} = 0 \qquad (2.19)$$

Both Equations (2.18) and (2.19) are known as the Fresnel paraxial wave equations. Note that the eigenfunctions and eigenvalues, $\tilde{\phi}_E$ and $\tilde{n}_{eff}$ in Equation (2.18) as well as $\tilde{\phi}_{E_n}$ and $\tilde{n}_{eff_n}$ in Equation (2.19) are different from the eigenfunctions and eigenvalues in Equations (2.15) and (2.16).

Interestingly enough, while ϕ_E and n_{eff} are not equal to $\tilde{\phi}_E$ and $\tilde{n}_{eff}$, Feit and Fleck proved that ϕ_{E_n} and $\tilde{\phi}_{E_n}$ are identical, while n_{eff_n} and $\tilde{n}_{eff_n}$ are simply related [34].

$$\phi_{E_n} = \tilde{\phi}_{E_n} \qquad (2.20)$$

$$a_{E_n} = \tilde{a}_{E_n} \qquad (2.21)$$

$$n_{eff_n} = -\left[1 - \left(1 + 2\tilde{n}_{eff_n}\right)^{1/2}\right] \qquad (2.22)$$

These relations are useful since the Fresnel paraxial wave equation can be used to obtain information about waveguide structures that violate the paraxial wave propagation assumptions.

Particularly for the RSoft Mode Solver module, imaginary-axis BPM is used in order

to determine optical mode eigenvalues and eigenfunctions. Essentially, the RSoft Mode Solver module simulates

$$2jk_0\tilde{n}_{eff_n}\frac{\partial\tilde{\phi}_{\mathbf{E_n}}}{\partial z} + \frac{\partial^2\tilde{\phi}_{\mathbf{E_n}}}{\partial y^2} + \frac{\partial^2\tilde{\phi}_{\mathbf{E_n}}}{\partial x^2} + k_0^2\left(n^2 - \tilde{n}_{eff_n}^2\right)\tilde{\phi}_{\mathbf{E}} = 0 \qquad (2.23)$$

As described by Equation (2.23), light propagates down an imaginary optic axis $(-jz$ instead of z), each of the waveguide-supported optical modes, n, grows exponentially in intensity, $\tilde{a}_{E_n}$ as light propagates along the imaginary optic axis. Ultimately, $\tilde{a}_{E_n}$ provides a measure of how well guided a mode, n, is for a given waveguide structure. The strick single-mode requirements for the waveguide structures that are used in the optical switches is satisfied by constraining $\tilde{a}_{E_1}$ to a minimum and maximum range and by setting $\tilde{a}_{E_1}$ to be greater than $\tilde{a}_{E_2}$.

In practice, numerical convergence is guaranteed provided that the Equation (2.23) is solved with an implicit numerical method, $n_0 > n_{eff_n}$ (e.g., $n_0 = n_{core}$), and the propagation step size along the optic axis is $\Delta z \to \infty$ [?].

Note that once the transverse steps, Δx and Δy, are set sufficiently small, the transverse steps does not affect numerical convergence. Moreover, the computation region–particularly the W_x and W_y dimensions– does not need to be aggressively tweaked since the waveguide structures are straight and a transparent boundary condition (TBC) is used on the computation region edges.

In particular, since the investigated NEM-HIC devices will be composed of single-mode waveguides, the first design task is to define the cross-sectional dimensions of a dielectric channel rod waveguide that will only support a single mode. In particular, the correlation method is used in conjunction with transparent boundary conditions (TBC) in order to define the cross-sections that will support single-mode propagation.
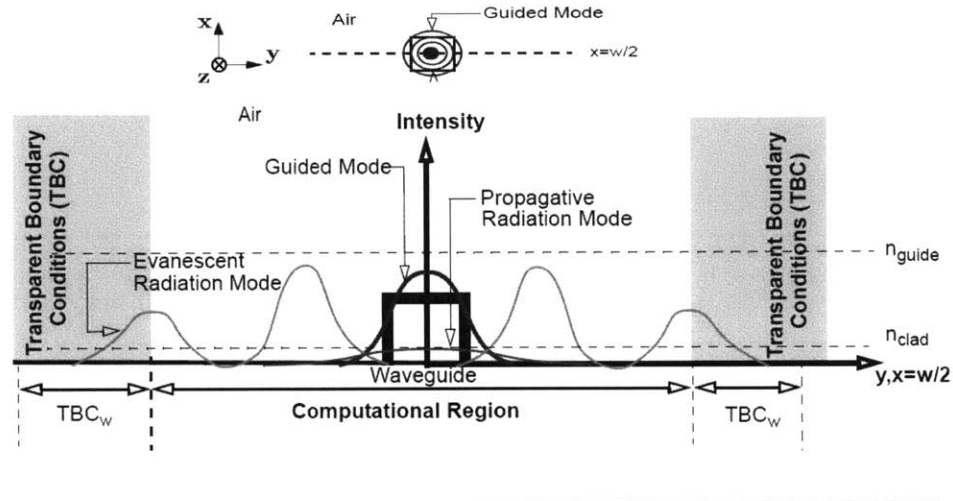
FIGURE 2.4: Depiction of the E_{pq}^x-polarized light intensity distributions for a single-mode square waveguide that is simulated by the correlation method with transparent boundary conditions (TBC). Pictorial diagram of the modal patterns taken along the y-axis at the centered height of the waveguide with denoted mode types.

Figure (2.4) is a pictorial diagram of the mode types that are involved in the correlation method simulation with TBC. Forward propagative guided modes, forward propagative radiation modes, and forward evanescent radiation modes are the mode types that are generated using the correlation method.
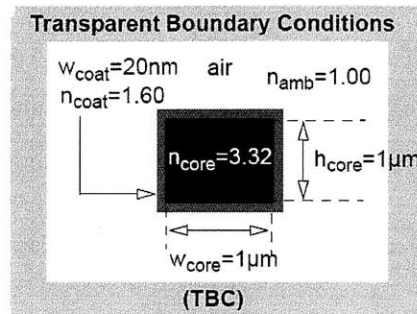
FIGURE 2.5: Index distribution of the waveguide consisting of a $1\mu m \times 1\mu m$ ($w_{core} \times h_{core}$) core ($n_{core} = 3.32$), a $20nm$-thick cladding ($n_{coat} = 1.60$) in air ($n_{back} = n_{air} = 1.00$).

(a) (b) (c)
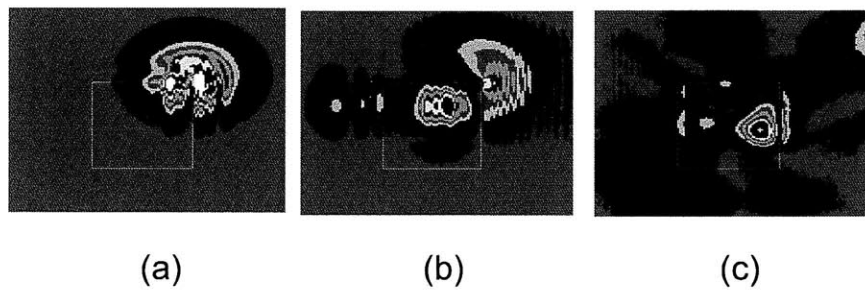
FIGURE 2.6: Excitation of a waveguide during a correlation method simulation. (a) A Gaussian beam of light centered at the waveguide's top right corner excites the waveguide. (b) Distribution of light in the waveguide's cross-section $10\mu m$ along the waveguide. (c) Distribution of light along the waveguide's cross-section $25\mu m$ along the waveguide.

Figure (2.6) graphically illustrates the evolution of a correlation method simulation with a layout of the two-dimensional index distribution that is shown in Figure (2.5) and various simulated eigenvector modal patterns along the waveguide at $z = 0\mu m$ [Figures

(2.6a)], $z = 10\mu m$ [Figure (2.6b)] and $z = 25\mu m$ [Figure (2.6c)] along the optical axis, where the optical axis is oriented into the page. In general, a z-invariant light guiding structure (e.g., a straight waveguide) is best excited asymmetrically in order to stimulate all of the supported modes in the waveguide. In particular, the waveguide structure in Figures (2.5) consists of a $1\mu m \times 1\mu m$ ($w_{core} \times h_{core}$) core cross-section with $n_{core} = 3.32$; the waveguide is coated with a $20nm$-thick conformal coat cladding layer with $n_{coat} = 1.60$ in air ($n_{back} = n_{air} = 1$). Prior to initiating the correlation simulation, a polarization is chosen. For a particular polarization, one specific mode is selected for imaging. After selecting a polarization and a mode to monitor, a $1.55\mu m$ wavelength Gaussian beam excites the waveguide in the top right corner [Figures (2.6a)] which, in turn, couples to all of the symmetric and non-symmetric modes. A Gaussian beam best approximates the distribution of light exiting a single mode fiber. After excitation, light gradually couples into the waveguide (Figure (2.6b)) where the light becomes trapped inside the high-index core by total internal reflection. After the light propagates over an axial distance of $25\mu m$ [Figure (2.6c)], the spatial distribution of the light reaches a cyclic steady state and the simulation automatically stops. For the most part, the cyclic steady state is defined as the repeated modal patterns (eigenvectors) of light as it propagates along the waveguide. Consequently, the correlation simulation terminates after reaching the cyclic steady state of modal evolution. Essentially, the cyclic steady state light distribution consists of a superposition of all the supported guided modes and propagative radiation modes of the waveguide. Upon simulation termination, the selected mode for a given polarization is imaged as a two-dimensional modal distribution along with an associated n_{eff}.

Incidentally, the off-centered Gaussian beam excitation becomes relevant when simulating actual waveguide excitation conditions, e.g., a fiber coupled to an on-chip waveguide. Furthermore, a misaligned fiber will excite higher-order modes (and propagative radiation modes) in the on-chip waveguide if the on-chip waveguide is not properly designed to effectively suppress higher-order modes.

The correlation-method simulation represents a guided mode as a two-dimensional si-
nusoidal field (eigenvector) that corresponds to a particular n_{eff} (eigenmode). Further-
more, a polarization mode is indexed by the number of zero-field nodes in the eigen-
vector. For example, E_{pq}^x E-field light with one node in the x-direction and 2 nodes in
the y-direction is indexed as E_{12}^x [Figure (2.7)]. In general, the modes for both light
orientations are indexed by the E_{pq}^x and E_{pq}^y nomenclature. The p subscript denotes the
number of nodes along the x-direction, and the q subscript denotes the number of nodes
along the y-direction. Additionally, n_{eff} ranges from the index of the guiding material
(n_{guide}) to the index of the cladding material (n_{clad}); low n_{eff} light is weakly confined to
the high index guide and propagates at high speeds; high n_{eff} light is tightly confined
to the high index guide and propagates at slow speeds. The fundamental mode has an
energy maximum at the center of the waveguide (i.e., E_{11}^x and E_{11}^y).
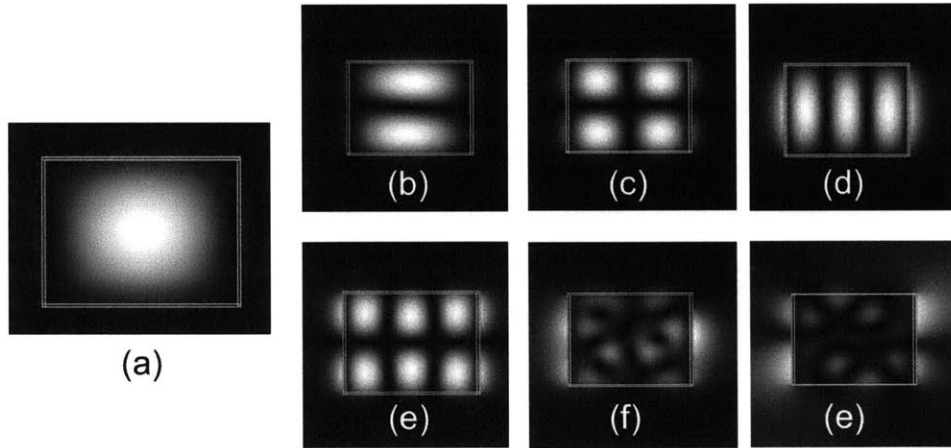
FIGURE 2.7: Correlation method simulation generated E_{pq}^x modal distributions for a
waveguide cross-section of $1\mu m \times 1\mu m$ ($w_{core} \times h_{core}$) and a $20nm$-thick, $n_{coat} = 1.60$
coat cladding. A waveguide length of $40\mu m$ was used to resolve modal steady state.
Forward propagative guided modes (a) E_{11}^x, (b) E_{12}^x, (c) E_{22}^x, (d) E_{31}^x and (e) E_{32}^x.
(f),(g) Unconfined higher-order modes.
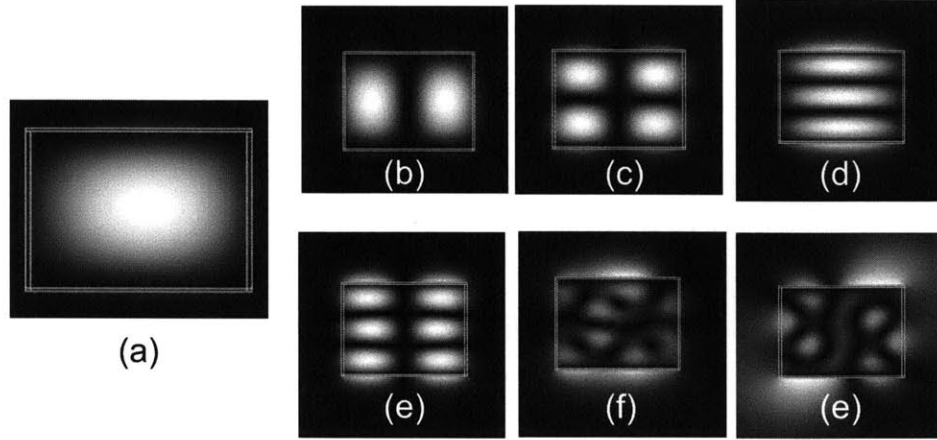
FIGURE 2.8: Correlation method simulation generated E_{pq}^y modal distributions for a waveguide cross-section of $1\mu m \times 1\mu m$ ($w_{core} \times h_{core}$) and a $20nm$-thick, $n_{coat} = 1.60$ coat cladding. A waveguide length of $40\mu m$ was used to resolve modal steady state. Forward propagative guided modes (a) E_{11}^y, (b) E_{21}^y, (c) E_{22}^y, (d) E_{13}^y and (e) E_{23}^y. (f),(g) Unconfined higher-order modes.

Figures (2.7) and (2.8) shows the E_{pq}^x and E_{pq}^y modal distribution patterns for all of the supported modes for a two-dimensional index distribution of a channel dielectric rod waveguide with a $1\mu m \times 1\mu m$ ($w_{core} \times h_{core}$) square high-index core with $n_{core} = 3.32$ and coated with a low-index coat cladding layer with $n_{coat} = 1.60$ in air ($n_{back} = n_{air} = 1.00$). A propagation length of $40\mu m$ insures that all evanescent modes adequately decay and do not contribute to the steady state modes. Accordingly, both E_{pq}^x and E_{pq}^y polarizations are able to support five distinctly confined forward propagative modes [Figure (2.7a), (2.7b), (2.7c), (2.7d), (2.7e) and Figure (2.8a), (2.8b), (2.8c), (2.8d), (2.8e) respectively]. In contrast, Figure (2.7f) and (2.7g) and Figure (2.8f) and (2.8g) represent two forward propagative radiation modes for E_{pq}^x-polarized light and TM-polarized light respectively which contributes to continuous radiative loss. Specifically, the eigenvalues of the two forward propagative radiation modes for both the E_{pq}^x and TM polarizations have a value lower than the waveguide cladding layers refractive index ($n_{eff} = 1.40 < n_{coat} = 1.60$) or below the refractive index of air ($n_{eff} = 0.90 < n_{back} = n_{air} = 1$). As the propagative radiation modes continuously remove light from the waveguide, the waveguide should not just be single-moded; the waveguide should also not support propagative radiation

modes in order to ensure that light remains confined to the waveguide.

2.1.4 Wide Angle Finite Difference Beam Propagation Method (WA FD BPM)

The commercially available software by the RSoft company contains a simulation module that uses several variations of the finite difference beam propagation method (FD BPMs) in order to model light propagation in three-dimensional structures [33].

In general, BPMs are limited in their direct application due to their paraxial and index contrast limitations. After all, BPMs use the Fresnel formulation of light propagation in order to determine the effects that variable waveguide cross-sections and topographical structure have on light propagation. However, an alternative Wide-Angle Finite-Difference Beam Propagation Method (WA FD BPM) can be used to abate the paraxial and index contrast limitations that are embedded in the implementation of traditional BPMs [35].

The WA FD BPM can be derived from the electric-field-formulated Helmholtz equation in Equation (2.10a). To begin with, the Helmholtz equation is formulated for structures with spatially-dependent refractive index distributions (i.e., $\nabla \left(\frac{\nabla \cdot n^2}{n^2} \cdot \mathbf{E} \right) \neq 0$). Therefore, the Helmholtz Hamiltonian for E_{pq}^x and E_{pq}^y electric fields are given as:

$\mathbf{E}_{pq}^x$ E-Field Hamiltonian.

$$\frac{\partial^2 \phi_{E_x}}{\partial z^2} - 2jk_0 \cdot n_{eff} \cdot \frac{\partial \phi_{E_x}}{\partial z} + \frac{\partial^2 \phi_{E_x}}{\partial y^2} + \frac{\partial}{\partial x} \left(\frac{1}{n^2} \cdot \frac{\partial}{\partial x} \left(n^2 \cdot \phi_{E_x} \right) \right)$$
$$+ \frac{\partial}{\partial x} \left(\frac{1}{n^2} \cdot \frac{\partial n^2}{\partial y} \cdot \phi_{E_y} \right) + k_0^2 \cdot \left(n^2 - n_{eff}^2 \right) \cdot \phi_{E_x} = 0 \quad (2.24)$$

E_{pq}^y E-Field Hamiltonian.

$$\frac{\partial^2 \phi_{E_y}}{\partial z^2} - 2jk_0 \cdot n_{eff} \cdot \frac{\partial \phi_{E_y}}{\partial z} + \frac{\partial^2 \phi_{E_y}}{\partial x^2} + \frac{\partial}{\partial y}\left(\frac{1}{n^2} \cdot \frac{\partial}{\partial y}\left(n^2 \cdot \phi_{E_y}\right)\right)$$

$$+ \frac{\partial}{\partial y}\left(\frac{1}{n^2} \cdot \frac{\partial n^2}{\partial x} \cdot \phi_{E_x}\right) + k_0^2 \cdot \left(n^2 - n_{eff}^2\right) \cdot \phi_{E_y} = 0 \quad (2.25)$$

The fifth term in both Equations (2.24) and (2.25) cross couples E_{pq}^x-polarized light to E_{pq}^y-polarized light and vice versa. As an aside, E_{pq}^x-polarized light can be converted to E_{pq}^y-polarized light with large and abrupt variations in refractive index along the y-axis via the $\frac{\partial}{\partial x}\left(\frac{1}{n^2} \cdot \frac{\partial n^2}{\partial y} \cdot \phi_{E_y}\right)$ term in Equation (2.24). Therefore, HIC structures can be designed to function as efficient passive polarization converters [36], [37], [38], [39]. However, since the investigated NEM-HIC devices are not designed to cross-couple polarizations, the semi-vectorial form is only considered. Therefore, Equations (2.24) and Equation (2.25) reduce to:

E_{pq}^x E-Field Hamiltonian.

$$\frac{\partial^2 \phi_{E_x}}{\partial z^2} - 2jk_0 \cdot n_{eff} \cdot \frac{\partial \phi_{E_x}}{\partial z} + \frac{\partial^2 \phi_{E_x}}{\partial y^2} + \frac{\partial}{\partial x}\left(\frac{1}{n^2} \cdot \frac{\partial}{\partial x}\left(n^2 \cdot \phi_{E_x}\right)\right)$$

$$+ 0 + k_0^2 \cdot \left(n^2 - n_{eff}^2\right) \cdot \phi_{E_x} = 0 \quad (2.26)$$

E_{pq}^y E-Field Hamiltonian.

$$\frac{\partial^2 \phi_{E_y}}{\partial z^2} - 2jk_0 \cdot n_{eff} \cdot \frac{\partial \phi_{E_y}}{\partial z} + \frac{\partial^2 \phi_{E_y}}{\partial x^2} + \frac{\partial}{\partial y}\left(\frac{1}{n^2} \cdot \frac{\partial}{\partial y}\left(n^2 \cdot \phi_{E_y}\right)\right)$$

$$+ 0 + k_0^2 \cdot \left(n^2 - n_{eff}^2\right) \cdot \phi_{E_y} = 0 \quad (2.27)$$

Stated more explicitly, the cross-sectional index along the optical axis does not vary rapidly enough to invoke appreciable cross-coupling of modes. The terms in Equations (2.26) and (2.27) will be recast in order to better elucidate the derivation of the WA FD BPM.

$\mathbf{E}_{pq}^x$ E-Field Hamiltonian.

$$\mathcal{X}^2 \phi_{E_x} - 2jk_0 \cdot n_{eff} \cdot \mathcal{X}\phi_{E_x} + \mathcal{P}_{E_x} \cdot \phi_{E_x} = 0 \qquad (2.28)$$

$\mathbf{E}_{pq}^y$ E-Field Hamiltonian.

$$\mathcal{X}^2 \phi_{E_y} - 2jk_0 \cdot n_{eff} \cdot \mathcal{X}\phi_{E_y} + \mathcal{P}_{E_y} \cdot \phi_{E_y} = 0 \qquad (2.29)$$

where:

$$\mathcal{X} = \frac{\partial}{\partial z}$$

$$\mathcal{P}_{E_x} = \frac{\partial^2}{\partial y^2} + \frac{\partial}{\partial x}\left(\frac{1}{n^2} \cdot \frac{\partial}{\partial x}\left(n^2 \cdot\right)\right) + k_0^2 \cdot \left(n^2 - n_{eff}^2\right)$$

$$\mathcal{P}_{E_y} = \frac{\partial^2}{\partial x^2} + \frac{\partial}{\partial y}\left(\frac{1}{n^2} \cdot \frac{\partial}{\partial y}\left(n^2 \cdot\right)\right) + k_0^2 \cdot \left(n^2 - n_{eff}^2\right)$$

Equations (2.28) and (2.29) have a quadratic form which can be solved to yield:

E_{pq}^x E-Field Hamiltonian.

$$\frac{\partial \phi_{E_x}}{\partial z} = j\left(k_0 \cdot n_{eff} \pm \sqrt{k_0^2 \cdot n_{eff}^2 + \mathcal{P}_{E_x}}\right) \cdot \phi_{E_x} \qquad (2.30)$$

E_{pq}^y E-Field Hamiltonian.

$$\frac{\partial \phi_{E_y}}{\partial z} = j\left(k_0 \cdot n_{eff} \pm \sqrt{k_0^2 \cdot n_{eff}^2 + \mathcal{P}_{E_y}}\right) \cdot \phi_{E_y} \qquad (2.31)$$

Taylor series expansion can be used in order to linearize Equations (2.30) and (2.31) and the linearized equation can be used to simulate light propagation. However, Equations (2.30) and (2.31) can be much more accurately linearized with the Padé approximant

[40].

$$\frac{\partial \phi_{E_x}}{\partial x} = j \frac{N_m \left(P_{E_x} \right)}{D_n \left(P_{E_x} \right)} \cdot \phi_{E_x} \qquad (2.32)$$

Where $N_m \left(P_{E_x} \right)$ and $D_n \left(P_{E_x} \right)$ are defined in Table (2.2).

TABLE 2.2: Various orders of Padé approximants

Padé Order	$\mathbf{N_m \left(P_{E_x} \right)}$	$\mathbf{D_n \left(P_{E_x} \right)}$
Padé $(1, 0)$	$N_1 \left(P_{E_x} \right) = \frac{P_{E_x}}{2 \cdot k_0^2 \cdot n_{eff}^2}$	$D_0 \left(P_{E_x} \right) = 1$
Padé $(1, 1)$	$N_1 \left(P_{E_x} \right) = \frac{P_{E_x}}{2 \cdot k_0^2 \cdot n_{eff}^2}$	$D_1 \left(P_{E_x} \right) = 1 + \frac{P_{E_x}}{2 \cdot k_0^2 \cdot n_{eff}^2}$
Padé $(2, 2)$	$N_2 \left(P_{E_x} \right) = \frac{P_{E_x}}{2 \cdot k_0 \cdot n_{eff}} + \frac{P_{E_x}^2}{4 \cdot k_0^3 \cdot n_{eff}^3}$	$D_2 \left(P_{E_x} \right) = 1 + \frac{3 \cdot P_{E_x}}{4 \cdot k_0^2 \cdot n_{eff}^2} + \frac{P_{E_x}^2}{16 \cdot k_0^2 \cdot n_{eff}^2}$

Similar to the correlation method, TBCs are used for WA FD BPM simulations.

The NEM-HIC structures were simulated using Equation(2.32) with a Padé(1,1) order because Padé(1,1) approximants optimally provide accurate and stable results. A demonstration of the stability and accuracy will be provided in the upcoming Integrated Devices Chapter.

2.1.5   Bi-Directional Eigenmode Propagation Method (BEPM)

A two-dimensional bi-directional eigenmode propagation method (BEPM) is used to model light propagation in arbitrary two-dimensional HIC structures. In comparison to other optical simulation methods, BEPM is a recently developed [39] and steadily evolving [41] optical simulation method that can accurately and efficiently model Helmholtz light propagation in rectilinear piecewise structures that are composed of arbitrary refractive indices. In particular, a freely-available two-dimensional BEPM simulation package named CAvity Modeling FRamework (CAMFR) [42], [32], [43] was used to model bi-directional light propagation in HIC structures [32]. Moreover, BEPM simulations are

extremely effective for modeling light propagation in arbitrary directions within materials of arbitrarily defined refractive indices and abrupt material distributions. CAMFR has discretized regions of constant index distributions in order to construct exponential waveform solutions that are governed by the Helmholtz Hamiltonian. Markedly, such a method of discretization relaxes the need to specify a field at discretized meshpoints in optical structures.

The BEPM simulation model is derived from the Helmholtz equation [Equation (2.11)] with piecewise constant regions of refractive indices. Each piece-wise optical wave solution satisfies the boundary conditions.

$$\nabla_y^2 \mathbf{E} + \nabla_z^2 \mathbf{E} + k_0^2 \cdot n^2 \cdot \mathbf{E} = 0 \tag{2.33}$$

Equation (2.33) is the two-dimensional form of Equation (2.11).
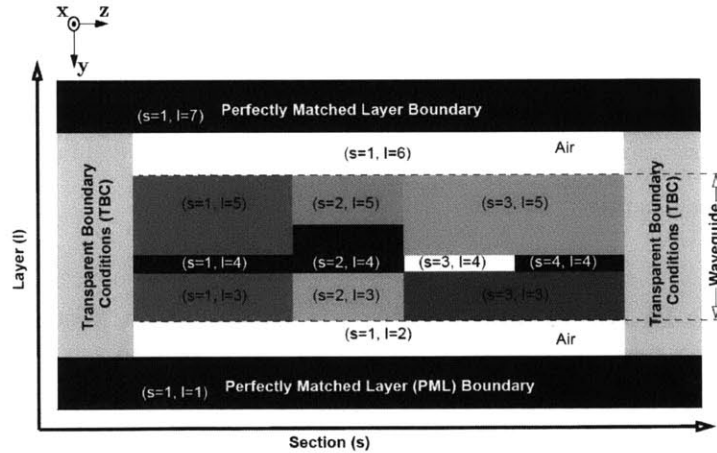
FIGURE 2.9: Computational window containing a multi-sectioned two-dimensional waveguide that is composed of various refractive indices surrounded by air with a perfectly matched layer boundary. The structure was used for a bi-directional eigenmode propagation method (BEPM) simulation. The computational window is enclosed by perfectly matched layer (PML) boundary conditions on the top and bottom, and transparent boundary conditions (TBCs) on the left and right.

Figure (2.9) illustrates an arbitrary dielectric distribution in a CAMFR computational window. Each region of constant refractive index is denoted by a section subscript s, from left to right, and a layer subscript l, from bottom to top. For simplicity, a series of grayscale rectangular structures are defined in the computational window. Each rectangular region represents a dielectric medium with an associated refractive index. Moreover, the colored rectangular regions are discretized into regions of constant refractive index. Furthermore, each region will have an associated electric field optical wave which satisfies the Helmholtz Hamiltonian in Equation (2.33).

The electric field optical wave that is used in Equation (2.33) is given as:

$$\mathbf{E}\left(y,z,t\right) = \hat{x}\left(\varphi_x\left(\mathbf{y}\right)\cdot\varphi_x\left(\mathbf{z}\right)\right)\cdot exp\left(-j\omega_0\cdot t\right) \tag{2.34}$$

where $\varphi_x\left(\mathbf{y}\right)$ is the transversal eigenvector describing light confinement and $\varphi_x\left(\mathbf{z}\right)$ is the propagation eigenvector describing the bi-directional light propagation.

In the x-direction, $\varphi_x\left(\mathbf{y}\right)$ is constructed from a superposition of waves in the layer regions of constant refractive index:

$$\varphi_x\left(\mathbf{y}\right) = \sum_{s,l}\varphi_x^{s,l}\left(y\right) = \sum_{s,l}\sum_{n}t_n^{s,l}\cdot\varphi_{x_n}^{s,l}\left(y\right) \tag{2.35}$$

where n is the number of optical waves and $t_n^{s,l}$ is the nth optical wave amplitude of the eigenvector field distribution for a region denoted by layer l and section s. Equation (2.35) is a solution of superpositioned optical waves that satisfy the boundary conditions of the adjacent regions of constant refractive index. Boundary conditions are matched at each regional interface. The piece-wise solutions of each index invariant layers are then pieced together and weighted to create a global solution for the entire device. Increased accuracy for CAMFR (also for BEPM in general) is achieved by increasing the number of modes (n) in Equation (2.35).

In the z-direction, $\varphi_x(z)$ defines the bi-directional propagation of light across the various regions of constant refractive index:

$$\varphi_x(\mathbf{z}) = \sum_{s,l} f^{s,l} \cdot \varphi_x^{s,l}(y) = \sum_{s,l} b^{s,l} \cdot \varphi_x^{s,l}(-z) \qquad (2.36)$$

$f^{s,l}$ is the forward propagation amplitude, $b^{s,l}$ is the backward propagation amplitude. s is a section of constant refractive index. The boundary that separates each section (s) of constant refractive index determines the forward $\left(f^{s,l}\right)$ and backward $\left(b^{s,l}\right)$ coefficients for both regions as stipulated by continuity conditions of tangential field components.
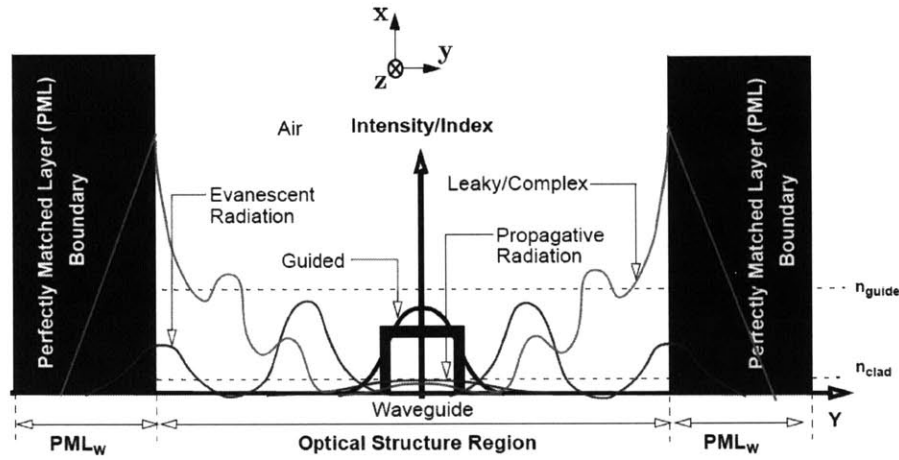
FIGURE 2.10: Mode types represented for optical structures bounded by perfectly matched layer (PML) boundary conditions implemented with a complex distance approach.

Figure (2.10) is an illustration of a *closed* one-dimensional optical structure. In this instance, the optical structure consists of a centered one-dimensional waveguide in air. This optical structure is enclosed (thus rendering the optical structure *closed*) by two *walls* that are defined to have the same refractive index of the optical structure that the walls are adjacent to. The enclosing *walls* serve as boundary conditions to the optical structure and referred to as perfectly match layers (PML). PML boundaries are designed to match the adjacent refractive index(es), so that there are no wave reflections at the

edge of the PML boundaries. Moreover, the PML boundaries are absorptive to any waves that penetrate the boundaries.

Particular to the bound optical structure in Figure (2.10), four types of standing electromagnetic waves are supported: (1) evanescent, (2) propagative (3) leaky/complex and (4) guided waves. Notice in the figure that the guided and propagative waves experience exponential decay before reaching the PML boundary, while the evanescent and leaky/complex waves are artificially terminated within the PML boundary. Exciting the optical structure can result in the excitation of all four waves. However, as the waves are made to propagate along the z axis (into the page), only the guided wave(s) will remain as the other waves will eventually be attenuated, and eventually absorbed by the PML boundary as the waves spread within the optical structure.

CAMFR, the bi-directional eigenmode expansion method-based simulation software, represents and simulates optical structures in a similar fashion as the example closed optical structure in Figure (2.10).

Particular to CAMFR, PML boundaries are created using complex coordinate stretching. [44]. Complex coordinate stretching is a way of implementing PML boundaries by maintaining an equal refractive index with the adjacent material (e.g., $n_{PML} = n_{air}$), while gradually introducing a light attenuating complex thickness. Implementing PML in BEPM does not require specialized boundary condition optimizations since BEPM PML boundary conditions do not introduce parasitic reflections due to finite difference discretization effects.

$$\varphi_x^{s=1,l=7}(\tilde{y}) \rightarrow \varphi_x^{s=1,l=7}\left(\int_0^y s_y(y') \cdot dy'\right) \tag{2.37}$$

In Equation (2.37), $s_y(y)$ is a region specific function that remains equal to one in the simulation window and becomes complex in the PML region [e.g., $s = 1$, $l = 7$ in Figure (2.9)]. Moreover, at the junction between the PML region and the adjacent index [i.e., air in Figure (2.9)], $\varphi_x^{s=1,l=7}(y) = \varphi_x^{s=1,l=6}(y)$. As light penetrates the PML region, the complex distance attenuates the incoming light without generating reflections.

Specifically, the PML region has a linear attenuation profile. In general, Equation (2.37) represents how the complex coordinate stretching is incorporated into the optical wave of the upper PML region. Subsequently, the Helmholtz Hamiltonian is transformed to:

$$\left(\frac{\partial}{\partial y} \cdot \frac{1}{s_y} \cdot \frac{\partial}{\partial y} \cdot \frac{1}{s_y} \right) \cdot \mathbf{E} + \nabla_z^2 \mathbf{E} + k_0^2 \cdot n^2 \cdot \mathbf{E} = 0 \qquad (2.38)$$

Depending on the conditions that are used for the perfectly matched layer (PML), radiative and leaky modes can be simulated. A thick PML layer with weak attenuation effectively creates radiative modes that are gradually attenuated over a long length extending into the PML. A thin PML with strong attenuation effectively creates leaky modes. Incident light entering a strongly attenuating PML region is instantly absorbed.

2.2 Electromechanical Operation

Microelectromechanical (MEM) technology involves the creation of mechanically movable millimeter- to micrometer-scale structures. Unlike macroscopic structures, MEM structures are largely dominated by surface effects while volumetric effects become inconsequential to the actuation performance to the first order. More specifically, surface effects like electrostatic forces from charged surfaces, and meniscus forces from aqueous displacement are easily transduced into mechanical deflection. Volumetric effects like material weight and inertial forces contribute negligibly to the mechanical deflection of MEM structures [45], [46].

A variety of MEM structures have been successfully created with semiconductor planar fabrication techniques. Not only are semiconductor planar fabrication techniques capable of producing high-quality micron-scale structures with accuracy and precision, these techniques can also be used to mass produce arrays of micron-scale structures at a low cost. Therefore, the majority of commercially successful MEM structures are created with semiconductor fabrication techniques.

Almost immediately following the success of MEM devices, researchers endeavored to further push the limits of MEM technology by creating mechanically movable micron- to nanometer-scale structures. Naturally, mechanically movable micron- to nanometer-scale structures are classified under the rubric of nanoelectromechanical (NEM) technology. Even though many of the same semiconductor fabrication techniques that are used to realize MEM structures are also accommodative to NEM structures, the reduction in scale presents nuanced challenges and advantages specific to NEM technology.

As the name implies, the investigated NEM-HIC devices fall under the rubric of NEM technology due to the electrostatic waveguide beam dimensions and separations that are required to guide $1550nm$ wavelength light. As a rule of thumb, the wavelength of the light (λ_0) to be guided normalized by the guiding medium's refractive index specifies the dimensions of a single-moded waveguide [i.e., dimension $\left(\sim \frac{\lambda_0}{n_{core}} \right)$]. In particular, $1550nm$ wavelength light that is guided in a HIC waveguide with a differential refractive index of $\Delta n = 2.32$ is most optimally guided in a waveguide with a characteristic dimensional length between $200nm - 600nm$. Therefore, HIC waveguides functionalized for electromechanical operation are designed with and crafted from NEM technology.

Although much of the analysis that follows is universally applicable to both MEM and NEM technologies, there are some size-dependent effects that are specific to NEM technology. Throughout this thesis, size-dependent NEM effects will be highlighted when relevant to the discussion.

2.2.1   Modeling Electromechanical Actuation

All of the electromechanical simulation methods are based on the Euler-Bernoulli vibrating beam formulation which is one of four prevailing vibrating beam theories (Euler-Bernoulli, Rayleigh, shear and Timoshenko) that describe the mechanics of a vibrating beam [47]. Although the Euler-Bernoulli formulation does not capture second-order beam effects (i.e., beam shear and beam rotation), the commonly-used Euler-Bernoulli formulation is considered to be sufficient for modeling the MEMS of all of the optical switch devices since this formulation provides a high level of accuracy for slender beam geometries, geometries that are used in the MEMS of these devices.

The MEMS of each of the optical switch devices are simulated using three different types of models: (1) a quasi-static, electromechanical parallel-plate structure with one degree of motion freedom (QS-1D model), (2) a quasi-static, multi-beam-articulated mechanical structure with three degrees of motion freedom (QS-3D model) and (3) a dynamic, electromechanical parallel-plate structure with one degree of motion freedom (D-1D model).

The QS-1D model is numerically simulated with Matlab scripts. The QS-3D model is simulated with an open-source, Matlab-compatible software called SUGAR. SUGAR is based on the nodal method, a particular implementation of a finite-element method (FEM) simulation.[3] The D-1D model is simulated with Simulink using a finite-difference, time-domain method (FDTD) simulation approach; specifically, an implicit, FDTD algorithm is employed.

What follows is a description of the governing equations that are used for each model by using Lagrange Mechanics [48], [49], [50]. Lagrange Mechanics is a versatile method for formulated equations for static and dynamic systems [48]. As a direct result of Lagrange's equations being based on the principle of virtual work, the set of equations that must be solved are much more simple than those created from vectorial analysis

---

[3]SUGAR uses an implementation which is similar to the well-known SPICE simulation tool used for large-scale circuit simulations.

of Newton's laws of motion (e.g., using Lagrange Mechanics, constraint forces can be eliminated from problem considerations) [49].

In the most general form, Lagrange's equations are formulated to account for non-conservative forces for nonholonomic systems [49]:

$$\frac{d}{dt}\left(\frac{\partial L}{\partial q_i}\right) - \frac{\partial L}{\partial q_i} = Q_i + \sum_{j=1}^{m} \lambda_i a_{ji} (i = 1, 2, \ldots, n), \qquad (2.39)$$

where

$L = V + T$	The Lagrangian
V	Conservative Time-Independent Potential Energy
T	Conservative Kinetic Energy
q_i	Generalized Coordinate
i	Degree Of Motion Freedom
Q_i	Non-Conservative Energy
λ_i	The Lagrange Multipler
$a_j i$	
n	Number Of Degrees Of Freedom
m	Number of Constraints

Equation (2.39) represents n-number of equations that are to be solved. In addition to these equations, m-number of constraints to the degrees of freedom of the q_i generalized coordinates are incorporated into the function as constraint forces along the path of the generalized coordinate [48]. The Lagrange multiplier is used to relate the generalized variable path constraints to constraint forces [48]. In addition to these equations, m-number of constraints must be incorporated to establish generalized variable-trajectory dependency through a given parameter space (as stipulated by a nonholonomic system). Essentially, n-number of equations of free generalized variables and m-number of equations of constraints on those generalized variables are to be solved for the q_i and λ_i unknowns [48]. L is the Lagrangian function and is defined as the difference

between the kinetic (T) and potential (V) energies of a conservative system where V is defined as a function of position only. Q_i represents forces that are not derivable from V. Q_i includes forces that will either add (e.g., time-dependent driving forces) or remove (non-conservative friction forces) energy from the conservative system represented by L [smith-advanced-1960].

Equation (2.39) is used for both the QS-3D and D-1D models. For the QS-1D model, the Lagrange's equations take on a much more simplified form:

$$\frac{d}{dt}\left(\frac{\partial L}{\partial q_i}\right) - \frac{\partial L}{\partial q_i} = 0 \qquad (2.40)$$

TABLE 2.3: Energy functions for an electromechanical parallel plate actuator that is comprised of a zero-thickness parallel plate capacitor (C_{cap}) attached to a lumped element suspension spring (k_{eff}).

Generalized Variable

x_i	g_x

g_x: Deflection of parallel plate

Conservative Energy

Kinetic Energy		
	T	Not Applicable (N/A)
Potential Energy		
	U	$\mathbf{U_{bend} = \frac{1}{2}k_{eff}g_x^2}$
		$\mathbf{U_{estatic} = \frac{1}{2C_{cap}}Q_x^2}$

k_{eff}: Spring constant of suspension

spring

Q_x: Charge on parallel plate

C_{cap}: Capacitance

Non-Conservative Energy

Dissipation Energy		
	D	N/A
Work Energy		
	W	N/A

Table (2.3) presents the energies associated with a one-dimensional parallel plate electrostatic actuator (i.e., a parallel plate actuator) and identifies the separation between the plates (or electrodes) g_x as the generalized variable that transfers energy between the two types of conservative potential energies. Specifically, g_x transfers energy between the conservative energy of a one-dimensional zero-thickness electrostatic parallel plate actuator and the energy associated with the spring that suspends the one-dimensional zero-thickness electrostatic parallel plate actuator. Hence, a change in g_x redistributes the energy between the spring suspension ($\mathbf{U_{bend}}$) and the zero-thickness electrostatic parallel plate actuator ($\mathbf{U_{estatic}}$) without any loss of energy. In general, Lagrange equations can be directly formulated from a table similar to Table (2.3).

$$\partial\left(T+U\right) = \sum_{i=1}^{N}\left(\frac{d}{dt}\left(\frac{\partial\left(T+U\right)}{\partial\dot{x}_i}\right) - \frac{\partial\left(T+U\right)}{\partial x_i}\right) = 0 \qquad (2.41)$$

A force equation can be formulated by summing all of the conservative energy terms and varying the summated energy over a generalized variable.

Moreover, if the generalized variables (x_i) and their associated generalized velocities $\dot{x}_i$ are independent, then the two bracketed terms for each x_i and $\dot{x}_i = \frac{dx_i}{dt}$ in Equation (2.41) are equal to zero:

$$\frac{d}{dt}\left(\frac{\partial\left(T+U\right)}{\partial\dot{x}_i}\right) - \frac{\partial(T+U)}{\partial x_i} = 0 \text{ for } i = 1, 2, \cdots N \qquad (2.42)$$

Additionally, the non-conservative work energy (**W**) and dissipation energy (**D**) can be included in the formulation of the Lagrange equation [Equation (2.42)]:

$$\frac{d}{dt}\left(\frac{\partial\left(T+U\right)}{\partial\dot{x}_i}\right) - \frac{\partial(T+U)}{\partial x_i} + \frac{\partial D}{\partial\dot{x}_i} - \frac{\partial W}{\partial x_i} = 0 \text{ for } i = 1, 2, \cdots N \qquad (2.43)$$

Essentially, W adds energy to the conservative system, while D removes energy from the conservative system.

In order to solve a multivariate Lagrange equation, a specific number of constraint equations $(M_{constraint})$ need to be specified in order to balance the number of degrees of freedom (N_{DOF}) of a system with n_{x_i} (the number of generalized variables). Stated more explicitly, if n_{xi} and N_{DOF} are not equal, $M_{constraint} = n_{x_i} - N_{DOF}$ constraint equations must be defined in order to uniquely solve the Lagrange equations.

$$\frac{d}{dt}\left(\frac{\partial\left(T+U\right)}{\partial\dot{x}_i}\right) - \frac{\partial(T+U)}{\partial x_i} + \frac{\partial D}{\partial\dot{x}_i} - \frac{\partial W}{\partial x_i} - \sum_{l=1}^{M_{constraint}}\lambda_1\frac{\partial G_l}{\partial x_i} = 0 \ \ for \ i = 1, 2, \cdots N$$

$$(2.44)$$

In the final analysis, the constraint equations (G_l) with Lagrange multipliers (λ_l) for a system that are specified for each x_i general variables are used to derive a uniquely solvable equation for each x_i generalized variable.

Before examining the three simulation methods that are used to model the electrome-chanical behavior of the electromechanical optical switches, a few variables will now be defined.
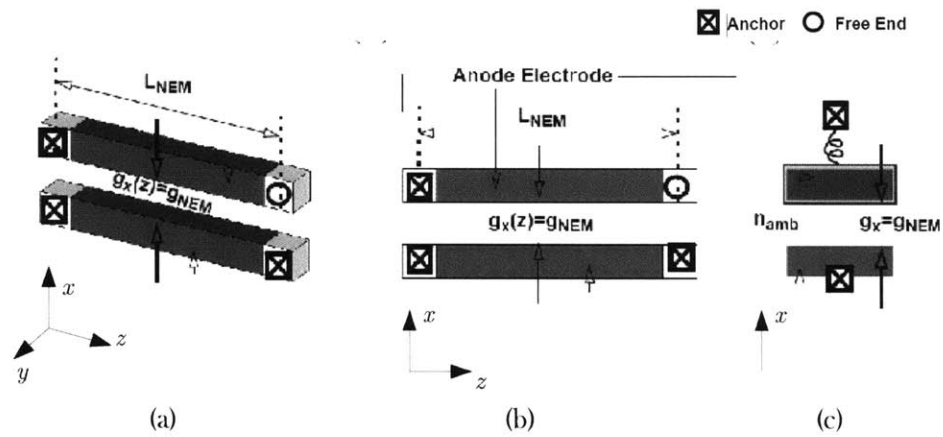
FIGURE 2.11: Schematic of three types of electromechanical cantilever beam models in the undeflected configurations: (a) undeflected three-dimensional beam, (b) undeflected two-dimensional beam, (c) undeflected one-dimensional beam

Figures (2.11) and (2.12) and depict three representational levels of an electrostatic cantilever beam (cantilever beam) parallel plate actuator.
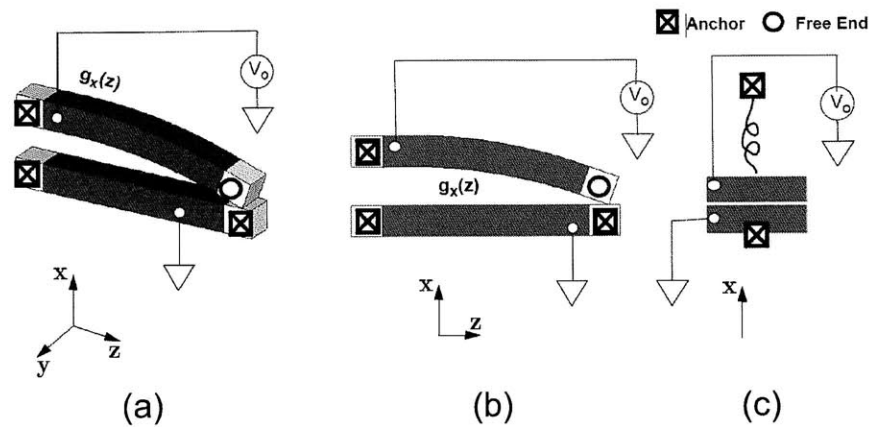
FIGURE   2.12:   (a)   Electrostatically-actuated   three-dimensional   beam,   (b)
electrostatically-actuated   two-dimensional   beam,   (c)   electrostatically-actuated
one-dimensional beam.

Figures (2.11a) and (2.12a) represent a three-dimensional cantilever beam parallel plate
actuator in the undeflected and deflected configurations, respectively. Figures (2.11b)
and (2.12b) represent a two-dimensional cantilever beam parallel plate actuator. Fig-
ures (2.11c) and (2.12c) represent a one-dimensional cantilever beam parallel plate ac-
tuator. Although the three-dimensional cantilever beam parallel plate actuator rep-
resentation most closely models an actual cantilever beam parallel plate actuator, the
two-dimensional and one-dimensional cantilever beam parallel plate actuator representa-
tions can accurately capture the classical mechanics of an actual cantilever beam parallel
plate actuator under certain circumstances.

$$g_x(z,t)\big|_{z=z_{end}} = 0 \qquad g_x(z,t)\big|_{z=z_{end}} = 0 \qquad \frac{\partial^2 g_x(z,t)}{\partial z^2}\bigg|_{z=z_{end}} = 0 \qquad \frac{\partial g_x(z,t)}{\partial z}\bigg|_{z=z_{end}} = 0$$

$$\frac{\partial^2 g_x(z,t)}{\partial z^2}\bigg|_{z=z_{end}} = 0 \qquad \frac{\partial g_x(z,t)}{\partial z}\bigg|_{z=z_{end}} = 0 \qquad \frac{\partial^3 g_x(z,t)}{\partial z^3}\bigg|_{z=z_{end}} = 0 \qquad \frac{\partial^3 g_x(z,t)}{\partial z^3}\bigg|_{z=z_{end}} = 0$$
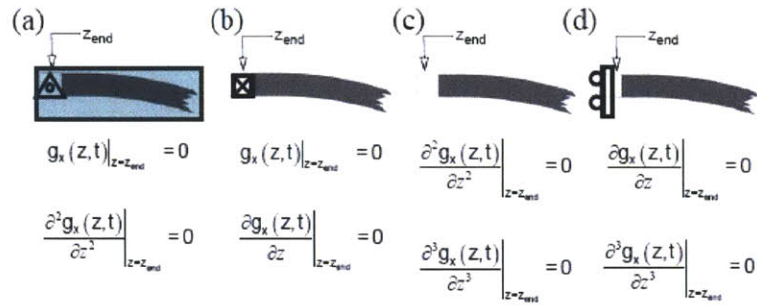
FIGURE 2.13: The four basic types of boundary conditions for a beam: (a) hinged end, (b) fixed end, (c) free end, and (d) guided end.

The specific boundary conditions of vibrating beams are discussed next. Figure (2.13) presents the four basic boundary conditions which can be used to bend a beam with an applied force.

The cantilever beam parallel plate actuator is defined as a beam with boundary conditions illustrated in Figure (2.13b) where $z_{end} = 0$, and Figure (2.13c) where $z_{end} = L_{NEM}$. In other words, the cantilever beam is defined as a beam that is fixed or anchored at one end ($z_{end} = 0$) and unconstrained and free to move at the other end ($z_{end} = L_{NEM}$).

As a result, the boundary conditions of the cantilever beam parallel plate actuator is given by:

$$g_x\left(z = L_{NEM}\right)\big|_{F_{estatic}=0} = g_x\left(z = 0\right)\big|_{F_{estatic}=0} = g_{NEM} \tag{2.45}$$

where $g_x\left(z\right)$ is defined as the generalized variable for both a three-dimensional and two-dimensional cantilever beam parallel plate actuator, g_x is the generalized variable for

the one-dimensional parallel plate actuator, and g_{NEM} is defined as the initial separation between the fixed bottom cathode electrode and freely moving top anode electrode. Specifically for the three- and two-dimensional parallel plate actuator, g_{NEM} is maintained along the length of the top anode electrode beam [Figures (2.11a), (2.11b)].

After applying a voltage (V_0) to the cantilever beam parallel plate actuators [Figure (2.12a), (2.12b), (2.12c)], the boundary conditions are then defined by:

$$g_x \left(z = L_{NEM} \right) |_{F_{estatic} \neq 0} = g_x |_{F_{estatic} \neq 0} < g_{NEM} \qquad (2.46a)$$

$$g_x \left(z = 0 \right) |_{F_{estatic} \neq 0} = g_{NEM} \qquad (2.46b)$$

Thus, applying V_0 results in an electrostatic force $(\mathbf{F}_{estatic})$ which creates a beam deflection. Consequently, the end point conditions of each of the parallel plate actuator representations are given by Equations (2.46a) and (2.46b). $g_x \left(z = L_{NEM} \right)$ and g_x are free to move, while $g_x \left(z = 0 \right)$ is anchored.

The following discussion will reference the information in Table 2.4. As a demonstration of the Lagrangian method, the one-dimensional cantilever beam parallel plate actuator has two potential energy terms: an electrostatic potential energy term that is associated with the charge attraction of two oppositely charged plates and the stored spring energy term associated with the suspension of the movable plate. Moreover, for the case of static actuation, the kinetic energy of the beams inertia is disregarded $(T = 0)$. Therefore, the total energy associated with static actuation is expressed as:

$$(U_{bend} + U_{estatic} + T) = \frac{1}{2} \cdot k_{eff} \cdot (g_{NEM} - g_x)^2 + \frac{1}{2} \cdot \frac{Q_x^2}{C_{cap}} + 0 \qquad (2.47)$$

Equation (2.47) represents the balance of all of the conservative energy of the one-dimensional parallel plate actuator system. The relationship among charge, capacitance

and voltage is given by $Q = C_{cap} \cdot V_0$ with capacitance specifically defined as

$$C_{cap} = \epsilon_0 \cdot n_{back}^2 \cdot \frac{A_{NEM}}{g_x},$$

where n_{back} is the refractive index of the ambient material (air), and A_{NEM} is the area of the cantilever beams electrostatic surface that is used as the parallel plate actuators anode. Equation (2.47) can be reformulated in terms of a voltage (V_0) and a displacement (g_x).

$$(U_{bend} + U_{estatic}) = \frac{1}{2} \cdot k_{eff} \cdot (g_{NEM} - g_x)^2 + \frac{1}{2} \cdot V_0^2 \cdot \left(\epsilon_0 \cdot n_{back}^2 \cdot \left(\frac{A_{NEM}}{g_x} \right) \right) \quad (2.48)$$

Consequently, the derivative of Equation (2.48) is given as:

$$\frac{\partial (U_{bend} + U_{estatic})}{\partial g_x} = -k_{eff} \cdot (g_{NEM} - g_x) - \frac{1}{2} \cdot V_0^2 \cdot \left(\epsilon_0 \cdot n_{back}^2 \cdot \left(\frac{A_{NEM}}{g_x^2} \right) \right) = 0 \quad (2.49)$$

At this point, the phenomenon of instability is highlighted. Instability is a readily observed physical phenomenon that can be mathematically determined. Moreover, by taking an additional derivative of Equation (2.49), the point of instability can be ascertained.

$$\frac{\partial^2 (U_{bend} + U_{estatic})}{\partial g_x^2} = k_{eff} \cdot + V_0^2 \cdot \left(\epsilon_0 \cdot n_{back}^2 \cdot \left(\frac{A_{NEM}}{g_x^3} \right) \right) \quad (2.50)$$

Setting Equation (2.50) to zero establishes the point where the one-dimensional cantilever beam parallel plate actuator transitions from stable solutions to unstable solutions. Generally speaking, stable solutions are designated by the solutions to Equation (2.50) where a positive change in force results in a positive change in displacement [i.e.,

Equation (2.50) < 0]. On the other hand, unstable solutions are designated by the solutions to Equation (2.50) where a negative change in force results in a positive change in displacement [i.e., Equation (2.50) > 0]. In short, an incremental change in deflection should yield a positive incremental change in force [Equation (2.50) > 0], otherwise the force-deflection balance will become unstable [Equation (2.50) < 0]. Therefore, simultaneously solving the energy divergence equation [Equation (2.49)] and the force divergence equation Equation (2.50) yields stability-bounding and energy-minimizing solutions. Accordingly, solving Equation (2.49) and Equation (2.50) yields a specific voltage and parallel plate actuator separation, which are known as the pull-in voltage ($V_{S_{PI}}$) and the pull-in gap ($g_{S_{PI}}$).

$$g_{S_{PI}} = \frac{2}{3} \cdot g_{NEM} \tag{2.51a}$$

$$V_{S_{PI}}^2 = \frac{8}{27} \cdot \frac{k_{eff} \cdot g_{NEM}^3}{\epsilon_0 \cdot n_{back}^2 \cdot A_{NEM}} \tag{2.51b}$$

Simply stated, $g_{S_{PI}}$ and $V_{S_{PI}}$ mark the transition state where an electrostatically-deflected beam uncontrollably snaps into the oppositely charged beam.

Additionally, external forces (F_{ext}) acting upon a one-dimensional beam linearly alters the $g_{S_{PI}}$ but quadratically alters the $V_{S_{PI}}$.

$$g_{S_{PI}} = \frac{2}{3} \cdot g_{NEM} \cdot \left(1 + \frac{P_{ext}}{g_{NEM} \cdot k_{NM}} \right) \tag{2.52a}$$

$$V_{S_{PI}}^2 = \frac{8}{27} \cdot \frac{k_{NM} \cdot g_{NEM}^3}{\epsilon_0 \cdot n_{back}^2 \cdot A_{NEM}} \cdot \left(1 + \frac{P_{ext}}{g_{NEM} \cdot k_{NM}} \right)^3 \tag{2.52b}$$

where P_{ext} is the resultant pressure of an external force acting on a specific area (i.e., $P_{ext} \cdot A_{NEM} = F_{ext}$) of the one-dimensional parallel plate actuator. Similar to the derivation of $g_{S_{PI}}$ and $V_{S_{PI}}$ in Equation (2.51), a derivation of the $g_{S_{PI}}$ and $V_{S_{PI}}$ in Equation (2.52) can be found in reference [51].

Moreover, adding a dielectric coating with a thickness w_{coat} and a refractive index n_{coat} to the one-dimensional parallel plate actuators cathode and anode electrodes results in a pull-in gap and a pull-in voltage given by:

$$g_{S_{PI}} = \frac{2}{3} \cdot g_{NEM} \cdot \left(1 + \frac{P_{ext}}{g_{NEM} \cdot k_{NM}}\right) \cdot \left(1 + \frac{2w_{coat}}{g_{NEM} \cdot n_{coat}^2}\right) \quad (2.53\text{a})$$

$$V_{S_{PI}}^2 = \frac{8}{27} \cdot \frac{k_{NM} \cdot g_{NEM}^3}{\epsilon_0 \cdot n_{back}^2 \cdot A_{NEM}} \cdot \left(1 + \frac{P_{ext}}{g_{NEM} \cdot k_{NM}}\right)^3 \cdot \left(1 + \frac{2w_{coat}}{g_{NEM} \cdot n_{coat}^2}\right)^2 \quad (2.53\text{b})$$

Similar to the derivation of $g_{S_{PI}}$ and $V_{S_{PI}}$ in Equation (2.42), a derivation of the $g_{S_{PI}}$ and $V_{S_{PI}}$ in Equation (2.53) with $P_{ext} = 0$ can be found in reference [52].
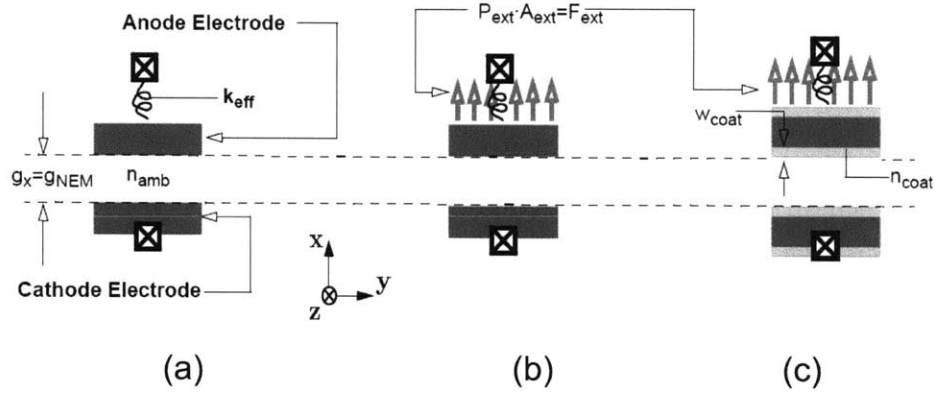
FIGURE 2.14: Schematic of one-dimensional parallel plate actuators: (a) undeflected one-dimensional parallel plate actuator. (b) undeflected one-dimensional parallel plate actuator with an external force acting on the anode electrode, (c) undeflected one-dimensional parallel plate actuator with a dielectric coating and an external force acting on the anode electrode.
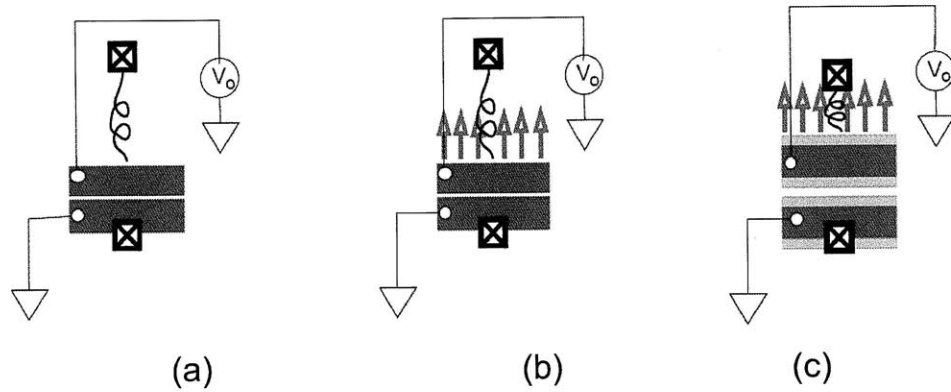
FIGURE 2.15: (a) Electrostatically-actuated one-dimensional parallel plate actuator, (b) electrostatically-actuated one-dimensional parallel plate actuator with an external force acting on the anode electrode, (c) electrostatically-actuated one-dimensional parallel plate actuator with a dielectric coating and an external force acting on the anode electrode.

Figures (2.14) and (2.15) illustrate the one-dimensional parallel plate actuator for the three different cases; each of the three case are mathematically expressed in Equations (??), (2.52) and (2.53).

Figures (2.14a) and (2.15a) illustrate an ideal one-dimensional parallel plate actuator in two states; the parallel plate actuator is composed of two complimentary parallel capacitive plates (an anode and a cathode plate) with an area of A_{NEM} (into the page). The cathode plate is anchored; the anode plate is attached to an anchored suspension with a spring constant k_{eff}. For a given k_{NM} suspension, the pull-in voltage and pull-in gap of the parallel plate actuator have only a geometric dependence on initial separation g_{NEM} and the plate area A_{NEM}[Equation (??)].

Figures (2.14b) and (2.15b) illustrate the two states of a one-dimensional parallel plate actuator with an external force (F_{ext}) acting on the movable anode electrode; F_{ext} is the result of an external pressure ($\mathbf{P_{ext}}$) acting across a lump element area A_{ext}. Possible sources of F_{ext} can be attributed to nonidealities arising from fabrication (e.g.,

beam material deposition), multi-material compositions of MEM/NEM structures, thermal mismatch of constituent materials comprising the MEM/NEM structures[45] and residual charge accumulation in electrically-isolated conductors [51]. P_{ext} can have a substantial affect on the pull-in voltage and pull-in gap of the one-dimensional parallel plate actuator [Equation (2.52)]. Therefore, P_{ext} can be used advantageously to diminish the effects of pull-in voltage/pull-in gap uncertainty arising from geometric fabrication irregularities [47].

Figures (2.14c) and (2.15c) illustrate a one-dimensional parallel plate actuator coated with a dielectric material with F_{ext} acting on the anode electrode. A coated parallel plate actuator ensures non-calamitous operation and repeatability by prevention of an anode-to-cathode electrical short and providing a physical stop upon pull-in voltage. Moreover, careful selection of both dielectric material and the deposition method for the dielectric coating can be used to reduce the effects of P_{ext} due to residual charge accumulation [53],[54],[55].

2.2.2   Finite Element Method (FEM)

A high level of device model abstraction is required in order to effectively and efficiently capture the complexity of multiple-beam articulated devices. A program called SUGAR is used in order to simulate complex multi-beam articulated devices. SUGAR is a Matlab-based microelectromechanical simulation program that uses parameterization algorithms that are similar to the popular SPICE circuit simulator [56], [57]. Analogous to SPICE's nodal analysis, which determines undefined interstitial voltages and currents in a circuit that is driven by voltage and/or current sources (boundary conditions), SUGAR determines undefined interstitial node displacements and angular deflections for an articulated beam structure that is driven by external loads and boundary conditions. Specifically, external loads are defined as point forces and moments. In other words, SUGAR calculates the transverse deflection, axial deflection and angular displacement of an articulated structure in response to the point forces, moments and electrostatic

forces. The important thing to realize is that complex three-dimensional mechanical/-electromechanical structures can efficiently and effectively be simulated with SUGAR without requiring computationally-intensive algorithms.

Table (2.4) on the following three pages lists the conservative energies, non-conservative energies and boundary conditions that are used for simulating three-dimensional structures in SUGAR. Since SUGAR is only used for electrostatic analysis, the kinetic energy is not considered.

TABLE 2.4: Energy functions used to formulate the Lagrange equations for electrostatic actuation modeled by the Nodal Method.

Generalized Variable

x_i	$v_i,\ v_j,\ \theta_i,\ \theta_j,\ ,\ u_i,\ u_j$

v_i: Transverse deflection at Node i.
v_j: Transverse deflection at Node j.
θ_i: Rotation at Node i.
θ_j: Rotation at Node j.
u_i: Axial Extension/ Compression at Node i.
u_j: Axial Extension/ Compression at Node j.

Conservative Energy

Kinetic Energy		
	T	N/A
Potential Energy		
	U	$U_{\text{tran}} = \int\limits_{0}^{L_{NEM}} \frac{EI}{2}\left(\frac{\partial^2 v_{ij}(x)}{\partial x^2}\right)^2 \partial x$
		$U_{\text{estatic}} = \int\limits_{0}^{L_{NEM}} \frac{EA}{2}\left(\frac{\partial^2 u_{ij}(x)}{\partial x^2}\right)^2 \partial x$

E: Young's (elastic) modulus.
I: Moment of inertia of a beam.
A: Cross-section of a beam.
$v(x)$: Transverse displacement profile of a deflected beam.
$u(x)$: Axial displacement profile of a deflected beam.

Non-Conservative Energy

Dissipation Energy		
	D	N/A
Work Energy		
	$\mathbf{W}_{\text{force}}$	$F_i \cdot \delta v_i,\ F_j \cdot \delta v_j,\ F_i \cdot \delta u_i,\ F_j \cdot \delta u_j$, etc.

$F_i/\ F_j$: Point force at Node $i/\ j$.
$\delta v_i/\ \delta v_j$: Transverse deflection of Node $i/\ j$.

Continued on Next Page...

Table 2.4 – Continued

$\delta u_i / \; \delta u_j$: Axial extension of Node $i/\;j$.

$\mathbf{W_{estatic}}$ $-\frac{\epsilon_0 V_0^2 h}{2} \left[\int_0^{L_{NEM}} \aleph(z)\,\mathbf{H}_i(z)\,\partial z \right]\Big|_{z=0} \cdot \delta v_i$

$-\frac{\epsilon_0 V_0^2 h}{2} \left[\int_0^{L_{NEM}} \aleph(z)\,\mathbf{H}_j(z)\,\partial z \right]\Big|_{z=0} \cdot \delta v_j$

$-\frac{\epsilon_0 V_0^2 h}{2} \left[\int_0^{L_{NEM}} \aleph(z)\,\mathbf{H}_{i*}(z)\,\partial z \right]\Big|_{z=0} \cdot \delta v_{i*}$

$-\frac{\epsilon_0 V_0^2 h}{2} \left[\int_0^{L_{NEM}} \aleph(z)\,\mathbf{H}_{j*}(z)\,\partial z \right]\Big|_{z=0} \cdot \delta v_{j*}$

$\aleph(z) = \frac{\alpha_{fringe}\left(g_{NEM}+v_{ij}(z)+v_{i*j*}(z)\right)/h}{\left(g_{NEM}+v_{ij}(z)+v_{i*j*}(z)\right)^2}$

V_0: Applied Voltage.

$v_{ij}(z)$: Transverse deflection profile of a beam between Nodes i and j.

$H_{ij}(z)$: Hermitian shape function.

h: Beam thickness.

L_{NEM}: Length of suspended beam element.

Constraints

Equal Transverse Deflection at Node i		
	$\mathbf{G}_1$	$v_{ij}(0) = v_i$
Equal Axial Deflection at Node i		
	$\mathbf{G}_2$	$u_{ij}(0) = u_i$
Equal Slope at Node i		
	$\mathbf{G}_3$	$\frac{\partial v_{ij}(z)}{\partial z}\Big|_{z=0} = \theta_i$
Equal Transverse Deflection at Node j		
	$\mathbf{G}_4$	$v_{ij}(L_{ij}) = v_j$
Equal Axial Deflection at Node j		
	$\mathbf{G}_5$	$u_{ij}(L_{ij}) = u_j$
Equal Slope at Node j		
	$\mathbf{G}_6$	$\frac{\partial v_{ij}(z)}{\partial z}\Big|_{z=L_{ij}} = \theta_i$

$u_{ij}(x)$: Axial deflection profile of a beam between Node i and Node j.

l_{ij}: Length of a beam between Node i and Node j.

Each beam element in a network of beams is defined by two connecting nodes (Node i and Node j). Each node can be defined by a point force/ moment with an associated potential energy $\mathbf{W_{force}}$, an effective point force that is generated from the potential energy of a parallel plate actuator $\mathbf{W_{estatic}}$, or an anchor which removes all three degrees of freedom of a node. However, if the node does not have potential forces or anchors

applied to it, the node is free to move and must obey continuity constraints of the other adjoining nodes. Specifically, the shape of a SUGAR beam element between Node i and Node j $(v_{ij}(z))$ under a transverse displacement is defined by a superposition Hermitian shape functions.

$$v_{ij}(z) = H_1(z) \cdot v_i + H_2(z) \cdot \theta_i + H_3(z) \cdot v_j + H_4(z) \cdot \theta_j \qquad (2.54)$$

where v_i and v_j are the transverse displacements at Node i and Node j, respectively. θ_i and θ_j are the angular displacements at Node i and Node j, respectively. $H_1(x)$, $H_2(x)$, $H_3(x)$, and $H_4(x)$ are the Hermitian shape functions that are used to satisfy boundary conditions and are given by:

$$H_1(z,L) = 1 - 3\left(\frac{z}{L}\right)^2 + 2\left(\frac{z}{L}\right)^3 \qquad\qquad H_2(z,L) = z - 2\left(\frac{z^2}{L}\right) + 2\left(\frac{z^3}{L^2}\right)$$

$$H_3(z,L) = 3\left(\frac{z}{L}\right)^2 - 2\left(\frac{z}{L}\right)^3 \qquad\qquad H_4(z,L) = -\left(\frac{z^2}{L}\right) + 2\left(\frac{z^3}{L^2}\right)$$

$$H_5(z,L) = 1 - \left(\frac{z}{L}\right) \qquad\qquad\qquad H_6(z,L) = \left(\frac{z^2}{L}\right)$$

where L is the length of a suspended beam element. The set of Hermitian shape functions that are used to specify the shape of a beam element in SUGAR.

The angle of rotation of a beam element can be denoted as $\theta = \frac{\partial v_{ij}(x)}{\partial x}$.

Similar to transverse displacement, the shape of a SUGAR beam element between Node i and Node j $(u_{ij}(x))$ under an axial displacement is defined by a superposition Hermitian shape functions.

$$u_{ij}(x) = H_5(x) \cdot u_i + H_6(x) \cdot u_j \qquad (2.55)$$
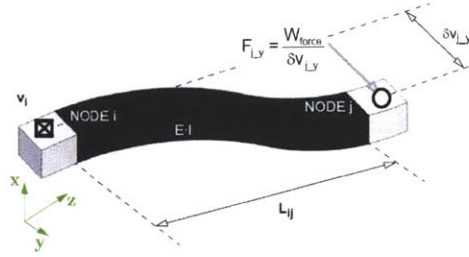
FIGURE 2.16: A schematic of a three-dimensional SUGAR beam element defined between node i and node j. Node i is anchored; Node j is transversely displaced in the y-direction by δv_{y_j} by a point force F_{y_j}.

Figure (2.16) illustrates a three-dimensional cantilever beam that is defined in SUGAR and that is anchored at Node i undergoing a deflection as a point force is applied to Node j. Essentially, a point force with an associative potential energy of W_{force} displaces Node j in the y-direction by $\partial v_j\,(y)$. Consequently, the beam element assumes a Hermitian polynomial shape between Node i and Node j as defined by Equation (2.54).
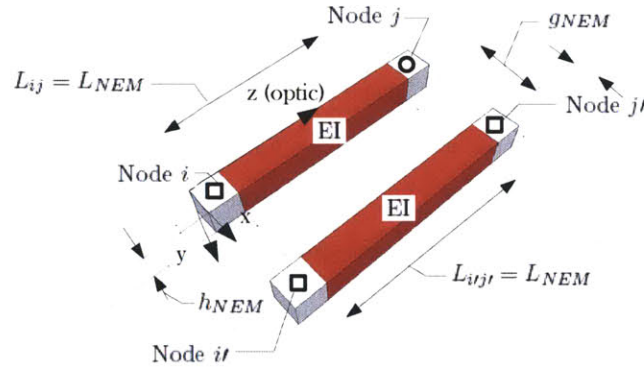
FIGURE 2.17: Schematic of a three-dimensional SUGAR parallel plate actuator. Two electrostatic beam elements of equal width and height are separated by g_{NEM}. Nodes i, i' and j' are anchored. The application of voltage creates a v_{y_j} displacement of node j via an equivalent point force F_{y_j} that is defined by the non-potential energy $\mathbf{W_{estatic}}$.

$v_{x_j} \neq 0 \quad \Theta_{x_j} = 0$

$v_{y_j} = 0 \quad \Theta_{y_j} = 0$

$v_{z_j} = 0 \quad \Theta_{z_j} = 0$

$F_{y_j} = \frac{\mathbf{W}_{estatic}}{\delta v_{x_j}}$

z (optic)

$v_{x_{j'}} = 0 \quad \Theta_{x_{j'}} = 0$

$v_{y_{j'}} \neq 0 \quad \Theta_{y_{j'}} = 0$

$v_{z_{j'}} = 0 \quad \Theta_{z_{j'}} = 0$

$v_{x_i} = 0 \quad \Theta_{x_i} = 0$

$v_{y_i} = 0 \quad \Theta_{y_i} = 0$

$v_{z_i} = 0 \quad \Theta_{z_i} = 0$

y

$v_{x_{i'}} = 0 \quad \Theta_{x_{i'}} = 0$

$v_{y_{i'}} = 0 \quad \Theta_{y_{i'}} = 0$

$v_{z_{i'}} = 0 \quad \Theta_{z_{i'}} = 0$
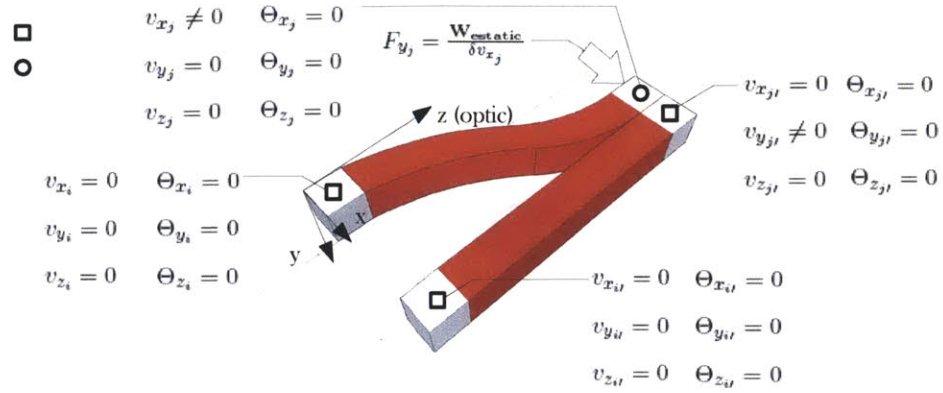
FIGURE 2.18: The application of voltage creates a v_{y_j} displacement of node j via an equivalent point force F_{y_j} defined by the non-potential energy $\mathbf{W}_{\mathbf{estatic}}$.

Pursuing this further, Figures (2.17) and (2.18) shows a three-dimensional cantilever beam parallel plate actuator that is implemented in SUGAR. First, a parallel plate actuator is defined by parallel arranged beams that must have equal height (h) but can have different widths (w_{ij}, $w_{i',j'}$). Specifically, the parallel plate actuator structure is defined by three anchored nodes (Nodes i, i' and j') and one unconstrained node (Node j).

Upon application of a voltage [Figure (2.18)], Node j deflects and the deflected beam assumes a Hermitian shape. Markedly, SUGAR implements a parallel plate actuator by transforming the electrostatic attractive force to equivalent point forces acting on the connected nodes (Node i, j, $i*$, $j*$). Consequently, the electrostatic energy, $W_{estatic}$ in Table 2.5, is specified by the four integrals that are evaluated at each node of the parallel plate actuator.
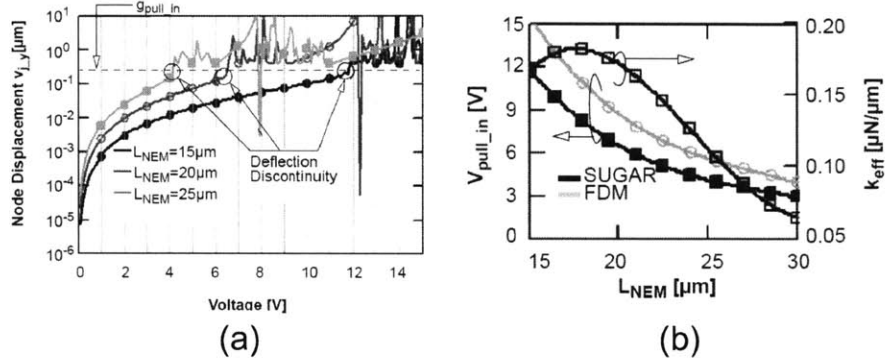
FIGURE 2.19: (a) SUGAR simulation identifying the point of pull-in by scanning over a range of deflections as a function of voltage for a cantilever beam parallel plate actuator with an anode-to-cathode separation $g_{NEM} = 1\mu m$. (b) Comparison of static pull-in voltage calculated from SUGAR and the finite difference method (FDM) as described in Section 2.2.2. The spring constant of the beam used in the SUGAR simulation is plotted as well.

The SUGAR program is not explicitly designed to find the pull-in condition of deflection instability. In order to identify V_{SPI} and g_{SPI} from a SUGAR simulation, a multi-beam articulated structure is simulated over a range of voltages and each freely moving node is tracked for discontinuities in the nodes transverse displacement vectors $(v_{x_n}, v_{y_n}, v_{z_n})$ and rotation vectors $(\theta_{x_n}, \theta_{y_n}, \theta_{z_n})$, where n represents a node. For example, in the case of the cantilever beam parallel plate actuator [Figure (2.18)], there is one freely moving node (node j) with one direction of displacement $(v_j(y))$ and one rotation vector (θ_{x_j}).

Figure (2.19) illustrates the discontinuities in deflection for three cantilever beams that differ in length ($L_{NEM} = 15\mu m$, $20\mu m$, $25\mu m$). θ_{x_j} (not plotted) follows the same trend as v_{y_j}. As a result of an iterative, SUGAR simulation, Figure (2.19b) shows a plot of parallel plate actuator length vs. $V_{S_{PI}}$ for a SUGAR simulated three-dimensional cantilever beam parallel plate actuator and a two-dimensional FD simulated cantilever beam parallel plate actuator using the Newton-Raphson numerical algorithm. Since the cantilever beam parallel plate actuator cross-sections are different for the two-dimensional and three-dimensional simulated cantilever beam parallel plate actuators, the pull-in voltages are shifted. The lump element spring constant (k_{eff}) for the three-dimensional cantilever beam structure is plotted as well.

2.2.3   Finite Difference Time Domain Implicit Method (FDTD)

MathWorks Simulink(R) Model

In the dynamic analysis, all of the investigated NEM-HIC devices are modeled as one-dimensional parallel plate actuators with a dependency on current ($\dot{Q}_x = \frac{dQ_x}{dt}$) and velocity ($\dot{g}_x = \frac{dg_x}{dt}$), where Q_x is the charge and g_x is the separation distance.

Simulink(R) was used to simulate the ($\dot{Q}_x$) and ($\dot{g}_x$) coupled time equations that describe the dynamic behavior of a one-dimensional parallel plate actuator. Generally, a one-dimensional parallel plate actuator is considered a stiff system which, by its very definition, is difficult to solve since typical numerical methods yield unstable results unless extremely small time discretization are used. As a result, an implicit Simulink numerical method is used in order to circumvent computationally intensive simulations.

TABLE 2.5: Energy Functions that are used in the formulation of the Lagrange equations for a lumped element dynamically actuated MEMS parallel plate actuator.

Generalized Variable

Continued on Next Page...

Table 2.5 – Continued	
x_i	g_x, Q_0

g_x: Displacement.

Q_0: Charge.

Conservative Energy

Kinetic Energy		
	$\mathbf{T}_{spring}$	$\frac{1}{2}m_{NM}\dot{g}_x^2$

m_{NM}: Mass of suspended structure.

Potential Energy		
	$\mathbf{U}_{spring}$	$-\frac{1}{2}k_{eff}\left(g_{NEM} - g_x\right)^2$
	$\mathbf{U}_{estatic}$	$\frac{1}{2}\frac{Q_0^2}{C_{cap}} = \frac{1}{2}\frac{1}{\left(\epsilon_0 n_{back}^2\right)\frac{A_{NEM}}{g_x}}Q_0^2$
	$\mathbf{U}_{estatic}^*$	$\frac{1}{2}C_{cap}V_0^2 = \frac{1}{2}\left[\left(\epsilon_0 n_{back}^2\right)\frac{A_{NEM}}{g_x}\right]V_0^2$

k_{eff}: Spring constant.

g_{NEM}: Initial anode-to-cathode separation.

Q_0: Charge.

C_{cap}: Capacitance of one-dimensional parallel plate actuator.

A_{NEM}: Area of the parallel plate actuator's anode plate.

n_{back}: Background refractive index.

V_0: Applied voltage.

Non-Conservative Energy

Dissipation Energy		
	$\mathbf{D_{damp}}$	$\frac{1}{2}C_{damp}\dot{g}_x^2$
	$\mathbf{D_\Omega}$	$\frac{1}{2}R_\Omega \dot{Q}_0^2$

C_{damp}: Damping coefficient.

R_ω: Resistance leading to the parallel plate.

Work Energy		
	$\mathbf{W_{force}}$	$\partial W_{force} = F_0 \cdot \delta g_x$
	$\mathbf{W_{volt}}$	$\partial W_{volt} = V_0 \cdot \delta Q_0$

F_0: Applied force.

Constraints

Stagnation		
	$\mathbf{G}_{stag}$	$\frac{1}{2}\left[\epsilon_0 n_{back}^2 \frac{A_{NEM}}{g_{NEM}}\right]V_0^2$

From Table (2.5), the Lagrange equation for a current- and velocity-dependent one-dimensional parallel plate actuator is defined as:

$$(\mathbf{T}_{\text{spring}} + \mathbf{U}_{\text{spring}} + \mathbf{U}_{\text{estatic}} + \mathbf{D}_{\text{damp}} + \mathbf{D}_\Omega - \mathbf{G}_{\text{stag}})$$

$$= \frac{1}{2} m_{NM} \cdot \dot{g}_x^2 - \frac{1}{2} \left[k_{eff} \left(g_{NEM} - g_x \right)^2 \right]$$

$$+ \frac{1}{2} \left[\left(\epsilon_0 \cdot n_{back}^2 \right) \frac{A_{NEM}}{g_x} \right] V_0^2$$

$$+ \frac{1}{2} \mathbf{C}_{\text{damp}} \cdot \dot{g}_x^2 + \frac{1}{2} \mathbf{R}_\Omega \dot{Q}^2 - \frac{1}{2} \left[\epsilon_0 n_{back}^2 \frac{A_{NEM}}{g_{NEM}} \right] V_0^2 \quad (2.56)$$

The kinetic energy ($\mathbf{T}_{\text{spring}}$) is represented by the moving one-dimensional plate with a mass of m_{NM}. The potential energy is represented by two potential energy terms ($\mathbf{U}_{\text{spring}}$, $\mathbf{U}_{\text{estatic}}$). $\mathbf{U}_{\text{spring}}$ is the potential energy of the suspension spring of the one-dimensional parallel plate actuator system. $\mathbf{U}_{\text{estatic}}$ is the potential energy associated with the one-dimensional parallel plate actuators charged electrode capacitor that is characterized by an area ($\mathbf{A}_{\text{NEM}}$), a separation (g_x) and a dielectric material ($\epsilon_0 \cdot n_{back}^2$). The dissipation energy is represented by a mechanical damping term ($\mathbf{D}_{\text{damp}}$) and a resistive damping term ($\mathbf{D}_\Omega$). The $\mathbf{G}_{\text{stag}}$ term is an energy constraint term associated with the mechanical phenomenon of stagnation.

Stagnation accounts for the mechanical energy imparted into a system that does not result in movement. Specifically, for the one-dimensional parallel plate actuator, stagnation is defined as the imparted energy from voltage (V_0) that does not result in the movement of the capacitor plate ($g_x = g_{NEM}$). Moreover, stagnation occurs in steady state as time goes to infinity ($t \to \infty$) and all variables that change with time vanish [Equation (2.57)].

$$V_0 \neq 0 \qquad g_x = g_{NEM} \qquad t \to \infty \qquad \dot{g}_x = 0 \qquad \dot{Q}_x = 0 \qquad (2.57)$$

Applying the set of the constraints in Equation (2.57) to Equation (2.56) yields:

$$(\mathbf{T_{spring}} + \mathbf{U_{spring}} + \mathbf{U_{estatic}} + \mathbf{D_{damp}} + \mathbf{D_{\Omega}} - \mathbf{G_{stag}})$$

$$= 0 - 0$$

$$+ \frac{1}{2} \cdot \left[\left(\epsilon_0 \cdot n_{back}^2 \right) \cdot \frac{A_{NEM}}{g_{NEM}} \right] \cdot V_0^2$$

$$+ 0 + 0 - \mathbf{G_{stag}} \quad (2.58)$$

Equation (2.58) defines the constraining energy ($\mathbf{G_{stag}}$) that accounts for stagnation in Table (2.5).

Having a complete description of all energy terms (conservative energy, dissipation energy, and constraining energy), Equation (2.56) can be equated to zero and evaluated at an arbitrary input voltage (V_0) that results in an arbitrary deflection (g_x) after all transient terms (g_x, Q_x) have vanished after time has elapsed ($t \rightarrow \infty$).

$$V_0 \neq 0 \qquad g_x \neq g_{NEM} \qquad t \rightarrow \infty \qquad \dot{g}_x = 0 \qquad \dot{Q}_x = 0 \qquad (2.59)$$

Applying the set of conditions in Equation (2.59) to Equation (2.56) yields:

$$(\mathbf{T_{spring}} + \mathbf{U_{spring}} + \mathbf{U_{estatic}} + \mathbf{D_{damp}} + \mathbf{D_{\Omega}} - \mathbf{G_{stag}})$$

$$= 0 + \frac{1}{2} \cdot k_{eff} \cdot (g_{NEM} - g_x)^2 + \frac{1}{2} \cdot \left[\left(\epsilon_0 \cdot n_{back}^2 \right) \cdot \frac{A_{NEM}}{g_x} \right] \cdot V_0^2$$

$$+ 0 + 0 - \frac{1}{2} \cdot \left[\left(\epsilon_0 \cdot n_{back}^2 \right) \cdot \frac{A_{NEM}}{g_{NEM}} \right] \cdot V_0^2 = 0 \quad (2.60)$$

The $\mathbf{G}_{stag}$ and $\mathbf{U}_{estatic}$ terms are then combined to yield

$$\frac{1}{2} \cdot k_{eff} \cdot (g_{NEM} - g_x)^2 + \frac{1}{2} \cdot \left[\left(\epsilon_0 \cdot n_{back}^2 \right) \cdot \frac{A_{NEM}}{g_x} \right] \cdot V_0^2 \cdot \frac{g_{NEM} - g_x}{g_{NEM}} = 0 \qquad (2.61)$$

Equation (2.60) is the force balance equation for quasi-static beam deflection. In order to account for the kinetic energy that is associated with the translation of the beam, the beam's quasi-static force with no external forcing term is reformulated into a bending potential energy term.

Differentiating Equation (2.56) with respect to the variable g_x yields:

$$\frac{d}{dt}\left(\frac{\partial \mathbf{T_{spring}}}{\partial \dot{g}_x}\right) + \frac{\partial \mathbf{U_{spring}}}{\partial g_x} + \frac{\partial \mathbf{U_{estatic}}}{\partial g_x} + \frac{\partial \mathbf{D_{damp}}}{\partial \dot{g}_x} + \frac{\partial \mathbf{D_\Omega}}{\partial \dot{g}_x} - \frac{\partial \mathbf{G_{stag}}}{\partial g_x} =$$

$$m_{eff} \cdot \ddot{g}_x + [k_{eff} \cdot (g_{NEM} - g_x)] - \frac{1}{2} \cdot \left[\left(\epsilon \cdot n_{back}^2 \cdot \frac{A_{NEM}}{g_x}\right)\right] \cdot \frac{V_0^2}{g_x}$$

$$+ \mathbf{C_{damp}} \cdot \dot{g}_x + 0 - 0 = 0 \quad (2.62)$$

Applying the set of conditions in Equation (2.59) to Equation (2.62) yields:

$$- k_{eff} \cdot (g_{NEM} - g_x) - \frac{1}{2} \cdot \left[(\epsilon_0 \cdot n_{back}^2) \cdot \frac{A_{NEM}}{g_x}\right] \cdot \frac{V_0^2}{g_x} = 0 \quad (2.63)$$

Stability is assured by taking the derivative of Equation (2.63) with respect to g_x and setting it to zero. The dynamic pull-in gap $(g_{D_{PI}})$ for the dynamic one-dimensional parallel plate actuator, can be obtained by combining Equation (2.61) and Equation (2.63) and solving for g_x which is the intersection of stagnation and static equilibrium. The dynamic pull-in voltage $(V_{D_{PI}})$ can then be obtained by substituting $g_{D_{PI}}$ into Equation (2.63).

$$g_{D_{PI}} = \frac{1}{2} \cdot g_{NEM} \quad (2.64)$$

$$V_{D_{PI}}^2 = \frac{1}{8} \cdot \frac{g_{NEM}^3 \cdot k_{eff}}{A_{NEM} \cdot (\epsilon_0 \cdot n_{back}^2)} \quad (2.65)$$

Comparing Equation (2.64) and Equation (2.65) with Equation (??a) and Equation (??b) that electromechanical systems that are driven in dynamic operation (i.e., kinetic energy is different from zero) will have a greater controllable stroke, or deflection range. Additionally, dynamic electromechanical systems require less voltage in order to reach

and exceed pull-in instability ($V_{S_{PI}}$ vs. $V_{D_{PI}}$).

The dynamics of the one-dimensional parallel plate actuator can be modeled by state equations that represent the time dependent generalized variables.

$$\mathbf{T}_{spring} + \mathbf{U}_{spring} + \mathbf{U}_{estatic} + \mathbf{D}_{damp} + \mathbf{D}_{\Omega} - \partial \mathbf{W}_{force} - \partial \mathbf{W}_{volt} - \mathbf{G}_{\mathbf{stag}} =$$

$$\frac{1}{2} \cdot m_{NM} \cdot \dot{g_x}^2 + \frac{1}{2} \cdot k_{eff} \cdot (g_{NEM} - g_x)^2 + \frac{1}{2} \cdot \frac{Q^2}{\left(\epsilon_0 \cdot n_{back}^2\right) \cdot \frac{A_{NEM}}{g_x}}$$

$$+ \frac{1}{2} \cdot \mathbf{C}_{\mathbf{damp}} \cdot \dot{g_x}^2 + \frac{1}{2} \cdot R_{\Omega} \cdot \dot{Q}^2 - \partial \mathbf{W}_{\mathbf{volt}} - \mathbf{G}_{\mathbf{stag}} \quad (2.66)$$

Equation (2.66) is the two variable (Q, g_x) energy equation. The work energy of an applied force ($\partial \mathbf{W}_{\mathbf{force}} = F_0 \cdot \delta g_x$) and an applied voltage ($\partial \mathbf{W}_{\mathbf{force}} = V_0 \cdot \delta Q$) is added to the energy equation. Lagranges equation formulated from Equation (2.66) with g_x as the generalized variable is given by:

$$\frac{d}{dt} \left(\frac{\partial \mathbf{T}_{\mathbf{spring}}}{\partial \dot{g_x}} \right) + \frac{\partial \mathbf{U}_{\mathbf{spring}}}{\partial g_x} + \frac{\partial \mathbf{U}_{\mathbf{estatic}}}{\partial g_x} + \frac{\partial \mathbf{D}_{\mathbf{damp}}}{\partial \dot{g_x}} + \frac{\partial \mathbf{D}_{\Omega}}{\partial \dot{g_x}} - \frac{\partial \mathbf{W}_{\mathbf{force}}}{\partial g_x} - \frac{\partial \mathbf{W}_{\mathbf{volt}}}{\partial g_x} - \frac{\partial \mathbf{G}_{\mathbf{stag}}}{\partial g_x} =$$

$$m_{NM} \cdot \ddot{g_x} - k_{eff} \cdot (g_{NEM} - g_x) + \frac{1}{2} \cdot \frac{Q^2}{\left(\epsilon_0 \cdot n_{back}^2\right) \cdot A_{NEM}} + C_{damp} \cdot \dot{g_x} + 0 - F_0 - 0 - 0 = 0$$

$$(2.67)$$

Similarly, Lagranges equation formulated from Equation (2.66) with Q as the generalized variable is given by:

$$\frac{d}{dt} \left(\frac{\partial \mathbf{T}_{\mathbf{spring}}}{\partial \dot{Q}} \right) + \frac{\partial \mathbf{U}_{\mathbf{spring}}}{\partial Q} + \frac{\partial \mathbf{U}_{\mathbf{estatic}}}{\partial Q} + \frac{\partial \mathbf{D}_{\mathbf{damp}}}{\partial \dot{Q}} + \frac{\partial \mathbf{D}_{\Omega}}{\partial \dot{Q}} - \frac{\partial \mathbf{W}_{\mathbf{force}}}{\partial Q} - \frac{\partial \mathbf{W}_{\mathbf{volt}}}{\partial Q} - \frac{\partial \mathbf{G}_{\mathbf{stag}}}{\partial Q} =$$

$$+ 0 + 0 + \frac{Q}{\left(\epsilon_0 \cdot n_{back}^2\right) \cdot \frac{A_{NEM}}{g_x}} + 0 + 0 + R_{\Omega} \cdot \dot{Q} - 0 - V_0 - 0 = 0 \quad (2.68)$$

Equation (2.67) and Equation (2.68) represent two coupled equations that can be effectively solved by numerical integration.

$$\dot{Q} = \frac{1}{R_\Omega} \left[V_0 - \frac{Q \cdot g_x}{(\epsilon_0 \cdot n_{back}^2) \cdot A_{NEM}} \right] \tag{2.69}$$

$$\ddot{g}_x = \frac{1}{m_{NM}} \cdot \left[F_0 + k_{eff} \cdot (g_{NEM} - g_x) - \frac{1}{2} \cdot \frac{Q^2}{(\epsilon_0 \cdot n_{back}^2) \dot{A}_{NEM}} - C_{damp} \cdot \dot{g}_x \right] \tag{2.70}$$

The two equations that describe the charge-gap separation dynamics of the one-dimensional parallel plate actuator are given in Equations (2.69)and (2.70). From the two equations in Equations (2.69)and (2.70), three relevant device characteristics can be extracted: displacement (g_x), power ($\dot{Q} \cdot V_0$), and impact force ($\ddot{g}_x \cdot m_{eff}$).
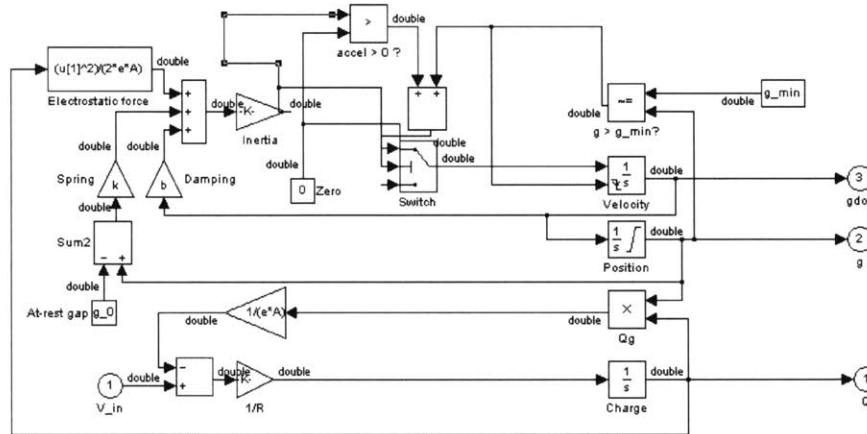
FIGURE 2.20: Simulink model used for direct numerical integration of the coupled equations in Equation (2.61).

The Simulink diagram in Figure (2.20) is used to model the time-dependency characteristics of displacement, impact force and power of a one-dimensional cantilever beam parallel plate actuator.

The choice of driving voltage (V_0) is directly related to the speed of displacement, the amount of force imparted by a pulled-in capacitor plate and the amount of power that

is used during the deflection.

Three regimes of operation can be signified by an input voltage in relation to $V_{D_{PI}}$:

1. $V_0 < V_{D_{PI}}$

2. $V_0 \cong V_{D_{PI}}$

3. $V_0 > V_{D_{PI}}$

First, the $V_0 < V_{D_{PI}}$ operational regime is characterized by an input voltage that is less than the requisite voltage for dynamic pull-in. In this operational regime, the two capacitor plates do not come into contact. The time that is required for all transients to settle (t_{RSA}), i.e., the time to reach steady state, is primarily governed by the cantilever beams resonant frequency and the damping characteristics of the ambient (C_{damp}) (e.g. air at room temperature and atmospheric pressure).

Second, the $V_0 \cong V_{D_{PI}}$ operational regime is characterized by an input voltage that is equal to the requisite voltage for dynamic pull-in; in this operational regime, the two capacitor plates make contact. Furthermore, the switching time is primarily governed by the charging time of the parallel plate actuators capacitor plates.

Third, the $V_0 > V_{D_{PI}}$ operational regime is characterized by an input voltage that exceeds the requisite voltage to achieve dynamic pull-in. In this operational regime, the two capacitor plates also make contact. Moreover, the switching time is primarily governed by the amount of voltage applied and the charging time of the parallel plate actuators capacitor plates.
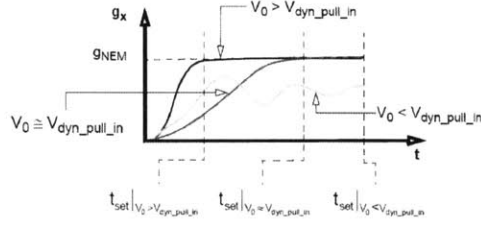
FIGURE 2.21: Dynamic response of a one-dimensional parallel plate actuator for three voltages that are initiated at $t = 0s$.

Figure (2.21) illustrates the three voltage operational regimes of the dynamic response of the one-dimensional parallel plate actuator. Firstly, the one-dimensional parallel plate actuator that is actuated with $V_0 > V_{DPI}$ has the benefit of comparatively faster operation and greater displacement strokes with the premium of mechanical wear from contacting surfaces, comparatively higher impact force, and non-symmetrical switching times. Secondly, the one-dimensional parallel plate actuator actuated with $V_0 < V_{DPI}$ has the benefit of reduced mechanical wear as the parallel plate actuator plates do not come into contact, symmetrical switching times with the premium of reduced displacement stroke, and comparatively slower switching times. Additionally, the size and weight of the nanoelectromechanical high-index-contrast (NEM-HIC) devices allows for sub-microsecond switching speeds.

After reaching pull-in, a lower voltage (V_{HPI}) can be used to maintain the one-dimensional parallel plate actuators anode and cathode plates in intimate contact.

V_{HPI} can be derived from Equation (2.61) by allowing all time dependencies to decay as time goes to infinity, and constraining the anode-to-cathode separation to a g_x

separation defined as $g_x = 2w_{coat}$ in order to account for the insulating coat cladding on the parallel plates.

$$t \to \infty \qquad\qquad g_x = 2w_{coat} \qquad\qquad \dot{g}_x = 0 \qquad (2.71)$$

$V_{H_{PI}}$ is given as:

$$V_{H_{PI}}^2 = 2 \left(\frac{2w_{coat}}{g_{NEM}}^2 \right) \left(1 - \frac{2w_{coat}}{g_{NEM}} \right) \cdot \frac{k_{NM} \cdot g_{NEM}^3}{\left(\epsilon_0 \cdot n_{back}^2 \right) \cdot A_{NEM}} \qquad (2.72)$$

The voltages and gaps associated with anode plate pull-in and holding for a one-dimensional parallel plate actuator are reviewed for comparison. For the sake of simplicity, the one-dimensional parallel plate actuator model assumes $P_{ext} = 0$ and w_{coat} is 20% of the gap which separates the electrode surfaces of the anode and cathode plates (g_{NEM}).

$$g_{S_{PI}} = 0.67 \cdot g_{NEM} \qquad (2.73)$$

$$V_{S_{PI}}^2 = 0.296 \cdot \frac{k_{NM} \cdot g_{NEM}^3}{\left(\epsilon_0 \cdot n_{back}^2 \right) \cdot A_{NEM}} \qquad (2.74)$$

$$g_{D_{PI}} = 0.50 \cdot g_{NEM} \qquad (2.75)$$

$$V_{D_{PI}}^2 = 0.125 \cdot \frac{k_{NM} \cdot g_{NEM}^3}{\left(\epsilon_0 \cdot n_{back}^2 \right) \cdot A_{NEM}} \qquad (2.76)$$

$$g_{H_{PI}} = 0.29 \cdot g_{NEM} \qquad (2.77)$$

$$V_{H_{PI}}^2 = 0.119 \cdot \frac{k_{NM} \cdot g_{NEM}^3}{\left(\epsilon_0 \cdot n_{back}^2 \right) \cdot A_{NEM}} \qquad (2.78)$$

The onset of parallel plate actuators instability during static actuation is established by $V_{S_{PI}}$ [Equation (2.74)] that uncontrollable deflects the parallel plate actuators movable anode plate beyond the range of stable travel; stable travel is limited to $g_{S_{PI}}$) [Equation (2.73)]. A parallel plate actuator that is dynamically actuated reaches pull-in instability at a lower $V_{D_{PI}}$ [Equation (2.76)] but has a wider range of stable travel since the $g_{D_{PI}}$

[Equation (2.75)] is lower than g_{SPI}; a dynamically actuated parallel plate actuator takes into account the moment of inertia due to the moving anode plate. Equation (2.77) is the parallel plate actuator's anode-to-cathode plate separation threshold (g_{hold}) which must be exceeded in order to hold the two plates of the parallel plate actuator in intimate contact with $V_{H_{PI}}$ that is given in Equation (2.78).

2.3 Conclusion

This chapter covered the two sets of simulation methods that were used to develop, analyze and optimize the seven optical MEMS switches evaluated in this thesis. The first set of simulation methods consists of three different methods and are used to analyze and optimize the optical operation of the switch devices; the second set of methods consists of two different methods and are used to analyze and optimize electromechanical operation.

Since the optical MEMS switches are based on single-mode, high-index-contrast, planar waveguide structures, three different simulation methods were used in order to analyze the optical performance: A three-dimensional Fast-Fourier-Transform Beam Propagation Method (FFT BPM) simulation software was used in order to determine specified cross-sectional dimensions that will only support quasi-TE_{00} and quasi-TM_{00} polarized light. A three-dimensional Finite-Difference Beam Propagation Method (FD BPM) simulation and a two-dimensional Bidirectional Eigenmode Propagation Method (BEPM) simulation software were used in concert in order to optimize the structure of the optical MEMS switches for optimal optical performance.

MEMS operation of the optical MEMS switches is simulated using two different software packages: one that analyzes three-dimensional MEMS structures for quasi-static electromechanical actuation and a second analyzes one-dimensional lumped-element modeled MEMS structures for dynamic electromechanical actuation. Specifically, quasi-static electromechanical actuation is analyzed using a three-dimensional Finite-Element Method (FEM) and dynamic actuation is analyzed using a one-dimensional Finite-Difference Method (FDM).

Chapter 3

Integrated Structures

Optical switches, while being conceptually simple devices, can be considered a workhorse photonic circuit element, that is used for a wide range of purposes [13]. Optical switches can be used either to modulate, route or delay optical signals. Here, the focus is to create an optical switch with relatively modest modulation speeds. The overarching goal was to convert a typical (stationary) optical interconnect into a reconfigurable optical interconnect in order to increase PIC flexibility. Essentially, the design goal was to create *smart* interconnects that could route optical signals on lightpaths that would normally be static.

However, enhancing the functionality of static interconnects should not come at the cost of the interconnect's fundamental operation. Typical optical interconnects do not have an optical power loss budget. Nor do interconnects consume any power. So, part of the challenge of designing a dynamically-reconfigurable interconnect was to also insure that these new devices had low loss and low power operation.

Considering the design goals of the low-power reconfigurable interconnect devices, optical switching that is based on moving waveguides has several advantages over other candidate technologies. Optical switching that is based on thermo-optical effects involves the consumption of large amounts of power which makes scaled integration impractical. Also, thermal-optical optical switches are not directly amendable to being latched [13].

Optical switching that is based on electro-optical effects is material-system dependent. Similar to thermal-optical switches, electro-optical switches are not particularly compatible with being integrated with latches [13]. Compared to optical switches that are based on other physical effects, acousto-optical switches are known to have a large device footprint, which limits large-scalability. Again, acousto-optic actuators are not particularly compatible with being integrated with latches [13]. Optical switching that is based on magneto-optic effects often require post-fabrication integration, requiring (off-chip) bulk isolators and circulators for their operation [13]. Optical switching that is based on liquid crystals are challenged by unintended coupling and post-fabrication alignment issues [13]. Bubble actuators, which are based on free-space optics, are challenged by production and packaging issues.[13]

Electrostatic MEMS actuators were used to modulate the optical switches. Electrostatic actuators draw negligible current and consequently can be designed to operate with negligible static current. Moreover, spatial manipulation of waveguiding structures can create dramatic isolation and coupling effects which are simply not possible with other material manipulations (e.g., electro-optical refractive index modulation)–even in material systems with strong non-linear material effects. Specifically, using materials with refractive-index differences on the order of 1 or 2 allows for the creation of submicron structures which can be used to guide, confine and couple micron-order wavelength light. These submicron structures are only required to move distances ranging from a few hundred nanometers to a few microns in order to create pronounced changes in the guidance, confinement and coupling behavior of light.

Operational Performance Metrics

The MEMS actuators of all seven optical switches are designed to have a quasi-static *pull-in* voltage of 10 volts ($V_{SPI} = 10V$) as simulated by three-dimensional SUGAR calculations. The material properties (e.g., elastic modulus) of the two-material mechanical structures in SUGAR are specified as lumped element values, allowing an effective spring constant (k_{NM}) and mass (m_{NM}) to be determined. One-dimensional

Simulink models are constructed from the SUGAR-derived parameters k_{NM}, m_{NM} as well as the effective overlap plate area between the anode and cathode plates and the lump element squeeze-film damping constant. The Simulink model is used to determine the speed at which each optical switch can be modulated from the as-fabricated configuration to the mechanically-deflected configuration, after *pull-in*. The transition of an optical switch from the as-fabricated to the mechanically-deflected configuration is denoted as force-driven actuation (FDA). The Simulink model is also used to determine the force-driven actuation speed (t_{RSA}) for a dynamic *pull-in* voltage of $V_{DPI} = 10V$ as well as the minimum voltage required to establish dynamic *pull-in* ($V_{DPI_{min}}$) and the corresponding force-driven actuation speed for $V_{DPI_{min}}$. In addition, the one-dimensional Simulink model is used to determine the minimum voltage that is required to sustain the mechanically-deflected configuration ($V_{HOLD_{min}}$). Finally, the same one-dimensional Simulink model is used to determine the time required for an optical switch to be modulated from the mechanically-deflected configuration to the as-fabricated configuration, after the actuation voltage is reduced to $0V$. The transition from the mechanically-deflected to the as-fabricated configuration is denoted as release-settle actuation (RSA). Release-settle actuation time (t_{RSA}) is defined as the time required for the (one-dimensional) moving cathode plate to have a $\pm 10nm$ oscillation. Each optical switch is comprised of waveguides with two distinct sections–a suspended and an anchored waveguide section–with a common core that runs contiguously through both sections. The anchored waveguide section is a three-dimensional waveguide, consisting of a core, a lower cladding and an upper cladding layer. The suspended wave/-guide section is a two-material waveguide, consisting of a core and a coat cladding layer. Mechanically, the anchored waveguide section supports the free-standing suspended waveguide section. The core and the coat cladding layers are specifically chosen in order to optimize the optical performance of a particular optical switch device.

Optical Switch Generations at a Glance

Figures (3.1) - (3.7) depict the seven electromechanical optical switch devices in the two states of operation: the as-fabricated configuration and the mechanically-deflected configuration.

Each optical switch structure is divided into units along the optical axis, the z-axis. One or more units are grouped into three-digit-numbered regions. The regions are connected to one another at interfaces that (naturally) effect axial light propagation (e.g., Region 000). The interfaces are defined as a change in waveguide direction and/or an abrupt change in refractive index. Each optical switch structure is composed of two or more waveguiding structures which are labeled by letters (e.g., WVG A). Consequently, a particular section of each waveguiding structure will be indexed by region number and waveguiding structure number (e.g., Section 001A).

Devices 01, 02 and 03 are electromechanical optical switches that are based on two coupled *discontinuous* waveguide structures. These devices are capable of modulating a single lightpath on and off. To wit: Device 01, Device 02 and Device 03 are on/off optical switches. Devices 04, 05, 06 and 07 are based on two *continuous* coupled suspended waveguides that are supported on both ends–the so-called fixed-fixed beam mechanical form. These devices are capable of modulating two lightpaths on and off concurrently. To wit: Devices 04, 05, 06 and 07 are 2 × 2 optical switches.
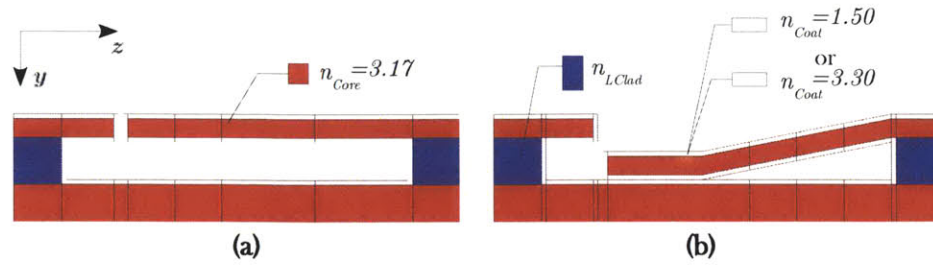
FIGURE 3.1: Side view of Device 01 in (a) the as-fabricated, on-state and (b) the mechanically-deflected, off-state configurations. Red indicates high index material, while blue indicates low-index material.

Device 01 [Figure (3.1)] is an on/off electromechanical optical switch that is comprised of two butt-coupled (discontinuous) anti-resonant reflecting waveguides. One of those waveguides is deflected by a waveguide-integrated parallel-plate MEMS actuator that is composed of the suspended waveguide and the substrate. The suspended waveguide acts as a cantilever.
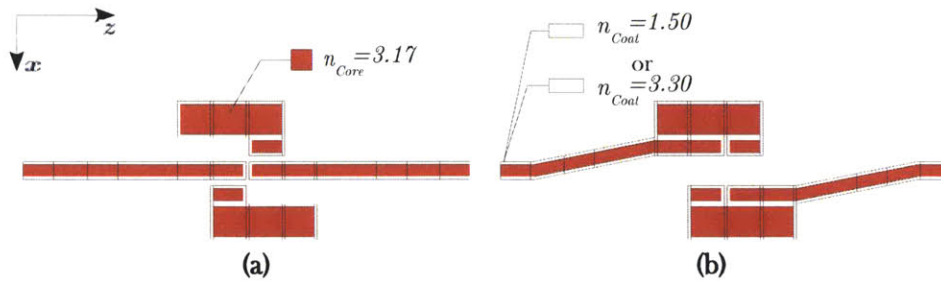
FIGURE 3.2: Top view of Device 02 in (a) the as-fabricate on-state and (b) the mechanically-deflected off-state configurations.

Similar to Device 01, Device 02 [Figure (3.2)] is an on/off electromechanical optical switch that is comprised of two butt-coupled (discontinuous) anti-resonant reflecting waveguides. Both waveguides are modulated by two waveguide-integrated parallel-plate MEMS actuators that are composed of the suspended waveguides which function as cantilevers and adjacent cathode/anode.
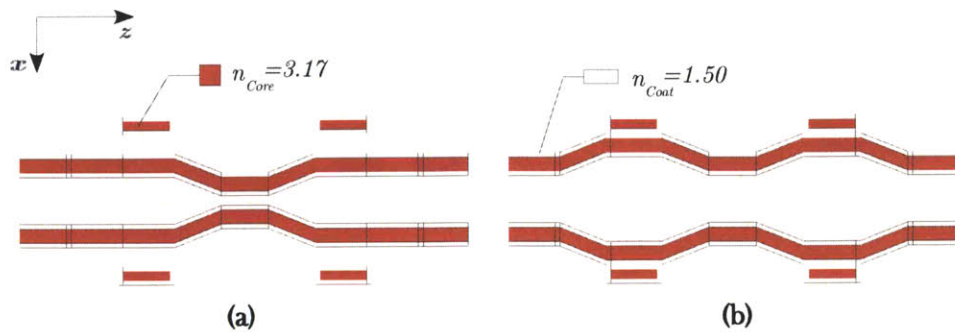
FIGURE 3.3: Top view of Device 03 in (a) the as-fabricated on-state and (b) the mechanically-deflected off-state configurations.

Device 03 [Figure(3.3)] is an on/off electromechanical optical switch that is comprised of two codirectionally-coupled discontinuous total internal reflection waveguides. Both waveguides are modulated by two waveguide-integrated parallel-plate MEMS actuators that are composed of the suspended waveguides which function as cantilever suspensions, and adjacent cathode/anode.
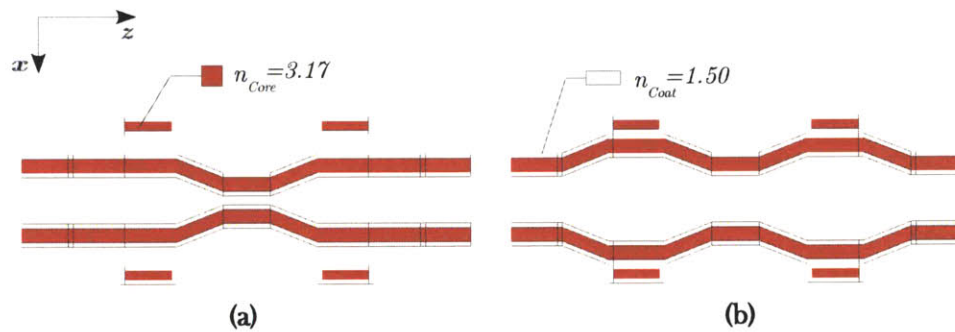
FIGURE 3.4: Top view of Device 04 in (a) the as-fabricated cross-state and (b) the mechanically-deflected bar-state configurations.

Device 04 [Figure (3.4)] is a 2×2 electromechanical optical switch that is comprised of two codirectionally-coupled (continuous) total internal reflection waveguides. Both waveguides are modulated by two waveguide-integrated parallel-plate MEMS actuators (not shown). The suspended waveguides act as fixed-fixed beam suspensions.
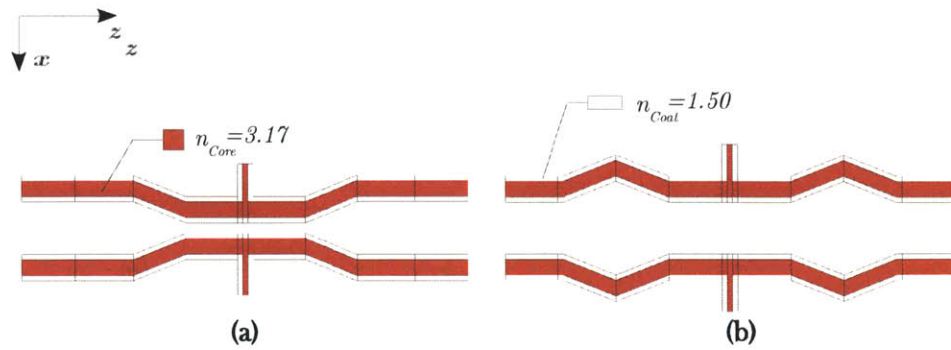
FIGURE 3.5: Top view of Device 05 in (a) the as-fabricated cross-state and (b) the mechanically-deflected bar-state configurations.

Device 05 [Figure (3.5)] is an 2×2 electromechanical optical switch that is comprised of two codirectionally-coupled (continuous) total internal reflection waveguides. Both waveguides are modulated by two waveguide-tethered parallel-plate MEMS actuators (not shown) that are supported by folded flexure suspensions. The suspended waveguides function as fixed-fixed beam suspensions.
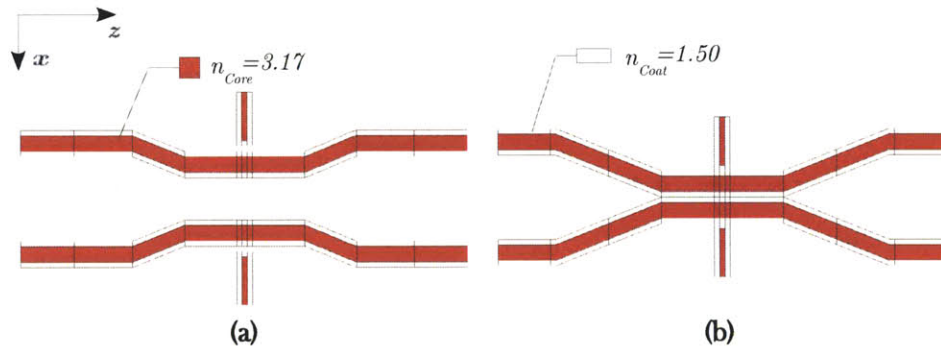
FIGURE 3.6: Top view of Device 06 in (a) the as-fabricated bar-state and (b) the mechanically-deflected cross-state configurations.

Device 06 [Figure (3.6)] is a 2×2 electromechanical optical switch that is comprised of two codirectionally-coupled (continuous) total internal reflection waveguides. Both waveguides are modulated by two rigid bumper beams, extending from remote parallel-plate MEMS actuators that are supported by folded flexure suspension.
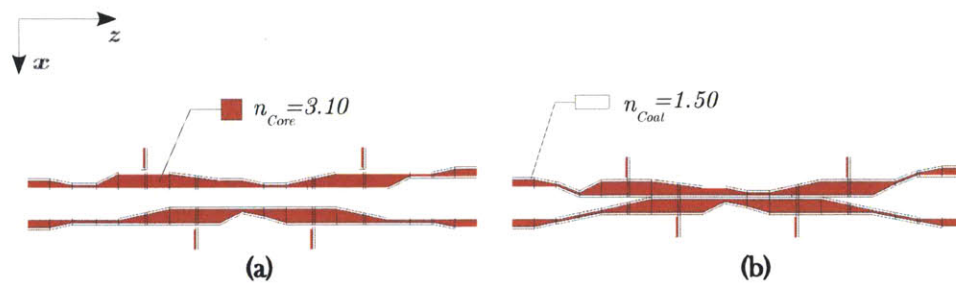
FIGURE 3.7: Top view of Device 07 in (a) the as-fabricated bar-state and (b) the mechanically-deflected cross-state configurations.

Device 07 [Figure (3.7)] is a 2×2 electromechanical optical switch that is comprised of two adiabatically-coupled (continuous) total internal reflection waveguides. Both waveguides are modulated by two rigid bumper beams, extending from remote parallel-plate MEMS actuators (not shown) that are supported by folded flexure suspensions.

Chapter Structure

After briefly introducing all seven devices in the first introductory section, the next seven sections of the twelve sections are dedicated to each of the seven optical switches. The next four sections contain supplementary design information that pertains to Devices 04, 05, 06 and 07.

Each of the seven device sections will cover the device design and operation as well as an assessment of the device's performance. In addition to the performance assessment, suggestions for the device improvement will be discussed, which lead into a discussion on the motivation for the subsequent device generation that follows.

The subsection entitled *Device Design* offers a brief account of the three-step design strategy that is employed in the design of each of the optical switches. First, the optical operation is optimized for transmission, reflection and, in the case of the 2×2 optical switches, crosstalk. Second, parallel-plate MEMS actuator(s) are designed to modulate the optical switches between the two optimized configurations with a 10-volt actuation

voltage. Third, the optical design is then altered slightly in order to accommodate the presence of the parallel-plate MEMS actuator(s) should the actuators alter the optimal optical performance.

The subsection entitled *Device Operation* consists of four parts that discuss the specifics of the as-fabricated configuration, force-driven actuation, the mechanically-deflected configuration and release-settle actuation.

The subsubsection entitled *As-Fabricated Configuration* covers the specifics of the material and the structure of the optical switch in the as-fabricated configuration. The particular type of lightpath that is established in the as-fabricated configuration is discussed.

The subsubsection entitled *Force-Driven Actuation* discuss what happens during the period where the optical switch is modulated from the as-fabricated to the mechanically-deflected configuration. For a 10-volt actuation voltage, each optical switch will have a characteristic time in which the force-driven actuation is completed ($t_{FDA_{10V}}$). Moreover, each switch will also have a minimum voltage, below $10V$, at which the optical switch can still be actuated ($V_{FDA_{min}}$). Naturally, actuation with $V_{FDA_{min}}$ will complete force-driven actuation switching on a time scale greater than $t_{FDA_{10V}}$. After force-driven actuation, the actuation voltage can then be reduced to a minimum voltage $V_{HOLD_{min}}$ which will still hold the mechanically-deflected configuration.

The subsubsection entitled *Mechanical-Deflected Configuration* covers the specifics of the material and the structure of the optical switch in the mechanically-deflected configuration. The particular type of lightpath that is established in the mechanically-deflected configuration is discussed.

The subsubsection entitled *Release-Settle Actuation* discusses the switching action of the switch that takes place after a hold voltage, the voltage that is used to maintain the mechanically-deflected configuration, is removed. Releasing the optical switch from the

mechanically-deflection state results in the optical switch returning to the as-fabricated configuration. Depending upon the optical switch structure, the optical switch will require a time t_{RSA} to return to the as-fabricated configuration. Specifically, t_{RSA} is the time that is required for the moving components of the optical switch to reach less than 10 nanometers of mechanical oscillations as the optical switch returns to the as-fabricated configuration.

The subsection entitled *Next Generation* discuss the motivation for moving onto the next optical switch generation.

The supplementary information section entitled *Device 04: Design in Detail* contains a detailed treaties on the optical and electromechanical optimization processes for Device 04. The optimization processes are representative of the optimization processes that was used for the other six devices. The supplementary information section entitled *Device 05, 06, 07: The Latch Actuator* details the design of the parallel-plate MEMS actuator that is used to mechanically latch the mechanically-deflected configuration of Devices 05, 06 and 07. The supplementary information section entitled *Devices 05, 06, 07: The Waveguide Actuator* details the design of the parallel-plate MEMS actuator that is used to remotely actuate Devices 05, 06 and 07. The supplementary information section entitled *Device 07: The Adiabatically Coupled Waveguide Device Design* details the design of the cross-state lightpath of Device 07.

3.1   Device 01

Device 01 is an electromechanical on/off optical switch that uses a single parallel-plate MEMS actuator in order to modulate one waveguide between two different spatial configurations.
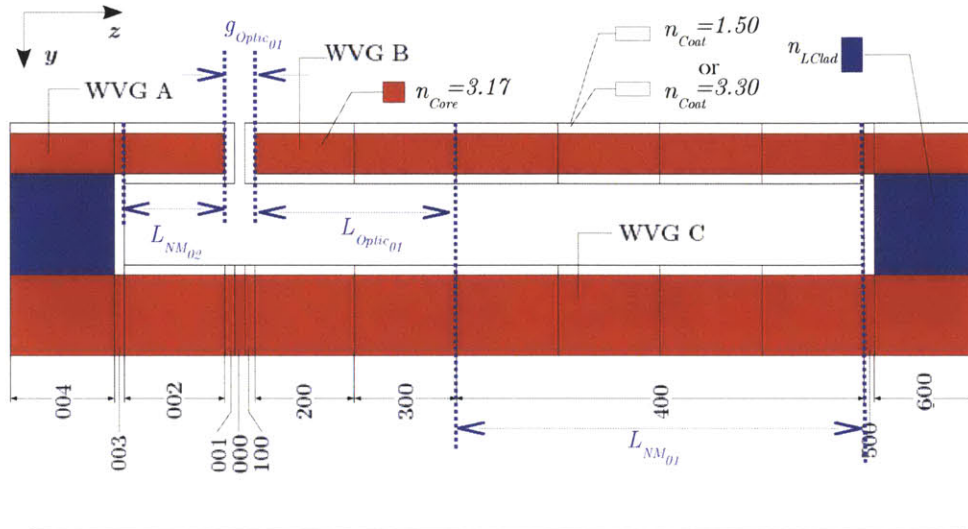
FIGURE 3.8: The side view of Device 01 in the as-fabricated configuration which establishes a coupled transmission lightpath.

As shown in Figure (3.8), the as-fabricated, on-state configuration of Device 01 is modeled as a 3-component, 11-region waveguide structure. Two of the waveguide structures (WVGs A and B) are ridge waveguides, composed of two different waveguide types: a three-material anchored waveguide and a two-material suspended waveguide. The third waveguide structure (WVG C, the substrate) is a plane waveguide, composed of two different waveguide types: a single-material, anchored waveguide and a two-material, anchored waveguide. Regarding WVG A: Sections 004A and 003A are anchored while Sections 002A and 001B are suspended and rigid. Regarding WVG B: Sections 100B, 200B and 300B are suspended, movable and rigid, Section 400B is suspended and flexibly movable and Sections 500B and 600B are anchored. All of the sections of WVG C are immovable.

In the as-fabricated, on-state configuration, a lightpath is established between WVGs A and B.
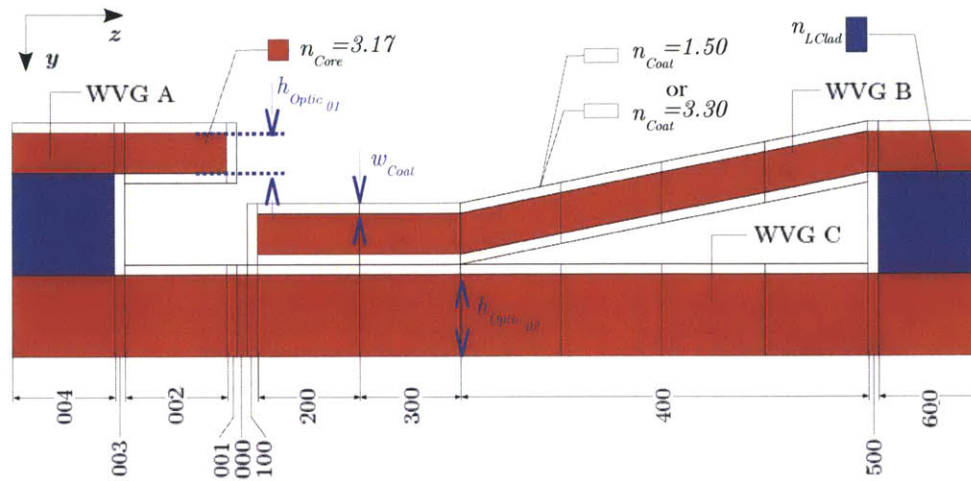
FIGURE 3.9: The side view of Device 01 in the mechanically-deflected configuration which terminates the coupled transmission lightpath

As shown in Figure (3.9), in the mechanically-deflected, off-state configuration, WVG B is elastically deformed from out of the initial axial alignment with WVG A and into intimate contact with WVG C. As a result, the lightpath established between WVGs A and B is terminated. This state is designed such that most of the guided light in WVG B is absorbed by WVG C and most of the guided light in WVG A is radiated into the air. Specifically, Sections 100B, 200B and 300B are in intimate contact with Sections 100C, 200C and 300C and Section 400B is slanted as a result of the mechanical deflection. All other sections remain the same.

The waveguide structures of Device 01 are constructed from a subset of several different material types: MBE-grown, gallium-rich and aluminum-rich $Al_{1-x}Ga_xAs$ materials, an Al-Ga-As-based oxide created from the aluminum-rich $Al_{1-x}Ga_xAs$ material, a crystalline GaAs material, and an GaAs material formed by the atomic layer deposition process.

The three-material, anchored-waveguide sections of WVGs A and B, which are total

internal reflection (TIR) ridge waveguides, are composed of a gallium-rich $Al_{1-x}Ga_xAs$ core, an Al-Ga-As-based oxide lower-cladding, and a GaAs upper-cladding layer. The gallium-rich $Al_{1-x}Ga_xAs$ core is formed by a reactive-ion-etch (RIE) process which completely etches the material into a rectangular cross-sectioned ridge. This same RIE process is also used to form the aluminum-rich $Al_{1-x}Ga_xAs$ ridge which is subsequently oxidized in order to create the Al-Ga-As-based oxide material in order to serve as the lower-cladding layer. After the core and the lower-cladding layers are formed, the ALD process is used to deposit the GaAs material around the core and lower-cladding layers, forming the upper-cladding layer.

The two-material, anchored-waveguide sections of WVGs A and B–also TIR ridge waveguides–are composed of a gallium-rich $Al_{1-x}Ga_xAs$ core and a GaAs lower-cladding layer. Again, the RIE process is used in order to form the gallium-rich $Al_{1-x}Ga_xAs$ core of this section type. However after being formed, the core layer undergoes a sacrificial etch which releases this core layer from the lower layer that previously supported the core layer. Simply by the virtue of the ALD process, the side-wall deposition of the GaAs material connects the previously-suspended, core layer to the substrate. Naturally, the length of this anchored-waveguide section type is approximately equal to the coat-cladding thickness.

The two-material, suspended-waveguide sections of WVGs A and B–also TIR ridge waveguides–are composed of a gallium-rich $Al_{1-x}Ga_xAs$ core layer and a GaAs coat-cladding layer. Similar to the core layer of the two-material, anchored-waveguide sections, the core layer of this section type is formed by an RIE and a sacrificial etch process. However, as a freely-suspended structure, the GaAs material, as deposited by the ALD process, forms a coat-cladding layer around the core layer.

The single-material sections of WVG C are composed of GaAs core layer. The two-material sections of WVG C is composed of GaAs core layer and a GaAs top-coating layer. The core layer represents the substrate. Consequently the core layer of WVG C exists as a planar waveguide and does not undergo any intentional structural changes

during the front-end processing. The GaAs top-coating layer is formed as a result of the ALD process, which is primarily used to form the coat-cladding layers of WVGs A and B.

Device Design

Device 01 is designed for maximized transmission and minimized reflection for both the quasi-TE and quasi-TM polarizations in the as-fabricated configuration. The suspended waveguide sections of Wavguides A and B have a square cross-section with a core width $(w_{A,B})$ and a core thickness (h_{CORE}) of $w_{A,B} = h_{Optic_{01}} = 100nm$, a $n_{CORE} = 3.17$ core refractive index, a n_{Coat} coat-cladding refractive index and a w_{Coat} coat-cladding thickness. Two-dimensional Eigenmode simulations were used to optimize the core and the coat cladding layer thickness and refractive index for an on-state transmission of $-3.3 \cdot 10^{-4}dB$ and an on-state reflection of $-36dB$ for TE_0 mode light propagation.

The on-state of Device 01 relies primarily on butt coupling in order to establish the on-state lightpath. As a result, transmission increases as the separation between the end facets of the two butt-coupled waveguides decreases. Specifically, for the waveguides that are used for Device 01, transmission increases as the core-to-core separation decreases regardless of the refractive index of the coat cladding. Respecting the minimum feature size of $w_{Litho} = 100nm$, as specified by the lithographic technology used, a $g_{Optic_{01}} = 100nm$ surface-to-surface axial separation of the waveguide cores of WVGs A and B is established.

In order to further reduce transmission loss, a conformal coat cladding is applied [via the atomic layer deposition (ALD process)] to the waveguide cores of WVGs A and B, which reduces the axial separation between the two waveguides. Specific to the design of Device 01, a gap-fill performance up to aspect ratios of 20:1 is required in order to establish a $g_{cOptic_{01}} = 10nm$ coat-cladding-to-coat-cladding axial separation between WVGs A and B given that the core thickness is $h_{Optic_{01}} = 100nm$ and the coat-cladding thickness is $w_{coat} = 45nm$.

In the off-state configuration, transmission is minimized and reflection is minimized. In order to minimize transmission, the suspended waveguide section of WVG B undergoes an out-of-plane (y-axis) elastic deformation which causes the two waveguides to be

misaligned. In the off-state configuration WVG B forms an intimate contact with the substrate (WVG C) over an $L_{Optic_{01}}$ length, thus establishing directional coupling. The directional coupling established between WVGs B and C serves to absorb the optical power guided by WVG B.

Device Operation

The As-Fabricated Configuration

In the as-fabricated on-state configuration, the discontinuous anti-reflection resonant waveguide sections of WVGs A and B are in axial alignment. Butt coupling establishes the lightpath between WVGs A and B. The coat cladding layer thickness is chosen in order to reduce the air gap which axially separates WVG A from WVG B in order to reduce radiation loss. The surface-to-surface lithographically-defined separation $(g_{ON00_{AB}} = w_{LITHO} \equiv 100nm)$ between the waveguide cores of WVGs A and B and the thickness of the coat cladding $(t_{COAT} = 45nm)$ maximizes on-state transmission. The core refractive index $(n_{CORE} = 3.17)$ and the coat cladding layer refractive index $(n_{COAT} = 3.4)$ minimize on-state reflection.

Force-Driven Actuation

The mechanically-deflected off-state configuration is established in $t_{FDA} = 700ns$ with the application of the dynamic pull-in voltage (V_{DPI}) of $V_{DPI} = 10V$. A minimum dynamic pull-in voltage $(V_{DPI_{min}})$ of $V_{DPI_{min}} = 2.5V$ establishes the mechanically-deflected off-state configuration in $t_{FDA} = 2.1\mu s$. The mechanically-deflected off-state is maintained with a minimum hold voltage $(V_{HOLD_{min}})$ of $V_{HOLD_{min}} = 0.5V$.

The Mechanically-Deflected Configuration

In the mechanically-deflected off-state configuration, the deformed suspended waveguide section of WVG B assumes a sinusoidal shape from the tip of the suspended waveguide

section to the base of the anchored waveguide section. Moreover, a portion of the suspended waveguide forms an intimate contact with the top surface of the substrate. The length over which the suspended waveguide section forms an intimate contact with the substrate surface depends upon g_{NEM} as well as the total length of the suspended waveguide section of WVG B (L_{NM}). The mechanically-deflected off-state can be maintained with a voltage $V_{HOLD_{min}}$ or larger.

Light traveling from WVG A to WVG B (reverse transmission), travels along a straight lightpath which is terminated at the end facet of the rigid suspended waveguide section of WVG A. As a result, light traveling along this lightpath is either reflected and/or radiated.

Release-Settle Actuation

Release-settle actuation reestablishes the as-fabricated on-state from the mechanically-deflected off-state configuration in $t_{RSA} = 240\mu s$. During release-settle actuation, the deformed suspended waveguide section of WVG B is released from the initial intimate contact with Substrate C.

The Next Generation

Primarily, the directional dependence of off-state reflection inspired the next evolutionary design step for the electromechanical optical switch. Secondly, a higher mechanical resonant frequency was desired. The idea was to design the next optical switch to have a parallel-plate MEMS structure with a smaller as-fabricated plate separation (smaller than $g_{ON_{AC,BC}} = 1.5\mu m$) since the suspended waveguide sections can maintain optical isolation with a smaller separation than the separation that is required for the long-length anchored waveguide sections.

3.2 Device 02

Device 02 is an electromechanical on/off switch that uses two parallel-plate MEMS actuators in order to modulate two waveguides between two different spatial configurations.
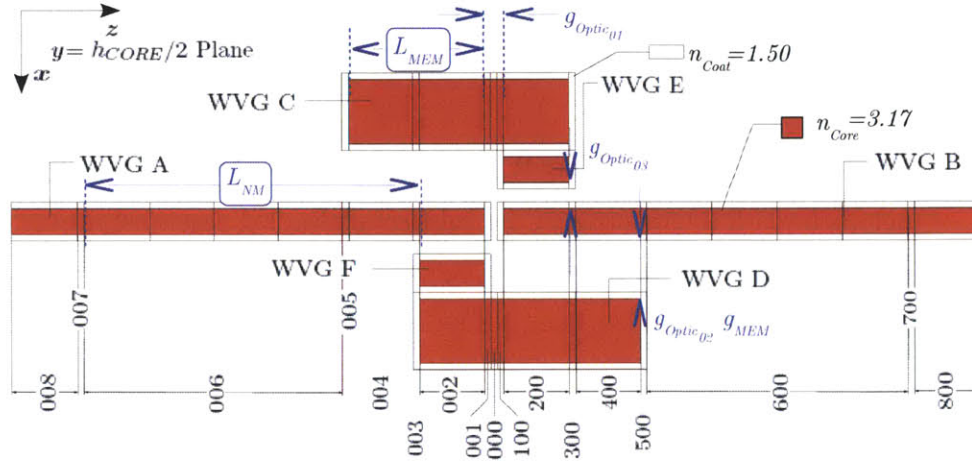
FIGURE 3.10: The top view of Device 02 in the as-fabricated configuration which establishes a coupled lightpath.

As shown in Figure (3.10), the as-fabricated on-state configuration of Device 02 is modeled as a six-component, 17-region waveguiding structure. Two of the waveguiding structures (WVGs A and B) are ridge waveguides, composed of two different waveguide types–a three-material anchored waveguide [not seen in Figure (3.10)] and a two-material suspended waveguide. The other two waveguiding structures (WVGs C and D) are used as light absorbers. Each of the three sets of two waveguides–WVGs A and B, WVGs C and D and WVGs E and F–have rotational symmetry about the y-axis at the center of Region 000. Consequently, Sections 008A and 007A as well as Sections 700B and 800B are anchored; Sections 005A and 004A as well as Sections 500B and 400B are suspended and flexible; Sections 003A, 002A and 001A as well as Sections 300B, 200B and 100A are suspended and flexible but are intended to be rigid. Sections 005C–001C, 000C and 100C–300C, Sections 003D–001D, 000D and 100D–500D, Sections 100E–300E and Sections 003F–001F are anchored.

In the as-fabricated configuration Device 02 is in the on-state; two discontinuous wave-guides exist in a cantilevered axial alignment. The on-state lightpath is established between WVGs A and B via small-gap butt-coupling.
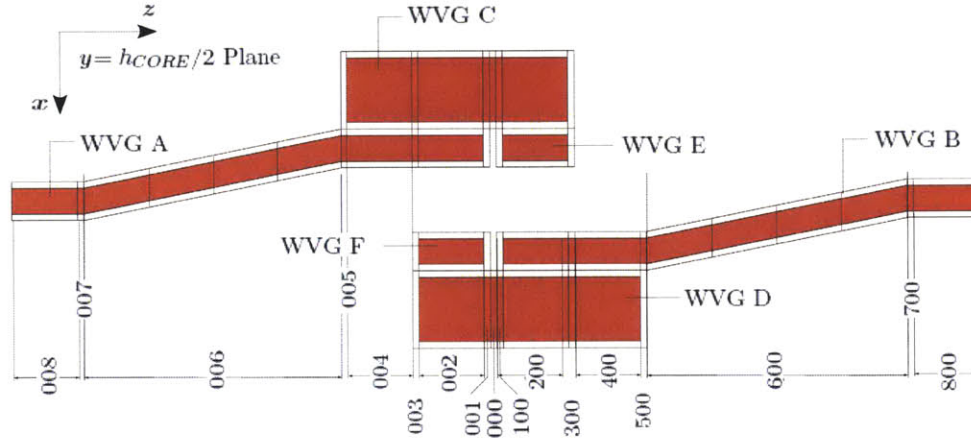
FIGURE 3.11: The top view of Device 02 in the mechanically-deflected configuration which terminates the coupled lightpath.

As shown in Figure (3.11), in the mechanically-deflected, off-state configuration, both WVGs A and B are elastically deformed from out of the initial, axial alignment with each other. WVGs A and B are driven into intimate contact with WVGs C and D, respectively, and into axial alignment with WVGs E and F, respectively. As a result, the lightpath initially established between WVGs A and B is terminated. Two new light-paths are established: A lightpath between WVGs A and E and one between WVGs B and F. Specifically, Sections 005A - 001A are in intimate contact with Sections 004C - 001C and Sections 100B - 500B are in intimate contact with Sections 100D - 500D. Sections 006A and 600B are slanted as a result of the mechanical deflection. All other sections remain the same.

The waveguide structures of Device 01 are constructed from a subset of several different material types: MBE-grown, gallium-rich and aluminum-rich $Al_{1-x}Ga_xAs$ materials, an Al-Ga-As-based oxide created from the aluminum-rich $Al_{1-x}Ga_xAs$ material, and an GaAs material formed by the atomic layer deposition process.

The three-material, anchored-waveguide sections of WVGs A and B, which are total internal reflection (TIR) ridge waveguides, are composed of a gallium-rich $Al_{1-x}Ga_xAs$ core, an Al-Ga-As-based oxide lower-cladding, and a GaAs upper-cladding layer. The gallium-rich $Al_{1-x}Ga_xAs$ core is formed by a reactive-ion-etch (RIE) process which completely etches the material into a rectangular cross-sectioned ridge. This same RIE process is also used to form the aluminum-rich $Al_{1-x}Ga_xAs$ ridge which is subsequently oxidized in order to create the Al-Ga-As-based oxide material in order to serve as the lower-cladding layer. After the core and the lower-cladding layers are formed, the ALD process is used to deposit the GaAs material around the core and lower-cladding layers, forming the upper-cladding layer.

The three-material, anchored-waveguide sections of WVGs C, D, E and F are composed of a gallium-rich $Al_{1-x}Ga_xAs$ core, an aluminum-rich $Al_{1-x}Ga_xAs$ lower-cladding, and a GaAs upper-cladding layer. Again, the RIE process is used in order to form the core layer. The lower-cladding is formed first by undergoing a RIE process and then an oxidation process. The resultant aluminum-rich $Al_{1-x}Ga_xAs$ lower-cladding is formed as a mesa structure with a partial laterally-etch recess with respect to the top core layer. After the core and the lower-cladding layers are formed, the ALD process is used to deposit the GaAs material around the core and lower-cladding layers, forming the upper-cladding layer.

The two-material, anchored-waveguide sections of WVGs A and B–also TIR ridge waveguides–are composed of a gallium-rich $Al_{1-x}Ga_xAs$ core and a GaAs lower-cladding layer. Again, the RIE process is used in order to form the gallium-rich $Al_{1-x}Ga_xAs$ core of this section type. However after being formed, the core layer undergoes a sacrificial etch which releases this core layer from the lower layer that previously supported the core layer. Simply by the virtue of the ALD process, the side-wall deposition of the GaAs material connects the previously-suspended, core layer to the substrate; the length of this anchored-waveguide section type is approximately equal to the coat-cladding thickness.

The two-material, suspended-waveguide sections of WVGs A and B–also TIR ridge waveguides–are composed of a gallium-rich $Al_{1-x}Ga_xAs$ core layer and a GaAs coat-cladding layer. Similar to the core layer of the two-material, anchored-waveguide sections, the core layer of this section type is formed by an RIE and a sacrificial etch process. However, as a freely-suspended structure, the GaAs material, as deposited by the ALD process, forms a coat-cladding layer around the core layer.

Device Design

Device 02 is designed for maximized transmission and minimized reflection for both the quasi-TE and quasi-TM polarizations in the as-fabricated configuration. The suspended-waveguide sections of WVGs A and B are square in cross-section with a core width ($w_{A,B}$) and a core thickness (h_{CORE}) of $w_{A,B} = h_{CORE} = 100nm$, a core layer refractive index (n_{CORE}) of $n_{CORE} = 3.17$, a coat-cladding layer refractive index (n_{COAT}) of $n_{COAT} = 1.44$ and a coat-cladding layer thickness (t_{COAT}) of $t_{COAT} = 45nm$.

The on-state of Device 02 relies primarily on butt-coupling in order to establish the on-state lightpath. As a result, the closer the end facets of two butt-coupled waveguides are to one another, the greater the transmission. Specifically for the waveguides that are used for Device 02, transmission increased as the closer the core layers of the suspended-waveguide sections were to each other regardless if the refractive index of the coat-cladding layer was greater or lesser than the refractive index of the core layer. Respecting the minimum feature size (w_{LITHO}) of $w_{LITHO} = 100nm$, the surface-to-surface axial separation of the two waveguide cores of WVGs A and B ($g_{ON00_{A,B}}$) is set to $g_{ON00_{A,B}} = 100nm$.

Next, in order to reduce Raleigh scattering at the core/air interface, a coat-cladding layer was used to further reduce the separation between WVGs A and B. However, the separation reduction that is created by the deposition of the coat-cladding layer must have a finite value. Considering that the coat-cladding layer will be deposited by atomic layer deposition, the surface-to-surface separation (of the coat cladding layer) between WVGs A and B ($g_{cON00_{A,B}}$) is set to $g_{cON00_{A,B}} = 10nm$.

Device Operation

The As-Fabricated Configuration

In the as-fabricated, on-state configuration, the discontinuous anti-reflection resonant waveguide sections of WVGs A and B are in axial alignment. A lightpath is established

via small-gap butt-coupling. A coat cladding layer thickness (t_{COAT}) of $t_{COAT} = 45nm$ is chosen in order to reduce radiation loss at the end facets of WVGs A and B by reducing the air gap which axially separates the suspended-waveguide sections of WVGs A and B. A coat-cladding layer refractive index (n_{COAT}) of $n_{COAT} = 3.4$ and a core layer refractive index (n_{CORE}) of $n_{CORE} = 3.0$ are chosen in order to minimize the on-state reflection and maximize the on-state transmission.

Force-Driven Actuation

The mechanically-deflected, off-state configuration is established in $t_{FDA} = 500ns$ with the application of the dynamic pull-in voltage (V_{DPI}) of $V_{DPI} = 10V$. A minimum dynamic pull-in voltage ($V_{DPI_{min}}$) of $V_{DPI_{min}} = 3.6V$ establishes the mechanically-deflected off-state configuration in $t_{FDA} = 1.0\mu s$. The mechanically-deflected off-state is maintained with a minimum hold voltage ($V_{HOLD_{min}}$) of $V_{HOLD_{min}} = 1.8V$.

The Mechanically-Deflected Configuration

In the mechanically-deflected, off-state configuration, the deflected, suspended waveguide sections of WVGs A and B come to rest on WVGs C and D, respectively. As a result, WVGs A and E and WVGs B and F are in axial alignment, thus establishing butt-coupling. As a result, light is coupled into WVGs C and/or D instead of between WVGs A and B, thus terminating light transmission from either WVGs A and B. Once coupled into WVGs C and D, the guided light can then be leaked into the substrate or radiated into the air.

Release-Settle Actuation

Release-settle actuation reestablishes the as-fabricated on-state from the mechanically-deflected off-state configuration in $t_{RSA} = 46\mu s$. During release-settle actuation, the deformed suspended waveguide sections of WVGs A and B are simultaneously released from the initial intimate contact with WVGs C and D, respectively.

The Next Generation

Moving forward, Device 03 has a design which is more resilient to fabrication irregularities (as compared to Device 02) because of the different optical principle that is used to establish the coupled lightpath. Moreover, Device 03 is designed to be more mechanically resilient than Device 02 since Device 03 uses a robust oxide coating (instead of a semiconductor coating).

3.3   Device 03

Device 03 is an electromechanical on/off optical switch that uses two parallel-plate MEMS actuators in order to modulate two waveguides between two different spatial configurations.
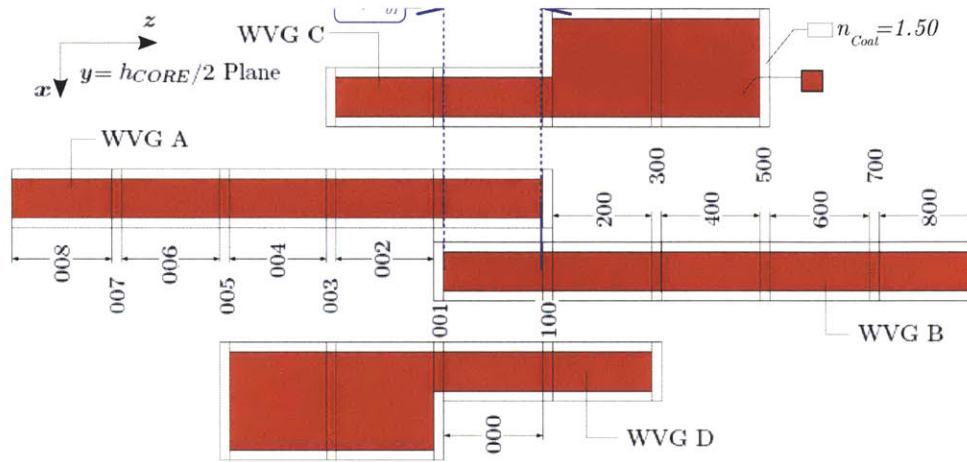
FIGURE 3.12:   The top view of Device 03 in the as-fabricated configuration which establishes a coupled lightpath.

As shown in Figure (3.12), the as-fabricated, on-state configuration of Device 03 is modeled as a 4-component, 17-region waveguide structure. Two of the waveguide structures (WVGs A and B) are ridge waveguides, composed of two different waveguide types–a three-material, anchored-waveguide and a two-material, suspended-waveguide structure. WVGs A and B have rotational symmetry about the y-axis at the center of Region 000. The other two waveguide structures (WVGs C and D) are also ridge waveguides, having rotational symmetry about the y-axis at the center of Region 000. Regarding WVGs A and B: Sections 008A, 007A, 700B and 800B are anchored, Sections 006A - 004A and 400B - 600B are suspended and flexibly movable and Sections 003A - 100A and 001B - 300B are suspended[1], rigid and movable. Regarding WVGs C and D: Sections 003C - 00C and 000D - 300D are suspended and rigid while Sections 100C - 500C and 005D - 001D are anchored.

---

[1]Note that Sections 003A - 100A and 001B - 300B can also be anchored waveguide sections.

In the as-fabricated, on-state configuration, a lightpath is established between the two parallel-aligned, discontinuous waveguides (WVGs A and B).
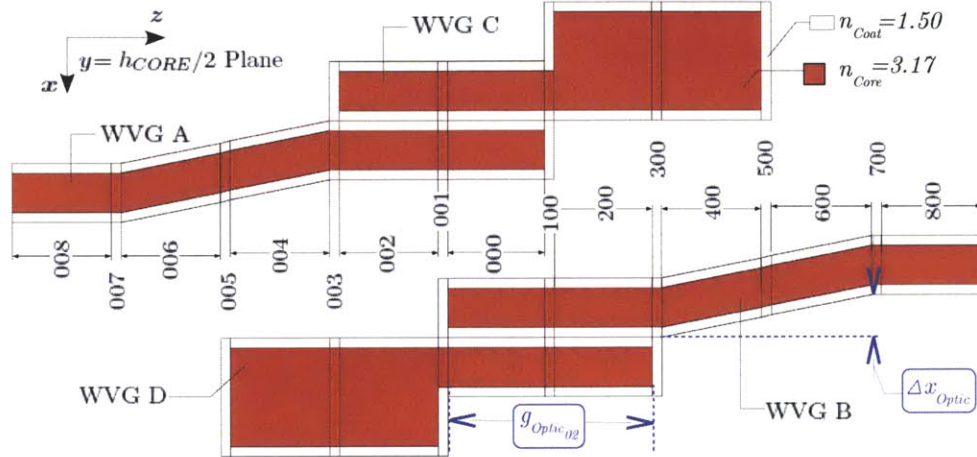
FIGURE 3.13: The top view of Device 03 in the mechanically-deflected configuration which terminates the coupled lightpath.

As shown in Figure (3.13), in the mechanically-deflected, off-state configuration, the suspended-waveguide sections of WVGs A and B are elastically deformed from out of the initial parallel alignment and into intimate contact with WVGs C and D, respectively. Consequently, Device 03 has an arrangement such that Sections 003A - 100A form an intimate contact with Sections 003C - 100C. Similarly, Sections 001B - 300B form an intimate contact with Sections 001D - 300D. Sections 006A - 004A and Sections 400A - 600A become slanted in response to the mechanical deflection. All other sections remain the same.

Device 03 uses four materials for each of the waveguide structures: MBE-grown, gallium-rich and aluminum-rich $Al_{1-x}Ga_xAs$ materials, an Al-Ga-As-based oxide created from the aluminum-rich $Al_{1-x}Ga_xAs$ material, and an Al_2O_3 material formed by the atomic layer deposition process.

The three-material, anchored-waveguide sections of WVGs A and B, which are total

internal reflection (TIR) ridge waveguides, are composed of a gallium-rich $Al_{1-x}Ga_xAs$ core, an Al-Ga-As-based oxide lower-cladding, and an Al_2O_3 upper-cladding layer. The gallium-rich $Al_{1-x}Ga_xAs$ core is formed by a reactive-ion-etch (RIE) process which completely etches the material into a rectangular cross-sectioned ridge. This same RIE process is also used to form the aluminum-rich $Al_{1-x}Ga_xAs$ ridge which is subsequently oxidized in order to create the Al-Ga-As-based oxide material in the lower-cladding layer. After the core and the lower-cladding layers are formed, the ALD process is used to deposit the Al_2O_3 material around the core and lower-cladding layers, forming the upper-cladding layer.

The three-material, anchored-waveguide sections of WVGs C and D are composed of a gallium-rich $Al_{1-x}Ga_xAs$ core, an aluminum-rich $Al_{1-x}Ga_xAs$ lower-cladding, and an Al_2O_3 upper-cladding layer. Again, the RIE process is used in order to form the core layer. The lower-cladding of this section undergoes three process steps: an RIE, an oxidation and a sacrificial etch process. The resultant aluminum-rich $Al_{1-x}Ga_xAs$ lower-cladding is formed as a mesa structure with a partial laterally-etch recess with respect to the top core layer. After the core and the lower-cladding layers are formed, the ALD process is used to deposit the Al_2O_3 material around the core and lower-cladding layers, forming the upper-cladding layer.

The two-material, anchored-waveguide sections of WVGs A, B, C and D–also TIR ridge waveguides–are composed of a gallium-rich $Al_{1-x}Ga_xAs$ core and an Al_2O_3 lower-cladding layer. Again, the RIE process is used in order to form the gallium-rich $Al_{1-x}Ga_xAs$ core of this section type. However after being formed, the core layer of this section type undergoes a sacrificial etch which liberates this core layer from the previously-supporting lower layer. After undergoing the ALD process, side-wall deposition of the Al_2O_3 material forms a connection between the suspended core to the substrate; the length of these anchored-waveguide sections are equal to the coat-cladding thickness.

The two-material, suspended-waveguide sections of WVGs A, B, C and D–also TIR ridge waveguides–are composed of a gallium-rich $Al_{1-x}Ga_xAs$ core layer and an Al_2O_3

coat-cladding layer. Similar to the core layer of the two-material, anchored-waveguide sections, the core layer of this section type is formed by an RIE and a sacrificial etch process. However, as a freely-suspended structure, the Al_2O_3 material, as deposited by the ALD process, forms a coat-cladding layer around the core layer.

Device Design

Device 03 is designed for maximized transmission and minimized reflection for both the quasi-TE_{00} and quasi-TM_{00} polarizations in the as-fabricated configuration. The suspended waveguide sections of WVGs A and B are square in cross-section with a $w_{Optic} = 300nm$ core width and a $h_{Optic} = 300nm$ core thickness, a $n_{Core} = 3.17$ core refractive index, a $n_{Coat} = 1.50$ coat-cladding refractive index and a $w_{Coat} = 50nm$ coat cladding width.

Two-dimensional eigenmode simulations revealed that a $g_{cOptic} = 10nm$ surface-to-surface separation and a $L_{Optic_{01}} = 6.0\mu m$ overlap length allows Device 03 to have simultaneously maximized quasi-TE and quasi-TM on-state transmission of $-9.0 \cdot 10^{-3} dB$ and $-6.9 \cdot 10^{-1} dB$ and on-state reflection of $-69dB$ and $-24dB$, respectively.

The overlap length between WVGs A and C and WVGs B and D is $L_{Optic_{02}} = 4\mu m$, the length that establishes full co-directional coupling between those two sets of waveguides for a $g_{cOptic_{02}} = 0nm$ surface-to-surface separation. In the mechanically-deflected configuration, WVGs A and B make full contact with WVGs C and D, respectively.

Since the anchored anode plate of the parallel-plate actuator is integrated along the side surface of the core of WVGs C and D and the moving cathode plate is integrated along the side surface of the core of WVGs A and B, the overlap plate area of the parallel-plate actuator is constrained to $1.2\mu m^2$. The overlap plate area of the parallel-plate actuator is constrained to $1.2\mu m^2$ due to the core thickness being $h_{MEM} \equiv h_{h_{Optic_{02}}} = 300nm$ as

required for optimal as-fabricated on-state transmission and reflection, and the overlap length between WVGs A and C and WVGs B and D being $L_{MEM} \equiv L_{Optic_{02}} = 4\mu m$ as required for optimal mechanically-deflected off-state transmission and reflection.

In order for Device 03 to be operated with a 10-volt actuation voltage, the total length of the suspended waveguide sections of WVGs A and B is $41\mu m$.

Device Operation

The As-Fabricated Configuration

The as-fabricated on-state [Figure (3.12)] is established as a two-waveguide, coupled lightpath. Specifically, three coupling mechanisms are used in order to establish the lightpath: mode, butt and proximity coupling.

As is typical for closely-spaced, coupled waveguides which both have geometries on the order of the wavelength of the light that is guided, the modes that the waveguides support overlap. This modal overlap facilitates optical power exchange between the two waveguides. In this case, the mode-coupling coefficient for each waveguide (κ_{AB} and κ_{BA} for WVGs A and B, respectively), determines the amount of optical power transferred to a particular waveguide. Both mode-coupling coefficients are functions of the E-fields of the light that is guided by both waveguides as well as the refractive index of that particular waveguide. Frequently, mode-coupling is synonymous with (co)directional coupling.

Since the two coupled waveguides are discontinuous, butt coupling is established and facilitates optical power transfer between the two waveguides. Naturally, since most directionally-coupled waveguides are continuous, butt coupling does not contribute to optical power transfer between waveguides. Butt-coupling, optical power transfer is excited in Regions 001 or 100 if WVG A or B is initially excited, respectively. In this case, the butt-coupling coefficient for each waveguide (c_{AB} and c_{BA} for WVGs A and B, respectively) determines the amount of optical power transferred to a particular waveguide. Both butt-coupling coefficients are functions of the E- and H-field modal profiles

of light that can be guided by both waveguides.

Finally, proximity coupling is a mechanism of optical power transfer that occurs regardless of the amount of modal overlap [?]. Normally, proximity-coupled optical power transfer is negligible. However, since Device 03 is designed with extremely, closely-spaced waveguides ($g_{cON00_{AB}} = 10nm$) with confinement factors on the order of 50%, proximity coupling contributes significantly to the optical power transfer. In this case, the proximity-coupling coefficient for each waveguide (χ_A and χ_B for WVGs A and B, respectively) determines the amount of optical power transferred between waveguides. Both proximity-coupling coefficients are functions of the E-field modal profile of light that can be guided by that particular waveguide, consequently, there is only one subscript for the proximity-coupling coefficient (e.g., χ_A vs. c_{AB}). However, note that both proximity-coupling coefficients are functions of the other's refractive index.

Particularly and in summary for Device 04, the coupled waveguides are discontinuous, in extreme close-proximity and designed to guide light with a confinement factor on the order of 50%. Consequently, the mode, butt and proximity coupling contribute to optical power transfer and the coefficient of each coupling mechanism is defined as:

$$\kappa_{AB,BA} = \kappa_{AB} = \kappa_{BA} \neq 0$$

$$c_{AB,BA} = c_{AB} = c_{BA} \neq 0$$

$$\chi_{A,B} = \chi_A = \chi_B \neq 0$$

Force-Driven Actuation

The mechanically-deflected off-state configuration is established in $t_{FDA} = 500ns$ with the application of the dynamic pull-in voltage (V_{DPI}) of $V_{DPI} = 10V$. A minimum dynamic pull-in voltage ($V_{DPI_{min}}$) of $V_{DPI_{min}} = 2.3V$ establishes the mechanically-deflected off-state configuration in $t_{FDA} = 1.5\mu s$. The mechanically-deflected off-state configuration is maintained with a minimum hold voltage ($V_{HOLD_{min}}$) of $V_{HOLD_{min}} = 0.5V$.

The Mechanically-Deflected Configuration

In the mechanically-deflected off-state configuration, the cantilevered sections of WVGs A and B are elastically deformed simultaneously in order to form a intimate contact with WVGs C and D, respectively, establishing small-gap codirectional, butt-coupling. The three optical coupling mechanisms are used to absorb and redirect optical power from the input/output waveguide ports of WVGs A and B in order to establish the off-state configuration.

Release-Settle Actuation

Release-settle actuation reestablishes the as-fabricated on-state from the mechanically-deflected off-state configuration in $t_{RSA} = 110\mu s$. During release-settle actuation, the suspended waveguide sections of WVGs A and B are liberated from the initial intimate contact with Optical Absorbers C and D.

The Next Generation(s)

Moving forward, the discontinuous coupled waveguide design was abandoned. So naturally, the cantilever-beam flexure based, suspended waveguide section structure was also abandoned. Instead, later generations were designed with two continuous waveguides that had suspended waveguide sections in a fixed-fixed beam mechanical form. Therefore optical switches that were able to simultaneously modulate two lightpaths can be developed. As a result, the later optical switch generations have a broader utility. The later optical switches can be used as either on/off, 1×2, or 2×2 switches (instead of just being limited to on/off switch applications). Also, by switching to a double clamped flexure design (i.e., a fixed-fixed beam flexure based suspended waveguide structure), the devices have a much more robust design. The later generations are much less sensitive to out-of-plane misalignment that could occur during fabrication or device operation.

3.4   Device 04

Device 04 is an electromechanical 2×2 optical switch that uses two parallel-plate MEMS actuators in order to modulate two suspended waveguides between two spatial configurations.
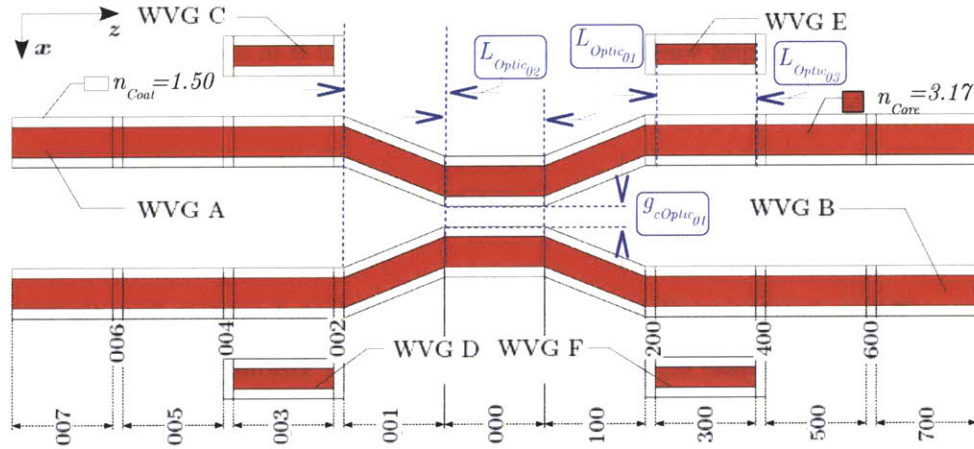
FIGURE 3.14: An (not-to-scale) artistic rendering of the top view of Device 04 in the as-fabricated configuration which allows coupled light transmission.

As shown in Figure (3.14), the as-fabricated cross-state configuration of Device 04 is modeled as a 6-component, 15-region waveguiding structure. Two of the waveguiding structures (WVGs A and B) are continuous, ridge waveguides, composed of two different waveguide types: three-material, anchored waveguides (Sections 007A, 006A, 600A and 700A and Sections 007B, 006B, 600B and 700B) and two-material, suspended waveguides (Sections 005A - 000A and 100A - 500A and Sections 005B - 000B and 100B - 500B). WVGs A and B have rotational symmetry about the y-axis at the center of Region 000 (on the $y = h_{CORE}/2$ plane). The other four waveguiding structures (WVGs C, D, E and F) are discontinuous, three-material anchored waveguides; each of the waveguides have the same geometry and material composition.

In the as-fabricated cross-state configuration, the cross-state lightpath is established between the two suspended sections of WVGs A and B, which are in directional coupling alignment. WVGs C, D, E and F are positioned such that they are in optical isolation to WVGs A and B.

FIGURE 3.15: An (not-to-scale) artistic rendering of the top view of Device 04 in the mechanically-deflected configuration which allows throughput light transmission.

As shown in Figure (3.15), the mechanically-deflected bar-state configuration of Device 04 has an arrangement such that Sections 004A - 002A form an intimate contact with Sections 004C - 002C, Sections 200A - 400A with Sections 200E - 400E, Sections 004B - 002B with Sections 004D - 002D and Sections 200B - 400B with 200F - 400F. Sections 005A, 500A, 005B and 500B are slanted. All other sections remain the same.

In the mechanically-deflected bar-state configuration, the bar-state lightpath is established after the suspended waveguide sections of WVGs A and B are deflected towards the WVGs C and E and WVGs D and F, respectively. WVGs C, D, E and F have specific geometries (e.g., the waveguide core layer) which are chosen to minimize optical power absorption.

Device 04 uses four materials for each of the waveguide structures: MBE-grown, gallium-rich and aluminum-rich $Al_{1-x}Ga_xAs$ materials, an Al-Ga-As-based oxide created from

the aluminum-rich $Al_{1-x}Ga_xAs$ material, and an atomic layer deposition- (ALD-) created, Al_2O_3 material.

The three-material, anchored-waveguide sections of WVGs A, B, C and D, which are total internal reflection (TIR) ridge waveguides, are composed of a gallium-rich $Al_{1-x}Ga_xAs$ core, an Al-Ga-As-based oxide lower-cladding, and an Al_2O_3 upper-cladding layer. The gallium-rich $Al_{1-x}Ga_xAs$ core is formed by a reactive-ion-etch (RIE) process which completely etches the material into a rectangular cross-sectioned ridge. The same RIE process that is used to form the core is also used to form an aluminum-rich $Al_{1-x}Ga_xAs$ ridge which is later oxidized in order to create the Al-Ga-As-based oxide material that is used for the lower-cladding layer. After forming the core and lower-cladding layers, the Al_2O_3 material is deposited around the core and lower-cladding layers in order to form the upper-cladding layer.

The two-material, anchored-waveguide sections of WVGs A and B–also TIR ridge waveguides–are composed of a gallium-rich $Al_{1-x}Ga_xAs$ core and an Al_2O_3 lower-cladding layer. The gallium-rich $Al_{1-x}Ga_xAs$ core is formed by an RIE (same aforementioned RIE process) and a sacrificial etch process. Simply by the virtue of the ALD process, the side-wall deposition of the Al_2O_3 material connects the previously-suspended, core layer to the substrate. Naturally, the length of these anchored-waveguide sections is approximately equal to the coat-cladding thickness.

The two-material, suspended-waveguide sections of WVGs A and B–also TIR ridge waveguides–are composed of a gallium-rich $Al_{1-x}Ga_xAs$ core layer and an Al_2O_3 coat-cladding layer. Similar to the core layer of the two-material, anchored-waveguide sections, the core layer of the two-material, suspended-waveguide sections are formed by an RIE and a sacrificial etch process. After becoming freely suspended, a conformal layer of Al_2O_3 material is applied the core layer by the ALD process.

Device Design

The design begins by specifying the cross-sectional geometry of the suspended waveguide sections of WVGs A and B that will support a single propagating TE and TM mode with a 0.50 confinement factor.

After that, the as-fabricated, cross-state configuration is optimized for full co-directional coupling with minimum polarization-dependent loss by adjusting $g_{Optic_{01}}$, $L_{OPTIC_{01}}$, $L_{Optic_{02}}$, $\Delta x_{Optic_{01}}$, while ensuring that the angle of the as-fabricated, slanted waveguide section does not introduce no more than $-0.02 dB$ transmission loss (the condition for adiabaticity).

Next, the minimum surface-to-surface separation that is required to isolate the suspended waveguide sections of WVGs A and B is determined. Since both suspended waveguide sections will be deflected simultaneously, a $g_{MEM} = 500 nm$ core-to-core electrode separation (core-to-core separation) of the parallel-plate actuator is defined.

Next, an $L_{NM} = 72 \mu m$ length of the Spring suspended waveguide sections of WVGs A and B is required in order to for Device 04 to be actuated (in quasi-static actuation) with a 10-volt actuation voltage with a the waveguide-integrated parallel-actuator defined with an electrode separation of g_{MEM} and an electrode plate area of $h_{Optic_{01}} \times L_{Optic_{03}}$.

Device Operation

The As-Fabricated Configuration

In the as-fabricated cross-state configuration, both suspended waveguide sections of WVGs A and B are in a directional-coupled arrangement. Specifically, the two suspended waveguide sections are fabricated to have a surface-to-surface separation in Region 000 (in the bar-state configuration) of $10 nm$ ($g_{cOptic_{01}} = 10 nm$), which establishes small-gap codirectional coupling.

Force-Driven Actuation

The mechanically-deflected bar-state configuration is established in $t_{FDA} = 500ns$ with the application of the dynamic pull-in voltage (V_{DPI}) of $V_{DPI} = 10V$. A minimum dynamic pull-in voltage $(V_{DPI_{min}})$ of $V_{DPI_{min}} = 1.0V$ establishes the mechanically-deflected bar-state configuration in $t_{FDA} = 1.5\mu s$. The mechanically-deflected bar-state is maintained with a minimum hold voltage $(V_{HOLD_{min}})$ of $V_{HOLD_{min}} = 0.5V$.

The Mechanically-Deflected Configuration

In the mechanically-deflected bar-state configuration, the suspended waveguide section of WVG A forms an intimate contact with WVGs E and F. Similarly, the suspended waveguide section of WVG B forms an intimate contact with WVGs D and F. The bar-state transmission through WVGs A and B is maximized by minimizing optical power absorption due to WVGs C, D, E and F.

Minimized optical power absorption is achieved in two ways. First, the core width of WVGs C and D are specified to be wider than the core width of the suspended waveguide sections of WVGs A and B in order to limit the amount of optical power absorbed by WVGs C, D, E and F. Second, the length of WVGs C, D, E and F is set such that any optical power absorbed from the suspended waveguide sections of WVGs A and B will be returned to that waveguide section via asymmetric codirectional coupling.[2]

Release-Settle Actuation

Release-settle actuation reestablishes the as-fabricated cross-state from a mechanically-deflected bar-state configuration in $t_{RSA} = 2\mu s$. During release-settle actuation, the suspended waveguide sections of WVGs A and B are released from the initial intimate contact with WVGs C, D, E and F.

---

[2]Note that small-gap coupling effects also apply for the mechanically-deflected bar-state configuration

The Next Generation

Moving forward, electromechanical performance improvement becomes the design focus. The idea was to minimize the release-settle time (t_{RSA}), to eliminate the need for V_{HOLD} and to eliminate the constraints that optimal optical performance has on the MEMS operation.

3.5   Device 05

Device 05 is an electromechanical 2×2 optical switch that uses two parallel-plate MEMS actuators in order to modulate two waveguides, simultaneously, between two different spatial configurations.

FIGURE 3.16: An (not-to-scale) artistic rendering of the top view of Device 05 in the as-fabricated configuration which establishes a coupled lightpath.

As shown in Figure (3.16), the as-fabricated cross-state configuration of Device 05 is modeled as a 2-component, 13-region waveguiding structure. The two waveguides, denoted as WVGs A and B, are continuous, ridge waveguides that are composed of three different waveguide types: three-material, anchored waveguides (Sections 006A and 600A and Sections 006B and 600B), two-material, anchored waveguides (Sections 005A and 500A and Sections 005B and 500B) and two-material, suspended waveguides (Sections 004A - 000A - 400A and Sections 004B - 000B - 500B). Moreover, the two-material, suspended waveguide sections of WVGs A and B have sections that are designed to be mechanically flexible (Sections 004A and 400A and Sections 004B and 400B) and mechanically rigid (Sections 003A - 000A - 300A and Sections 003B - 000B - 300B). WVGs A and B have rotational symmetry about the y-axis at the center of Region 000 (on the y=$h_{CORE}/2$ plane).

In this as-fabricated cross-state configuration, a lightpath is established between WVGs A and B via full codirectional-coupling. Full codirectional-coupling is specifically established between over Sections 003A - 000A - 300A and Sections 003B - 000B - 300B.
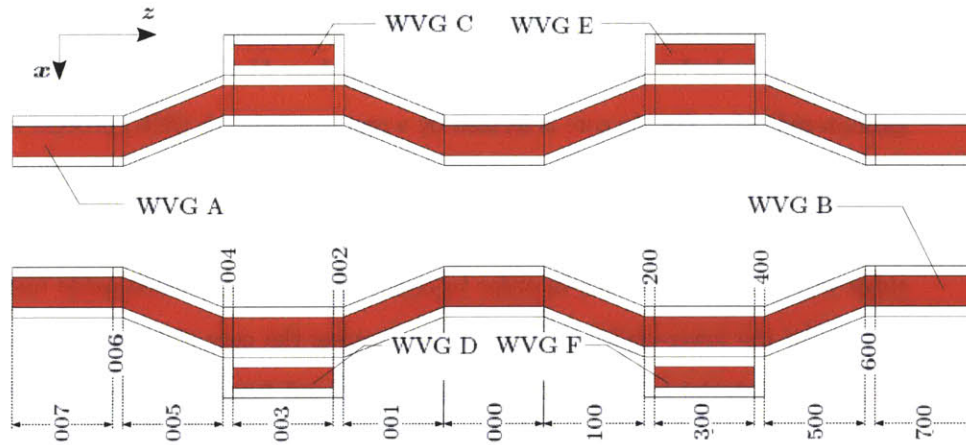

FIGURE 3.17: An (not-to-scale) artistic rendering of the top view of Device 05 in the mechanically-deflected configuration which allows throughput light transmission.

As shown in Figure (3.17), the mechanically-deflected bar-state configuration of Device 05 has an arrangement such that ridge suspended sections of WVGs A and B (Sections 003A - 000A - 300B and Sections 003B - 000B - 300B) are translated along the x-axis in opposite directions while retaining their as-fabricated shape. The right edges of Section 004A and Section 004B as well as the left edges of Section 400A and Section 400B are translated along the x-axis in accordance with the ridge suspended waveguide sections of WVGs A and B, thus creating slanted structures.

In the mechanically-deflected bar-state configuration, WVGs A and B are simultaneously translated from their initial full codirectional-coupling alignment into optical isolation. The 90° waveguiding junction extending from WVGs A and B (Sections 001A - 000A - 100A and Sections 001B - 000B - 100B) forms a contiguous connection with a pair of remote parallel-plate MEMS actuators that are not shown in Figure (3.17). Consequently, Device 05 is designed as an optical switch that employs tethered waveguide actuation for switching. Tethered waveguide actuation is used in order to decouple

waveguiding functionality from MEMS functionality-a design decision which was anticipated to improve overall device performance.

Device 05 uses four materials for each of the waveguide structures: MBE-grown, gallium-rich and aluminum-rich $Al_{1-x}Ga_xAs$ materials, an Al-Ga-As-based oxide created from the aluminum-rich $Al_{1-x}Ga_xAs$ material, and an atomic layer deposition- (ALD-) created, Al_2O_3 material.

The three-material, anchored-waveguide sections of WVGs A and B, which are total internal reflection (TIR) ridge waveguides, are composed of a gallium-rich $Al_{1-x}Ga_xAs$ core, an Al-Ga-As-based oxide lower-cladding, and an Al_2O_3 upper-cladding layer. The gallium-rich $Al_{1-x}Ga_xAs$ core is formed by a reactive-ion-etch (RIE) process which completely etches the material into a rectangular cross-sectioned ridge. The same RIE process that is used to form the core is also used to form an aluminum-rich $Al_{1-x}Ga_xAs$ ridge which is later oxidized in order to create the Al-Ga-As-based oxide material that is used for the lower-cladding layer. After forming the core and lower-cladding layers, the Al_2O_3 material is deposited around the core and lower-cladding layers in order to form the upper-cladding layer.

The two-material, anchored-waveguide sections of WVGs A and B–also TIR ridge waveguides–are composed of a gallium-rich $Al_{1-x}Ga_xAs$ core and an Al_2O_3 lower-cladding layer. The gallium-rich $Al_{1-x}Ga_xAs$ core is formed by an RIE (same aforementioned RIE process) and a sacrificial etch process. Simply by the virtue of the ALD process, the side-wall deposition of the Al_2O_3 material connects the previously-suspended, core layer to the substrate. Naturally, the length of these anchored-waveguide sections is approximately equal to the coat-cladding thickness.

The two-material, suspended-waveguide sections of WVGs A and B–also TIR ridge waveguides–are composed of a gallium-rich $Al_{1-x}Ga_xAs$ core layer and an Al_2O_3 coat-cladding layer. Similar to the core layer of the two-material, anchored-waveguide sections, the core layer of the two-material, suspended-waveguide sections are formed by an

RIE and a sacrificial etch process. After becoming freely suspended, a conformal layer of Al_2O_3 material is applied the core layer by the ALD process.

Device Design

The tether beam width w_{TETHER} is defined as $w_{TETHER} = w_{LITHO} = 100nm$, the minimum feature size, in order to minimize Rayleigh scattering at the T-junction that is formed by the intersection of the suspended waveguide section with the tether beam. The addition of the tether beams decouples the parallel plate MEMS actuator from the suspended waveguide sections.

Most of the parameters are defined for optimal cross-state performance. Cross-state crosstalk is minimized by adjusting nine parameters: coat cladding layer refractive index, n_{COAT}, and width, w_{COAT}; the core layer refractive index, n_{CORE}, width w_{CORE}, thickness h_{CORE}; the surface-to-surface separation $(g_{cBAR_{AB}})$ and overlap length $L_{OPTIC00_{AB}}$ of the suspended waveguide sections of WVGs A and B in Region 00; and the slanted waveguide transitional offset $(\Delta x_{TRAN_{01,10}})$ and length $(L_{TRAN_{01,10}})$.

Device Operation

The As-Fabricated Configuration

In the as-fabricated cross-state configuration, the suspended waveguide sections of WVGs A and B are in parallel alignment. The lightpath that is established between WVGs A and B in this configuration is formed by small-gap and co-directional coupling.

Force-Driven Actuation

The mechanically-deflected bar-state configuration is established in $t_{FDA} = 7\mu s$ under force-driven actuation (FDA) with an (dynamic) actuation voltage (V_{DPI}) of $V_{DPI} =$

$10V$. A minimum dynamic actuation voltage $(V_{DPI_{MIN}})$ of $V_{DPI} = 2V$ establishes the mechanically-deflected bar-state configuration in $t_{FDA} = 20\mu s$. The mechanically-deflected bar-state configuration is maintained with a minimum hold voltage $(V_{HOLD_{min}})$ of $V_{HOLD_{min}} = 1.5V$.

The Mechanically-Deflected Configuration

In the mechanically-deflected, bar-state configuration, both waveguides are elastically deformed from parallel alignment via the connected tether beams. The suspended beam waveguide sections of WVGs A and B have a total suspension length (L_{NM}) of $L_{NM} = 180\mu m$ which allows both waveguide sections to be deflected $400nm$ with an actuation voltage of $10V$ by a parallel-plate MEMS actuator with a cathode/anode overlap area (A_{NEM}) of $A_{NEM} = 9\mu m^2$.

In this configuration, a single-waveguide lightpath is established, meaning that a single propagating mode will enter and exit the same waveguide. Light entering either WVG A or B will leave WVG A or WVG B, respectively, with minimal interference from the tether beam.

Release-Settle Actuation

The as-fabricated cross-state is reestablished from the mechanically-deflected bar-state in $t_{RSA} = 3.3ms$. During release-settle actuation, the elastically-deformed suspended waveguide sections of WVGs A and B experienced small-amplitude oscillations.

The Next Generation

Tethering a parallel-plate actuator to the suspended waveguide sections of WVGs A and B made it possible to independently optimize the optical and MEMS performance of Device 05. The next step in the optical switch design evolution was to completely eliminate the Rayleigh scattering at the suspended waveguide section and tether beam T-junction in order to improve optical performance.

3.6 Device 06

Device 06 is an electromechanical 2×2 optical switch that uses two parallel-plate MEMS actuators in order to modulate two waveguides, simultaneously, between two different configurations.
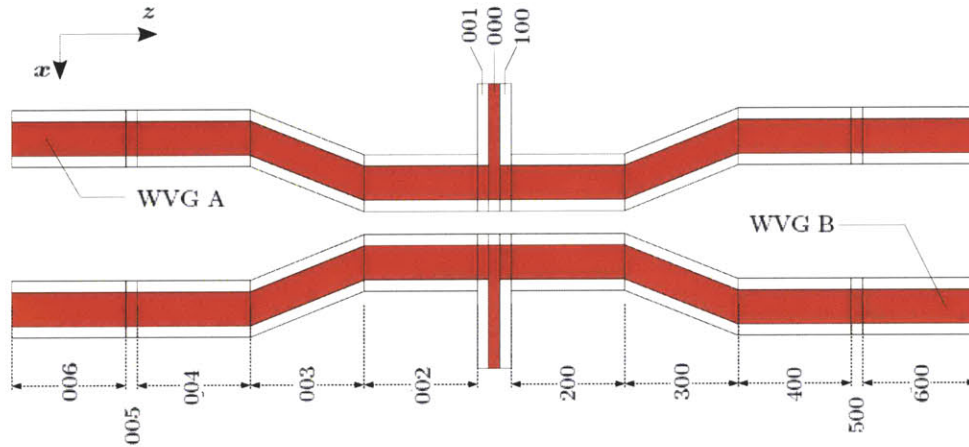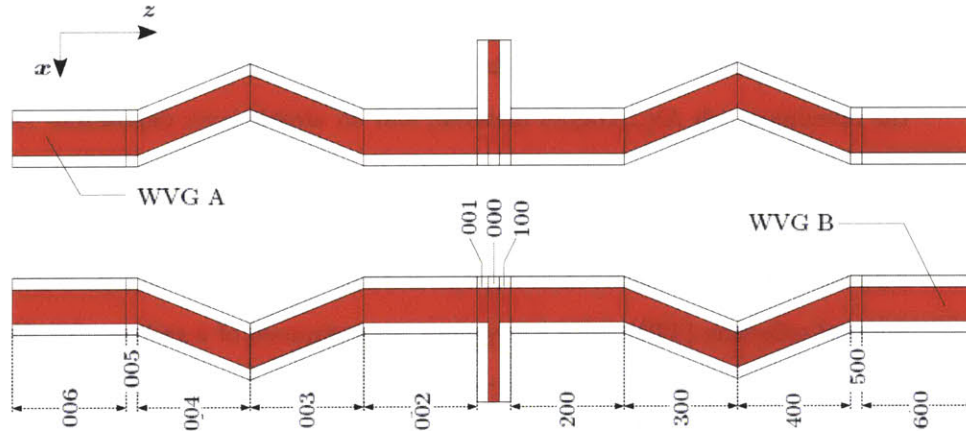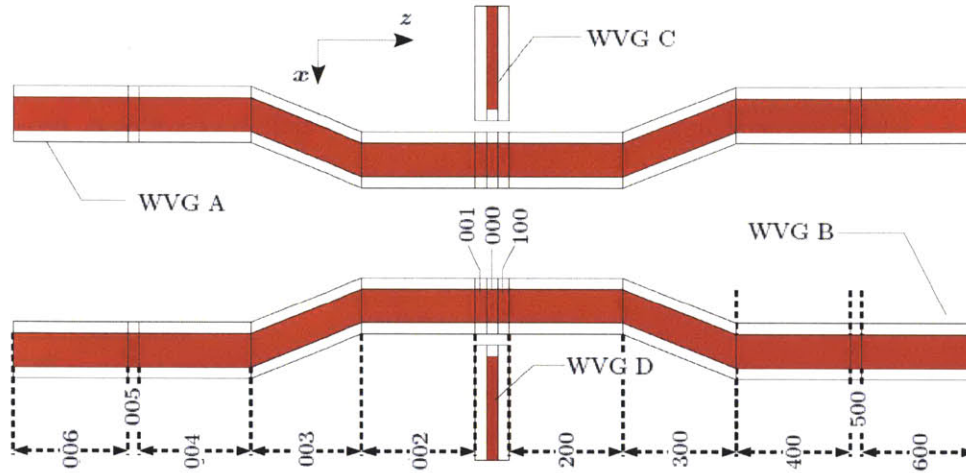

FIGURE 3.18: An (not-to-scale) artistic rendering of the top view of Device 06 in the as-fabricated configuration which establishes two throughput lightpaths.

As shown in Figure (3.18), the as-fabricated, bar-state configuration of Device 06 is modeled as a 4-component, 13-region waveguide structure. The two waveguides that are denoted as WVGs A and B are the primary waveguides that are used to guide light. WVGs A and B are continuous, ridge waveguides that are composed of three different waveguide structures: a three-material, anchored waveguide (Sections 006A and 600A and Sections 006B and 600B), a two-material, anchored waveguide (Sections 005A and 500A and Sections 005B and 500B), and a two-material, suspended waveguide (Sections 004A - 000A - 400A and 004B - 000B - 400B) structure. The two-material, suspended-waveguide structure can be further distinguished by two sections: Sections 003A - 000A - 300A and 003B - 000B - 300B are rigid while Sections 004A, 400A, 004B and 400B are flexible.

The other two waveguides that are denoted as WVGs C and D are used to deflected WVGs A and B with minimal interference to the light guided by WVGs A and B. WVGs

C and D are cantilevered, waveguiding structures that are connected to remote MEMS actuators [the actuators are not shown in Figure (3.18)]. WVGs C and D have a two-material, rigid suspended-waveguide structure. WVGs A and B as well as WVGs C and D have rotational symmetry about the y-axis at the center of Region 000 (on the y = $h_{CORE}/2$ plane).

In the as-fabricated, bar-state configuration, all of the waveguides are in optical isolation. Consequently, light entering WVGs A or B exits WVGs A or B, respectively.
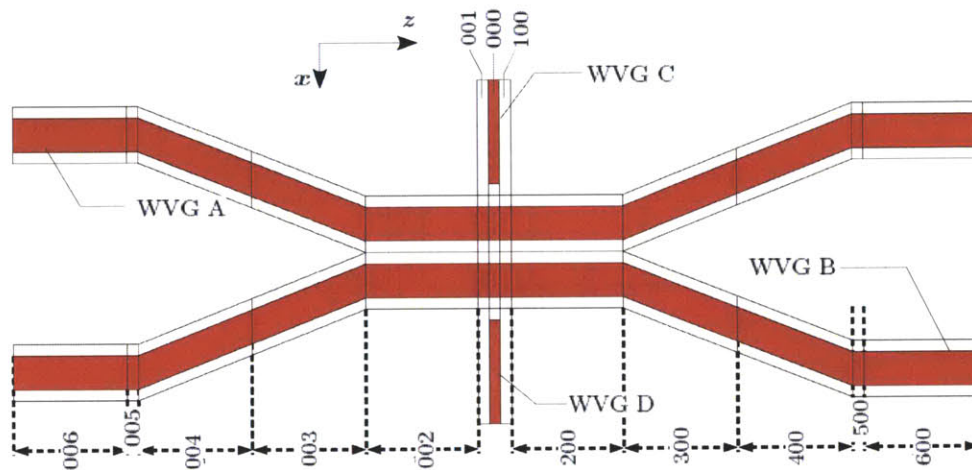
FIGURE 3.19: An (not-to-scale) artistic rendering of top view of Device 06 in the mechanically-deflected configuration which establishes a cross-coupled lightpath.

As shown in Figure (3.19), the mechanically-deflected, cross-state configuration of Device 06 has an arrangement such that the suspended sections of WVGs A and B are simultaneously translated along the x-axis towards one another. Consequently, rigid suspended-waveguide sections (Sections 003A - 000A - 300A and 003B - 000B - 300B) are translated without deformation of shape. Moreover, Sections 002A - 000A - 200A and Sections 002B - 000B - 200B are in intimate contact. The flexible suspended-waveguide sections (Sections 004A and 400A and Sections 004B and 400B) are deformed into a slant.

Physically, the mechanically-deflected cross-state configuration is actualized by the transduction of motion by WVGs C and D from remote MEMS actuators [not shown in Figure

(3.19)] to WVGs A and B. Before WVGs C and D contact WVGs A and B, the motion
of WVGs C and D are governed by the spring suspension of the remote MEMS actua-
tors. Upon contacting WVGs A and B, the motion of WVGs C and D as well as that
of WVGs A and B are governed by the spring suspension of WVGs A and B. In other
words, the deformable, suspended waveguide sections of WVGs A and B determines the
movement dynamics of Device 06.

Device 06 uses four materials for each of the waveguide structures: MBE-grown, gallium-
rich and aluminum-rich $Al_{1-x}Ga_xAs$ materials, an Al-Ga-As-based oxide that is created
from the aluminum-rich $Al_{1-x}Ga_xAs$ material, and an atomic layer deposition- (ALD-)
created, Al_2O_3 material.

The three-material, anchored-waveguide sections of WVGs A and B, which are total
internal reflection (TIR) ridge waveguides, are composed of a gallium-rich $Al_{1-x}Ga_xAs$
core, an Al-Ga-As-based oxide lower-cladding, and an Al_2O_3 upper-cladding layer. The
gallium-rich $Al_{1-x}Ga_xAs$ core is formed by a reactive-ion-etch (RIE) process which com-
pletely etches the material into a rectangular cross-sectioned ridge. The same RIE pro-
cess that is used to form the core is also used to form an aluminum-rich $Al_{1-x}Ga_xAs$
ridge which is later oxidized in order to create the Al-Ga-As-based oxide material used for
the lower-cladding layer. After forming the core and lower-cladding layers, the Al_2O_3
material is deposited around the core and lower-cladding layers in order to form the
upper-cladding layer.

The two-material, anchored-waveguide sections of WVGs A and B–also TIR ridge wave-
guides–are composed of a gallium-rich $Al_{1-x}Ga_xAs$ core and an Al_2O_3 lower-cladding
layer. The gallium-rich $Al_{1-x}Ga_xAs$ core is formed by an RIE (same aforementioned
RIE process) and a sacrificial etch process. Simply by the virtue of the ALD process,
the side-wall deposition of the Al_2O_3 material connects the previously-suspended, core
layer to the substrate. Naturally, the length of these anchored-waveguide sections is
approximately equal to the coat-cladding thickness.

The two-material, suspended-waveguide sections of WVGs A, B, C and D–also TIR ridge waveguides–are composed of a gallium-rich $Al_{1-x}Ga_xAs$ core layer and an Al_2O_3 coat-cladding layer. Similar to the core layer of the two-material, anchored-waveguide sections, the core layer of the two-material, suspended-waveguide sections are formed by an RIE and a sacrificial etch process. After becoming freely suspended, a conformal layer of Al_2O_3 material is applied the core layer by the ALD process.

Device Design

Cross-state zero-gap full codirectional coupling transmission is simultaneously maximized for both the quasi-TE and quasi-TM propagation modes by varying the core width ($w_{A,B}$), thickness (h_{CORE}) and refractive index (n_{CORE}) of the suspended waveguide section of WVGs A and B as well as the conformal coat cladding thickness (t_{COAT}) and refractive index (n_{COAT}). Three-dimensional beam propagation simulations revealed that for $w_{A,B} = h_{CORE} = 300nm$, a core-to-core separation ($g_{CROSS00_{A,B}}$) of $g_{CROSS00_{A,B}} = 100nm$ cross-state transmission is simultaneously maximized for both TE and TM for a variety of core and background refractive indexes that had a refractive index difference of $\Delta n = 1.73$. Two-dimensional eigenmode simulations revealed that for the specific refractive indexes of $n_{CORE} = 3.17$ and $n_{COAT} = 1.44$ quasi-TE and quasi-TM transmission is $-0.36dB$ and $-7.4dB$, respectively.

The first step is to define a set of waveguide cross-section geometries and refractive indexes in order to have a mode confinement factor of 0.50 for both the TE and TM modes.

After that, the mechanically-deflected cross-state configuration is optimized for full small-gap, co-directional coupling between the suspended waveguide sections of WVGs A and B with a surface-to-surface separation ($g_{cCROSS00_{AB}}$) of $g_{cCROSS00_{AB}} = 0nm$ in the presence of a bumper beam with a core width (w_{Bump}) of $w_{Bump} = 100nm$.

In the mechanically-deflected cross-state configuration, the suspended waveguide section of WVGs A and B is composed of a straight waveguide section and two sets of slanted waveguide sections. The mechanically-deflected configuration is established by two, symmetrically-arranged, remote MEM systems that are connected to the suspended (cantilevered) tether beams (WVGs C and D)–the remote MEM systems are not shown in Figures (3.18) or (3.19).

The first set of slanted waveguide sections are lithographically defined and are directly connected to the central straight waveguide section on both ends. The lithographically-defined slanted waveguide sections are always angled at $\Theta_{TRAN} = 10°$ in both the as-fabricated and mechanically-deflected configurations. The constant-angle slanted waveguide sections are lithographically defined in order to ensure optimized cross-state coupling since these sections contribute to the zero-gap co-directional coupling.

The second set of slanted waveguide sections exist only in the mechanically-deflected configuration; in the as-fabricated configuration, these waveguides have zero slant and are straight waveguides.

In order for the suspended waveguides to be deflected into intimate contact, the plate-to-plate actuators of the remote MEM systems are defined to have a $g_{cMEM} = 510nm$ plate-to-plate separation as measured from the surface of the coat-cladding layer, which is half the $g_{cOptic_{01}} = 1\mu m$ surface-to-surface waveguide separation between WVGs A and B in Region 000 plus the $g_{cOptic_{02}}$ surface-to-surface separation between WVGs A and B with WVGs C and D in the as-fabricated, bar-state configuration.

Since a remote, parallel-plate actuators of the remote MEM systems are used to actuate the suspended waveguide sections of WVGs A and B, the effective electrode area (A_{NEM}) is arbitrarily specified to be $A_{NEM} = 6\mu m^2$ by defining the overlap length of the moving cathode and the anchored anode (L_{NEM}) to be $L_{NEM} = 20\mu m$, given that the core layer thickness is $h_{Optic_{01}} = 300nm$ as required for optimal cross-state transmission.

The laterally-operated parallel-plate actuator is attached to a folded flexure suspension system in the as-fabricated configuration. Upon force-driven actuation, the compliance of the moving structure increases as the remote parallel-plate actuators make contact with the two suspended waveguide sections of WVGs A and B.

Both the parallel-plate actuator and the spring compliance of the suspended waveguide sections of WVGs A and B are simultaneously optimized for low-voltage, fast switching. Specifically, the optical device designed to be modulated with a 10-volt dynamic actuation voltage (V_{DPI}).

Device Operation

The As-Fabricated Configuration

In the as-fabricated configuration, the two suspended waveguide sections of WVGs A and B are in optical isolation. Exciting either end of the WVGs A or B will result in the incident radiation being transmitted on the same waveguide into which it is initially excited.

Force-Driven Actuation

The mechanically-deflected cross-state configuration is established in $t_{FDA} = 8\mu s$ with the application of the dynamic pull-in voltage (V_{DPI}) of $V_{DPI} = 10V$. A minimum dynamic pull-in voltage $(V_{DPI_{min}})$ of $V_{DPI_{min}} = 2.4V$ establishes the mechanically-deflected cross-state configuration in $t_{FDA} = 23\mu s$. The mechanically-deflected cross-state is maintained with a minimum hold voltage $(V_{HOLD_{min}})$ of $V_{HOLD_{min}} = 1.4V$.

The Mechanically-Deflected Configuration

In the mechanically-deflected cross-state configuration, both suspended waveguide sections of WVGs A and B are deformed by WVGs C and D, respectively, creating a

flat-bottom V-shaped deflection profile in WVGs A and B. WVGs A and B are in intimate contact in Regions 002, 001, 000, 100, and 200 while Regions 003 and 300 are reconfigured from straight waveguides to slanted waveguides.

The suspended waveguide section of WVGs A and B have a total suspended length, extending from Regions 004–001, 000, 100–400, (L_{NM}) of $L_{NM} = 180\mu m$. Considering that the length of each of the two slanted waveguide sections (L_{TRAN}) is $L_{TRAN} = 2.3\mu m$ and the length over which WVGs A and B form an intimate contact $(L_{OPTIC00_{AB}})$ is $L_{OPTIC00_{AB}} = 8.9\mu m$, the waveguide sections in Regions 003 and 300 are slanted at an angle of $\Theta_{NEM} = 7.5 \cdot 10^{-5} deg$.

Release-Settle Actuation

The as-fabricated bar-state configuration is reestablished from the mechanically-deflected cross-state configuration in $t_{RSA} = 3.2ms$. During release-settle actuation, the elastically-deformed suspended waveguide sections of WVGs A and B are released from the initial intimate contact with each other as WVGs C and D are disengaged.

The Next Generation

Moving forward from Device 06, the focus was directed toward improving the optical operation switching the cross-coupled light transmission mechanism from small-gap codirectional coupling to small-gap adiabatic coupling, a coupling mechanism which is known for its increased insensitivity to feature variations and wider bandwidth support[58].

3.7 Device 07

Device 07 is an electromechanical 2×2 optical switch that uses two remote parallel-plate MEMS actuators in order to modulate two waveguides, simultaneously, between two different spatial configurations.
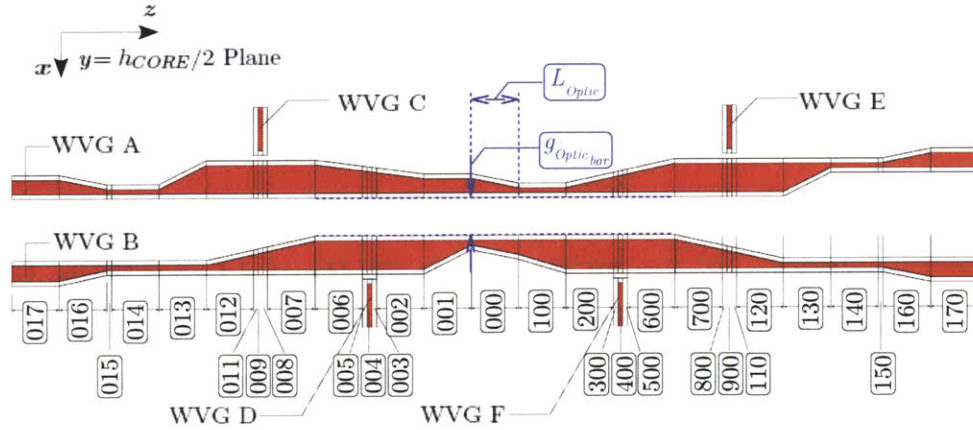
FIGURE 3.20: An (not-to-scale) artistic rendering of the top view of the optical section of Device 07 in the as-fabricated bar-state configuration.

As shown in Figure (3.20), the as-fabricated, bar-state configuration of Device 07 is modeled as a 6-component, 33-region waveguide structure. The two waveguides denoted as WVGs A and B are the primary waveguides that are used to guide light. WVGs A and B are continuous, ridge waveguides that are composed of three different waveguide structures: a three-material, anchored-waveguide (Sections 017A, 016A, 160A, 170A and Sections 017B, 016B, 160B and 170B), a two-material, anchored-waveguide (Sections 015A and 150A and Sections 015B and 150B) and a two-material, suspended-waveguide (Sections 014A–011A, 009A–001A, 000A, 100A–900A, and 110A–170A and Sections 014B–011B, 009B–001B, 000B, 100B–900B, and 110B–170B) structure. The two-material, suspended-waveguide structure can be further distinguished by two sections: Sections 014A and 140A and Sections 014B, 013B, 130B and 130B are deformable suspended-waveguide sections while Sections 013A–011A, 009A–001A, 000A, 100A–900A and 110A–130A and Sections 012B, 011B, 009B–001B, 000B, 100B–900B, 110B and 120B are rigid suspended-waveguide sections. The other four waveguides, denoted as WVGs C, D, E and F, are used to deflect WVGs A and B with minimal interference to the light guided by WVGs A and B. WVGs C, D, E and F are rigid cantilevered, waveguide structures that are connected to remote MEMS actuators [the actuators are not shown in Figure (3.20)]. WVGs C, D, E and F have a two-material,

suspended-waveguide structure.

In the as-fabricated configuration, the bar-state lightpath is established; light entering WVG A exits WVG A, light entering WVG B exits WVG B. WVGs A and B are in optical isolation with each other as well as with WVGs C, D, E and F.
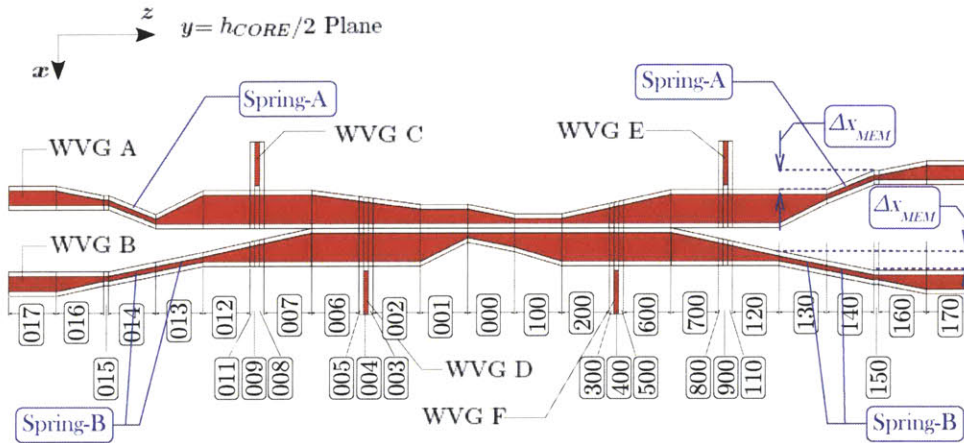
FIGURE 3.21: An (not-to-scale) artistic rendering of the top view of the optical section of Device 07 in the mechanically-deflected configuration which establishes a coupled lightpath in which the bumpers push the waveguides into contact.

As shown in Figure (3.21), the mechanically-deflected, cross-state configuration of Device 07 has an arrangement such that the suspended sections of WVGs A and B have been translated along the x-axis towards one another. The rigid, suspended-waveguide sections of WVGs A and B undergo an x-axis translation without deformation of shape. Due to the specific geometry of WVGs A and B, Sections 006A–001A, 000A and 100A–600A intimately contact Sections 006B–001B, 000B and 100B–600B. The deformable, suspended-waveguide sections of WVGs A and B assume a slanted shape in response to the waveguide deflection.

Physically, the mechanically-deflected cross-state configuration is actualized by the transduction of motion by WVGs C, D, E, F from remote MEMS actuators [not shown in Figure (3.21)] to WVGs A and B. Before WVGs C, D, E and F contact WVGs A and B, the motion of cantilevered waveguides are governed by the spring suspension of the

remote MEMS actuators. Upon contact, WVGs A, C and E move as a single unit as do WVGs B, D and F. Consequently, the motion of WVGs A, C and E are governed by the spring suspension of WVG A and the motion of WVGs B, D and F by the spring suspension of WVG B.

Device 07 uses four materials for each of the waveguide structures: MBE-grown, gallium-rich and aluminum-rich $Al_{1-x}Ga_xAs$ materials, an Al-Ga-As-based oxide created from the aluminum-rich $Al_{1-x}Ga_xAs$ material, and an atomic layer deposition- (ALD-) created, Al_2O_3 material.

The three-material, anchored-waveguide sections of WVGs A and B, which are total internal reflection (TIR) ridge waveguides, are composed of a gallium-rich $Al_{1-x}Ga_xAs$ core, an Al-Ga-As-based oxide lower-cladding, and an Al_2O_3 upper-cladding layer. The gallium-rich $Al_{1-x}Ga_xAs$ core is formed by a reactive-ion-etch (RIE) process which completely etches the material into a rectangular cross-sectioned ridge. The same RIE process that is used to form the core is also used to form an aluminum-rich $Al_{1-x}Ga_xAs$ ridge which is later oxidized in order to create the Al-Ga-As-based oxide material that is used for the lower-cladding layer. After forming the core and lower-cladding layers, the Al_2O_3 material is deposited around the core and lower-cladding layers in order to form the upper-cladding layer.

The two-material, anchored-waveguide sections of WVGs A and B–also TIR ridge waveguides–are composed of a gallium-rich $Al_{1-x}Ga_xAs$ core and an Al_2O_3 lower-cladding layer. The gallium-rich $Al_{1-x}Ga_xAs$ core is formed by an RIE (same aforementioned RIE process) and a sacrificial etch process. Simply by the virtue of the ALD process, the side-wall deposition of the Al_2O_3 material connects the previously-suspended, core layer to the substrate. Naturally, the length of these anchored-waveguide sections is approximately equal to the coat-cladding thickness.

The two-material, suspended-waveguide sections of WVGs A, B, C, D, E and F–also

TIR ridge waveguides–are composed of a gallium-rich $Al_{1-x}Ga_xAs$ core layer and an Al_2O_3 coat-cladding layer. Similar to the core layer of the two-material, anchored-waveguide sections, the core layer of the two-material, suspended-waveguide sections are formed by an RIE and a sacrificial etch process. After becoming freely suspended, a conformal layer of Al_2O_3 material is applied the core layer by the ALD process.

Device Operation

The As-Fabricated Configuration

In the as-fabricated configuration, the two suspended waveguide sections of WVGs A and B are in optical isolation to one another as well as to WVGs C, D, E and F. The tapers along the suspended waveguide sections are adiabatic.

Force-Driven Actuation

The mechanically-deflected cross-state configuration is established in $t_{FDA} = 10\mu s$ with the application of the dynamic pull-in voltage (V_{DPI}) of $V_{DPI} = 10V$. A minimum dynamic pull-in voltage ($V_{DPI_{min}}$) of $V_{DPI_{min}} = 2.4V$ establishes the mechanically-deflected bar-state configuration in $t_{FDA} = 20\mu s$. The mechanically-deflected cross-state is maintained with a minimum hold voltage ($V_{HOLD_{min}}$) of $V_{HOLD_{min}} = 1.4V$.

The Mechanically-Deflected Configuration

The total suspended length of WVGs A and B are defined as $L_{NM} = 200\mu m$–the waveguide sections extending throughout Regions 014–011, 009–001, 000, 100–900 and 110–140.

The suspended waveguide lengths of WVGs A and B that determine the spring constant

of those suspended beams, $L_{Spring_A} = xx\mu m$ and $L_{Spring_B} = xx\mu m$, respectively, are re-configured into tilted waveguide transitions with an x-axis translation of $\Delta x_{MEM} = xx$, the displacement required to switch WVGs A and B from the bar-state configuration (optical isolation) to the cross-state configuration (intimate contact). The suspended waveguide sections denoted as Spring-A are specified as being adiabatic for a transition angle of $\Theta_{MEM_A} = \Delta x_{MEM}/L_{Spring_A}$ =xx. Assuming that the total length of WVGs A and B are equal, the waveguide sections denoted as Spring-B are also adiabatic, having a transition angle, established in the mechanically-deflected configuration, that leads to no more than $-0.05dB$ loss in transmission.

Release-Settle Actuation

The as-fabricated bar-state configuration is reestablished from the mechanically-deflected cross-state configuration in $t_{RSA} = 3.3ms$. During release-settle actuation, the elastically-deformed suspended waveguide sections of WVGs A and B are released from the intimate contact with each other as WVGs C, D, E and F are disengaged.

Device Design

Device 07 is developed by first simultaneously maximizing the cross-state transmission of the TE and TM propagation modes in the mechanically-deflected configuration. Three-dimensional semi-vectorial beam propagation simulations were used in order to vary the suspended waveguide section's refractive indexes, geometries and lengths in order to si-multaneously maximize the cross-state transmission.

During cross-state transmission maximization simulations, several structural and mate-rial parameters were constrained. Θ_{NEM}, the slant angle of the mechanically-deflected spring beam, was limited to $\Theta_{NEM} \leq \Theta_{ACB_{max}}$, where $\Theta_{ADB_{max}}$ is the maximum angle over which a suspended waveguide can be slanted and still remain adiabatic.

The maximum width that a section of the suspended waveguide can be made is lim-ited to $w_{SM_{max}}$, the maximum core width that will only support a single mode of light

propagation.

All taper transitions lengths were at least long enough to retain adiabaticity; the condition of adiabaticity is a function of the start and end taper widths.

Also note that $w_{SM_{max}}$, $\Theta_{ACB_{max}}$ and taper transition lengths are functions of n_{CORE}, the refractive index of the core layer, h_{CORE}, the thickness of the core layer, n_{COAT},the refractive index of the coat cladding layer, and t_{COAT}, the thickness of the coat layer.

Next, both the length of the spring beam sections of the suspended waveguide and the remote parallel-plate MEMS actuator's electrode area were both adjusted in order for Device 07 to be modulated with a 10-volt actuation voltage.

After optimizing Device 07 for $10V$ actuation, the various sectional lengths of the suspended waveguide sections of WVGs A and B were again adjusted in order to ensure maximized cross-state transmission for light traveling in either the TE or TM polarization.

3.8   Device 04: Design in Detail

3.8.1   Introduction

In this section, the general design strategy employed in order to create each of the optical switch devices will be examined in the example device-design case of Device 04. Device 04 serves as the quintessential optical switch, offering insight into how optical switches are designed, model and optimized.

The design strategy follows a six-step process:

Step 01 Optical-System Design

Step 02 Optical-System Optical Simulations

Step 03 Optical-MEM-System Design

Step 04 Optical-MEM-System Optical Design

Step 05 Optical-MEM-System Optical Simulations

Step 06 Optical-MEM-System MEM Simulations

In **Step 01**, the two switch states are defined: the as-fabricated and the mechanically-deflected configurations are determined under the general assumption that the device will undergo linear (reversible), elastic deformation in order to mechanically switch between the two switch-state configurations. At this stage, a decision is made as to which switch-state configuration will be the first configuration to be designed, modeled and optimized. Consequently, the secondary configuration is designed, modeled and optimized under the constrains established for optimized optical operation of the primary switch-state configuration. A design model with two switch-state configurations is created. In **Step 02**, both switch-state configurations are modeled and optimized in their predetermined order. Each switch-state configurations of the design model will have multiple simulation models. In **Step 03**, a microelectromechanical system (MEMS) actuator is designed to best facilitate switching between the two switch-state configurations while minimally affecting the optical performance of both switch-state configurations. In general, for all

optical switches, the MEMS actuator that is used for mechanical switching is based on the particular parallel-plate MEMS actuator and is operated with a 10-voltage actuation voltage. In **Step 04**, a new two-state design model is created. This new two-state design model incorporates the optical and MEM systems. In **Step 05**, the design alterations of the optical system is modeled and optimized, accounting for the changes that arose during **Step 04**. Finally, in **Step 06**, the MEMS actuator is modeled and optimized for the fastest possible switching speed with a 10-voltage actuation voltage while maintaining the optical-system design constraints that ultimately emerge after **Step 05**.

3.8.2   Step 01: Optical-System Design

Device 04 is designed as an optical switch that is based on a two-waveguide, continuous codirectional coupler.
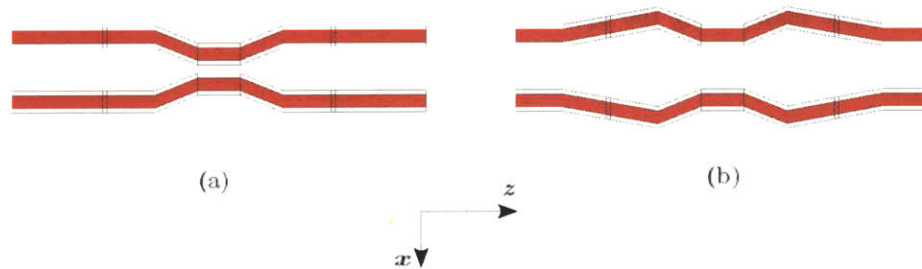
FIGURE 3.22: The Two States of D04-M 01 Design Model of Device 04: Top-down (not-to-scale) schematics of the design model of Device 04 (without an integrated MEMS) in the (a) as-fabricated cross-state and the (b) mechanically-deflected bar-state configurations.

Figure (3.22) is a top-down (not-to-scale) schematic of Device 04 in the cross-state [Figure (3.22a)] and the bar-state [Figure (3.22b)] configurations (without the MEMS actuator).

The cross-state lightpaths are established by mode and proximity coupling mechanisms; the bar-state lightpaths are established by waveguide isolation. Consequently, optimal operation of the cross state requires the adjustment of several variables whereas optimal operation of the bar state requires the adjustment of a few. As a result, the cross-state configuration is designated as the first configuration to be optimized in Step 02.

3.8.3   Step 02: Optical-System Optical Simulations
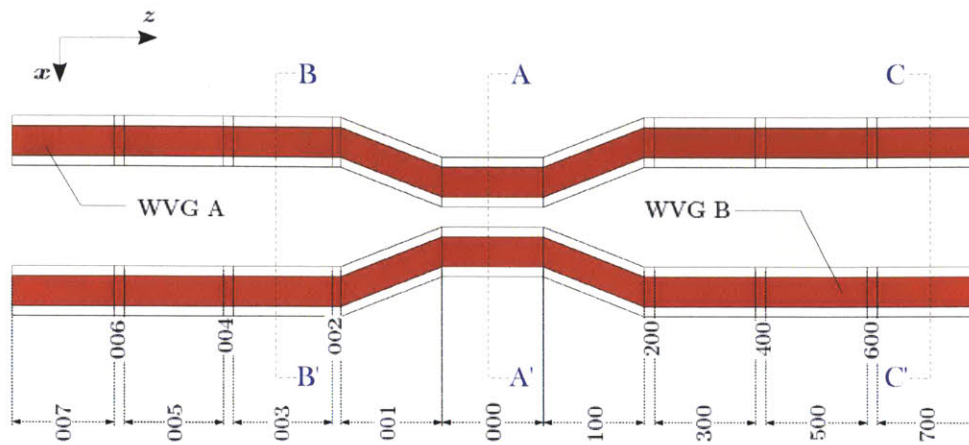
FIGURE 3.23: The D04-M01 Design Model in The As-Fabricated Configuration: Top-down (not-to-scale) schematic of the D04-M01 model (without MEMS) in the as-fabricated cross-state configuration.

Figure (3.23) is a not-to-scale schematic of the as-fabricated, cross-state configuration of the D04-M01 design model (Device 04 without a MEMS actuator), examined from the y-axis plane that bisects the waveguide core layer. Since the cross-state configuration is designated as the as-fabricated configuration, the spacings between waveguide sections are defined by fabrication.
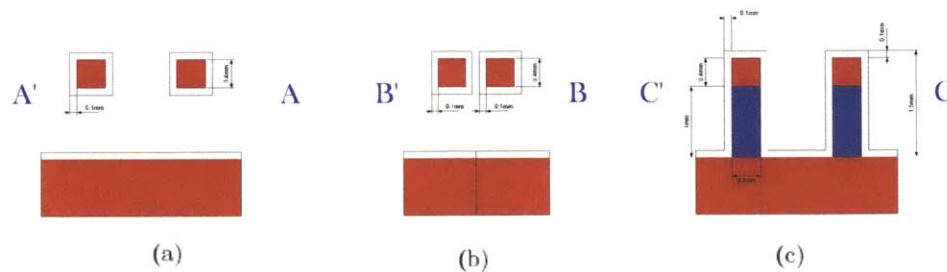
FIGURE 3.24: Side-view schematic (x-y plane) of the D04-M 01 Design Model at lines
A–A; B–Bánd C–C:

Figure (3.24) is a to-scale schematic of the cross-state configuration of the D04-M 01
Design Model, examined at three different x-y planes as denoted in Figure (??). Figure
(3.24a) corresponds to the is the x-axis plane denoted by Line A–A; Figure (3.24b) by
Line B–Bánd Figure (??c) by Line C–C:

At this stage, the nine unique parameters are specified: (1) $h_{Core} = 300nm$, (2) $w_{Optic} =$
$300nm$, (3) $n_{Core} = 3.17$, (4) w_{Coat}, (5) $n_{Coat} = 1.50$, (6) $g_{cOptic_{01}} = 10nm$, (7)
$g_{cIso_{02}=1\mu m}$, (8) $L_{Optic_{01}} = 6\mu m$ and (9) $L_{Optic_{02}} = 2.3\mu m$.

While ensuring that the waveguide cross-section remains strictly single-moded, all nine
parameters are adjusted in order to optimize cross-coupled optical power transmission
which is governed by mode- and proximity-coupling mechanisms.

In order to capture the three-dimensional structural effects, a three-dimensional model
of Device 04 is constructed in BeamPROP. Recall that as BeamPROP is based on the
beam propagation method, as the refractive index contrasts increases and geometries
decrease, simulation accuracy is challenged. In an attempt to not compromise accuracy,
Device 04–a two-material waveguide structure inside a background of air–is modeled as

a single-material waveguide structure inside an adjustable-refractive-index background in BeamPROP. Both the refractive index of the waveguide and background (as modeled in BeamPROP) are adjusted in uncover refractive-index-contrast ($n_{CORE} - n_{BACK}$) and mode-core-confinement (Γ_{TE} and Γ_{TM}) trends in coincidental full-power, optical power transmission for both TE- and TM-polarized light.
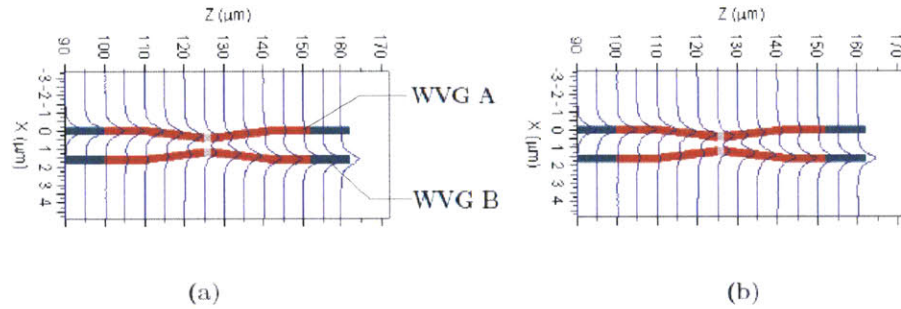
FIGURE 3.25: Contour plots for the D04-M01-BPROP 01 Simulation Model: The optical field amplitude in the xz plane for light traveling in (a) the quasi-TE$_{00}$ and (b) the quasi-TM$_{00}$ modes. Specifically for this Simulation Model, the single-material core is defined as $n_{CORE} = 3.17$ in a background refractive index of $n_{BACK} = 1.44$.

Figure (3.25) is the quasi-TE$_{00}$ and quasi-TM$_{00}$ propagating mode plots for the single-material waveguide beam propagation model of the D04-M 01 design model.

This is the initial model that is used to maximize the cross-state transmission and minimize the bar-state transmission for both the quasi-TE$_{00}$ and quasi-TM$_{00}$ polarizations. During the simulation, the D04-M 01 model is excited by quasi-TE$_{00}$- and quasi-TM$_{00}$-polarized light in two separate runs.

(a)   (b)
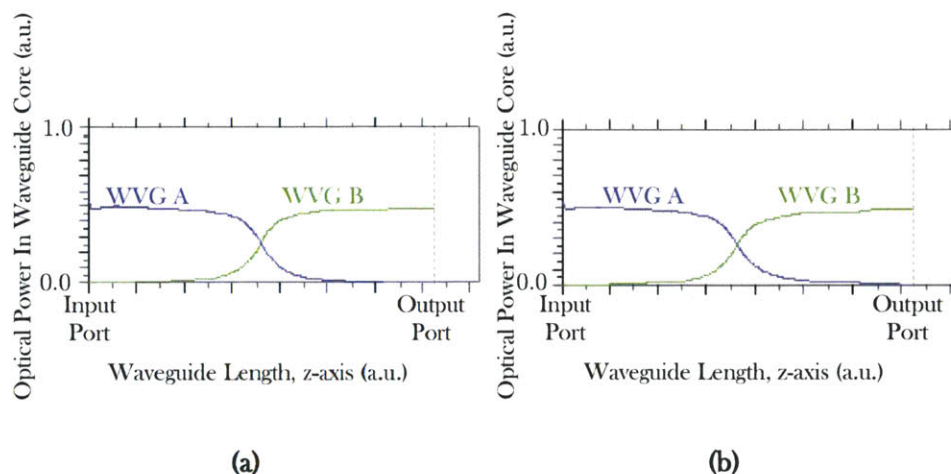
FIGURE 3.26: Optical-Power Evolution Through The D04-M01-BPROP 01 Simulation Model: The evolution of the optical power traveling in (a) the quasi-TE$_{00}$ and (b) the quasi-TM$_{00}$ modes through WVG A and B.

Figure (3.26) shows how optical power evolves through the D04-M01-BPROP 01 model as a function of position along the z-axis.

Table (3.1) lists nine parameters as well as the cross-state transmission and crosstalk for both the quasi-TE$_{00}$ and quasi-TM$_{00}$ polarizations for the four different D04-M01-BPROP simulation models.

TABLE 3.1: The parameters used for the D04-M01-BPROP 02, 03, 04 and 05 Simulation Models.

Variable	Description	02	03	04	05
n_{CORE}	The refractive index of the waveguide core.	2	3.2	3	1.5
n_{BACK}	The refractive index of the background.	1.5	2.8	2.5	1.0
$\Delta n_{COREback}$	The refractive index difference.	0.5	0.4	0.5	0.5
$w_{A,B}$, h_{CORE}, $g_{CROSS_{AB}}$	The characteristic waveguide dimension.	$500nm$	$400nm$	$400nm$	$700nm$
V_{NWP}	The normalized waveguide parameter.	2.681	2.512	2.689	3.172
$\Gamma_{CORE_{TE}}$	The normalized waveguide parameter.	0.48	0.50	0.55	0.60
$\Gamma_{CORE_{TM}}$	The normalized waveguide parameter.	0.48	0.50	0.54	0.61
Continued on Next Page...					

Table 3.1 – Continued

Variable	Description	02	03	04	05
$L_{OPTIC00_{AB}}$	The minimum length require to maintain adiabaticity as a $w_{optic} \times w_{optic}$ cross-section waveguide undergoes a $\Delta x = w_{optic}$ transition (BeamPROP Model 03).	$15\mu m$	$17\mu m$	$16\mu m$	$25\mu m$
L_{TRAN}	The length over which complete directional coupling is achieved for coupled continuous coupled waveguides with adiabatic transitions (BeamPROP Model 04).	$5\mu m$	$2\mu m$	$5\mu m$	$15\mu m$
$P_{CROSStx}$ (TE_{00})	Cross-state transmission of light in the TE_{00} mode.	$-0.09dB$	$-0.20dB$	$-0.20dB$	$-0.07dB$
$P_{CROSSxtalk}$ (TE_{00})	Cross-state crosstalk of light in the TE_{00} mode.	$-18dB$	$-35dB$	$-31dB$	$-29dB$
$P_{CROSStx}$ (TM_{00})	Cross-state transmission of light in the TM_{00} mode.	$-0.20dB$	$-0.20dB$	$-0.10dB$	$-0.22dB$
$P_{CROSSxtalk}$ (TM_{00})	Cross-state crosstalk of light in the TM_{00} mode.	$-22dB$	$-24dB$	$-18dB$	$-17dB$

Table (3.1) contains the optimized parameters for a low polarization-dependent full codirectional coupler that is modeled as a single-material core in a background material.
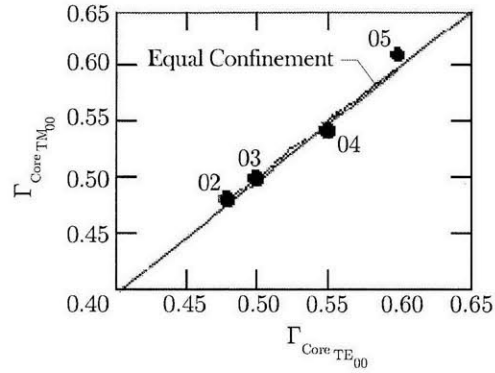
FIGURE 3.27: Optical-Power Confinement Plot For The D04-M01-BPROP 02, 03, 04 and 05 Simulation Models: Optical-power confinement of light traveling in the quasi-TE_{00} and quasi-TM_{00} modes for a straight single-material waveguide core in a background index described in Table (3.1).

The quasi-TE_{00} and quasi-TM_{00}-polarized, optical-power confinement factors for the D04-M01-BPROP 02, 03, 04 and 05 models are plotted in Figure (3.27). Notice that the confinement factor for the four selections are within a 15% range of 0.53; the difference in confinement for the two polarizations ($|\Gamma_{CORE_{TE}} - \Gamma_{CORE_{TM}}|$) for a given index selection is 2% or better.
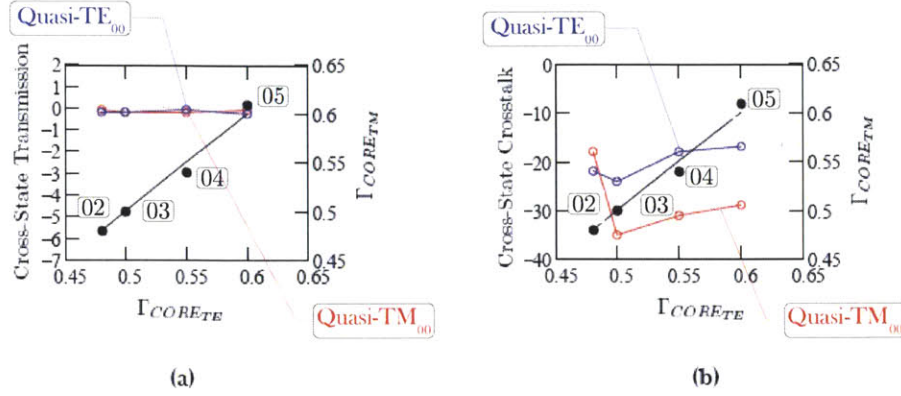
FIGURE 3.28: Cross-State Transmission and Crosstalk Plots for D04-M01-BPROP 02, 03, 04 and 05 Simulation Models: The cross-state (a) transmission and (b) crosstalk optical-power (in decibels)for both the quasi-TE$_{00}$ and quasi-TM$_{00}$ polarizations.

Figure (3.28a) shows that full codirectional coupling is achieved for light propagating in both the quasi-TE$_{00}$ and the quasi-TM$_{00}$ polarization modes, regardless of the core and background material refractive indexes as long as $\Gamma_{CORE_{TE}} = \Gamma_{CORE_{TM}}$=(0.5 or 0.6) and/or $V_{NWP} \approx 3.0$. However, judging by Figure (3.28b), a perceivable minimum in cross-state crosstalk can be seen. This minimum could be a result of $L_{TRAN} = 2\mu m$, $\Gamma_{CORE_{TE}} = \Gamma_{CORE_{TM}} = 0.50$, $V_{NWP} = 2.5$ or $\Delta n_{COREback} = 0.4$.

In an attempt to verify that the cross-state crosstalk minimum is a real optical effect, a two-dimensional models of Device 04 are constructed to have various combinations of $L_{TRAN} \approx 2\mu m$, $\Gamma_{CORE_{TE}} \approx 0.50$, $V_{NWP} \approx 2.5$ and $\Delta n_{COREback} \approx 0.4$. Ultimately, $\Delta n_{COREback} \approx 0.4$ is seen to not be a necessary condition for full codirectional coupling of light in the TE$_{00}$ mode. Instead, $L_{TRAN} \approx 2\mu m$ and $\Gamma_{CORE_{TE}} \approx 0.50$ allows for maximized codirectional coupling over a length of $L_{OPTIC00_{AB}} \approx 5\mu m$.

Specifically, for the two-dimensional two-material eigenmode model with optimized parameters of $w_{A,B} = 300nm$, $n_{CORE} = 3.17$, $n_{COAT} = 1.44$, $\Delta n_{COREback} = 1.73$, $L_{OPTIC00_{AB}} = 6\mu m$, $L_{TRAN} = 2.3\mu m$ and $g_{CROSS00_{AB}} = 100nm$ ($w_{COAT} = 50nm$ and $g_{cCROSS00_{AB}} = 10nm$), $P_{CROSStx} = -0.2dB$ and $P_{CROSSxtalk} = -35dB$ for the

TE$_{00}$ mode of light propagation was calculated. Note that for the two-dimensional two-material eigenmode model, $\Delta n_{COREcoat}$ is increased and $g_{CROSS_{AB}}$ is decreased in order to decrease $L_{OPTIC00_{AB}}$ to $L_{OPTIC00_{AB}} = 6\mu m$.
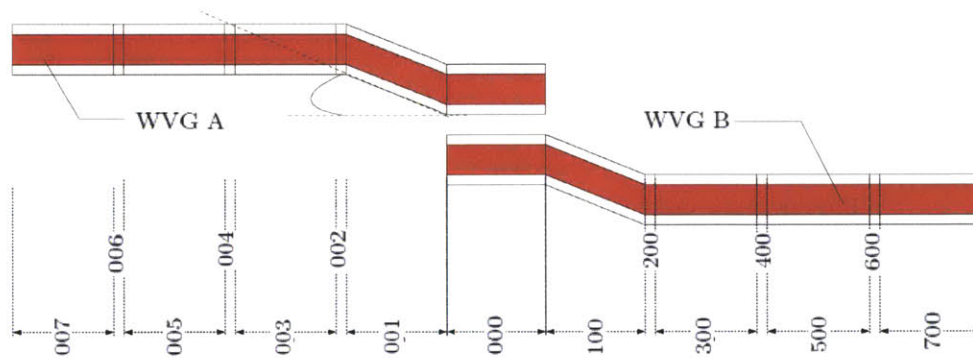
FIGURE 3.29: D04-M01-CAMFR 01 Model: Schematic of the two-dimensional CAMFR Simulation Model used to determine the maximum angle for adiabaticity.

Figure (3.29) is the two-dimensional two-material eigenmode model that was used to determine the maximum angle at which the tilted waveguide section in Regions 001 and 100 can be transitioned while maintaining adiabaticity.

(a)

(b)
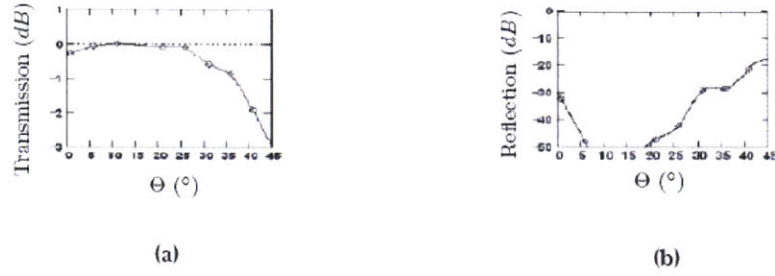
FIGURE 3.30: Optical-Power Transmission And Reflection Plots for The D04-M01-CAMFR 01 Simulation Model:The optical-power (a) transmission and (b) the reflection of the quasi-TE_0 mode.

Figure (3.30) shows the simulation results of the D04-M01-CAMFR 01 simulation model. Note that Θ_{ADB} is a function of n_{CORE}, n_{COAT}, $w_{A,B}$ and w_{COAT}. The condition for adiabaticity is satisfied for optical-power transmission larger than $-0.05dB$ for light traveling in either the TE_0 and TM_0 polarization modes. For the specific case of $n_{Core} = 3.17$, $n_{Coat} = 1.5$, $w_{Core} = 300nm$ and $w_{Coat} = 30nm$–the material and geometries that establishes optimal, maximized full codirectional coupling for both the TE_0 and TM_0 modes for the two-port, discontinuous codirectional coupler–the condition of adiabaticity for the tilted waveguide section is satisfied for a $\Theta_{Tran} \approx 20°$.
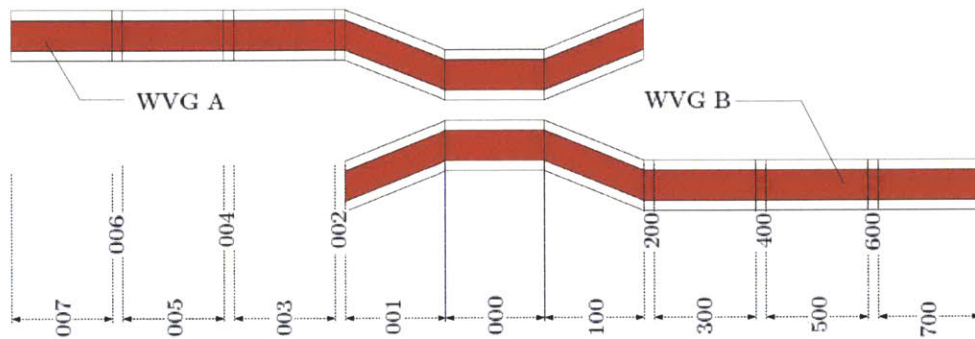
FIGURE 3.31: The D04-M01-CAMFR 02 Simulation Model: Schematic of the two-dimensional optical structure that was used to simulate light flow through the D0-M 01 design model in the as-fabricated, cross-state configuration using the eigenmode expansion method (CAMFR). WVGs A and B have a cross section comprised of two materials (core and coat-cladding layers) in a background of air.

Figure (3.31) is a schematic of the two-dimensional simulation model (the D04-M01-CAMFR 02 model) that is used to simulate light flow through the design model D04-M 01, in the as-fabricated cross-state configuration. The two waveguides (WVGs A and B) are two-material waveguides with a core layer ($n_{CORE} = 3.17$) and a coat cladding ($n_{COAT} = 1.44$) in a background of air ($n_{BACK} = 1.00$).
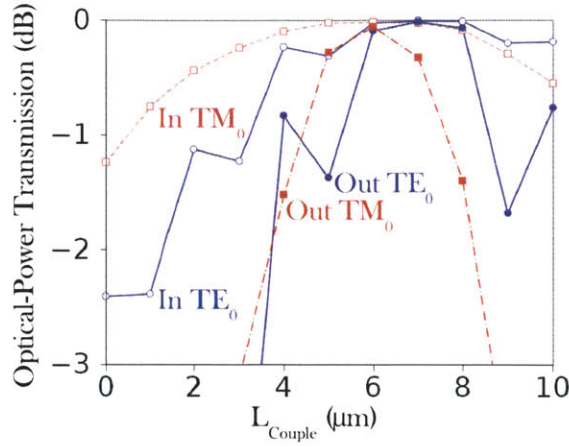
FIGURE 3.32: The Optical-Power Transmission Of Quasi-TE_{00}-polarized Light Through The D04-M01-CAMFR 02 Model: Transmission of optical power carried in the quasi-TE_0 polarization mode after the simulation model is excited with quasi-TE_0-polarized light.

As shown in Figure (3.32), given $n_{Core} = 3.17$, $n_{Coat} = 1.5$, $w_{Core} = 300nm$, w_{Coat} and $g_{Optic_{cross}} = 100nm$, the cross-state optical power transmission is maximized at $\mathbf{L_{Optic} = 6.0 \pm 0.5\mu m}$ for both the TE_0 and TM_0 polarizations.

A series of simulations were performed in order to establish coincidental, maximized transmission for TE_0- and TM_0-polarized light. The variables n_{Core}, n_{Coat}, w_{Core}, w_{Coat} and $g_{Optic_{cross}}$ were varied. Guided by the results of the BeamPROP simulations, a confinement factor approaching $\Gamma_{TE_0} \approx 0.50$ was initially established by setting $w_{Core} = 300nm$. Incidently, as compared to other values of w_{Core}, a $w_{Core} = 300nm$ ($\Gamma_{TE_0} \approx 0.50$) produces a coincidental, maximized transmission for TE_0- and TM_0-polarized light over a widest tolerance of L_{Optic}.

Accuracy for all runs was maintained with a PML power of -0.2, 30 modes, and an x and z grid discretization of $0.1nm$.[3]

---

[3]Since the D04-M01-CAMFR 02 Model consisted of only Manhattan geometries, each 10-point loop was completed in under $0.50min$.
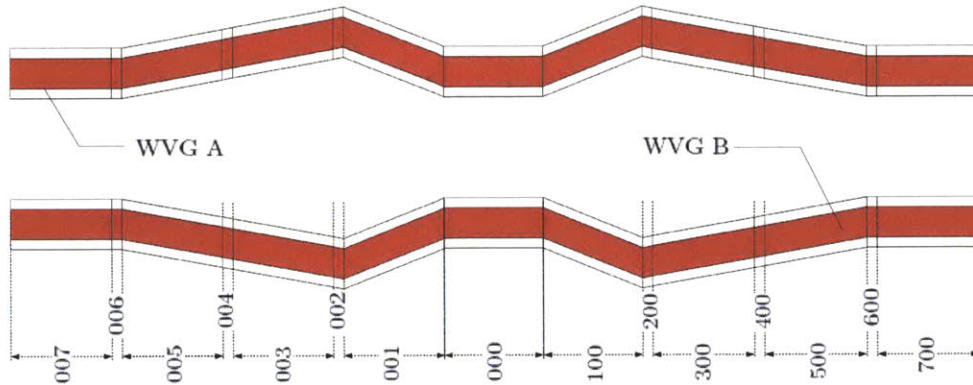
FIGURE 3.33: The D04-M 01 Design Model In The Mechanically-Deflected Bar-State Configuration: Top-down view of the D04-M 01 model (sans MEMS), examined on the xz plane at $y = \frac{h_{CORE}}{2}$.

Figure (3.33) is a not-to-scale schematic of the bar-state configuration of the D04-M 01 model (without a MEMS actuator), examined from the y-axis plane that bisects the waveguide core layer. As the cross-state configuration is designated to be the as-fabricated configuration, the bar-state configuration must be the mechanically-deflected configuration. Consequently, each of the waveguide sections are defined to be (1) movable and rigid, (2) deformable, and (3) anchored.

The waveguide sections in Regions 007, 006, 600 and 600 are defined as anchored structures. The waveguide sections in Regions 005 - 003 and 300 - 500 are defined as (suspended[4]) deformable structures. By defining the deformable waveguide sections to be of a particular length, the waveguide sections in Regions 002 - 000 - 200 are made to be movable and rigid, a posteriori.

Optimal optical operation of the bar-state configuration requires that WVGs A and B are positioned in optical isolation from each other. Also, the deformable waveguide

---

[4]While only the waveguide sections in Regions 002 - 000 - 200 are the only waveguide sections that are required to be suspended structures for optimal optical operation in the cross-state configuration, the deformable waveguide sections are defined as suspended structures as well. Defining the deformable waveguide sections as suspended structures simplifies the MEMS design.

sections must not undergo a deflection that will create optical losses. In other words, the deformable waveguide sections in the mechanically-deflected configuration must remain optically adiabatic. In summary, two parameters are specified at this stage:

- $g_{cBAR_{AB}}^{000}$

- $\Theta_{ADB}^{005,500}$, and $\Theta_{ADB}^{005,500} = \Theta_{ADB}^{003,300}$
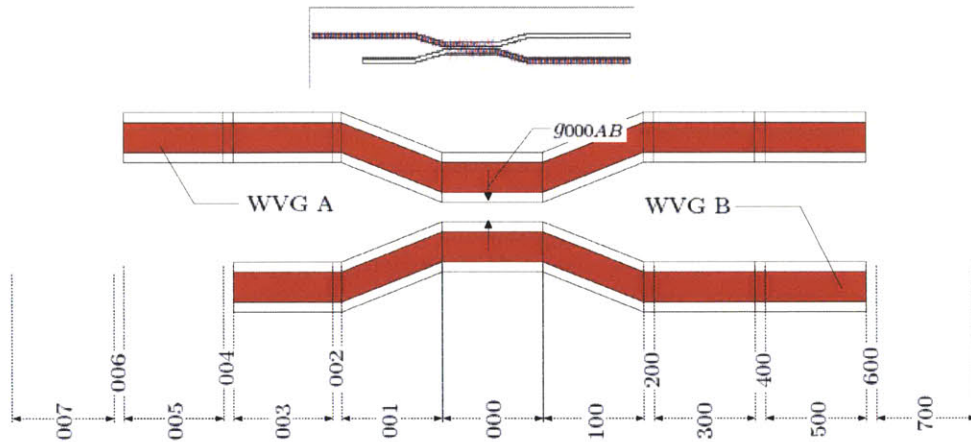
FIGURE 3.34: The D04-M01-CAMFR 03 Simulation Model: Schematic of the two-dimensional CAMFR Simulation Model used to determine the minimum separation between WVGs A and B required for optical isolation.

Figure (3.34) is an illustration of the D04-M01-CAMFR 03 simulation model that was used in order to ascertain the minimum separation distance between WVGs A and B that is required for optical isolation.
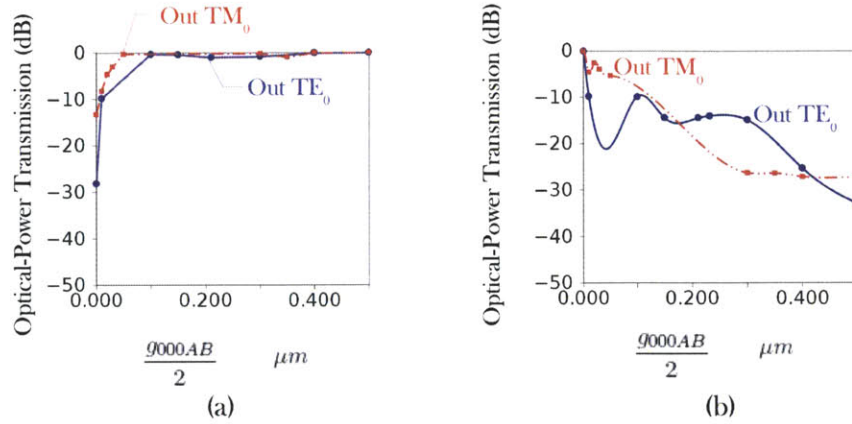
FIGURE 3.35: Optical-Power Transmission And Reflection Plots For The D04-M01-CAMFR 03 Model: The optical-power (a) transmission and (b) the reflection of the quasi-TE$_0$ and plane TM modes.

From Figure (3.35), a surface-to-surface waveguide separation of $g_{cOptic} = 1\mu m$ established a bar-state transmission (optical-power transmission in WVG B) of $-0.06dB$ and a crosstalk (optical-power transmission in WVG A) of $-33dB$ for TE$_0$-polarized light. For TM$_0$-polarized light, bar-state crosstalk levels off at $-27dB$, starting initially at a $g_{cOptic} \approx 400nm$; the quasi-TM_{00}, is assumed to follow a similar asymptotic trend but at a low level of crosstalk. Consequently, a $g_{cOptic_{bar}} = 1\mu m$ is sufficient for optical oscillation, thus constraining the minimum possible MEMS deflection of $\Delta g_{MEM} = 500nm$, assuming both waveguides will be deflected simultaneously.

3.8.4 Step 03: Optical-MEM-System Design

In order to establish the second switch state of D04-M 01, a MEMS actuator is required. Since small displacements are required, the parallel-plate MEMS actuator allows for the fastest actuation speeds. As a result, a parallel-plate MEMS actuator is integrated along the side surfaces of the suspended waveguides.

3.8.5 Step 04: Optical-MEM-System Optical Design

As it turns out, a few iterative cycles between Steps 04 and Step 05 reveal that the best MEMS configurations is given by Figures (3.36) and (3.37). Specifically for Device 04, the parallel-plate MEMS actuator is integrated along the sidewall surfaces of both suspended waveguide sections; the sidewall surfaces serve as moving cathodes to a set of stationary anodes. The addition of the stationary anodes alters the initial design created in Step 01.
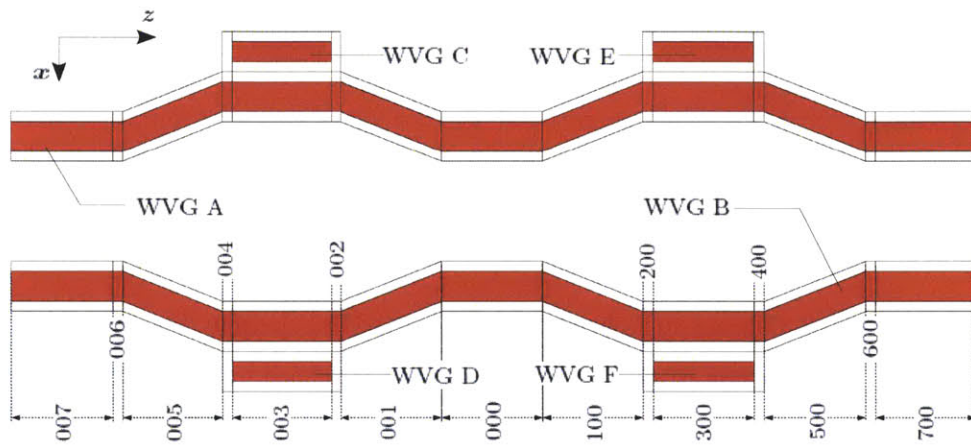
FIGURE 3.36: The D04-M 02 Design Model In The As-Fabricated, Cross-State Configuration: A not-to-scale schematic of the D04-M 02 model viewed on the $y = h_{CORE}/2$, xz-plane.

Figure (3.36) is a top view of the D04-M 02 design model in the as-fabricated, cross-state configuration. For the D04-M 02 model, a MEMS actuator is integrated into the design model. Specifically, four additional geometries are positioned in adjacent alignment to the two suspended waveguides (WVGs A and B).
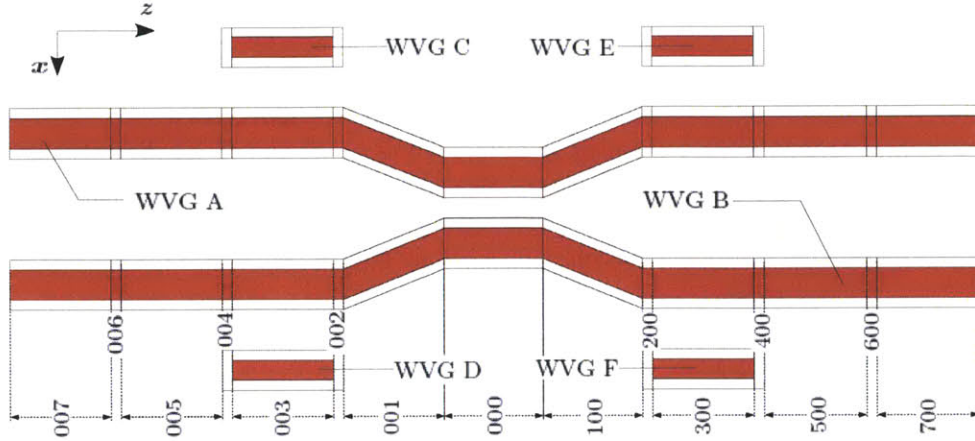
FIGURE 3.37: The D04-M 02 Design Model In The Mechanically-Deflected, Bar-State Configuration: A not-to-scale schematic of the D04-M 02 model viewed on the $y = h_{CORE}/2$, xz-plane.

Figure (3.37) a not-to-scale schematic the D04-M 02 model in the mechanically-deflected bar-state configuration. The MEMS actuator is defined to generate the required elastic deformation which was originally required for the mechanically-deflected, bar-state configuration first proposed for the D04-M 01 design model.

In the mechanically-deflected, bar-state configuration, WVG A makes intimate contact with the two discontinuous waveguides, WVGs C and E; WVG B makes intimate contact with WVGs D and F. As a result, the optical structure represented in Figure (3.37) should be designed so that transmission through WVGs A and B are minimally effected by WVGs C, D, E and F.

Observing the four material and geometric constraints that are required for the as-fabricated, cross-state configuration: (1) $n_{CORE} = 3.17$, (2) $n_{COAT} = 1.50$, (3) $w_{A,B} = h_{CORE} = 300nm$ and (4) $g_{cBAR_{AC,BD}} = 0nm$, the core width of WVGs C, D, E and F ($w_{Optic_{02}}$) and the overlap length between WVGs A, C and E and WVGs B, D and F ($L_{Optic_{02}}$) are the free geometric parameters that are to be optimized in order to maximize the bar-state transmission and to minimize the bar-state crosstalk and reflection.

3.8.6   Step 05: Optical-MEM-System Optical Simulations
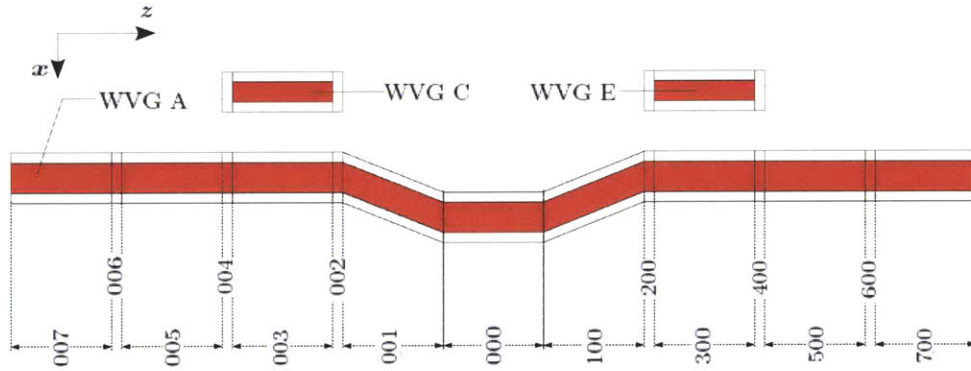
FIGURE 3.38: The D04-M02vB-CAMFR 01 Simulation Model: The two-dimensional model that was used to determine the minimal separation between the MEMS actuator electrodes (WVGs C and E) from the suspended waveguides (WVG A), that are required for optical isolation.

Figure (3.38) is an illustration of the D04-M02vB-CAMFR 01 simulation model that was simulated in order to ascertain the minimal surface-to-surface separation between the suspended waveguides and the stationary anodes required for optical isolation. Minimal surface-to-surface separation is achieved by the maximization of transmitted optical power above -0.01dB.
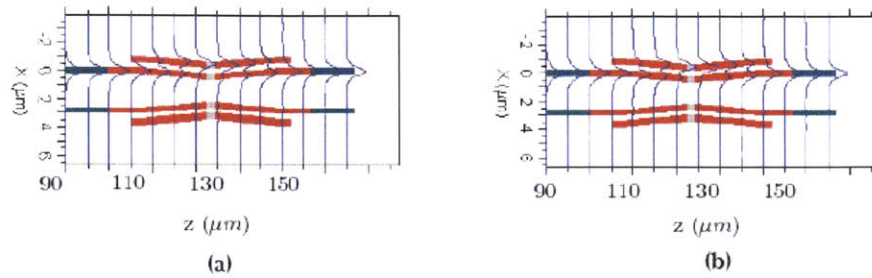
FIGURE 3.39: Propagating-Mode Contour Plot Of The D04-M02vA-BPROP 01 Model (Version A of Design Model 02): Contour plot of light traveling in (a) the quasi-$TE_0 0$ and (b) the quasi-TM_{00} modes.

Figure (3.39) is the image captured from the BeamPROP simulation of the optical system of the version A of the Optical-MEM System Design Model.[5] Superimposed on the BeamPROP geometry is the light-propagation profile for light traveling in the quasi-TE_{00} [Figure (3.39a)] and quasi-TM_{00} [Figure (3.39b)] polarizations. Notice the remarkable similarity of the light-propagation profiles, a similarity indicative of low polarization dependent loss.

---

[5]Comparing Figures (3.38) and (3.39), notice that instead of two symmetrically-arranged, discontinuous waveguides (WVGs C and E), adjacently aligned to WVG A, there is only one discontinuous waveguide (WVG C) adjacently aligned to WVG A. Also note that the WVG C in Figure (3.39) is not a straight waveguide; this WVG C follows the same waveguide contour of WVG A, extending throughout Regions 004–001, 000, 100–400. Upon later investigation (with CAMFR simulations), version B of the Optical-MEM System Design Model was found to produce comparable bar-state optical performance. Version B of the Optical-MEM System Design Model is thought to be the better mechanical design since the parallel plate (integrated along WVGs A, C and E) maintain a straight surface along the z-axis.
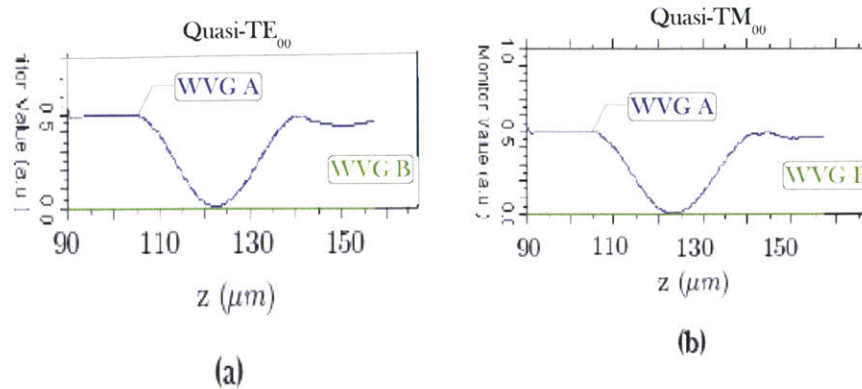
FIGURE 3.40: Bar-State, Transmission And Crosstalk Plots for D04-M02-BPROP 01: Optical power transmission and crosstalk of light carried in (a) the quasi-TE$_{00}$ and (b) the quasi-TM$_{00}$ polarization modes.

Figure (3.40) further shows the polarization independence first observed in Figure (3.39): the light loss for both quasi-TE$_{00}$ and -TM$_{00}$-polarized light is negligible as light is coupled from WVG A, to WVG C and back into WVG A. Also note that the during the co-directional coupling between WVGs A and C, no trace light radiation is coupled into WVG B; WVGs A and B are in optical isolation.
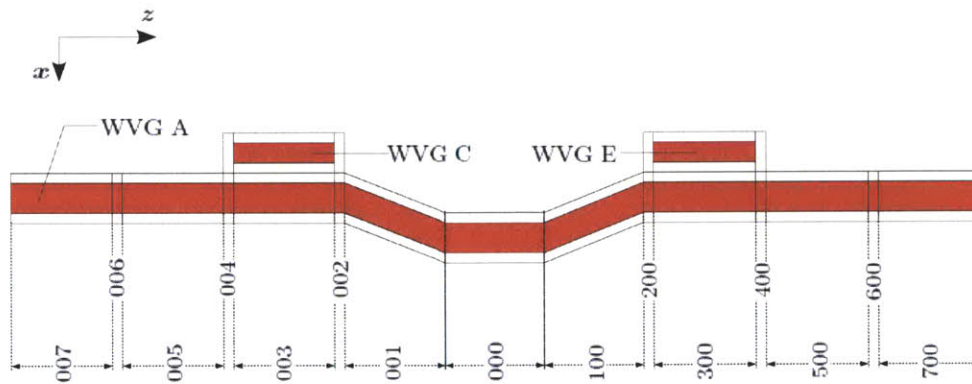
FIGURE 3.41: The D04-M02-CAMFR 02 Model: The two-dimensional, simulation model that was used to determine $L_{003,300}$ and $w_{Optic02}$.

Figure (3.41) is a schematic of the D04-M02vB-CAMFR 02 Model that was used to determine $L_{Optic_{02}}$ and $w_{Optic_{02}}$.
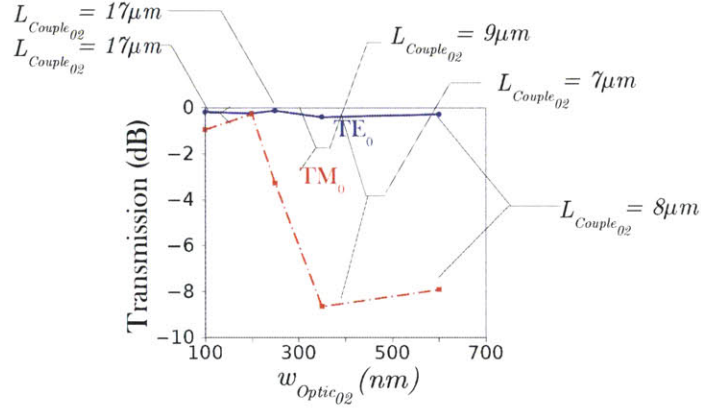
FIGURE 3.42: Transmission And Reflection For The D04-M02vB-CAMFR 02 Model: The (a) transmission and (b) reflection of optical power carried in the quasi-TE_0 polarization mode as a function of $w_{Optic_{02}}$.

Figure (3.42) is the simulation results form five optimization simulations of the D04-M02vB-CAMFR 02 Model. Specifically, $w_{Optic_{02}}$ was specified and $L_{Optic_{02}}$ was optimized for maximized transmission for TE_0-polarized light. After which, the same optimized structures were simulated for TM_0-polarized light. Coincident maximized transmission for TE_0- and TM_0-polarized light occurred at $w_{Optic_{02}} = 200nm$ for an $L_{Optic_{02}} = 17\mu m$. Consequently, the $A_{MEM} = (L_{MEM} = L_{Optic_{02}} = 17\mu m) \times (h_{Optic_{02}} = 300nm) = 5.1\mu m^2$ parallel-plate actuator area of the waveguide-integrated, MEM system is completely constrained by optimized operation of the optical system.
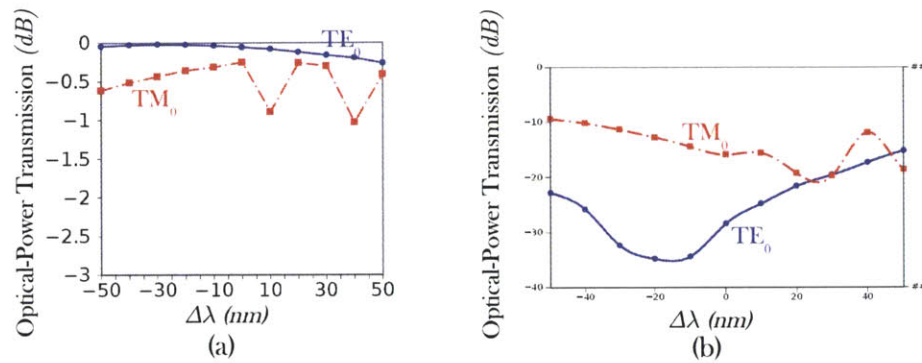
FIGURE 3.43: Cross-State Transmission and Crosstalk vs. $\Delta\lambda$ for the D04-M 02vB Model: (a) Cross-State Transmission vs. $\Delta\lambda$ for optical power carried in the TE_0 and TM_0 polarization modes as determined from the D04-M01-CAMFR 03 Simulation Model.

Figure (3.43) shows the expected bandwidth of Device 04 in the cross-state configuration as determined from the D04-M01-CAMFR 03 Simulation Model.

Consider Figure (3.43a): The bandwidth reduction (transmission below $-0.5dB$) for the cross-state transmission occurs at approximately a -40nm blueshift in the $\lambda_0 = 1.55\mu$, central frequency. This bandwidth reduction in primarily due to the co-directional coupling mechanism used for Device 04. There seems to be also a bandwidth reduction in the redshift frequency range. This apparent bandwidth reduction is certainly not a result of the co-directional coupling mechanism. This has been verified with a CAMFR simulation model used for Device 03, which uses the co-directional coupling mechanism as well.

Consider Figure (3.43b): Clearly, the cross-state crosstalk for the TM_0-polarized light destroys the utility of Device 04 as the crosstalk for light in this polarization mode is above $-20dB$. In order to restore utility, more sophisticated design of the transition waveguide section is required. Cross-state crosstalk for TE_0-polarized light is bandwidth-limited in the redshift frequency range. This redshift bandwidth limitation can be improved with improved transition waveguide section design.
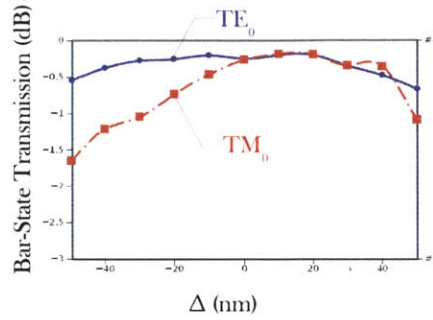
FIGURE 3.44: Bar-State Transmission vs. $\Delta\lambda$ for the D04-M 02 Design Model: Bar-state transmission for (a) TE_0-polarized and (b) TM_0-polarized light as simulated from the D04-M02 CAMFR 02 Model.

According to Figure (??), polarization-independent bandwidth support of Device 04 is limited by the bar-state transmission of TM_0-polarized light propagation. For TM_0-polarized light propagating, the bar-state configuration of Device 04 is unable to support any wavelengths blueshifted from $\lambda_0 = 1.55\mu m$ as transmission quickly falls below $-0.5dB$. For TE_0-polarized light propagation, bandwidth is limited to a $\pm 40nm$ due to the redshift transmission drop.

3.8.7   Step 06: Optical-MEM-System MEM Simulations
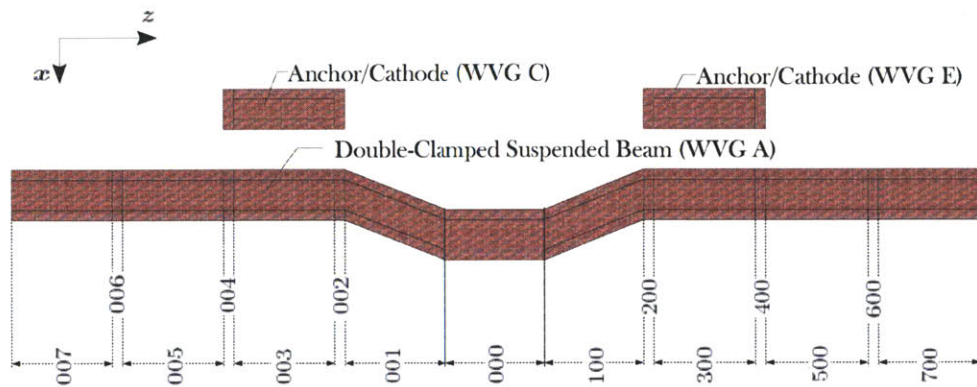
FIGURE 3.45: The D04-M02-SUGAR 01 Simulation Model: Top view of the SUGAR
Simulation Model

Figure (3.45) is a top view of the D04-M02-SUGAR 01 Model of the waveguide-integrated
MEM system. As SUGAR is able to simulate three-dimensional structures consisting
of a single material, the two-material (core inside of a coat-cladding layer) waveguide-
integrated MEM system is specified as an effective single-material system having effective
material characteristics (density, elastic modulus and Poisson's ratio) which are depen-
dent upon the percent volume of the two materials inside of the suspended structure.
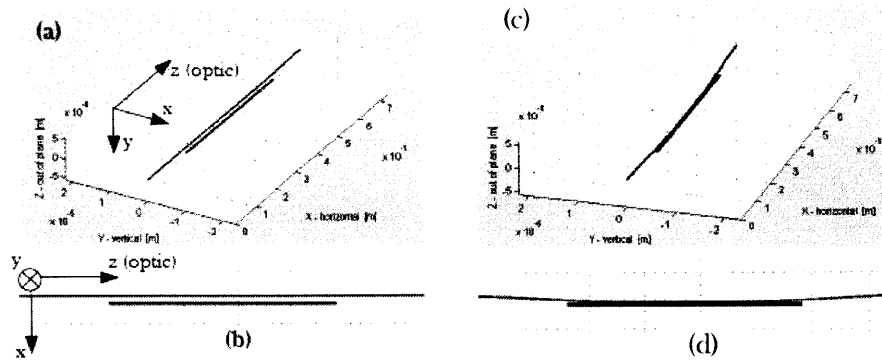
FIGURE 3.46: Deflection Profile Of The D04-M02vA-SUGAR 01 Model: (a),(b) The three-dimensional structure definition of the D04-M02vA-SUGAR 01 Model before and (c),(d) after the application of a voltage.

Figure (3.46) shows the screen captures taken from an optimized simulation run of the D04-M02vA-SUGAR 01 Model before [Figure (3.46a)] and after [Figure (3.46b)] the application of 10 volts.[6]

In general, after a SUGAR structure is created, all free variables are adjusted until the structure undergoes pull-in deflection. For Device 04, since the area of the parallel-plate actuator is constrained to a particular plate length and thickness as well as a minimum plate-to-plate separation (as required for the optimal operation of the optical system), the $L_{MEM}(\equiv L_{NM})$ is the only geometry which can be adjusted in order to satisfy the MEM system operation requirements of 10-volt, fast (deflection with a k_{MEM} ($\equiv k_{NM}$) $= 1N/m$) switching. As it turns out, due to the structural configuration of Device 04, only one requirement can be satisfied at a time.

After quasi-static actuation is determined from SUGAR simulation model(s), suspension spring constant(s), structural mass(es) and the area of the parallel-plate actuator(s) are

---

[6]Note that the structure represented in Figure (3.46) a SUGAR model derived from the D04-M02vA Design Model which has a single parallel-plate actuator integrated into each waveguide.

used in one-dimensional Simulink simulations in order to approximate the dynamic performance. In addition to the three SUGAR-simulation extracted parameters, a lump-element damping constant is calculated by reexamining the dimensions and spacings associated with the Optical-MEMS Design Model that is indicated by the optimized results of the SUGAR simulation.

All of the devices analyzed in this thesis are assumed to operate in air at room temperature and atmospheric pressure. Moreover, given the geometries of all of theses devices, squeezed-film damping is the only appreciable loss mechanism that arises during mechanical motion. Consequently, squeezed-film damping is approximated by:

$$c_{Damp} = \frac{\mu_{Damp} L_{Damp} w_{Damp}^2}{h_{Damp}^2}, \tag{3.1}$$

where $\mu_{Damp} = 18.6 \mu P \cdot s$ is the dynamic viscosity of air, h_{Damp}, w_{Damp}, L_{Damp} and P_{Damp} are the thickness, width, length and pressure, respectively, of the fluid (air) being squeezed. Recall that in general, a system can be considered critically-damped (c_{CDamp}) if $c_{CDamp} \equiv c_{Damp} = 2m_{NM}\omega_{NM}$.

If $c_{Damp} \ll c_{CDamp}$, damping is negligible and results in an effective lowering of the required voltage required for pull-in during force-driven actuation. However, negligible damping results in a considerable amount of ringing during release-settle actuation. Conversely, if $c_{Damp} \gg c_{CDamp}$, the damping is substantial and results in an increase in the voltage required for pull-in during force-driven actuation, while during release-settle actuation, moving components return to their original as-fabricated configuration, slowly, without ringing. Ideally, c_{Damp} should be $c_{Damp} \approx c_{CDamp}$.

Note that most of the device structures are underdamped with the most notable exception being Device 04. Device 04 has a structure which establishes (approximately) critical damping system dynamics due to the specific configuration of the parallel-plate actuators.

The following figures [Figure (3.47) – (3.48)] are three different three-dimensional, isometric views of the analysis models (D04-M02vA-SLink 01 and 02) of the D04-M02vA Design Model used to analyze the effect that squeezed-film damping has on Device 04.
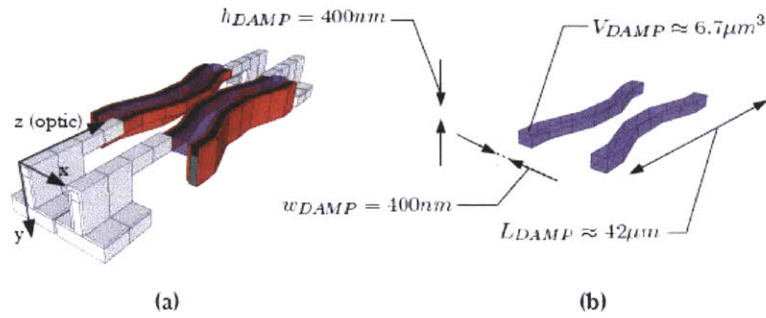
FIGURE 3.47: The D04-M02-SLink 01 Analysis Model: The analysis model used to analyze squeezed-film damping effects established during force-driven actuation. (a) The D04-M02vA SLink 01 Model with a volumetric outline of the volume of air squeezed during force-driven actuation. (b) The volumetric outline of the volume of air shown independent of the analysis model.

Figure (3.47) shows the volume of air that is squeezed during the initiation of force-driven actuation. The volume of air represented in Figure (3.47) establishes the strongest resistance to motion as the volume of air is the largest and the force generated from the parallel-plate actuator is the smallest. Given the optimized geometries and spacings of Device 04 as determined from SUGAR simulations, the squeezed-film damping constant is $c_{Damp} \approx 3.2 \times 10^{-3} \mu N/m/s$ which is on the order of the critical damping ($c_{CDamp} \equiv 2m_{NM}\omega_{NM} \approx 1.7 \times 10^{-3} \mu N/m/s$)

$L_{DAMP} = 186\mu m$

z (optic)

$h_{DAMP} = 400nm$

$V_{DAMP} \approx 60\mu m^3$

$w_{DAMP} \approx 800nm$

(a)   (b)
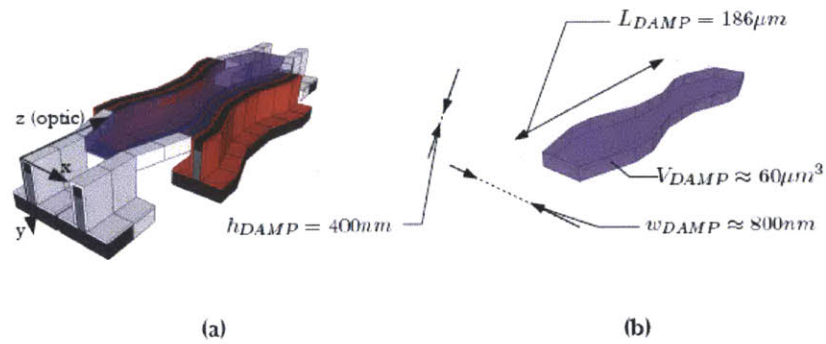
FIGURE 3.48: The D04-M02-SLink 02 Analysis Model: The analysis model used to analyze squeezed-film damping effects established during release-settle actuation. (a) The D04-M02vA SLink 02 Model with a volumetric outline of the volume of air squeezed during release-settle actuation. (b) The volumetric outline of the volume of air shown independent of the analysis model.

As illustrated in Figure (3.48), in the mechanically-deflected configuration a 60-μm^3 volume of air exists between the two deformed suspended waveguide sections which establishes a $c_{Damp} \approx 1.0 \times 10^{-3}\mu N/m/s$ damping constant. In this configuration, damping is approximated to be on the order of the $c_{CDamp} \equiv 2m_{NM}\omega_{NM} \approx 1.7 \times 10^{-3}$. Consequently, damping is anticipated to be sufficient in order to prevent the moving suspended waveguide sections from impacting one another during release-settle actuation.
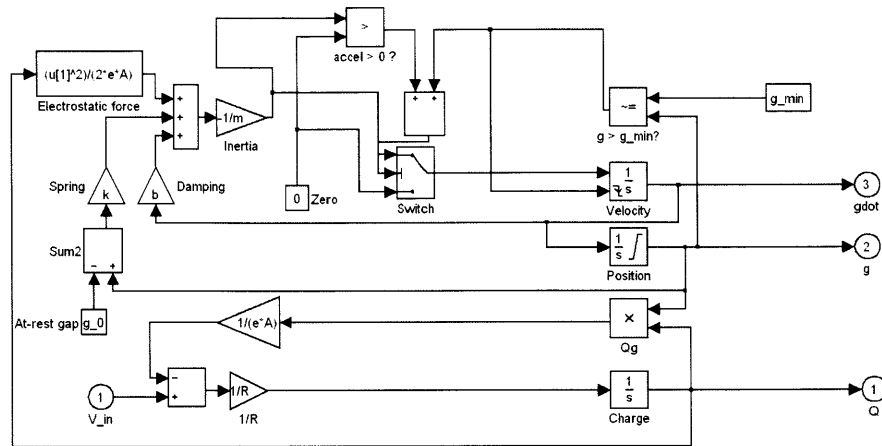
FIGURE 3.49: The Simulink schematic that was used simulate single-axis, dynamic actuation of Device 04.

Figure (3.49) is the Simulink module that was used to simulate the single-axis dynamic actuation of Device 04 given m_{NM}, A_{NEM} and k_{NM} as determined by SUGAR simulations and c_{Damp} approximations determined from squeezed-film damping analysis. This Simulink module is able to simulate pull-in and post-pull-in release effects.

(a)

(b)
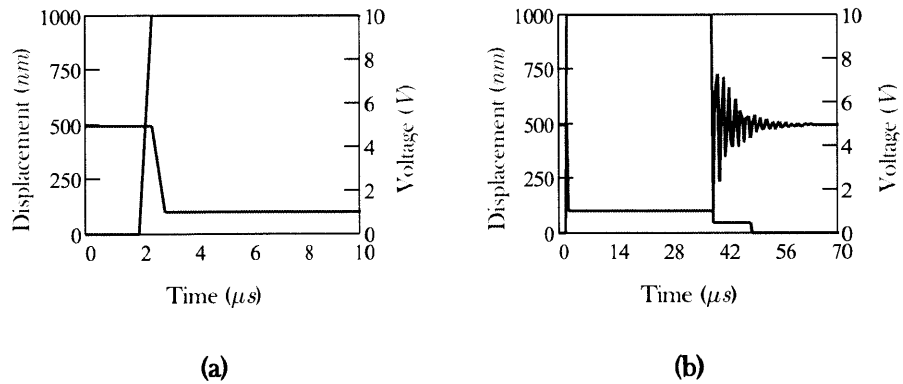
FIGURE 3.50: Displacement-Time Plots For Device 04 As Simulated With The Simulation Models D04-M02-SLINK 01, 02 and 03: (a)The Force-driven actuation and (b) the release-settle actuation cycles.

In Figure (3.50) shows the predicted temporal response of Device 04 which is modeled as a one-dimensional spring-damper-mass system.

In Figure (3.50a), a voltage is applied which causes pull-in. Notice that instead of 10 volts, a pull-in voltage (dynamic pull-in voltage) of 3.0 volts is used in order to initiate pull-in. This result is expect since $c_{DAMP} < c_{CDamp}$ and the momentum (due to m_{NM}) is accounted for[7].

Figure (3.50b) shows what happens after the 3.0-volt pull-in voltage is removed. At approximately $40\mu s$, the pull-in voltage is reduced $460mV$ which allows Device 04 to undergo release-settle actuation. Since $c_{DAMP} \leq c_{CDamp}$, Device 04 will undergo a few cycles of low-velocity positional oscillations. These low-velocity, positional oscillations are not anticipated to adversely compromise the structural integrity of the moving waveguides.

Ultimately, Device 04 is predicted to be capable of microsecond switching for both the force-driven and release-settle actuation. Specifically, during force-driven actuation, with a minimum Dynamic Pull-In Voltage of $V_{DPI_{min}} = 3.0V$, Device 04 is reconfigured from the as-fabricated to the mechanically-deflected configuration in $t_{FDA} = 1.5\mu s$; during release-settle actuation, Device 04 is reconfigured from the mechanically-deflected to the as-fabricated configuration in $t_{RSA} = 2\mu s$.

During release-settle actuation, the suspended-waveguide beams are predicted to undergo damped mechanical oscillations.

---

[7]Note that during quasi-static SUGAR simulations, momentum is not accounted for.

3.9   Device 07: The Optical System Design

3.9.1   Introduction

In this section, the focus will be on the design, modeling and optimization of the mechanically-deflected configuration of Device 07.

In **Step 01: Optical System Design**, the mechanically-deflected, cross-state configuration is designated as the primary switch-state configuration. The decision to have the cross-state configuration to be the mechanically-deflected configuration comes about from the desire to reduce the optical loss associated with the MEMS-optical system integration, arising from the design of Device 05: The tethered beams that are used to link the MEMS actuator to the suspended double-anchored, suspended waveguide beams creates a source of Rayleigh-scattering, optical loss. Consequently, for the device generations following Device 05, the MEMS actuators are designed to performed *push-action switching* with cantilevered beams covered with a low-index, coat-cladding layer instead of the *pull-action switching* performed by the MEMS actuators that use tethered beams, which are connected to the core of the suspended waveguide beams.
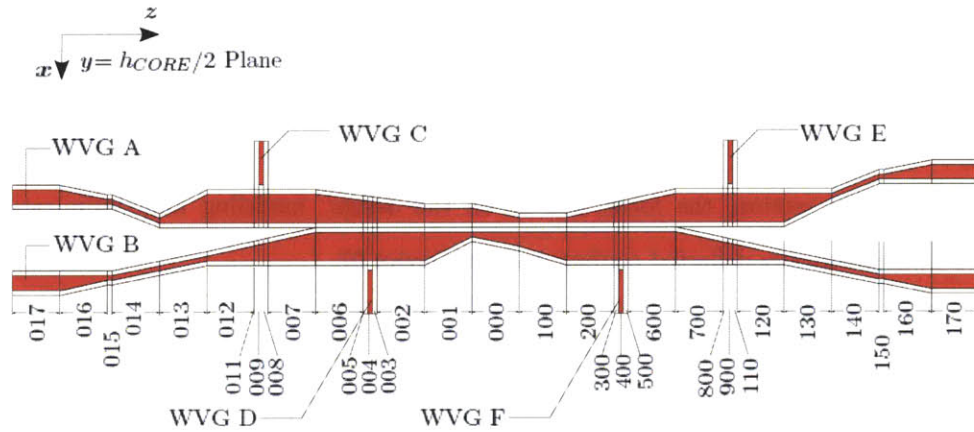
FIGURE 3.51: The D07-M 02 Design Model In The Mechanically-Deflected Cross-State Configuration: The not-to-scale schematic of the D07-M 02 model is viewed on the $y = h_{CORE}/2$, xz-plane.

Figure (3.51) is the design model of Device 07 in the mechanically-deflected, cross-state configuration, viewed on the $y = h_{CORE}/2$, xz-plane. WVGs A and B are in intimate contact with on another over regions 006-001, 000 and 100-600. Moreover, WVGs C and E are in intimate contact with WVG A, WVGs D and F with WVG B. Waveguide sections 014A, 014B, 013B, 140A, 140B and 130B are the only sections that are elastically deformable; all other sections are rigid. Note that unlike the prior device generations, Device 07 does not have optical symmetry.

Since Waveguides A and B are not geometrically symmetric, both waveguides had to be intentionally designed to have equal transmission, reflection and loss figures of merit. Therefore, while the two waveguides are not symmetric in structure, the two waveguides were engineered to have optical symmetry.
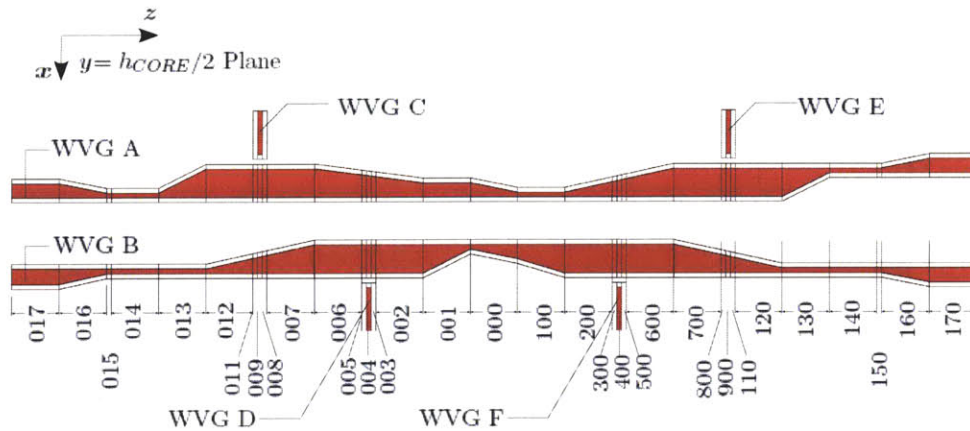
FIGURE 3.52: The D07-M 02 Design Model In The As-Fabricated Bar-State Configuration: The not-to-scale schematic of the D07-M 02 model is viewed on the $y = h_{CORE}/2$, xz-plane.

Figure (3.52) is the design model of Device 07 in the as-fabricated, bar-state configuration. Note how the elastically-deformable waveguide sections are defined to be straight waveguides. Also note that there is a physical separation between WVGs C and A, WVGs E and A, WVGs D and B and WVGs F and B. The minimum value of that separation is dependent upon the thickness of the device high-index device layer (h_{Optic}), the thickness of the coat-cladding layer (w_{Coat}) and the *hole-filling* performance of the process machine used to perform atomic layer deposition. Given $h_{Optic} = 300nm$, $w_{Coat} = 60nm$ and a atomic-layer-deposition machine capable of filling a hole with a 10:1 aspect ratio, a minimum $g_{Optic02=42nm}$ separation is possible. During lithographic definition, the four Bumper waveguides would be defined with a 282-nm separation.

In Table (3.2) each of the waveguide sections of WVGs A and B in the D04-M 02 design model are listed by design parameter, region number, core width and length. Also, brief descriptions of the structural configuration and function of each of those sections are provided.

TABLE 3.2: Parameters Of The D07-M 02 Design Model: optical parameter (▲), constrained fabrication parameter (♦), constrained MEMS parameter (■).

Parameter	Region	Width	Length	Description
▲	017, 170	$w_{017,170} = 600nm$	N/A	Bus width for low loss long-stretch on-chip waveguiding.
▲	016, 160	$w_{016A}^{-} = 600nm$, $w_{016A}^{+} = 150nm$ (Linear Taper); $w_{016B}^{-} = 600nm$, $w_{016B}^{+} = 150nm$ (Linear Taper)	$L_{016} = 2.3\mu m$	The 016A and 016B waveguide sections undergo linear, adiabatic width-tapering over a length of L_{016}.
▲	015, 150	$w_{015,150} = 150nm$	$L_{015} = 1.0\mu m$	Over the 015 and 150 waveguide regions, a section-length of $L_{015,150}$ is required in order to allow the guided mode to stabilize from the previous width-tapering transition.
♦■	014	$w_{014A} = 150nm$, $w_{014B} = 150nm$	$L_{014} = 200\mu m$	The minimum feature size where an absolute $\pm 10nm$ size variation has an insignificant effect on the compliance of the suspended waveguide suspension.
▲	013	$w_{013A}^{-} = 150nm$, $w_{013A}^{+} = 600nm$ (Linear Taper); $w_{013B} = 150nm$	$L_{013} = 2.3\mu m$	w_{013B} stays as a narrow single mode width while the 013A waveguide section undergoes a linear adiabatic width taper over L_{013}.
▲	012-007	$w_{012A-007A} = 600nm$; $w_{012B}^{-} = 150nm$, $w_{007B}^{+} = 600nm$ (Linear Taper)	$L_{012-007} = 2.3\mu m$	Waveguide sections 012A-007A are defined by a width of $w_{012A-007A}$, which is used to tightly confine light in order to reduce Rayleigh scattering loss from the bumper beam. WVG B undergoes a linear, adiabatic width-taper over sections 012B-007B over the sectional length of $L_{012-007}$.
			Continued on Next Page...	

Table 3.2 – Continued

Parameter	Region	Width	Length	Description
▲	006-002	$w_{006A}^- = 600nm$, $w_{002A}^+ = 480nm$ (Linear Taper); $w_{006B-002B} = 600nm$	$L_{006-002} = 2.3\mu m$	The 006B-002B waveguide sections are defined by a width of $w_{006B-002B}$, which tightly confines light in order to reduce Rayleigh-scattering, optical loss from WVG C, the bumper beam. WVG A undergoes a linear, adiabatic width-taper over sections 006A-002A over the section-length of $L_{006-002}$.
▲	001	$w_{001A} = 480nm$; $w_{001B}^- = 600nm$, $w_{001B}^+ = 100nm$ (Linear Taper)	$L_{001} = 2.3\mu m$	Waveguide section 001A maintains a width of w_{001A} over a section-length of L_{001} while waveguide section 001B undergoes a linear, adiabatic width-taper over a length of L_{001} in order to set the minimum width of the adiabatic coupler, $w_{ADCmin} = 100nm$.
▲	000	$w_{000A}^- = 480nm$, $w_{000A}^+ = 100nm$ (Linear Taper); $w_{000B}^- = 100nm$, $w_{000B}^+ = 480nm$ (Linear Taper)	$L_{000} = 25\mu m$	The Adiabatic-Coupling Region: The 000A waveguide section is transitioned from a width of $w_{ADCmax} = 480nm$ to a width of $w_{ADCmin} = 100nm$ while waveguide section 000B is transitioned from a width of $w_{ADCmin} = 100nm$ to a width of $w_{ADCmax} = 480nm$ in order to establish full, optical-power cross-coupling between WVGs A and B.
▲	100	$w_{100A} = 100nm$; $w_{100B}^- = 480nm$, $w_{100B}^+ = 600nm$ (Linear Taper)	$L_{100} = 2.3\mu m$	The 100A waveguide section maintains a width of $w_{10A} = w_{ADCmin} = 100nm$ in order to minimize coupling to the 100B waveguide section as this section undergoes a linear adiabatic width taper over a length of L_{100}.

Continued on Next Page. . .

Table 3.2 – Continued

Parameter	Region	Width	Length	Description
▲	200-600	$w^-_{200A} = 100nm$, $w^+_{600A} = 600nm$ (Linear Taper); $w_{200B-600B} = 600nm$	$L_{200-600} = 2.3\mu m$	WVG B maintains a constant width of $w_{200B-600B} = 600nm$ over sections 200B-600B in order to minimize coupling to WVG A as the 200A-600A sections undergo a linear, adiabatic width-taper over the section-length of $L_{200-600}$. The 200B-600B sections are also used to tightly confine the propagating light in order to reduce Rayleigh-scattering, optical loss from WVG F.
▲	700-120	$w_{700A-120A} = 600nm$; $w^-_{700B} = 600nm$, $w^+_{120B} = 150nm$ (Linear Taper)	$L_{700-120} = 2.3\mu m$	WVG A maintains a constant width of $w_{700A-120A} = 600nm$ over sections 700B-120B in order to minimize coupling to WVG B as its sections 700B-120B undergo a linear, adiabatic width-taper over the section-length of $L_{700-120}$. Sections 700B-120B is also used to tightly confine the propagating light in order to reduce Rayleigh-scattering, optical loss from WVG E.
▲	130	$w^-_{130A} = 600nm$, $w^+_{130A} = 150nm$ (Linear Taper); $w_{130B} = 150nm$	$L_{130} = 2.3\mu m$	The waveguide sections in region 130 are further spatially separated with a width-taper. Section 130B maintains a width of w_{130B} while section 130A undergoes a linear, adiabatic width-taper over the section-length of L_{130}.
◆■	140	$w_{140A} = 150nm$; $w_{140B} = 150nm$	$L_{140} = 2.3\mu m$	The minimum feature size where an absolute $\pm 10nm$ size variation has an insignificant effect on the compliance of the suspended waveguide suspension.

Continued on Next Page...

Table 3.2 – Continued

Parameter	Region	Width	Length	Description
▲	160	$w_{160A}^{-} = 150nm$, $w_{60A}^{+} = 600nm$ (Linear Taper); $w_{160B}^{-} = 150nm$, $w_{160B}^{+} = 600nm$ (Linear Taper)	$L_{160} = 2.3\mu m$	Waveguide sections 160A and 60B undergo linear, adiabatic width-tapering over a length of L_{160} in order to expand the guided optical mode for bus waveguiding.

3.9.2 Bus Waveguide Sections

FIGURE 3.53: Top-down (not-to-scale) schematic of Device 07 in the mechanically-deflected configuration with the bus waveguide sections highlighted.

In Figure (3.53), the D04-M 02 model is shown with the Bus waveguide sections denoted. The Bus sections are used for low-loss, long-stretch, on-chip light routing. Essentially, the Bus sections are made to be low-loss by designing these sections with wide core widths: a wide core width confines a greater amount of light to that core material. Conversely, a waveguide section with a narrow core width weakly guides optical power and thus exposes the guided optical power to leaky radiation modes, leading to radiation loss. Moreover, owing to the way ridge waveguide cores are typically fabricated[8], weakly-confined light may experience optical loss via scattering on the imperfectly-smooth, side-walls of the narrow waveguide during light propagation. Specifying the Bus sections to have wide cores lowers optical loss resulting from both radiation leakage and side-wall scattering.

However, an optimal core width exists. The core width of the Bus sections must have a maximum width which prevents higher-order modes form being supported; the condition

---

[8]Recall that the definition of waveguide side-wall requires a lithographical patterning process and an anisotropic etching process(es). During these fabrication processes pattern transfer fidelity can be compromised.

for strict single-mode light propagation should not be violated. Support of additional modes beyond the fundamental mode may lead to intermodal-coupling, optical loss.

3.9.3   Bus/Spring Taper Waveguide Sections

FIGURE 3.54: Top-down (not-to-scale) schematic of Device 07 in the mechanically-deflected configuration with the bus-to-spring adiabatic taper waveguide section highlighted.

In Figure (3.54), the D04-M 02 model is shown with four tapered waveguide sections denoted as Bus/Spring Taper. Just as the name suggests, the Bus/Spring Taper waveguide sections are used to adiabatically transition the core width of the Bus sections to the core-width of the suspended waveguide sections that are used to set the beam compliance of the suspended waveguide beams.

In general, linear tapers are used throughout the design of Device 07. Linear tapers are able to be used without taking up much space. Short linear tapers are made possible mainly due to the fact that Device 07 is based on a high refractive index material system. More still, the adiabatic taper sections are only required to undergo a 450-nm change in width.

Optimization of the section-lengths in the 016 and 160 regions (L_{016} and L_{160}) is determined by BProp[9] and CAMFR[10] simulations. Specifically, the asymptotic onset of adiabaticity [11] is determined for a $L_{016,160}$.

A range of lengths for $L_{016,160}$ is determined by BProp simulations while CAMFR simulations were used to determine the absolute values of $L_{016,160}$. BProp simulations were used to determine the onset of adiabaticity as $L_{016,160}$ is increased for both the quasi-TE_{00} and quasi-TM_{00} modes of light propagation. CAMFR simulations are then used to determine the absolute value of $L_{016,160}$ for only the quasi-TE_0 mode of light propagation.

3.9.4 Spring Waveguide Sections
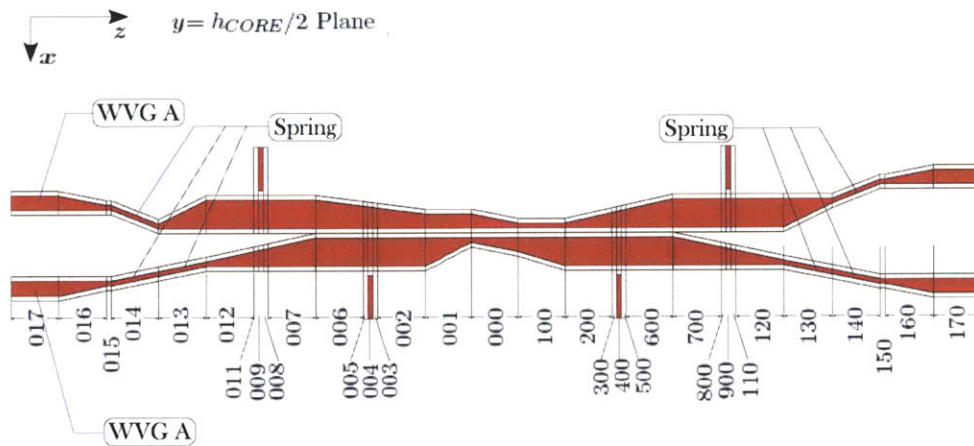
FIGURE 3.55: Top-down (not-to-scale) schematic of Device 07 in the mechanically-deflected configuration. The spring beam waveguide sections are highlighted (Sections 014A, 014B, 013B, 130B, 140B and 140A).

In Figure (3.55), the D04-M 02 model is shown with the Spring waveguide sections highlighted. For WVG A, the compliance of the double-clamped suspended waveguide

---

[9]BProp:The commercially-available, beam-propagation method (BPM), optical-structure simulation software (BeamPROP) developed by the RSOFT company.

[10]CAMFR:The open-source, eigenmode expansion method (EEM), optical-structure simulation software developed by the Photonics Group of the Department of Information Technology at Ghent University in Belgum.

[11]CAMFR-Simulate structures are considered adiabatic for transmission ¿ $-0.05dB$.

beam is specified by the section-length and core-width of the 014A and 140A sections. Similarly, for WVG B, the compliance of the suspended beam is specified by the section-length and core-width of the 014B, 013B, 140B and 130B sections.

The design of the Spring sections requires that both optical system and MEMS, performance criterion are met. The Spring waveguide sections are best defined to have narrow core-widths (i.e., $w_{spring} < h_{core}$) in order to (a) minimize the overall device length and (b) suppress undesired, out-of-plane deflections. However, w_{spring} must still be able to guide light propagating in either of the two fundamental polarization modes without loss greater than $-0.05dB$. More still, considering fabrication design tolerances, w_{spring} must have a width which does not cause extreme changes in the compliance of the suspended waveguide beam as a result of absolute width changes, arising from imperfect feature definition. Assuming a minimal feature/spacing lithographic resolution (g_{Litho}) and absolute tolerance (g_{Tol}) of $100nm$ and $10nm$, respectively, the core-width of the Spring sections (w_{spring}) are specified as $w_{spring} = 150nm$.

3.9.5   Spring-Beam/Contact-Bumper Taper Waveguide Sections
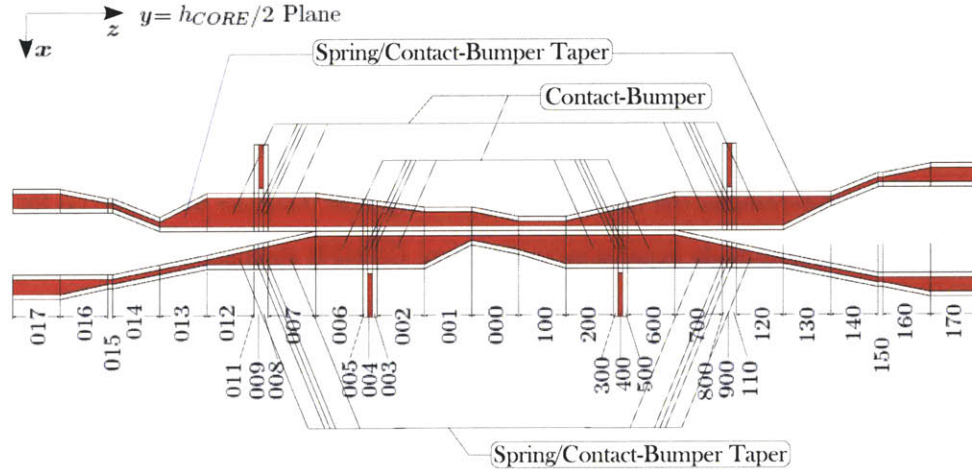
FIGURE 3.56: Top-down (not-to-scale) schematic of Device 07 in the mechanically-deflected configuration. The spring-to-bumper contact taper waveguide section is highlighted.

In Figure (3.56), the D04-M 02 model is shown with the Spring-Beam/Bumper-Contact Width-Tapered waveguide sections highlighted. Adiabatic linear tapers are used to transition the core width of the Spring waveguide sections from/to the Bumper-Contact sections. The bumper-contact waveguide sections have a specific width which reduces Rayleigh-scattering, optical loss that may occur at the T-junctions formed between WVGs A and WVGs C, WVGs A and E, WVGs B and D and WVGs B and F upon mechanical deflection. The function and form of the Bumper-Contact waveguide section will be shortly discussed in greater detail in the following section.

Notice how the two Spring/Bumper-Contact Taper sections along WVG A are staggered with respect to the Spring/Bumper-Contact Taper sections along WVG B. This staggered layout is done intentionally so as to not cause premature evanescent coupling.

The same simulation protocol was used to specify the minimum section-length of the Bus/Spring Taper sections: First, BProp simulations were performed in order to determine the minimum section-length that establishes adiabatic, fundamental-mode expansion/contraction of the quasi-TE_{00} and the quasi-TM_{00} mode-types. Second, CAMFR simulations are performed in order to (a) exactly determine the minimum length of $L_{013,130}$, $L_{012-007}$ and $L_{700-120}$ that ensures adiabatic, fundamental-mode expansion/-contraction for the quasi-TE_0 mode-type.

After determining the minimum length of $L_{013,130}$, $L_{012-007}$ and $L_{700-120}$ for adiabatic, fundamental-mode expansion/contraction, CAMFR simulations are performed in order to minimize premature coupling between WVGs A and B in the 013, 012-007, 700-120 and 130 regions. This additional step is required since WVGs A and B are in close proximity to one another in these regions (in the mechanically-deflected configuration).

3.9.6   Contact-Bumper Waveguide Sections
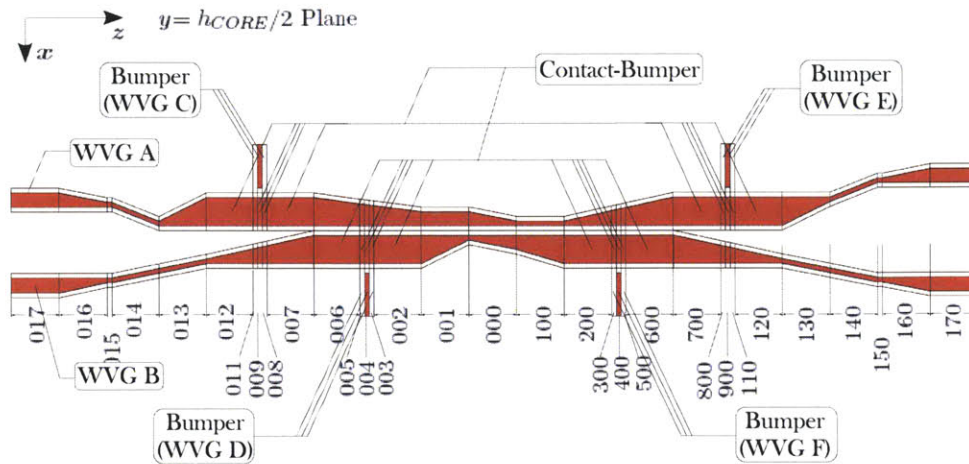
FIGURE 3.57: Top-down (not-to-scale) schematic of Device 07 in the (a) as-fabricated and the (b) mechanically-deflected configurations.

In Figure (3.57), the D04-M 02 model is shown with the Bumper waveguides (WVGs C, D, E and F) and the Contact-Bumper waveguide sections of WVGs A and B highlighted. The Bumper-Contact sections have a wide, single-mode core-width which minimizes Rayleigh-scattering, optical loss that occurs as a result of the Bumper waveguides making intimate contact with those waveguide sections.

Specifically, Rayleigh-scattering, optical loss is reduced in three ways: First, the Bumper waveguides, which have a core material with a high refractive index, are lithographically defined to be $100nm$, the minimum feature size: $w_{bump} \equiv g_{litho} = 100nm$.

Second, as-fabricated, WVGs A, B, C, D, E and F[12] exist as separate structures; their cores are not contiguous. Consequently, all of the waveguides are able to be completely coated with the low-index coat-cladding layer, which prevents the high-index cores of these waveguides from ever coming into contact. Third, since the Contact-Bumper sections are defined with wide core-widths, guided single-mode light is better confined to

---

[12]WVGs A, B, C, D, E and F are modeled as separated structures in the D07-M 02 design model. As the actual structure, WVGs C and E (and WVGs D and F) are connected in a U-shape configuration, which are ultimately attached to the remote MEMS actuator.

the center of those waveguide sections.

Similar to the way the waveguide sections in the 013, 012–007, 700–120 and 130 regions are designed to prevent premature coupling between WVGs A and B, the waveguide sections in the 006-002 and 200-600 regions are designed to prevent premature coupling as well.

BProp simulations are used to ensure that the Contact-Bumper beams did not support higher-order modes for light carried in either the quasi-TE_{00} and quasi-TM_{00} polarization modes. CAMFR simulations are used to ensure coupling between WAVs A and B is suppressed; light carried in both the quasi-TE_0 and the planar TM modes are examined.

3.9.7   Adiabatic-Coupler Waveguide Sections
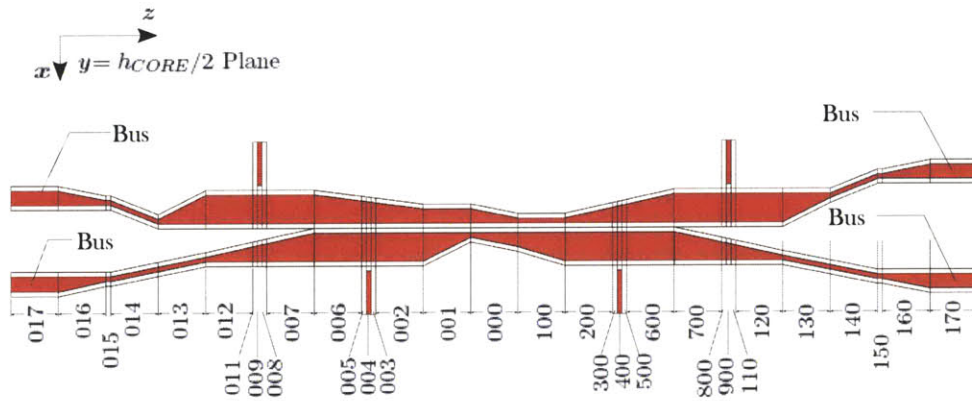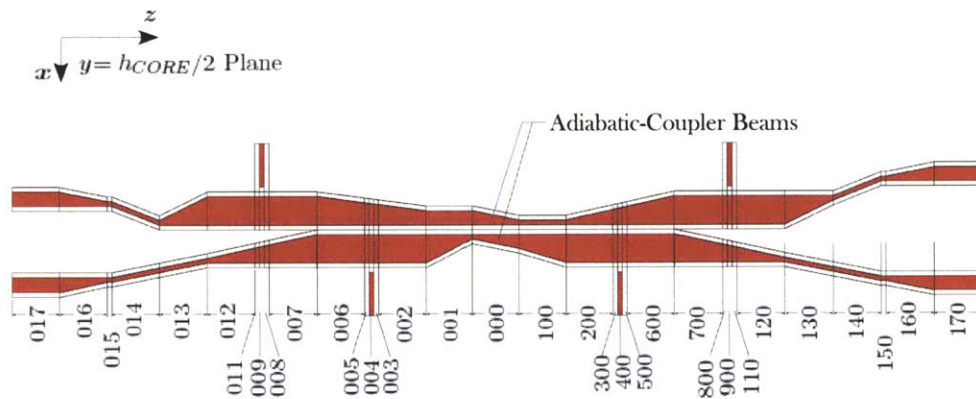

FIGURE 3.58: Top-down (not-to-scale) schematic of Device 07 in the mechanically-deflected configuration with the adiabatic coupled waveguide section highlighted.

In Figure (3.58), the D04-M 02 model is shown with the Adiabatic-Coupler waveguide sections highlighted. The 000 region is the region where adiabatic coupling is established; the 000A and 000B sections undergo adiabatic, linear, core-width tapering that allows evanescent optical power exchange without exciting higher order modes. Ideally, throughout the optical power exchange, light will only travel in the fundamental mode.

In order to establish full, adiabatic-coupling optical-power exchange, three parameters are specified: (1) w_{ADCmax} and (2) w_{ADCmin}, the maximum and minimum core-width, respectively and (3) L_{ADC}, the length over which full, adiabatic-coupling takes place.

The core-width at the beginning of the 00A section (w^-_{000A}) is defined as w_{ADBmax}, $w^-_{000A} \equiv w_{ADCmax} = 480nm$, the core-width at the end of the 000A section (w^+_{000A}) is defined by w_{ADCmin}, $w^+_{000A} \equiv w_{ADCmin} = 100nm$. Consequently, the 000B section has the complimentary linear, core-width taper defined as: $w^-_{000B} \equiv w_{ADCmin} = 100nm$ and $w^+_{000B} \equiv w_{ADCmax} = 480nm$, where the core-width at the beginning and end of the 000B section is defined as w^-_{000B} and w^+_{000B}, respectively.
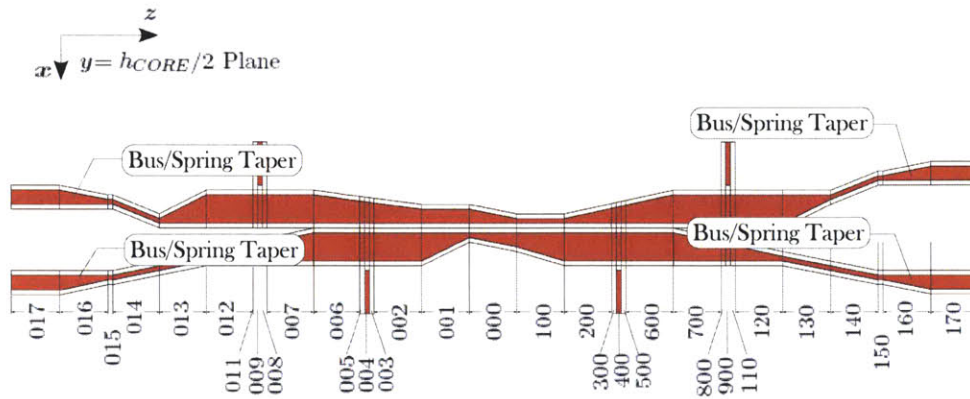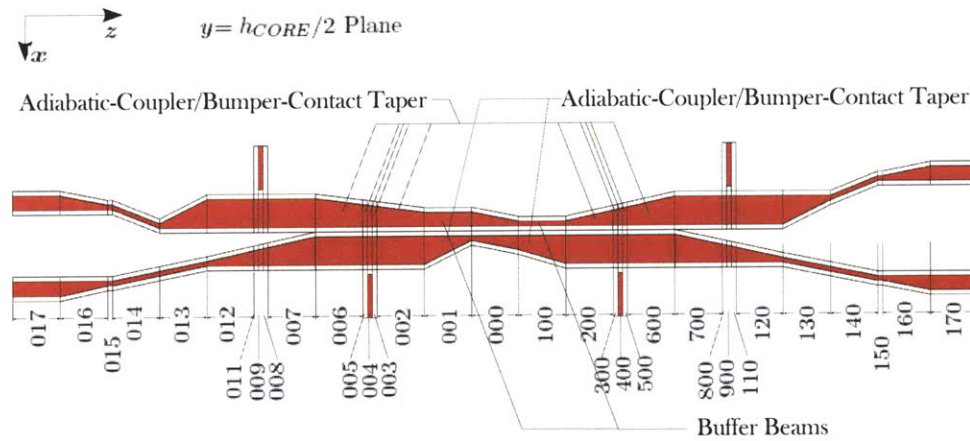

FIGURE 3.59: Top-down (not-to-scale) schematic of Device 07 in the mechanically-deflected configuration with the adiabatic coupling-to-bumper beam (ADC-BUMP) taper waveguide section highlighted.

In Figure (3.59), the D04-M 02 model is shown with the Adiabatic-Coupler/Bumper-Contact Width-Taper and the Buffer waveguide sections highlighted. The 001B waveguide section is used to transition the core width of the bumper contact waveguide section to the minimum core width of the adiabatic coupler section ($w_{ADC_{min}} = 100nm$). The 100B waveguide section is used to transition the maximum core width of the adiabatic coupler section ($w_{ADC_{max}} = 480nm$) to the core width of the bumper contact waveguide section. Again, a simple linear adiabatic taper is used for the transitional waveguide sections, the 001B and 100B waveguide sections.

Before and after the adiabatic coupling waveguide region (the 000 waveguide region), the highlighted waveguide sections in Figure (3.59) are used to maintain waveguide continuity while minimizing waveguide-to-waveguide coupling by creating a maximally mismatched $\Delta\beta$.

3.10   The Remote MEM Actuator

In this section, the waveguide MEMS that is used to modulate the lightpaths for Devices 05, 06, and 07 will be examined.

Device 05, 06 and 07 are electromechanical optical switches that have the optical operation and the MEMS operation decoupled. As a result, the MEMS operation can be optimized without being constrained by the optical performance requirements.

Typically, electrostatic-based MEM actuator relies on the use of two fundamental elements: an electromechanical actuator and a mechanical spring suspension. With the a-priori understanding that Device 05, 06 and 07 are composed of low-mass microstructures (suspended waveguides) that are to be deflected over submicron distances, the parallel plate actuator can be more efficiently used instead of the more often used comb-finger actuator. Particularly for submicron-cross section waveguide switching, the parallel-plate actuator can be designed for microsecond to submicrosecond order switching [?].
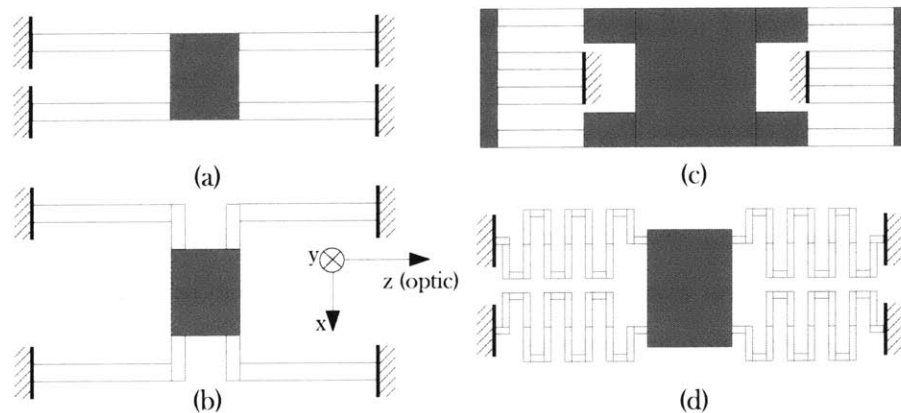
FIGURE 3.60: Various flexure designs. (a) fixed-fixed flexure, (b) crab-leg flexure. (c) folded flexure (d) serpentine flexure. [?]

In terms of defining the spring suspension, several standard MEMS flexures options [Figure (3.60)] are possible. All of the flexures are composed of four deformable suspended beams (white-colored geometry) that are connected to a central rigid structure

(gray-colored geometry) in a two-fold symmetry configuration. The central rigid structure defines the total approximate mass of the entire structure and is used to establish a guided-end boundary condition for the four spring beams. Consequently, each spring beam is subject to fixed-end and guided-end boundary conditions. Often, the central ridge structure is defined as the proof mass in traditional MEMS parlance. Note that the following flexure analysis is based on structures where displacement arise from only beam bending and beam torsion; displacement arising from shear, beam elongation and beam shortening is neglected.

For this project, the fixed-fixed flexure is ruled out since this flexure is susceptible to thin-film stress which can result in increased spring constant or out-of-plane buckling due to axial stress in the beams that is created during fabrication. The other three flexures, the serpentine, crab-leg and folded flexures, have a structure which renders them insensitive to residual thin-film stress [?].

In addition to being desensitized to thin-film stress, the serpentine flexure has a compact structure [?]. However, in a typical serpentine flexure form (e.g., $w_{SPAN} = h_{CORE} = 200nm$, $L_{MEAND} = 1\mu m$, $0\mu m < w_{MEAND} < 10\mu m$, $n_{MEAND} = 6$), the out-of-plane spring compliance (k_{NM_y}) is less than the lateral spring compliance (k_{NM_x} and k_{NM_z}): $k_{NM_y} < k_{NM_z}, k_{NM_x}$ where $k_{NM_x} < k_{NM_y}$, $k_{NM_x} = k_{NM_y}$, $k_{NM_x} > k_{NM_y}$ depending upon L_{Meand}. Particularly for the intended application, nanometer-order out-of-plane misalignment compromises the performance of the optical switches. Consequently, a serpentine flexure is not a viable option. The other two flexures, the crab-leg and folded flexures, are able to be designed to have a stiff out-of-plane spring constant while maintaining compliancy along a single lateral deflection direction.

The crab-leg flexure has a similar structure to that of the fixed-fixed flexure. The inclusion of a *thigh* beam differentiates the crab-leg flexure from the fixed-fixed flexure. The thigh beam gives the crab-leg flexure immunity from thin-film stress. In general, proper design requires that the thigh beam be shorter than shin beam. For example, given a crab-leg flexure with the dimensions $w_{SHIN} = w_{THIGH} = h_{CORE} = 200nm$

and $L_{SHIN} = 10\mu m$, $L_{SHIN} \lesssim 2\mu m$ in order to maintain a high stiffness for k_{NM_y}. Incidentally, maintaining a high stiffness for k_{NM_y} insures that $k_{NM_z} < k_{NM_x}$.
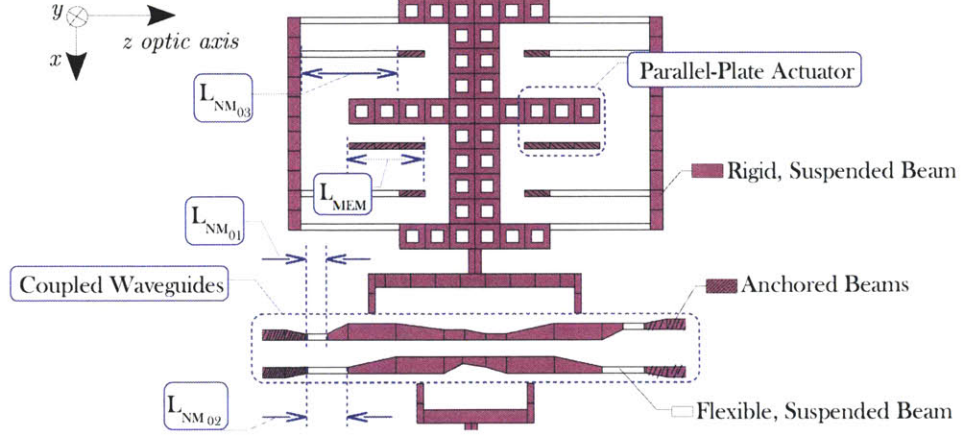
FIGURE 3.61: Top view of the remote MEM actuator of Device 07 in the as-fabricated configuration.

Figure (3.61) is a top view of the remote MEM actuator of Device 07 in the as-fabricated configuration, modeled as a single material articulated into a mechanical structure consisting of three types of mechanical forms: (1) a rigid, suspended beams, (2) flexible, suspended beams and (3) anchored beams. Note that in design, Device 07 is formed from high-index, core layers that have a conformal cladding of low-index material. For this particular model, the material in the beams is defined with material attributes (e.g., elastic modulus, Poisson ratio) that have composite representation of the volume at which both materials are present within the structure. Consequently, as the structure changes in dimensions, the material properties of the structure change as well. Each mechanical form is distinguished by a particular color shading and highlighted in Figure (3.61).

The MEM actuator is defined as a folded-flexure suspension that is designed to accommodate two, symmetrically-arranged parallel-plate MEM actuators that are position central to the suspension. As a separate system, the spring constant of the MEM system can be adjusted in order to establish a spring constant of $k_{MEM} \approx 1N/m$ by adjusting

the length of flexible, suspended beams ($L_{NM_{03}}$) of the MEM system. Moreover, the specific actuation voltage of $V_{SPI} = 10V$ can be achieve with adjusting the electrode area (A_{MEM}) of the parallel-plate MEM actuator by adjusting the length L_{MEM}.
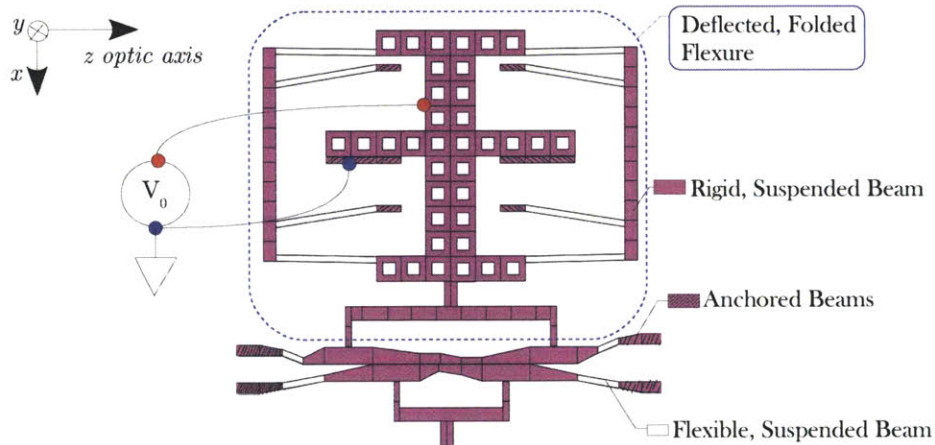
FIGURE 3.62: Top view of the remote MEM actuator of Device 07 in the mechanically-deflected configuration.

Figure (3.62) is a top view of the same remote MEM actuator in Figure (3.61) after undergoing mechanical actuation. A pull-in voltage is applied to the parallel-plate MEM actuators which translates rigid, suspended beams and deforms the flexible, suspended beams along the x-axis. The x-axis-motion of the MEM system is then imparted to the suspended waveguide beams. Specifically, the bumper beam assembly, extending from the central rigid shuttle beam of the MEM system pushes the suspended waveguide beam structure. Note that both suspended waveguides undergo simultaneous deflection, which ultimately leads to both waveguides being brought into intimate contact. The simultaneous deflection of the suspended waveguide beam rightfully indicates that both beams are actuated with two remote MEM systems.

In complete design, two symmetrically arranged MEM systems are positioned in adjacent alignment to the two suspended waveguides. Note that while the two MEM

systems are defined as symmetric structures, the bumper-beam assemblies attached to the MEM systems, which ultimately contacts and moves the suspended waveguides, are not symmetric. The bumper-beam assemblies have a design which is made to contact the suspended waveguides at wide-single-mode, rigid, suspended sections in order to minimize optical loss.

In final analysis, both MEM actuators are designed for fast switching by selecting $L_{NM_{03}}$ and L_{MEM} in order to generate a $0.5\mu N$ to move both waveguides $500nm$. In order to ensure single-axis motion, minimum out-of-plane deflection and increased insensitivity to thin-film stress effects, the folded-flexure suspension is to have a $k_{NM_{03}} = 1N/m$ spring constant while the spring constant of the suspended waveguide beams will each have a spring constant that are defined as $k_{NM_{01}} < 1N/m$ and $k_{NM_{02}} < 1N/m$, respectively.

3.11   The Latch MEMS

In this section, the design of the integrated latch MEMS will be discussed. The latch MEMS can be integrated in Devices 05, 06 and 07. Integration of the latch MEMS creates bistable switching: both switch states can be maintained without requiring a constant voltage, current or power source. In general, each 2×2 optical switch element uses two symmetrically arranged waveguide MEMS and four symmetrically arranged latch MEMS.

Without latching functionality, Devices 05, 06 and 07 have two configuration states: (1) the as-fabricated configuration and (2) the mechanically-deflected configuration. With latching functionality, those three devices have four configuration states: (1) the as-fabricated, (2) the unlatched as-fabricated, (3) the unlatched mechanically-deflected and (4) the latched mechanically-deflected configurations.

What follows is a discussion on the mechanics and electromechanics of Device 07 with latching functionality.
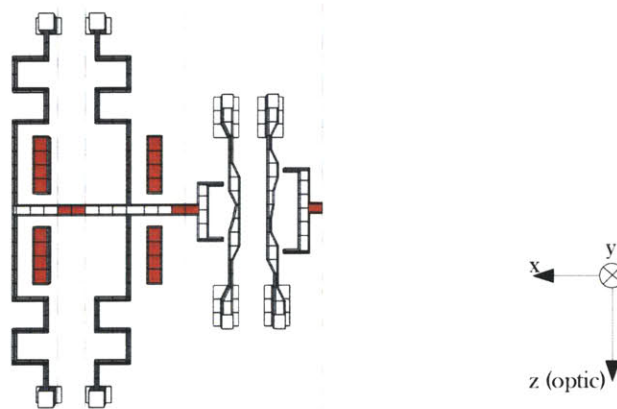
FIGURE 3.63: A not-to-scale top-down schematic of the waveguide MEMS of Device 07 in the as-fabricated configuration.

Figure (3.63) is the same not-to-scale top-down schematic of Device 07 that is presented in the previous subsection, where the two coupled waveguides and one waveguide MEM

actuator is shown. In order for Device 07 to accommodate a latch mechanism, the waveguide MEMS is altered.
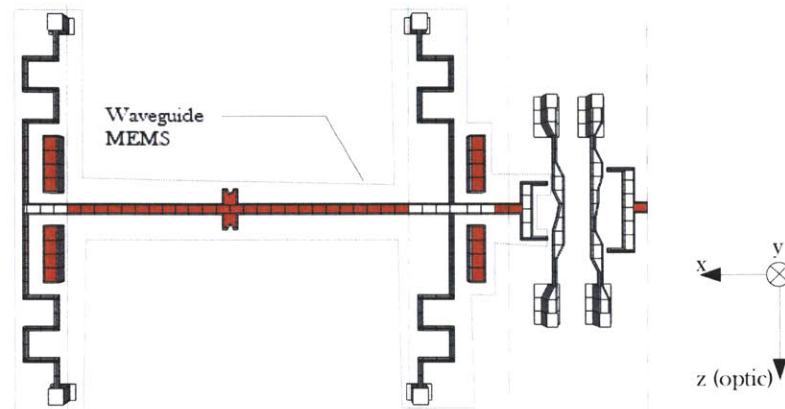
FIGURE 3.64: A not-to-scale top-down schematic of the extended-shuttle beam waveguide MEMS of Device 07 in the as-fabricated configuration.

Figure (3.64) is the not-to-scale schematic of Device 07 with the waveguide MEMS altered; the shuttle beam of the waveguide MEMS is extended in order to accommodate the latch MEMS. The two highlighted central sections of the shuttle beam in Figure (3.63) are extended [Figure (3.64)] while maintaining device symmetry, ensuring that the lowest order mechanical deflection mode is along the x-axis. Ultimately, the footprint of the latch MEMS determines the length of the waveguide MEMS's proof mass.

Notice in Figure (3.64) that there are two rigid beam protrusions extending from the center of the proof mass. These rigid beam protrusions serve as the waveguide MEMS's mating [?] latch coupling to the (not shown) latch MEM's coupling.
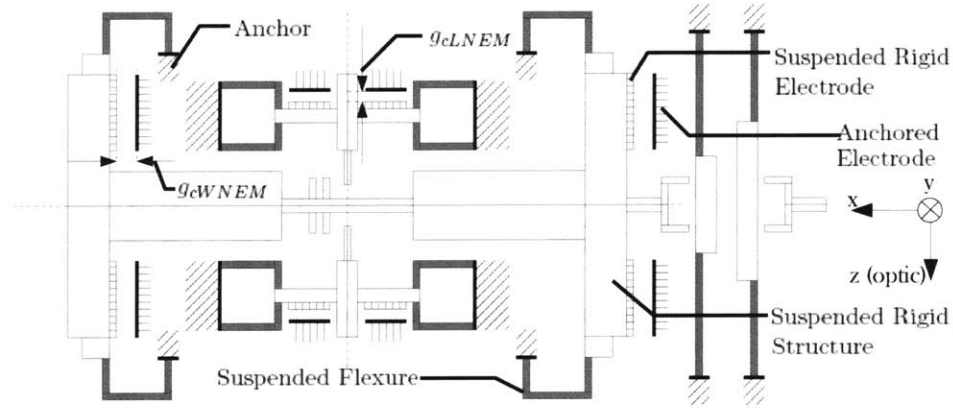
FIGURE 3.65: A not-to-scale top-down schematic of the waveguide and latch MEMS of Device 07 in the as-fabricated configuration. Highlighted in the picture is g_{cWNEM}, the surface-to-surface initial separation of one of the parallel-plate actuators of the waveguide MEMS and g_{cLNEM}, the surface-to-surface initial separation of one of the parallel-plate actuators of the latch MEMS.

The not-to-scale top-down schematic of Device 07 in the as-fabricated configuration represented in Figure (3.65) shows the position of the two latch MEMS in relationship to the waveguide MEMS. Designed sans latching, g_{cWNEM}, which is simply g_{cNEM}, has a minimum separation set by

$$g_{cWNEM} \equiv g_{cNEM} = \frac{1}{2}g_{cBAR00_{AB}} + g_{cBAR_{AC,BD}},$$

where $g_{cBAR00_{AB}}$ is the surface-to-surface separation between the two coupled waveguides (Waveguides A and B) that is required for optical isolation and $g_{cBAR_{AC,BD}}$ is the surface-to-surface separation between the bumper beams and the suspended waveguide sections which is determined by the coat-cladding thickness and other fabrication considerations. With latching, g_{cWNEM} must be increased in order to accommodate the translation of the curved coupling. Ultimately, g_{cWNEM} will depend on the minimum feature size. Similarly, g_{cLNEM} will also depend on the minimum feature size.

The latch MEMS has a twin crab-leg flexure suspension which, much like the folded-beam flexure suspension, desensitizes the latch MEMS from thin-film-stress-induced out-of-plane deflections. The choice of using the crab-leg flexure suspension for the

latch MEMS is arbitrary.

Since the latch MEMS will be used to hold the waveguide MEMS in the mechanically-deflected configuration, the crab-leg flexure suspension of the latch MEMS has structure and deflection constraints that are governed by the spring constant of the folded-beam flexure suspension of the waveguide MEMS. The latch MEMS design constraints will be discussed shortly.
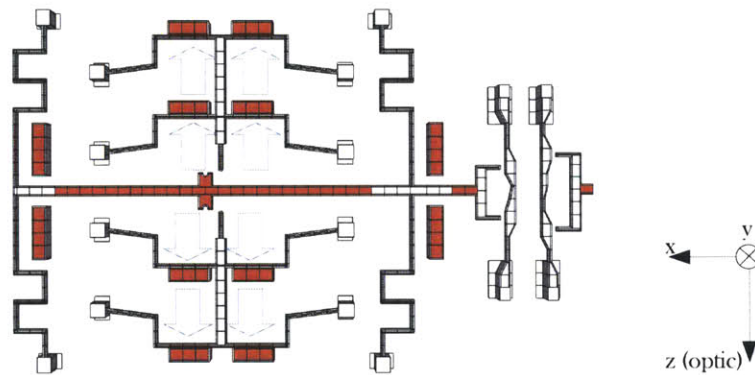
FIGURE 3.66: A not-to-scale top-down schematic of the waveguide and latch MEMS of Device 07 in the unlatched as-fabricated configuration.

Figure (3.66) depicts the unlatched as-fabricated configuration: the latch MEMS is actuated and the waveguide MEMS remains in the as-fabricated configuration. Before the waveguide MEMS is actuated, the latch MEMS is first actuated, disengaged into the so-called unlatch configuration. The parallel-plate actuators of the latch MEMS, operated in pull-in mode, deforms the crab-leg flexure suspension until $g_{cLNEM} = 0$.
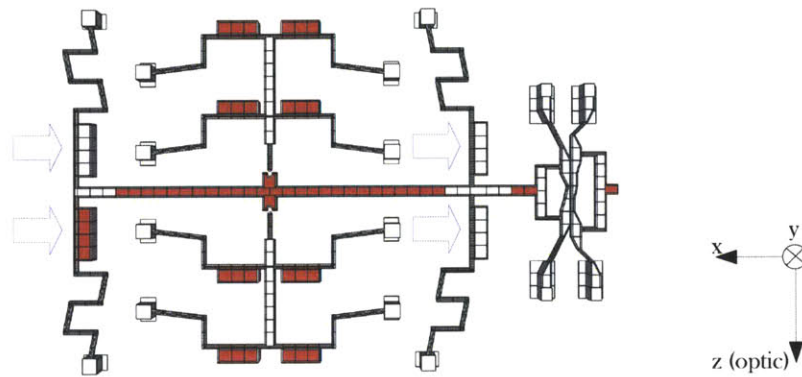
FIGURE 3.67: A not-to-scale top-down schematic of the waveguide and latch MEMS of Device 07 in the unlatched mechanically-deflected configuration.

In the unlatched mechanically-deflected configuration, as depicted in Figure (3.67), the waveguide MEMS undergoes a full pull-in deflection while the latch actuator remains in the deflected configuration.
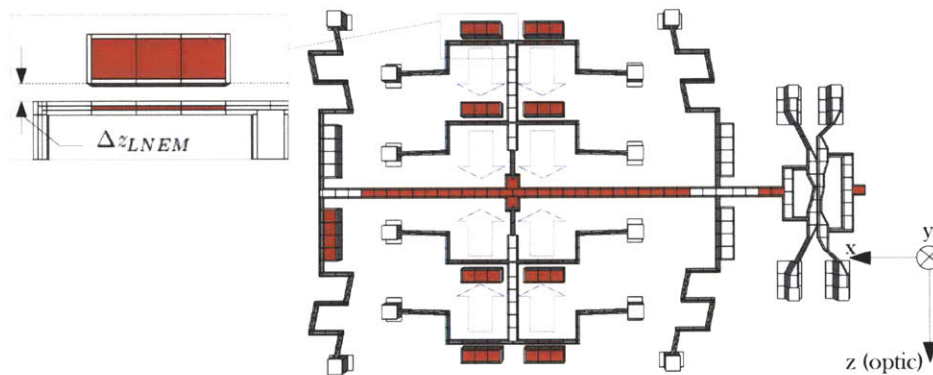
FIGURE 3.68: A not-to-scale top-down schematic of the waveguide and latch MEMS of Device 07 in the latched mechanically-deflected configuration. Highlighted in the schematic is $g_{cLNEM} - \Delta z_{LNM}$, the surface-to-surface separation of the latch MEMS parallel-plate actuator in the latched mechanically-deflected configuration where Δz_{LNEM} is the z-axis offset of the latch MEMS's suspension which establishes spring-loading, sustaining the waveguide MEMS in the mechanically-deflected configuration.

In the final latched mechanically-deflected configuration [Figure (3.68)], the curved coupling attached to the latched MEMS engages with the curved coupling attached to the shuttle beam of the waveguide MEM system. First, the voltage which originally held the

latch MEMS in the mechanically-deflected configuration is reduced to $0V$. After which, the hold voltage applied to the waveguide MEMS is reduced to $0V$. As a result, the waveguide MEMS maintains the mechanically-deflected configuration, while the latch MEMS maintain the waveguide MEMS's mechanically-deflected configuration with the spring-loaded force that is produced by the crab-leg flexure suspension.

The inset in Figure (3.68) is a close-up of one of the parallel-plate actuator of the Latch MEMS. The surface-to-surface separation between the coated cathode and anode electrodes is defined as $g_{cLNEM} - \Delta z_{LNEM}$ where Δz_{LNEM} is the z-axis offset of the latch MEMS's suspension which establishes the spring-loaded latching. Sufficient spring-loading is ensured by satisfying

$$k_{LNM} \Delta z_{LNM} > \frac{(k_{WNM})(g_{cWNEM})}{\mu_{Coat}} \qquad (3.2)$$

where μ_{COAT} is the friction coefficient of the coat cladding material (ALD-Si_xO_y), k_{LNM} is the lumped-element spring constant of the crab-leg flexure suspension of the latch actuator, k_{WNM} is the lumped-element spring constant of the folded-beam flexure suspension of the waveguide actuator.
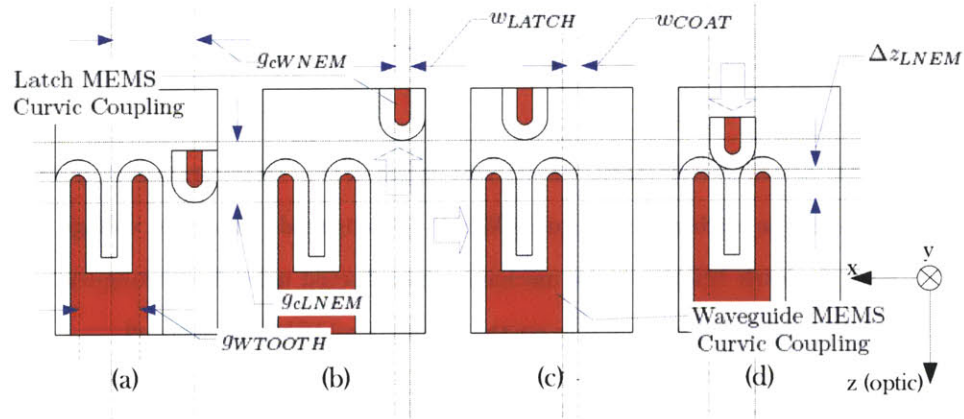
FIGURE 3.69: The four-stage sequence of latching. The (a) as-fabricated configuration, the (b) unlatched as-fabricated configuration, the (c) unlatched mechanically-deflected configuration and the (d) latched mechanically-deflected configuration.

Figure (3.69) displays the four-state switching sequence from the perspective of the latch

teeth. The latch tooth on the waveguide MEMS has a U-shaped curvic structure–two curve-ended suspended beams connected to a large suspended beam. The latch tooth on the latch MEMS has a single curvic structure. The latch teeth are designed to accommodate the thickness of conformal coat cladding.

The first switch state, the as-fabricated configuration [Figure (3.69a)], is established by spacing the latch teeth on the latch and waveguide MEMS by g_{cWNEM}. Note that there is an overlap length between the latch teeth; this intentional overlap length between the two latch teeth is used in order to establish spring loading.

The second switch state is the unlatched as-fabricated configuration [Figure (3.69b)]; the waveguide MEMS remains stationary as the latch MEMS undergoes pull-in deflection, clearing a way for the waveguide MEMS to be actuated orthogonal to the latch MEMS unobstructed.

In the third switch state, the unlatched mechanically-deflected configuration [Figure (3.69c)], both MEMS's are mechanically-deflected. Ideally, at this point, the center of both coupling structures are aligned.

In the fourth switch state, the latched as-fabricated configuration [Figure (3.69d)], the teeth on the latch and waveguide MEMS are engaged. First, the voltage which initially held the latch MEMS in the mechanically-deflected unlatched configuration is removed then the hold voltage holding on the waveguide MEMS is removed.

Depending on the fabrication-induced variation in features, the center-to-center separation between the latch teeth of the waveguide actuator (g_{WTOOTH})can be adjusted in order to accommodate x-axis misalignment between the latch tooth of the latch MEMS and the latch teeth of the waveguide MEMS.

The spring-loaded force of the latch MEMS applies a normal force through two line contacts in order to maintain the latched mechanically-deflected configuration. Using a

curved latch tooth guarantees that at least one line contact is maintained. A minimum area contact is less suspectable to contact misalignments as there is less probability for contact with surface irregularities.

Using the spring-loaded curvic tooth latch coupling, small dimensional variations can be elastically averaged after multiple latch-engagement cycles. This type of coupling is known to provide good repeatability and high stiffness as demonstrated in macroscopic structures like indexing tables and tool turrets [?].

The optical switches that incorporate latching are considered a class of MEMS devices that involve contacting and rubbing surfaces. As a result, operational stiction must be considered. Stiction arising from the latching action is not anticipated to be problematic since (a) all of the devices are coated with atomic layer deposited alumina (ALD-Al_2O_3), which is known to have a low adhesion work function and (b) the ratio of the contacting sidewall surface (of the latch mechanism) to the volume of the latch MEMS's suspension is low. Also note that the optical switches can also be coated with a self assembled monolayer (SAM) as a stiction prevention measure [?], [?].

3.12 Summary

Chapter 3 opened with a description of the targeted operational performance metrics that were used for each of the optical MEMS switch designs.

Following the chapter introduction, the first seven sections presented each optical switch device ad seriatim, discussing each design in four parts: (1) a description of the switch's two states (2) a description of the how the optical switches were optimized for both optical and MEMS operation, (3) a description of the operational performance and (4) a description of how the device designed evolved into the following generation.

In section 8, Device 04 is covered in detail by outlining the six-step design methodology that was used for creating each optical switch. The optical and MEMS simulations are highlighted with a in-depth discussion on how the results from the optical and MEMS simulations are applied to the integrated design. In section 9, the optical system of Device 07 is covered in detail. The multi-sectioned optical system is deconstructed section-by-section, describing the function of each section.

In sections 10 and 11, the two MEM systems, used in the design of Devices 05, 06 and 07, are covered in detailed; section 10 discusses the MEM system used to switch the configuration states of the optical systems of the three optical switches while section 11 discusses the MEM system used mechanically latch the configuration states. The suspension and actuator subsystems of the two MEM systems are discussed. Also, the two MEM systems are described in relationship to each other as well as in relationship to the optical systems of Devices 05, 06 and 07.

Chapter 4

Fabrication

4.1 Introduction

A semiconductor fabrication sequence has been developed in order to create the seven electromechanical optical switches that were discussed in the previous chapter. This introduction exposes the motivation that prompted the particular arrangement of the fabrication processes by first examining how high-index-contrast (HIC) waveguides are created and then by exploring an approach to functionalizing the HIC structures for micro/nanoelectromechanical actuation. Finally, the introduction ends with an adumbration of each of the process steps. The body of this chapter is dedicated to the discussion of each of the process steps; a dedicated section for each of the subprocesses will explain the fundamental aspects of the subprocesses as well as the advantages and limitations of using these subprocesses in order to create the electromechanical optical switches. When available, preliminary fabrication results will be presented in order to provide qualitative support to the viability of the proposed fabrication sequence.

4.2   The Proposed Process Sequence

Informed from preliminary, experimental-fabrication results, Table (4.1) is a proposed fabrication sequence that is designed specific for the realize the seven optical switches presented in the previous chapter.

TABLE 4.1: Proposed fabrication process sequence for the realization of MEMS optical switches. LITHO: a lithographic process step ADD: a process step used to deposit a material SUB: a process step used to remove a material CON: a process step that alters the material properties of a layer. SL: structural layer, PL: process layer, SPL: structural and process layer.

Process			Time	Temp. $(^\circ C)$
1		**Heterostructure Growth**		
	1a	[ADD] Molecular Beam Epitaxy (MBE) Growth (SPL)	Var. (hr)	$470 - 640$
2		**Contact Pad and Wire Definition**		
	2a	[LITHO] Pre-Spin Bake	$10min$	90
		[LITHO, ADD] Resist Spin (NR7-1000) (PL)	$20 - 30s$	25
		[LITHO] Post-Spin Bake (Hotplate)	$60s$	90
		[LITHO] Exposure	$10min$	25
		[LITHO] Post-Exposure Bake (Hotplate)	$60s$	100
		[LITHO] Development	$15s$	25
		[LITHO] Post-Development Bake (Oven)	$20min$	120
	2b	[ADD] E-beam Metal Evaporation (SL)	Var (min)	25+
	2c	[SUB] Liftoff	$10min$	25
	2d	[CON] Metal Anneal	30s	400
3		**Ridge and Mesa Definition**		
	3a	[LITHO, ADD] PECVD SiO$_2$ (PL)	Var	300
	3b	[LITHO] Pre-Spin Bake (Hotplate)	$10min$	90
		[LITHO] Resist Spin (HSQ)	$20 - 30s$	25
		[LITHO] Post-Spin Bake (Hotplate)	$2min/2min$	100/ 120
		[LITHO] Exposure	$10min$	25
		[LITHO] Development	$60min$	25
		[LITHO] Post-Development Bake	$20min$	120
	3c	[SUB] Reactive Ion Etch	$15 - 20min$	≈ 200 [59]
	3d	[SUB] Etch-Mask Strip	$10min$	25
	3e	[CON] Oxidation	$10 - 30min$	$400 - 450$
4		**Sheathed Ridge Definition**		
	4a	[LITHO, ADD] PECVD SiO$_2$ (SPL)	Var.	300
	4b	[LITHO] Pre-Spin Bake	$10min$	90
		[LITHO] Resist Spin (N7-1000) (PL)	$20 - 30s$	25
		[LITHO] Post-Spin Bake	$60s$	90
		[LITHO] Exposure	$10min$	25
		[LITHO] Post-Exposure Bake (Hotplate)	$60s$	100
		[LITHO] Development	$15s$	25
	Continued on Next Page...			

Table 4.1 – Continued

Process			Time	Temp. ($^{\circ}C$)
		[LITHO] Post-Development Bake (Oven)	$20min$	120
	4c	[SUB] RIE	$15 - 20min$	Var.
	4d	[SUB] Etch-Mask Strip		25
5		**Suspended Beam Definition**		
	5a	[SUB] Sacrificial Release Etch		75
	5a	[ADD] Atomic Layer Deposition (SL)		$200 - 500$

The five major, thematic process steps are highlighted in bold with a listing of subprocess steps. These subprocess steps are differentiated by the type: lithographic processes are denoted as "LITHO", processes that are used to deposit a layer of material as "ADD", processes that are used to remove a layer of material as "SUB" and processes that are used to chemically convert a layer of material to another is denoted as "CON". Moreover, for the ADD processes, the material deposited is specified along with the specification of whether that material is a structural layer (SL), process layer (PL) or both (SPL). An SL material is used for only for the operation of an optical switch, a PL material is used only for optical switch fabrication and SPL materials is used as both a SL and PL material. Finally, the duration and temperature of each process step is listed.

Structural Film Definition. Materials that serve as structural, process and structural/process layers are deposited during the Structural Film Definition process step. Specifically, from substrate to top surface, a heterostructure stack of InGaP/AlAs/aluminum-rich AlGaAs/AlGaAs/gallium-rich AlGaAs is deposited by the molecular beam epitaxy (MBE) growth process. The InGaP material is a process layer, used as an etch stop during the sacrificial etch process. The AlAs material is a process layer, used for film-stress reduction between the InGaP and the aluminum-rich AlGaAs materials. The aluminum-rich AlGaAs material is a structural/process film, serving as a lower-cladding layer to the anchored waveguides, a sacrificial layer to the suspended waveguides and an electrical-isolation layer, insulating the doped gallium-rich AlGaAs layer from the doped substrate. The AlGaAs layer is a process layer, used to reduce the film-stress between the aluminum-rich AlGaAs and gallium-rich AlGaAs layers. The gallium-rich AlGaAs material is a structural layer, used as the core layer for both the anchored and suspended waveguides, the core layer for the suspended MEMS flexures and suspended beams and the capacitive surfaces for the MEMS parallel plate actuators.

Contact Pad and Wire Definition. During the Contact Pad and Wire Definition process, lithography is used to define the heterostructure layer stack of metals that are able to form a low-resistance ohmic contact to GaAs-based materials. Additionally, the metal layer stack is chosen in order to sustain its low-resistance properties throughout the subsequent steps of the fabrication sequence.

Ridge and Mesa Structure Definition. The third process step is used for the definition of the ridge and mesa anchor structures.

Sheathed Ridge Structure Definition. The fourth process step is used to isolate the previously defined ridge anchor structures into anchored waveguides and soon to-be-released suspended beam structures.

Suspended Beam Definition. The fifth and final process step is used to create the suspended submicron beams by sacrificially etching the supporting process film in

the previously defined ridge anchor that was left exposed by the Sheathed Ridge Anchor

Definition process. Additional structural films are deposited on the suspended beam in

order to define the suspended waveguides.

4.3   Thin-Film Layer Growth/Deposition

In general, crystalline semiconductor materials have exceptionally high-strength [60].
As a result, electromechanical structures that are created from these materials are in-
triguingly resistant to cycling and fatigue failure due to repeated actuation [?]. The
strength of crystalline semiconductor material is attributed to the process in which that
material is created. Bulk semiconductor forming techniques such as the Czochralski
process and the Bridgman-Stockbarger process as well as thin-film growth techniques
such as the metallorganic chemical vapor deposition (MOCVD) process and the molec-
ular beam epitaxy (MBE) process are able to produce ultra-pure crystalline materials
with excellent mechanical properties that rivals the structural integrity of single-crystal
super alloy steel that is used in jet engine blades and nuclear reactors [60]. Of the two
techniques that are used in planar wafer fabrication (deposition and growth), molecular
beam epitaxy (MBE) processing was used to define the structural and process films that
were used to create the electromechanical optical switches in the gallium arsenide-on-
insulator (Gallium Arsenide on Insulator) material system.

4.3.1   Molecular Beam Epitaxy (MBE) Growth

Crystalline $GaAs/Al_{1-x}Ga_xAs$ heterostructure films can be created by either the de-
position process CVD or the growth process of molecular beam epitaxy (MBE). There
is major difference between a growth process and a deposition process: a growth pro-
cess adds film to a substrate via chemical reactions that involves the substrate material
whereas a deposition process adds a film to a substrate by physical adherence to the
substrate material. As a result, MBE processing is limited by the material that can be
grown on a substrate but is able to create high quality films. Conversely, CVD process-
ing produces lower quality films but is able to deposit a wide variety of films on a wide
variety of substrates. Fortuitously, MBE processing can be used to define the GaAs/
$Al_{1-x}Ga_xAs$ heterostructures in order to create the electromechanical optical switches
in the gallium arsenide-on-insulator material system.

In particular, the gas source MBE (MBE) growth method was used to create the GaAs/ $Al_{1-x}Ga_xAs$ heterostructure samples. More specifically, a Riber 32P MBE system was used to grow GaAs substrate compatible heterostructures with user-definable $Al_{1-x}Ga_xAs$ alloys of variable aluminum and gallium concentration and its attendant refractive index, electronic bandgap, and chemical properties. $Al_{1-x}Ga_xAs$ films with a 3% variation of alloy content and thickness are routinely grown in a Riber 32P MBE system [61], [62]. Essentially, MBE-grown GaAs/ $Al_{1-x}Ga_xAs$ heterostructure samples are easily engineered to have the optical, mechanical, and electrical qualities that are required for the fabrication of the electromechanical optical switches as well as the other photonic devices that might be monolithically integrated with the optical switches at the wafer level.

The MBE process begins with a desorption of moisture on the GaAs substrates by heating the sample to $250°C$ in an ultra high vacuum environment. The GaAs wafer is then moved into the growth chamber that is kept at an idle pressure of $10^{-10}Torr$. During the MBE process, gallium (Ga), arsenic (As), aluminum (Al), indium (In) and phosphorous (P) are the five elements that become selectively alloyed onto the substrate surface to form a heterostructure stack of films; silicon (Si) is used to dope films n-type. Ga, Al and In exist in molten form within effusion cells and are delivered to the substrate after being thermally evaporated at temperature within the $600°C$ to $1200°C$ temperature range; As, P, exist in gas form as arsine (AsH$_3$) and phosphine (PH$_3$) and are delivered to the substrate after being cracked or thermally decomposed.

During growth, the growth chamber pressure raises to $2 \cdot 10^{-5}Torr$ due to the presence of H_2 from the cracking of AsH_3 and/ or PH_3. The $2 \cdot 10^{-5}Torr$ pressure still allows the independently controlled elements to be delivered to the substrate in the molecular flow regime; the elements have a mean free path larger than the distance between the element source and substrate surface. As a result, low defect (10^2cm^{-2} - 10^4cm^{-2}) [63] crystalline materials are grown. The MBE process is performed at approximately $600°C$. The low growth temperature of the MBE process reduces the interfacial stress between two dissimilar layers (e.g., GaAs on $Al_{0.95}Ga_{0.05}As$) which improves the mechanical

robustness. However, the lattice constant of the two materials which is indicative of the alloy composition should be tightly controlled in order to avoid any undue thin film stress from occurring. The excess unused Column V molecules are continuously removed from the chamber. In-situ layer film quality and thickness is actively monitored with a reflection high energy electron diffraction (RHEED) system.

The topmost MBE thin-film layer is gallium arsenide (GaAs); GaAs serves as the core material for the etched ridge waveguides as well as the core material for the suspended structures. Additionally, the top surface of the GaAs layer is used to form the ohmic contacts.

The MBE thin-film layer underneath the GaAs layer is high-aluminum content aluminum gallium arsenide ($Al_{1-x}Ga_xAs$), where $x < 0.4$; $Al_{1-x}Ga_xAs$ serves as the bottom layer of the mesa anchor that supports the suspended sections of the electromechanical actuators. Additionally, the $Al_{1-x}Ga_xAs$, upon undergoing a later oxidation process is converted into an aluminum oxide (Ox-Al_xO_y). The Ox-Al_xO_y film then functions as an anchor support (structural film), a lower index cladding to the anchored waveguides (structural film), and a sacrificial layer for the suspended waveguides (process film).

An InGaP layer functions as a lattice-matched process film, serving as an etch-stop layer during the reactive ion etch (RIE) process during the Ridge and Mesa Structure Definition Process. The InGaP layer is specifically used for Device 01 in order to relax the fabrication tolerance that are associated with the design-specific gap closer separation (g_{NEM}). Specifically, the InGaP layer was used as an etch stop layer for the RIE-processed GaAs and $Al_{1-x}Ga_xAs$ thin-film layers in a chlorinated etch chemistry.

MBE Test Structures.

A heterostructure wafer (Wafer A) was grown for process development. A second heterostructure wafer (Wafer WB) was also created. Wafer WB is envisaged as being

accommodative to the seven mechanical optical switches as well as other photonic devices.

GaAs (280nm)

$Al_{0.85}Ga_{0.15}As$ (500nm)
$Al_{0.90}Ga_{0.10}As$ (500nm)

$Al_{0.95}Ga_{0.05}As$ (1000nm)

AlAs (20nm)

InGaP (100nm)

GaAs Substrate

$2\mu m$
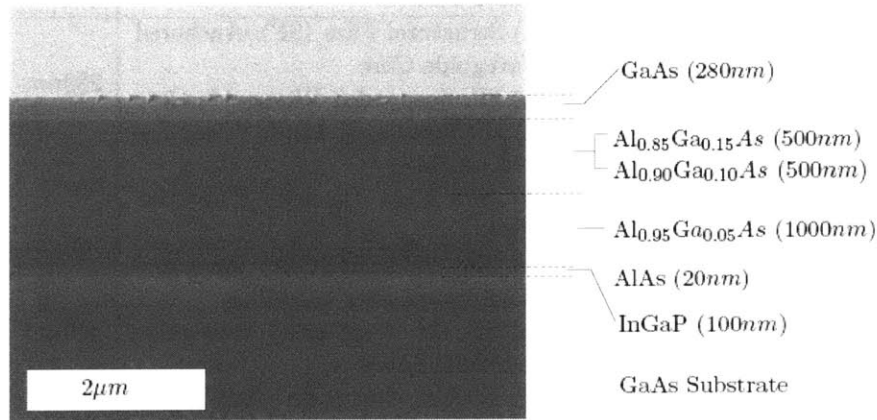
FIGURE 4.1: GaAs Heterostructure Wafer A: 45° SEM of the cleaved $5mm \times 5mm$ sample cleaved from Wafer A following MBE growth. Thin-film layer information is given in Table (4.2)

Wafer A was used for process development, nanomechanical structural analysis, and optical analysis. As can be seen in Figure (4.1), each of the six layers of the heterostructure stack can be distinguished by their interfaces vis-a-vis the color changes in the scanning electron micrograph (SEM). By virtue of growing the heterostructure film stack on a 2-inch GaAs (100) wafer, the wafer can be easily cleaved into square samples. Cleaving is the act of nicking a corner of a wafer or sample to initiate a crack that propagates along that wafer or sample; the simple act of applying out-of-plane pressure bisects the wafer or sample. Cleaving produces atomically smooth side surfaces which, incidentally, is used to produce the optical quality waveguide facets for testing. Coincidentally, following the Structural and Process Film Definition Process, the 2-inch GaAs wafer is cleaved into $5mm \times 5mm$ test samples to increase the number of experiments during process development at the expense of handling wafer pieces as opposed to a full wafer.

TABLE 4.2: Wafer A layer description. An SEM of a $5mm \times 5mm$ sample cleaved from Wafer A is shown in Figure (4.1).

Layer	Material	Film Function	Thickness	Doping
06	GaAs	(a) Structural Film (SF): Anchored Waveguide Core (b) SF: Suspended Waveguide Core (c) SF: Suspended Anode Wire/ Capacitor Plate (d) SF: Mesa Cathode Capacitor Plate	$280nm$	undoped
05	$Al_{0.85}Ga_{0.15}As$	(a) SF: Oxidized (Ox): Anchored Waveguide Lower Cladding (b) SF: Ox: Suspended Waveguide Sacrificial Layer (c) SF: Ox: Suspended Anode Sacrificial Layer (d) SF: Mesa Cathode Support/ Electrical Isolation (e) Process Film (PF): Stress Matching	$500nm$	undoped
04	$Al_{0.90}Ga_{0.10}As$	(a) SF: Ox: Anchored Waveguide Lower Cladding (b) SF: Ox: Suspended Waveguide Sacrificial Layer (c) SF: Ox: Suspended Anode Sacrificial Layer (d) SF: Mesa Cathode Support/ Electrical Isolation (e) Process Film (PF): Stress Matching	$500nm$	undoped
03	$Al_{0.95}Ga_{0.05}As$	(a) SF: Ox: Anchored Waveguide Lower Cladding (b) SF: Ox: Suspended Waveguide Sacrificial Layer (c) SF: Ox: Suspended Anode Sacrificial Layer (d) SF: Mesa Cathode Support/ Electrical Isolation (e) Process Film (PF): Stress Matching	$1\mu m$	undoped
02	$AlAs$	PF: GSMBE Growth Cap	$20nm$	undoped
01	InGaP	PF: Etch Stop	$100nm$	undoped
00	GaAs (100)	(a) PF: Substrate (b) PF: Optical Quality Cleaves	$350\mu m$	n^+

Table (4.2) identifies the six layers in the Wafer A's heterostructure stack by film material, function, thickness and doping.

As stated before, the heterostructure stack is grown on a GaAs (100) wafer. Since a GaAs (100) wafer is used, the wafer can be cleaved to produce optical quality waveguide facets post-fabrication.

The InGaP layer serves as a process film that prevents the chlorine-based etch gas that is used in the Material Subtraction: Reactive Ion Etch Subprocess from etching into the substrate during the Ridge and Mesa Structure Definition Process.

The $AlAs$ layer is a process film that is required for the growth of the $GaAs/\text{Al}_{1-x}\text{Ga}_x\text{As}$ heterostructure stack during the Material Addition: MBE Heterostructure Growth Subprocess.

The $\text{Al}_{0.95}\text{Ga}_{0.05}\text{As}$ serves as both a structural and process film. After being oxidized in the Material Conversion: $\text{Al}_{1-x}\text{Ga}_x\text{As}$-Alloy Oxidation Subprocess, the resultant $Ox - Al_xO_y$ structural film serves as the low-index lower cladding layer for the anchored waveguide. Also, in the capacity of a structural film, the portion of the $\text{Al}_{0.95}\text{Ga}_{0.05}\text{As}$ that is not oxidized after the Material Conversion: $\text{Al}_{1-x}\text{Ga}_x\text{As}$-Alloy Oxidation Subprocess serves as a support and electrical insolation material for the mesa cathode and for the n^{++} doped GaAs substrate. In terms of $\text{Al}_{0.95}\text{Ga}_{0.05}\text{As}$ being a process film, the suspended waveguide and suspended anode are created in the Material Subtraction: Sacrificial Release Subprocess after the $Ox - Al_xO_y$ film is sacrificially etched.

The $Al_{0.90}Ga_{0.10}As$ serves as both a structural and a process film. Similar to the $Al_{0.95}Ga_{0.05}As$ layer, the $Al_{0.90}Ga_{0.10}As$, upon being converted to Ox-Al_xO_y, serves as the lower cladding layer for the anchored waveguide and a sacrificial material to the suspended waveguide and anode. Furthermore, as is, the $Al_{0.90}Ga_{0.10}As$ becomes the structural support and electrical isolation layer for the mesa cathode and for the GaAs substrate. Nevertheless, the $Al_{0.90}Ga_{0.10}As$ has the additional function of being

a graded layer to ensure the heterostructure stack has negligible thin-film stress as the high-aluminum content $Al_{1-x}Ga_xAs$ layers are graded to GaAs.

The $Al_{0.85}Ga_{0.15}As$ layer is a structural and process film, intended to serve in the same capacity as the $Al_{0.90}Ga_{0.10}As$ layer. However, as will be explained later, the $Al_{0.90}Ga_{0.10}As$ does not fully oxidize on the same time scale as the other bottom layers. As a result, the $Al_{0.85}Ga_{0.15}As$ layer cannot be fully oxidized without structural compromise to the higher aluminum content $Al_{1-x}Ga_xAs$ layers. Considered as a shortcoming, the $Al_{0.85}Ga_{0.15}As$ layer can simply be increased in aluminum content and/or reduced in sized in order to insure that layer can be effective as a structural and process film.

The GaAs layer is used as a structural film in four capacities: a core layer for the anchored and suspended waveguides, a core layer for mechanical flexures and electrodes for the parallel-plate actuator. Both the suspended and anchored waveguides have a *GaAs* core which is defined in Process 3: Ridge and Mesa Structure Definition. The *GaAs* mechanical flexures are formed in Process 3: Ridge and Mesa Structure Definition and released in Process 5: Suspended Beam Definition Process. The exposed side surfaces of the etched GaAs are used as capacitor plates for the gap closer vis-a-vis the conductive suspended anode beam core, mesa cathode, and the substrate.

TABLE 4.3: Proposed Layer Description of Wafer B.

Layer	Material	Film Function	Thickness	Doping
20	GaAs	Type VI Metal Contact. Oxidation Barrier	$10nm$	n^{++}
19	$Ga_xAl_{1-x}As$	Type VI Core	$100s$ of nm ($\approx 150nm$)	undoped
18	GaAs-Based (e.g., $InGaAsN$)	Type VI Quantum Wells. Type VI Core	$100s$ of nm (Multi-layer)	undoped
17	$Ga_xAl_{1-x}As$	Type VI Core	$100s$ of nm ($\approx 150nm$)	undoped
16	GaAs	Type VI Electrode	$10nm$	n^+
15	$Al_{1-x}Ga_xAs$	Stress Matching	$10nm$ (Multilayer)	undoped
14	$AlAs$	Type I, V & VI clad. Type VI/ Type I & V isolation. Type VI sacrificial. Totally oxidizable.	$500nm$	undoped
13	$Al_{1-x}Ga_xAs$	Stress Matching	$10nm$ (Multilayer)	undoped
12	$Al_{1-x}Ga_xAs$	Type III Core. Type I & V Clad. Selectively Oxidizable	$500nm$	undoped
11	GaAs	Type V Metal Contact	$10nm$	n^+
10	$Ga_xAl_{1-x}As$	Type I, III & V core	$100s$ of nm ($\approx 300nm$)	undoped
09	GaAs	Type V Electrode	$10nm$	n^+
08	$Al_{1-x}Ga_xAs$	Type III core. Type I & V clad. Selectively oxidizable.	$500nm$	undoped
07	$Al_{1-x}Ga_xAs$	Stress matching.	$10nm$ (Multilayer)	undoped
06	$AlAs$	Type I & V clad. Type V sacrificial. Totally oxidizable.	$500nm$	undoped
05	$Al_{1-x}Ga_xAs$	Stress matching.	$10nm$ (Multilayer)	undoped
04	InGaP	Type V metal contact. Type V electrode. Etch stop.	$10nm$	n^{++}
03	$Al_{1-x}Ga_xAs$	Stress matching.	$10nm$ (Multilayer)	undoped
02	$AlAs$	Type III Aligner. Totally oxidizable.	$\approx 50\mu m$	undoped
01	$Al_{1-x}Ga_xAs$	Stress matching.	$10nm$	undoped
00	GaAs (100)	Substrate.	$500\mu m$	n^+

Table (4.3) is the proposed MBE heterostructure stack that can be used to accommodate a variety of waveguide-based devices jointly with the seven electromechanical

optical switches, thus, achieving wafer-level monolithic integration.

Specifically, Wafer WB is capable of being processed to include Type I (mechanically-passive, electrically-passive, optically-passive), Type III (mechanically-active, electrically-passive, optically-passive), Type V (mechanically-active, electrically-active, optically-passive), and Type VI (mechanically-active, electrically-active, optically-active) waveguides on the same sample. Type I and V waveguides will be in the same heterostructure layer, the waveguides of Type VI will be isolated from the top of the heterostructure, and the Type III waveguide layer is positioned on the top and at the bottom of the Type I and V waveguide layers. Table (4.3) specifies each of the layers of the Wafer WB heterostructure stack by the films material composition, function, thickness, and doping level.

4.4   Nanometer Lithography

Ridge and mesa structure definition requires the use of a high-resolution lithographic definition technology in order to pattern the waveguide-defining submicron features. As the metal pads and wire regions have already been defined at this point, the ridge and mesa structures must be aligned to the metal pads and wire regions. Also, the waveguide patterns must be formed perpendicular to a cleavage plane in order to facilitate facet creation after the front-end processing (i.e., the fabrication processing sequence covered in this chapter).

For the purpose of experimental demonstration, the submicron features were written using scanning electron beam (e-beam) lithography (SEBL). SEBL is the preferred fabrication technology for the generation of masks for other optical exposure systems (e.g., optical lithography) and low-volume manufacture or one-off design development of ultrasmall high-performance devices. Note that SEBL is not anticipated to be used for high-resolution ($CD = 100nm$), high-throughput mass production. Instead, projection printing technology (e.g., extreme ultraviolet (EUV) systems) are likely to be used [64].

4.4.1 Scanning Electron Beam Lithography (SEBL)

Resist Application

Before the e-beam-sensitive resist is applied to a sample (or wafer), the sample's surface is cleaned. The surface of the sample is cleaned in a liquid solution (a liquid solution innocuous to the preexisting etched features on the samples surface). The cleaning liquids are then neutralized with neutralizing agents (typically in liquid form). The neutralizing agents are then rinsed in deionized water which is subsequently removed from the surface with inert nitrogen gas. Finally, the sample is heated on a hotplate (or in an oven) in order to evaporate the residual moisture from the surface. Following the surface cleaning treatment, the e-beam resist is spin casted upon the sample's surface. Usually the e-beam resist is drop-deposited and spin casted in order to yield a film thickness $\approx 10 - 100nm$. Compared to the typical film thickness of resist films that is used in optical exposure systems $(1 - 2\mu m)$, e-beam resists are considerably thinner. After spin casting, a hotplate or oven is used to evaporate solvents from the e-beam resist.

E-beam Exposure

During the SEBL process, a computer numerical controlled (CNC) nanometer-wide $(< 10nm)$ collimated beam of electrons (e-beam) is continuously scanned across the surface of the e-beam-sensitive resist. Pattern fidelity is ensured by controlling three interactions:

1. The E-beam and the Resist Interactions
2. The SEBL Apparatus and the E-beam Interactions
3. The CNC software and the SEBL Apparatus Interactions

The e-beam and the resist interactions: Closely spaced features receive higher e-beam doses than isolated features. As a result, separations between the closely spaced features will be narrower than intended while the features will be wider. Similarly, isolated

features will be narrower than intended. Simply stated, the aforementioned effects are considered proximity effects. Proximity effects can be accounted for with an appropriate modulation in the e-beam dose. Adjusting the pattern widths via e-beam dose modulation is more effective than changing layout dimensions. However, experimenters may not have access to the SEBL system. In this case, additional dummy features can be used to mitigate the overdose/underdose effects.

Line spacing, or, more generally, packing density, as well as feature size, determines whether a feature or spacing is larger or smaller than intended. For instance, a large feature (a micron-sized feature that is used is a mesa cathode) separated from a small feature (a submicron-sized feature that is used is a suspend waveguide) is likely to yield a much smaller separation between the large and small features. Moreover, the small feature will most likely increase in size. Regardless of the lithographic technology, minimum/maximum linewidth/line spacing design rules can be used to mitigate proximity effects. Also, adherence to minimum/maximum linewidth and line spacing rules is beneficial to other diffusion-based fabrication processes.

The SEBL apparatus and the e-beam interactions. The SEBL apparatus is usually operated at high bias voltages, which (by preventing the resist from being exposed by backscattered electrons) reduces feature widening. Depending upon the resist exposure-dose requirements, the SEBL apparatus can be operated at current levels of $\approx 100pA$ As a result, feature widening can result from electron interactions within the e-beam. Essentially, for a high-voltage-operated SEBL apparatus, current levels of $100pA$ translates into electron mean free paths $1.33\text{-} 13.4\mu m$. Therefore, in order for electron interactions to be eliminated, the SEBLs column height, the distance between the e-beam source and sample, must be $\approx 1m$ and the SEBL must be operated at current levels of $10pA$. Unfortunately, such low currents become time-prohibitive as most e-beam resists require substantially higher current levels.

Inherent in the operation of the SEBL apparatus is that the e-beam has a limited range over which it can be deflected to define a pattern without stage translation. This

e-beam deflection range is called a scan field. The smaller the scan field, the better controlled the e-beam and the better the resolution. However, having small fields increases the likelihood of stitching errors, the alignment of features across many fields. Features intended for waveguiding are particularly sensitive to stitching errors; stitching errors translate directly into sidewall roughness as the e-beam defined pattern is transferred into the underlying waveguiding materials. In this regard, a large e-beam field may be desirable in order to sacrifice resolution for global pattern fidelity.

The CNC software and the SEBL apparatus interactions: Typically, in addition to the set of magnetic lenses that are used to collimate the e-beam, two more sets of magnetic lenses are used to deflect the e-beam in the horizontal and/or vertical scanning directions as well as to blank (turn on and off) the e-beam in order to define arbitrarily shaped patterns. The typical horizontal/vertical scanning scheme is problematic for defining structures which are intended to be used to guide light (waveguide quality structures). Modified e-beam deflection and blanking schemes are required in order to prevent nanoscopic bumps from forming along the outside edges of the features.
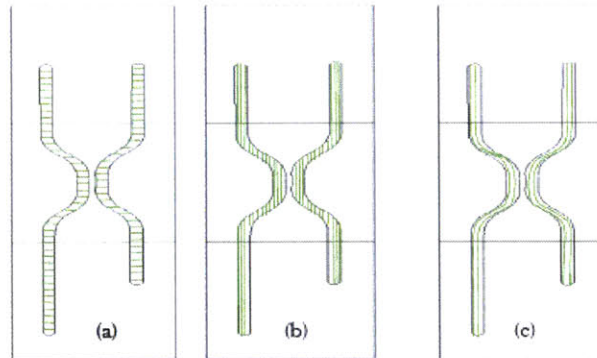
FIGURE 4.2: E-beam scan patterning strategies for curved directional coupled-based features. (a) Single-axis (transverse) scan patterning. (b) Single-axis (longitudinal) scan patterning. (c) Curved single pixel line scan patterning.

Figure (4.2) shows three different scan patterning strategies: Figures (4.2a) and (4.2b) shows two single-axis scan patterns over three scan fields while Figure (4.2c) shows a curved-single pixel line scan pattern. As discussed in depth in [?], (curved) single pixel line pattern strategies are well suited for defining waveguide-quality features. The single-axis patterning is flawed due to the difference in x- and y-axis deflection of the electron beam of the e-beam system. Not only does the difference in electron beam deflection result in width variations along the pattern but also in potentially rough sidewalls since the e-beam has to blank abruptly during patterning. In contrast, the curved-single pixel line scan patterning, the electron beam is directed along the contours of the curved waveguides. Only at the beginning and end of the defined feature does the e-beam need to be blanked.

Resist development

Contingent upon whether the e-beam resist is positive- or negative-tone, a sample is exposed to a liquid solution which removes the exposed (chemically converted) patterns in the resist (positive-tone resist) or the unexposed portion in the resist (negative-tone resist). Typically, a positive resist is used in SEBL technology, specifically, the poly (methyl methacrylate) (PMMA) resist. However, more exotic negative resists are being explored as well, specifically, the hydrogen silsesquioxane (HSQ) resist.

The Poly(Methyl Methacrylate) (PMMA) e-beam resist:

Poly (methyl methacrylate) is the typical e-beam resist that is used to define submicron planar geometries. E-beam irradiation severs the chemical bonds within the PMMA; the portion of PMMA which has severed chemical bonds, can then dissolve after being exposed to a methyl isobutyl ketone/isopropyl alcohol (MIBK:IPA, 1:2) solution (temperature: $20^\circ C$, time: min). Note that PMMA development involves submerging $10mm \times 10mm$ samples into a MIBK:IMP (1:2,by volume) solution (temperature: $20^\circ C$, time: min) and then into an IPA solution (temperature: $20^\circ C$, time: $1.5min$). Since the PMMA is so thin, the lift-off process is used to form a more robust mask from the pre-patterned PMMA. Inverted patterns (e.g., ridge structures are defined as trenches)

are defined in the PMMA. After PMMA patterning, metal is evaporated onto the sample. After metal evaporation, the samples undergo the lift-off process-a metal mask is formed by removing the PMMA and the evaporated metal on top of that PMMA. Defining an etch-mask with PMMA features requires seven steps:

1. Resist Coating

2. Solvent Evaporation

3. Pattern Definition

4. Resist Curing

5. Resist Development

6. Etch-mask Material Deposition

7. Lift-off Process

PMMA Spin (speed: $3600rpm$, time: $1min$), PMMA Bake (temperature: $180°C$, time $1hour$), PMMA solution (3% $750k$ PMMA in chlorobenzene). PMMA lift-off: NMP (temperature: $100°C$), ultrasonic bath ($60s$), acetone rinse (from a squirt bottle in a fume hood), iso-propanol rinse (from a squirt bootle in a fume hood).

The Hydrogen Silsesquioxane (HSQ) resist:

In addition to the PMMA direct-write positive-tone e-beam sensitive resist, a novel direct-write direct-etch-mask negative e-beam sensitive resist was investigated. HSQ is such a resist, one that maintains the promise of reduced process variability, and increased pattern fidelity. Reduced process variability and increased pattern fidelity comes with the reduction of the etch-mask definition processing steps. Etch-mask definition for a HSQ-e-beam system is a five step process:

1. Resist Coating

2. Solvent Evaporation

3. Pattern Definition

4. Resist Curing

5. Resist Development

E-beam lithography used with the HSQ e-beam resist:

HSQ is a flowable chemical compound that is composed of hydrogen, silicon, and oxygen in a caged structure arrangement. HSQ is typically used as a spin-on dielectric where the film is converted to a silicon dioxide film of variable composition (Si_xO_y) with thermal annealing. Recent investigations of HSQ have led to the discovery of its sensitivity to e-beam irradiation: HSQ can be used as a negative-tone resist for nanometer feature patterning [?]. Instead of solely relying on heat to chemically convert HSQ to Si_xO_y, the solidification of HSQ can be partitioned into a two-step chemical conversion process: the HSQ is first heated and then undergoes an e-beam irradiation. Specifically, for the fabrication study discussed in this thesis, the commercial form of HSQ (FOX - Flowable OXide resist - 16 from Dow Corning) is used for e-beam lithographic patterning.

After growing a $Al_xGa_{1-x}As$ heterostructure on a 2-inch GaAs wafer, the wafer is quartered. Next, a thin layer ($\approx 10nm$) of SiO_2 is sputtered onto the quarter wafer samples. After sputtering, the quarter wafer samples are diced into $10mm \times 10mm$ samples. HMDS, a thin-film adhesion promoter, is first spun (speed: $3300rpm/s$, time $60s$) onto the $10mm \times 10mm$ samples. Next, FOx-16 HSQ (in concentrated liquid form) is spun (speed: $3300 \; rpm/s$, time: $60s$) onto the $10mm \times 10mm$ samples with a targeted thickness of $300nm$. Directly following, a two-temperature hot-plate bake sequence (temperature: $150°C$ time: $2min$; temperature: $200°C$, time: $2min$) is performed in order to evaporate excess solvents and increase the density of HSQ film. At this point, the samples are ready for e-beam exposure. Note that the samples were allowed to remain in a class-100 cleanroom for up to one week prior to e-beam exposure. After one week, the samples were assumed to unusable and discarded.

E-beam lithography is performed using the Raith 150 scanning electron beam lithography (SEBL) system. Typical exposures were performed at a $100pA$ e-beam current level with a field sizes of $250\mu m$. Calibration, e-beam dose tests were performed prior to a run cycle. The dose tests were deemed to be good for two days; after two days, another dose test was performed. Typical operating conditions ranged from 60-$84MHz$,

$500\text{-}1000\mu C/cm^2$. Note that high doses were required in order to avoid scumming effects during development. Patterns were created in a non-standard way. Instead of defining arbitrary geometries with pixels, the electron beam was guided along the features in a single-line raster pattern.

Two developers were used: the Olin Corporation's proprietary tetramethylammonium hydroxide (TMAH) resist developer called OPD-262 (1 - 10% TMAH, 90 - 99% water) and tetramethylammonium hydroxide (TMAH). Initially, using the OPD-262 developer (time: 20min), the thin layer of SiO_2 was not sputtered upon the GaAs substrates as HMDS was observed to be sufficient for maintaining pattern adhesion. However, switching to TMAH required a thin layer of SiO_2 as HMDS was observed to not be sufficient.

TMAH development is carried out one to four samples at a time in Pyrex-brand borosilicate glassware in a laboratory fume hood in a class-100 cleanroom. Specifically, TMAH development requires three borosilicate petri dishes, containing TMAH, methanol, and deionized water. Stainless steel tweezers are used to handle the $10mm \times 10mm$ samples. The samples are submerged into each liquid at an angle in order to break the liquid's surface tension. The submersion sequence starts by introducing each of the $10mm \times 10mm$ samples into the TMAH bath (temperature: $20°C$, time: $60min$), then into the deionized water bath (temperature: $20°C$, time: $1min$) and then into methanol bath (temperature: $20°C$, time: $1min$). After removing the samples from the methanol bath, the samples are left under the fume hood in order to evaporate (temperature: $20°C$, time: $30min$) the remaining methanol. During TMAH development, bubbles formed, which is expected for alkaline solutions, and required the use mechanical agitation in order to have uniform HSQ development. Consequently, 1 minute into the 60-minute development, the glassware containing the development solution and sample was manually shaken by the hand of the operator.

The remaining patterned HSQ can be considered as a form of Si_xO_y; this film is referred to as HSQ-Si_xO_y.[1] Figure (4.3) shows a successful development of submicron lines in HSQ.
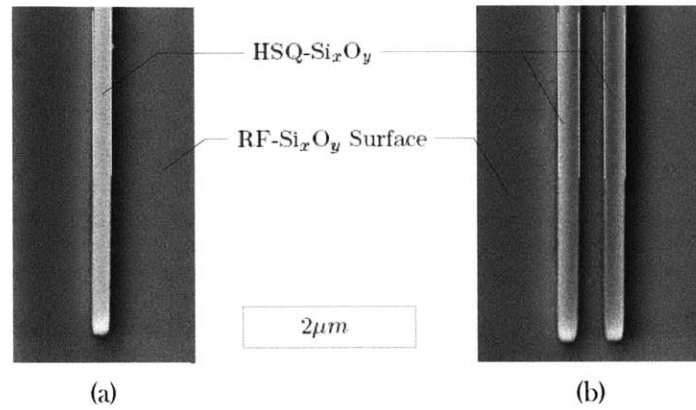
FIGURE 4.3: Top-Down SEM images of HSQ after development (on same sample). (a) HSQ-Si_xO_y etch-mask of the isolated waveguide (CAD pattern: 280-nm; SEM-measured pattern: 236-nm). (b) HSQ-Si_xO_y etch-mask pattern of two proximate waveguides (CAD pattern: 280-nm lines, 300-nm spacing, SEM-measured HSQ-Si_xO_y pattern: 260-nm lines, 319-nm spacing).
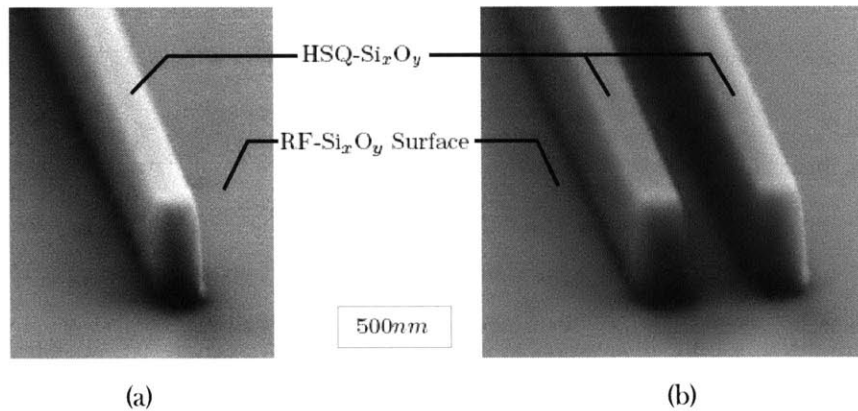
FIGURE 4.4: 45°-degree SEM images of HSQ after development (on same sample). (a) HSQ-Si_xO_y etch-mask of the isolated waveguide (CAD pattern: 280-nm; SEM-measured pattern: 236-nm). (b) HSQ-Si_xO_y etch-mask pattern of two proximate waveguides (CAD pattern: 280-nm lines, 300-nm spacing, SEM-measured HSQ-Si_xO_y pattern: 260-nm lines, 319-nm spacing).

---

[1]Note that while an additional heat treatment can be used to increase the resiliency of the HSQ-Si_xO_y, an additional heat treatment was not performed.

Figure (4.4a) is a 45° tilted view of a submicron line in isolation and Figure (4.4b) is a 45° tilted view of two (submicron lines) in close proximity.

HSQ Development.

Two issues during development were overcome during the optimization experiments: adhesion and feature distortions.
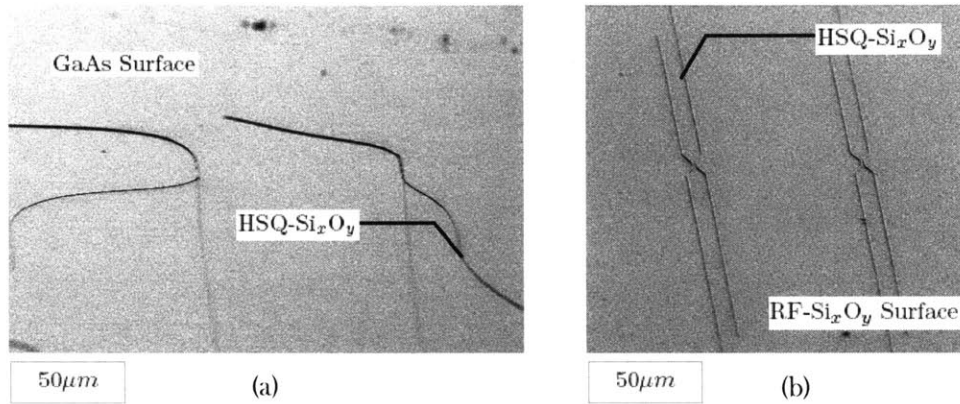
FIGURE 4.5: SEM (at 45°) images of two different samples post e-beam-exposed HSQ resist development. (a) HSQ-Si_xO_y features atop a GaAs surface. (b) HSQ-Si_xO_y features atop an RF-Si_xO_y-coated GaAs surface.

Application of the HSQ film to the GaAs surface was met with adhesion problems as shown in Figure (4.5a). Additionally, HSQ films that were applied directly to the surface of GaAs substrates has been observed to chemically leach impurities into the underlying GaAs [65]. In order to circumvent both adhesion and chemically leaching issues, a thin process film of SiO_2 was deposited onto the GaAs substrate in the initial stages of the lithographic subprocess. The idea is to present the HSQ-SiO_2 with a surface of material which promotes HSQ-SiO_2 adhesion during development while simultaneously providing a barrier layer of pure SiO_2 to prevent any remaining solvents in the HSQ-SiO_2 from leaching into the underlying $GaAs$. SiO_2 was deposited onto the GaAs substrate by the physical process of radio frequency (RF) sputtering (RF-SiO_2). Radio frequency (RF) sputtering is a physical process that is used to transfer a material to a substrate. In general, the RF sputtering process is able to coat substrates with a wide variety of

materials that have excellent film adhesion. During the RF sputter process, the arriving (SiO_2) molecules are able to adhere onto an atomically clean (GaAs) substrate surface, a surface that was created by the cleaning action of the generated RF plasma, resulting in an excellently adhered RF-SiO_2 film to the GaAs substrate.

HSQ-Si_xO_y

HSQ-Si_xO_y Skirt

RF-Si_xO_y Surface

$2\mu m$

(a)   (b)
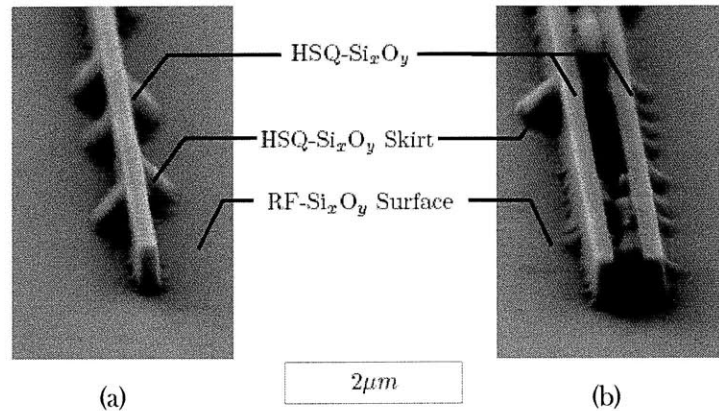
FIGURE 4.6: SEM (at 45°) image depicting HSQ-Si_xO_y submicron lines after gallium arsenide-on-insulator (e-beam) lithographic development.

Care must be taken to ensure proper development of HSQ features during the lithographic development subprocess. In Figure (4.6), both the submicron lines in close proximity, as well as the line in isolation, are shown to have undesired HSQ skirts along the length of the lines. Qualitative comparative analysis revealed that sample agitation was deterministic as to whether HSQ-Si_xO_y features would have HSQ skirts. During development, bubbles, which is indicative of exothermic reactions, were observed to gather at the edges of the patterned features. The bubbles were thought to inhibit the TMAH developer from diffusing to the non-crosslinked edges of the crosslinked HSQ during development which resulted in HSQ skirt features. So, unlike typical lithographic development, the development of e-beam exposed HSQ requires that the sample undergo ultrasonic agitation in order to prevent bubble formation and thus preventing the skirted edges from forming at the edge of the patterned features.

4.4.2   Reactive Ion Etch (RIE)

After the HSQ-Si_xO_y hard-mask is defined, the underlying MBE-grown GaAs/$Al_{1-x}Ga_xAs$ multilayer heterostructure film is patterned through the HSQ-Si_xO_y hard-mask to yield the ridge and mesa structures. The reactive ion etch (RIE) process is used to anisotropically etch the ridge and mesa structures into the MBE GaAs/$Al_{1-x}Ga_xAs$ film. The RIE process is required to be selective to both the AlGaAs and the GaAs materials over the SiO_2 material.

Since HSQ-Si_xO_y hard-mask is defined by e-beam lithography, mask integrity and pattern fidelity must be optimized in this instance. Typically, e-beam resists are used as a transfer mask to a more robust etch-mask before the substrate is patterned. The HSQ e-beam resist is an exception to that rule. Instead of HSQ being used as a transfer mask, upon being lithographically developed into HSQ-Si_xO_y, the HSQ-Si_xO_y is used as the etch-mask. As a result, in addition to optimizing the e-beam lithographic process to yield a high-fidelity HSQ-Si_xO_y pattern, the lithographic process must also be optimized to ensure that the HSQ-Si_xO_y can withstand the material subtraction process in which the HSQ-Si_xO_y is used as an etch mask.
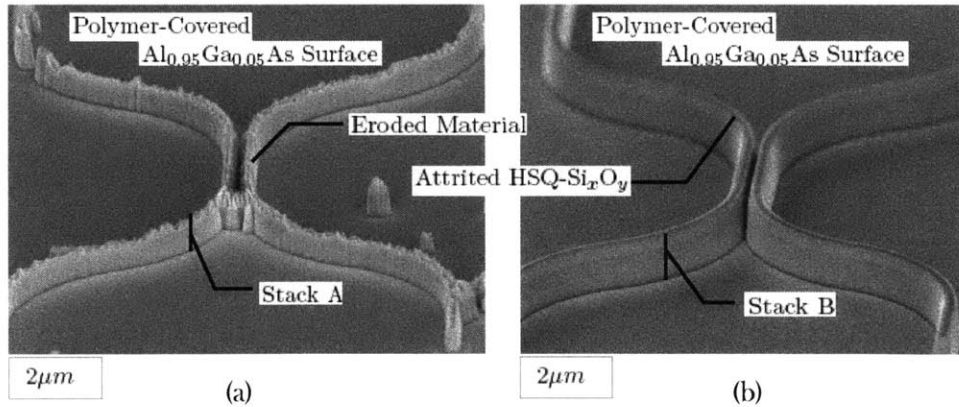
FIGURE 4.7: SEM (at 45°) images depicting two different Wafer A samples after undergoing the RIE process. During HSQ e-beam lithographic exposure, (a) a $360\mu C/cm^2$ and (b) a $849\mu C/cm^2$ e-beam dose was used to define the HSQ-Si_xO_y etch-mask that was used in the RIE process.

A visual comparison between Figure (4.7a) and Figure (4.7b) reveals the effect that the e-beam exposure dosage has on HSQ-Si_xO_y etch-mask robustness in the RIE material subtraction process.

Stack A		Stack B	
08	Eroded HSQ	08	Attrited HSQ
07	Eroded RF-SiO_2	07	RF-SiO_2
06	Eroded GaAs	06	$280nm$GaAs
05	$500nm\ Al_{0.85}Ga_{0.15}As$	05	$500nm\ Al_{0.85}Ga_{0.15}As$
04	Partially Etched $Al_{0.90}Ga_{0.10}As$	04	Partially Etched $Al_{0.90}Ga_{0.10}As$

At an e-beam dosage of $360\mu C/cm^2$, the post-development HSQ-Si_xO_y etch-mask was inspected to have impeccable pattern fidelity. However, upon being exposed to a $15min$ RIE process, the integrity of the HSQ-Si_xO_y etch-mask was visually observed (via SEM visual inspection) to be compromised. An e-beam exposure dosage increase from $360\mu m/cm^2$ to $849\mu m/cm^2$ was able to harden the HSQ-Si_xO_y etch-mask to the point where the integrity of the HSQ-Si_xO_y etch-mask was maintained during the RIE process. While, the increase in exposure dose is not observed to effect feature contrast, the increased dose does increase feature broadening. The increase in feature broadening is accounted for in the CAD design.

As an alternative to increasing the exposure dose in order to harden the HSQ-Si_xO_y pattern, a post-development bake could have been used. Haffner et al. [?] shows through experiment that a post-development bake (of $300°C$ or higher) of the HSQ-Si_xO_y pattern leads to the condensation reaction of the cage HSQ film structure to that of the network structure. As a result, the HSQ-Si_xO_y patterns are solidified and hardened.

After identifying the threshold of the e-beam exposure dose intensity which guarantees etch-mask robustness, the e-beam exposure dose must then be optimized in order to yield 90° sidewall ridges. As the waveguides of the electromechanical optical switches

are created from the etched ridges, sidewall verticality is critical to the optical perfor-
mance of the optical switches.

Variable concentrations of boron trichloride (BCl_3), argon (Ar) and dichlorine (Cl_2)
gases are used in the RIE process. Since the HSQ-Si_xO_y etch-mask has residual amount
of silicon carbon bonds within it, the HSQ-Si_xO_y will behave similar to a resin etch-mask.
As a result, the e-beam lithography process that was used to define the HSQ-Si_xO_y has
to be optimized conjointly with the etch chemistry of the RIE process.

A single-chamber parallel-plate reactive ion etch (RIE) apparatus (PlasmaTherm brand
system) was used to etch ridges into the $10mm \times 10mm$ patterned GaAs-substrate sam-
ples.

Before the samples were introduced into the RIE apparatus, the apparatus underwent a
pre-etch cleaning. Rotary and turbo pumps pumped the RIE process chamber to a base
pressure of $4 \cdot 10^{-5}Torr$. After reaching the $4 \cdot 10^{-5}Torr$ base pressure, the mass flow
controllers were used to regulate the flow rate of O_2 (flow rate: $15sccm$) and CF_4 (flow
rate: $30sccm$) as those gases were introduced into the process chamber. During gas in-
troduction to the chamber, the pressure in the chamber was stabilized to $26 \cdot 10^{-3}Torr$.
After chamber pressure stabilization, the cleaning plasma etch is initiated. The plasma
was created with a 450-volt DC bias voltage, a 110-volt auxiliary voltage, and $50W$ of
forward RF power with $0W$ being reflected. The cleaning etch lasts for 40 minutes.

Following the cleaning etch, the process chamber is vented to atmospheric pressure and
opened. There is no chemical pretreatment of the samples prior to being introduced to
the process chamber. One to three $10mm \times 10mm$ samples are loaded into the process
chamber at a time.

Once loaded, the process chamber is closed and again pumped to a base pressure of
$4 \cdot 10^{-5}Torr$. After reaching base pressure, the etch gas(es) (BCl_3, Cl_2, and/or Ar) are
introduced into the chamber. The combined flow rate of the gas(es) are stabilized to

$15sccm$ as the chamber pressure is minimized to $5 \cdot 10^{-3} Torr$. After the gas flow rate and pressure are stabilized, the glow discharge was initiated with a 500-volt DC voltage, 110-volt auxiliary voltage and $45W$ of forward RF power with $1.5W$ being reflected. This etch lasts for 15 minutes.
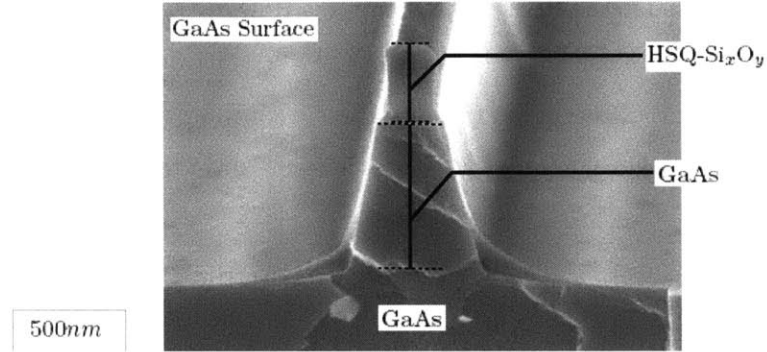
FIGURE 4.8: 45 tilted SEMS of three different cleaved samples after undergoing RIE processing with a boron trichloride (BCl_3), dichlorine (Cl_2) and argon (Ar) and flow ratio of $\frac{1}{3} \cdot BCl_3 : \frac{1}{3} \cdot Cl_2 : \frac{1}{3} \cdot Ar$.

For an RIE process which had an equal flow rates of Ar, Cl_2 and BCl_3 [Figure (4.8)], a GaAs ridge with slanted sidewalls resulted. The slanted sidewalls is conjectured to be the combined results of boron polymerization that is produced by the BCl_3 as well as the gas chemistry/ HSQ-Si_xO_y etch mask interactions. Notice that the HSQ-Si_xO_y etch mask is not compromised.
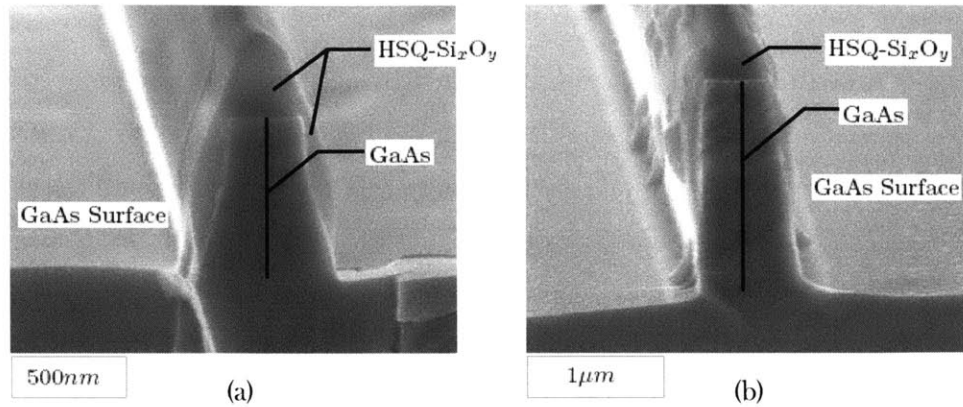
FIGURE 4.9: SEM (at 45°) images of two different cleaved samples after undergoing RIE processing with a flow concentrations of (a) $\approx 0 \cdot BCl_3 : \approx 0 \cdot Cl_2 : \approx 1 \cdot Ar$ and (b) $\approx 0 \cdot BCl_3 : \frac{1}{2} \cdot Cl_2 : \frac{1}{2} \cdot Ar$.

For an Ar-dominated flows [Figure (4.9a)], the HSQ-Si_xO_y was made to interact strongly with that gas chemistry.

For a RIE process which had equal flow rate concentrations of Ar and Cl_2 [Figure (4.9b)], a ridge with close to vertical sidewalls was produced. However, the HSQ-Si_xO_y etch mask was eroded, but not to the point where the top layer of GaAs was compromised.

The boron polymerization is thought to form a protective coating along the HSQ-Si_xO_y etch-mask during etching. All in all, the best verticality was achieved with an equal ratio of Cl_2 and Ar with a total flow rate of $15 sccm$ at a pressure of $15 mTorr$. The sidewall passivation from the HSQ-Si_xO_y reaction with the RIE gas chemistry was observed to be effective at preventing under-etching of the exposed ridge sidewall; passivation produced from the BCl_3 was not necessary.

After the ridge and mesa structures are etched into the GaAs/$Al_{1-x}Ga_xAs$ film, the HSQ-Si_xO_y etch mask is subsequently removed by undergoing another RIE process, an RIE process that is selective to the Si_xO_y material over the GaAs and the $Al_{1-x}Ga_xAs$ materials.

A dedicated single-chamber parallel-plate RIE apparatus for silicon-based etches is used to remove the HSQ-Si_xO_y etch mask from the $10mm \times 10mm$ reactive ion etched GaAs-substrate samples. Pressure stabilization and gas management is controlled entirely by a computer controlled system. By default, this RIE system is under base-pressure vacuum.

Before the samples are introduced into the RIE chamber, the chamber undergoes a pre-etch, cleaning etch. The chamber is evacuated by a turbomolecular pump backed by a mechanical pump, to the base pressure. After reaching base pressure, mass flow controller-managed tetrafluoro-methane (CF_4) and oxygen (O_2) gases are introduced into the chamber from the top through a showerhead nozzle. CF_4 and O_2 are passed through the chamber at $4sccm$ and $20sccm$, respectively, while the chamber is stabilized at $20 \cdot 10^{-3}Torr$. After pressure and flow rate stabilization, the 13.56-MHz RF power initiate a 123-W plasma glow discharge with a 294-V DC bias. The cleaning etch lasts for 10 minutes.

After the cleaning etch, the chamber is evacuated of all gases and open to atmospheric pressure. The previously-RIE processed 10mm x 10mm samples are loaded into the chamber one, two or three samples at a time. The chamber is again evacuated to the base pressure. After reaching base pressure, trifluoromethane (CHF_3) is delivered to the chamber at $15sccm$. The chamber is maintained at $10 \cdot 10^{-3}Torr$ at this point. The 13.56-MHz RF power initiates a 352-W etch plasma with a DC bias of $294V$. This etch typically lasts for 6 minutes.

4.5   AlGaAs Buried Oxide

All of the optical switch designs are based on high-index-contrast waveguides of two varieties: suspended ridge and (anchored) ridge waveguides. Particularly for the anchored ridge waveguides, high-index cores are required to have a lower cladding layer, a lower cladding of buried oxide. Unfortunately, for III-V material systems, high-quality native oxides cannot be readily grown. However, there are alternative methods for creating high-index-contrast waveguides in III-V material systems. The objective is to create III-V material-system compatible oxides analogous to the attributes of SiO_2 for the silicon material system: the oxides must be uniform, mechanically stable, and insulating.

4.5.1   Buried Oxide Creation Methods

III-V material systems are challenged by the fact that stable native oxide are not naturally occurring. Consequently, since buried oxide layer structures are central to high-index-contrast optics, other methods of producing high-index/low-index layered waveguide structures are required. For this project, the etched-ridge layer oxidation approach was employed. The etch-then-oxidize approach has the benefit of only requiring small volumes of $Al_{1-x}Ga_xAs$ material to be oxidized, which reduces the time required for oxidation. Specifically, $Al_{1-x}Ga_xAs$ layers are grown with the purpose of later converting those layers to a low-index oxide.

There are a number of ways to convert $Al_{1-x}Ga_xAs$ layers into oxide layers: thermal oxidation, anodic oxidation and liquid phase chemical-enhanced oxidation.

For thermal oxidation, $Al_{1-x}Ga_xAs$ is converted into an oxide as specific flowing gas vapors are made to react with that $Al_{1-x}Ga_xAs$ material inside of a heated chamber or tube. There are several varieties of thermal oxidation: dry-thermal oxidation, O_2-thermal oxidation and wet-thermal oxidation. Of the three methods, thermal oxidation has been demonstrated to yield the most stable, mechanically robust oxides without requiring a post anneal process [?], [?]. However, thermal oxides have been reported to

have inferior electrical properties due to the large amount of arsenic molecules trapped at oxide interfaces [?]. Note that thermal oxidation performed at the lower end of the temperature range leads to improved electrical properties.

Anodic oxidation involves the use of two electrodes. Anodic oxidation can either be performed in a electrolytic solution [?] or in a plasma [?] at room temperature. For anodic oxidation performed in an electrolytic solution, the resulting oxides are observed to be inhomogeneous whereas for anodic oxidation performed in a plasma, the resulting oxides are homogenous [?]. Compared to thermal oxides, anodic oxides have a lower arsenic pile-up at the interfaces, which translates into better electrical properties [?]. However, anodic oxides are noted for being unstable in air (at room temperature and atmospheric pressure) after undergoing oxidation [?]. Typically a post-oxidation high-temperature anneal (temperature:$\approx 300°C$, time $\approx 10min$) is performed in order to homogenize the oxide for improved stability. Also, the post-oxidation step leads to improved electrical properties as the width of the arsenic-accumulation regions decreases [?].

Liquid-phase chemical-enhanced oxidation (LPCEO), a near-room temperature oxidation process ($40°$-$70°C$), requires the use of a temperature regulator, a pH meter and an oxidation nitric acid solution containing gallium ions, deionized water and ammonia [?]. Of the three oxidation methods, liquid phase chemical-enhanced oxidation has faster reaction-limited linear oxidation rates. A post-oxidation high-temperature anneal is required in order to stabilize LPCEO-grown oxides.

The LPCEO is ostensibly the preferred method for fast large-scale oxidation. However, since relatively small volumes of aluminum-rich $Al_{1-x}Ga_xAs$ layers are to be oxidized, all of the oxidation methods can be adjusted for reasonable oxidation process time periods. Moreover, while anodic oxidation and LPCEO can be performed at room temperature, these two oxidation process will have similar thermal budgets to the other oxidation methods since post-oxidation anneals are required in order to stabilize the oxide layers. Consequently, any oxidation method can be used for the etch-then-oxidize buried

oxide process method. Specifically for this project, wet oxidation was used with the etch-then-oxidize process in order to create submicron-wide buried oxide layers.

4.5.2 AlGaAs Wet Oxidation

The science of $Al_{1-x}Ga_xAs$ wet oxidation is an inexact one and requires experimentation in order to properly characterize the process. There are many factors that govern the rate at which $Al_{1-x}Ga_xAs$ films oxidize. According to [66] and [?], the top six parameters, ordered from most to least important are:

01	Aluminum Content	x_{AlAs}
02	Oxidation Temperature	T_{ox}
03	Ridge Geometry	Ridge Width, Cartesian/Cylindrical
04	Oxidation Time	t_{ox}
05	Layer Thickness	h_{ox}
06	Ridge Spacing	g_{ox}

Also, oxidation-rate-dependent parameters that are associated with a particular oxidation set-up often go unreported: pre-oxidation processing (e.g., etching), pre-oxidation storage conditions and post-oxidation processing (e.g., sample staining).

Particular to this project, sparsely separated (g_{ox}) Cartesian submicron-wide $Al_{1-x}Ga_xAs$ ridge layers are to be oxidized. The oxidation temperature (T_{ox}) and aluminum concentration (x_{AlAs}) are selected so that the submicron-wide $Al_{1-x}Ga_xAs$ ridge layer can be oxidized on a $\approx$ 30-minute time scale.

Informed from the comparative analysis of available experimental data in Nakwask's seminal survey journal article [?], a $T_{ox} \approx 475°C$ and $x_{AlAs} \approx 0.70$ yields a initial oxidation rate of $B/A \approx 20nm/min$ [2]. Specifically, Nickel [67] reports a $B/A = 20nm/min \pm 10nm/min$ for $T_{ox} = 475°C \pm 25°C$, $x_{AlAs} = 0.78$ and $h_{ox} = 2\mu m$.

---

[2]Note that a $B/A \approx 20nm/min$ is appropriate for this project since oxidation occurs on both sides of the etched ridge which requires only approximately $150nm$-wide layers of $Al_{1-x}Ga_xAs$ material to be oxidized.

Contrast the oxidation conditions of Nickel [67] with those of Geib [?]. Geib reports a $B/A = 40nm \pm 50nm$ for a $T_{ox} = 400°C \pm 25°C$, $x_{AlAs} = 0.98$ and a $h_{ox} = 66.4nm$. Together, the distinction in the aforementioned oxidation parameters as well as the other experimental oxidation data presented in Nakwaski's article [?] suggest that (1) the $Al_{1-x}Ga_xAs$ layer thickness should be of a requisite thickness ($h_{ox} > 30nm$) in order to establish uniform oxidation, (2) lower x_{AlAs} values in the range of $0.78 \gtrsim x_{AlAs} \gtrsim 0.48$ are slow to oxidize, (3) lower x_{AlAs} values in the range of $0.78 \gtrsim x_{AlAs} \gtrsim 0.48$ require higher T_{ox} in order to oxidize and (4) lower x_{AlAs} values in the range of $0.78 \gtrsim x_{AlAs} \gtrsim 0.65$ have a B/A which is less effected by T_{ox} fluctuations.
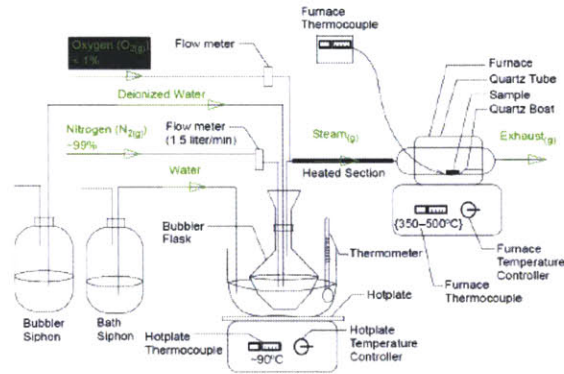
FIGURE 4.10: Diagram detailing the constituent parts of the in-house oxidation apparatus that was used for selective wet oxidation of $Al_{1-x}Ga_xAs$.

Experimental Set-up.

Figure (4.10) shows a diagram of the in-house wet oxidation apparatus. The water flow portion of the wet oxidation system consists of a bubbler siphon, a bath siphon, a bubbler flask, a bath water container, a hotplate, and thermometer and water flow tubing. The bubbler siphon feeds deionized water into the bubbler flask and the bath siphon feeds water into the container in which the bubbler flask is situated. The container sits atop the hotplate. A thermometer is submerged inside the bath water of the container in order to measure the temperature of the bath water. The gas flow portion of the wet oxidation

system consists of a nitrogen source, a flow meter, the bubbler flask, a quartz tube, and gas flow tubing which includes a section of tubing heated by a wrap-around heating strip. Nitrogen flows through the flow meter which controls the flow rate of the nitrogen into the bubbler flask. The nitrogen has a flow rate of $\sim 1.5 liter/min$ to ensure that it is above the saturation threshold at the oxidation temperatures [68]. An oxygen feed is also pictured with a black background. Note that the in-house wet oxidation system did not have an oxygen feed; the oxygen feed is there to clarify the discussion of the generalized wet oxidation process. From the flow meter, nitrogen flows into the bubbler flask where the nitrogen bubbles up through the heated deionized water. The resultant nitrogen/water vapor mixture flows through a heated tubing. Heating tape is wrapped around a quartz tube (heated tubing) in order to prevent condensation. Condensation affects the nitrogen/water vapor flow which affects oxidation rates. From the heated tubing, the nitrogen/water vapor is led into the heated quartz tube. Finally, the steam exits the quartz tube as exhaust. The water bath is set at approximately $90°C$ and the furnace is set at approximately $400°C$. The furnace temperature is process-critical, while the water bath temperature is allowed to vary by a few degrees.[3]

The Process

Selective wet oxidation involves three basic steps:

1   Gas Transport

2   Material/Gas Reactions

3   By-Product Transport

The delivery of the reactants to/into the $Al_{1-x}Ga_xAs$ film can be describe by the Deal and Grove model [69]:

$$t = \frac{w_{ox}^2}{B} + \frac{w_{ox}}{B/A} \tag{4.1}$$

---

[3]Note that since the publication of this document, the container/hotplate portion of the oxidation set-up has been replaced with a digital water bath. With the water bath, the temperature is fairly stable.

where at time t, the thickness of the oxide film, w_{ox}, can be derived from a parabolic rate constant B and a linear rate constant B/A. Depending upon the evolving thickness of the oxidation front, the Deal-Grove model can be adequately described as $t_{txn} = \frac{w_{ox}}{B/A}$ for thin oxides and $t_{diff} = \frac{w_{ox}^2}{B}$ for thick oxides.

Figures (4.11) and (4.12) shows the two regimes of oxide evolution for a ridge [Figures (4.11a)] and a mesa [Figure(4.12)a)] structure.

(a)   (b)
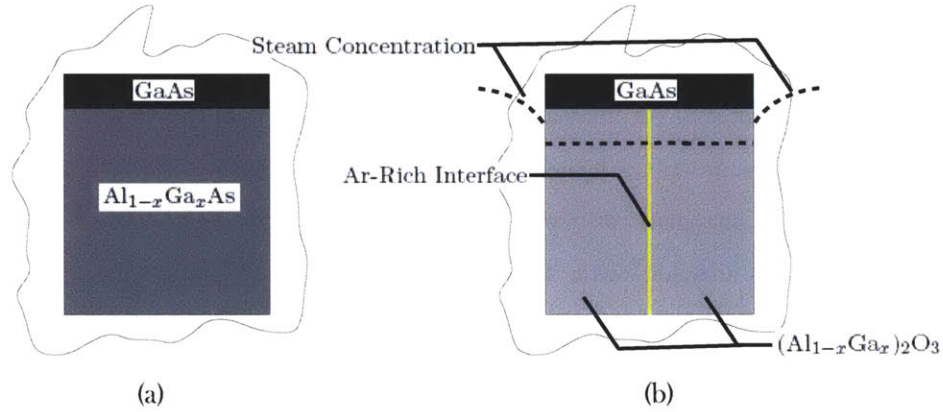
FIGURE 4.11: Schematic illustration of reaction-limited case for selective wet oxidation of an $Al_{1-x}Ga_xAs$ layers.

Consider Figure (4.11): the ridge structures that serve as the anchored high-index-contrast waveguides are designed to be fully oxidized. Essentially, the concentration of aluminum in the initially-grown AlGaAs lower cladding and the width of the anchored waveguide creates the condition where oxidation proceeds at a reaction-limited linear rate until that lower cladding is fully oxidized.
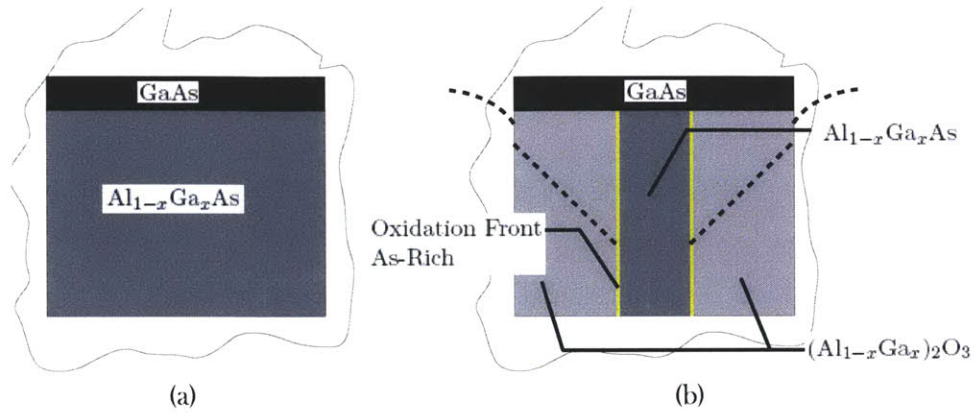
FIGURE 4.12: Schematic illustration of the selective oxidation process of $Al_{1-x}Ga_xAs$ layers. (a) Beginning ridge structure in an ambient of steam. (b) Partially oxidized ridge structure after undergoing diffusion-limited oxidation at a parabolic rate.

Naturally, wider ridge structures will not be fully oxidized on the same time scales as the narrow ridge structures that are used for the anchored waveguides. In fact, after an extended time, oxidation proceeds at a diffusion-limited, parabolic rate [Figure(4.12)]; oxidation proceeds at a reduced rate. Together, topological specification and oxidation-dynamics control can be effectively used to form two extremely different ridge structures within the same layer plane; robust mechanical anchors (AlGaAs-heterostructure ridges) can be formed right next to (anchored) High-Index-Contrast waveguides (AlGaAs-on-oxide submicron-width ridge structures).

Figure(4.12b) is an illustration of a post-oxidation ridge that could be used as a MEMS anchor. A portion of the AlGaAs lower cladding layer is oxidized while the center section of that layer remains as AlGaAs. During the sacrifical etch, the oxide will etch, the AlGaAs will not. As a result, a pedestal MEMS anchor will be created, a pedestal MEMS anchor of a specific width (and length).

Since the oxidation times are relatively short and the $Al_{1-x}Ga_xAs$ layers in the etched ridge structures have a submicron width, the oxidation front generally proceeds at a linear growth rate in the temperature range of $350°C$-$500°C$ [70]. Since the volume of the targeted $Al_{1-x}Ga_xAs$ layers are relatively small, no intrinsic defects or voids are

created during the oxidation process [70]. As a result, material contraction creates the thin-film stress.

In order to understand the chemical reactions that occur during selective oxidation, consider the various thermodynamically-favorable [at $T = 698K(425°C)$] reactions of AlAs and GaAs solid (s) materials with only O_2 gas (g) present:

$$2AlAs_{(s)} + 3O_{2(g)} \rightarrow Al_2O_{3(s)} + As_2O_{3(l)} \qquad \Delta\mathbf{G}^{698} = -1729kJ/mol \qquad (4.2)$$

$$2AlAs_{(s)} + 4O_{2(g)} \rightarrow Al_2O_{3(s)} + As_2O_{5(l)} \qquad \Delta\mathbf{G}^{698} = -1821kJ/mol \qquad (4.3)$$

$$2GaAs_{(s)} + 3O_{2(g)} \rightarrow Ga_2O_{3(s)} + As_2O_{3(l)} \qquad \Delta\mathbf{G}^{698} = -1246kJ/mol \qquad (4.4)$$

$$2GaAs_{(s)} + 4O_{2(g)} \rightarrow Ga_2O_{3(s)} + As_2O_{5(l)} \qquad \Delta\mathbf{G}^{698} = -1338kJ/mol \qquad (4.5)$$
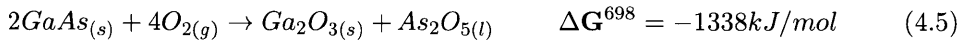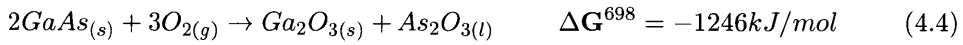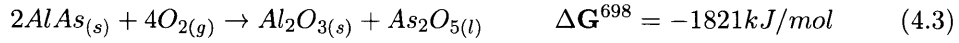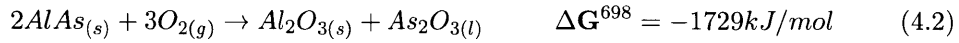
and the reaction [71], [?] of AlAs (s) and GaAs (s) materials with only (N_2 + H_2O) (g) present:

$$2AlAs_{(s)} + 6H_2O_{(g)} \rightarrow Al_2O_{3(s)} + As_2O_{3(l)} + 6H_{2(g)} \quad \Delta\mathbf{G}^{698} = -473kJ/mol \quad (4.6)$$

$$2AlAs_{(s)} + 8H_2O_{(g)} \rightarrow Al_2O_{3(s)} + As_2O_{5(s)} + 8H_{2(g)} \quad \Delta\mathbf{G}^{698} = -149kJ/mol \quad (4.7)$$

$$2GaAs_{(s)} + 6H_2O_{(g)} \rightarrow Ga_2O_{3(s)} + As_2O_{3(s)} + 6H_{2(g)} \quad \Delta\mathbf{G}^{698} = +10kJ/mol \quad (4.8)$$

$$2GaAs_{(s)} + 8H_2O_{(g)} \rightarrow Ga_2O_{3(s)} + As_2O_{5(s)} + 8H_{2(g)} \quad \Delta\mathbf{G}^{698} = +334kJ/mol \quad (4.9)$$

$$As_2O_{3(l)} + 3H_2 \rightarrow 2As + 3H_2O_{(g)} \qquad \Delta\mathbf{G}^{698} = -131kJ/mol \quad (4.10)$$

$$As_2O_{3(l)} + 3H \rightarrow 2As + 3H_2O_{(g)} \qquad \Delta\mathbf{G}^{698} = -1226kJ/mol$$

$$(4.11)$$
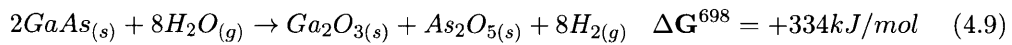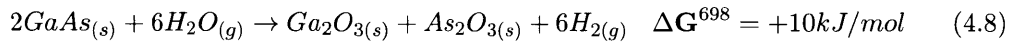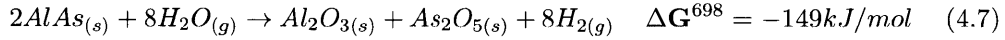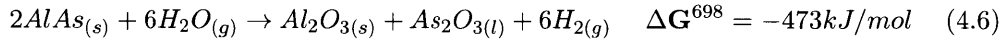
The conventional method to selectively oxidize $Al_{1-x}Ga_xAs$ is to use $N + H_2O$ (wet oxidation) in order to oxidize an aluminum-rich $Al_{1-x}Ga_xAs$ layer. The reactions in Equations (4.8) and (4.9) are not energetically favorable, therefore GaAs is unlikely to be converted to Ga_2O_3. In fact $Al_{1-x}Ga_xAs$ ($x > 0.15$) have been experimentally

verified to undergo extremely slow oxidation rates. Essentially, the reactions in Equations (4.6) and (4.7) are the primary reactions involved during wet oxidation; $Al_2O_3(s)$, $As_2O_3(s)$, $As_2O_3(l)$, and $H_2(g)$ are produced during wet oxidation. As the delivered water vapor continues to drive the oxidation process, the secondary reactions as describe by Equations (4.10) and (4.11) occur: As_2O_3 is either removed from the AlGaAs layer as an arsine hydride vapor [AsH_3 (g)] or converted into an arsenic precipitate, where it is incorporated into the growing oxide. Of the two chemical reactions, the conversion to arsenic is the more energetically favorable. Unfortunately, the converted arsenic often migrates to layer interfaces and creates surface defects.

Although not used in the in-house oxidation set-up, the addition of $< 1\%$ of pure oxygen can be used to drive GaAs reactions. Oxygen is sometimes used in order to create a competing reaction with the atomic hydrogen in order to remove the possibility of surface defects, thus leaving the As_2O_3 within the Al_xO_y film. The energetically favorable reaction is for the gallium in a $Al_{1-x}Ga_xAs$ film to form a gallium hydroxide (GaH) vapor. Another energetically favorable reaction is for the gallium to form a gallium oxide (Ga_xO_y) in a lesser amount and become incorporated into the Al_xO_y film.

Ridge Anchor Integrity

FIGURE 4.13: Schematic illustration of a two-layer heterostructure ridge during a linear reaction-rate limited oxidation.

Figure (4.13) shows the various oxide types that could result during wet-oxidation of high-aluminum ($x < 0.15$) $Al_{1-x}Ga_xAs$. As the oxidation front progresses in the linear reaction-rate limited, a porous amorphous aluminum oxide (AlO_xH_y) results. However, a thin ($< 10nm$) dense amorphous oxide is also created directly behind the evolving oxide front [70]. This dense oxide is composed of aluminum oxide (Al_2O_3) and arsenic oxide (As_2O_3). During oxidation, the oxidation temperature and the adsorbed and dis-associated water makes arsenic highly mobile within the film and is either converted into As_2O_3 or migrates towards interfaces or becomes interstitially incorporated in the oxide matrix as elemental arsenic [72].

In addition to the porous and the dense oxide films, a polycrystalline oxide film can also be produced. High temperature oxidations as well as post-oxidation annealing and even prolonged exposure to imaging electron beams (e.g., SEM imaging) can produce a thin crystalline Al_2O_3 oxide. A polycrystalline oxide is best avoided in order to maintain structural integrity since oxides formed from $Al_{1-x}Ga_xAs$ films have been experimen-tally observed to undergo a 20% size contraction.[73].

Sidewall Smoothing. In addition to the complete chemical conversion of $Al_{1-x}Ga_xAs$, having a large percentage of aluminum to Ox-Al_xO_y, an $Al_{1-x}Ga_xAs$ alloy material with a low amount of aluminum ($Ga_xAl_{1-x}As$) can also be converted to Ox-Al_xO_y by intro-ducing $< 1\%$ of oxygen gas into the oxidation furnace. Oxygen is able to drive the energetically-favorable chemical reactions given in Equations (4.4) and (4.5). The pres-ence of oxygen is able to oxidize gallium-rich $Al_{1-x}Ga_xAs$ layers as high as $x = 80\%$ [16]. Oxidation smoothing can also provide a possibility of reducing optical loss by reducing sidewall roughness as well as providing a diffusive means of creating gradual index dis-tributions [13]. In [74], a 10 - 100 fold reduction in sidewall roughness [from 50 nm - 100 nm to 1 nm - 2 nm] was experimentally observed for a laterally-oxidized (with 0.7% oxygen at 450°) $Ga_{0.7}Al_{0.3}As$ layer that was initially formed into a ridge structure by an inductively-coupled, plasma RIE-process.

Experiment

All of the widely-spaced oxidized submicron Cartesian ridge test structures are created by reactive ion etching a MBE-grown AlGaAs layer stack through a mask of e-beam-patterned HSQ-Si_xO_y. While some of the RIE-processed ridges undergo an additional RIE process in order to remove the HSQ-Si_xO_y etch mask, the samples that will be presented did not.

Prior to oxidation, samples are stored in a non-clean room laboratory for a few days with a maximum storage time of a week. Directly prior to oxidation, the samples are not exposed to any wet etches in order to remove any particulates or oxides that may have accumulated during storage.[4].

Note that all of the scanning electron micrographs (SEMs) of the oxidized samples did not undergo any pre-SEM imaging processing, which includes the standard gold sputtering routinely used for improved SEM imaging[5]

Figure (4.14) shows two SEM images of two different heterostructure samples having etched ridge structures in a (nonfunctional) directionally-coupled waveguide configuration.

---

[4]Some experimentalists use a 1:4 hydrochloric acid: water ($HCl:H_2O$) *etched-surface-freshening* wet etch process [75] prior to oxidation

[5]Note that a ($\sim$ 5-*min*) etch staining [a wet etch in 1:1:10 hydrochloric acid:hydrogen peroxide:water ($HCl:H_2O_2:H_2O$)] is another method that can be used in order to enhancing SEM imaging specifically for AlGaAs-oxidized samples [75].
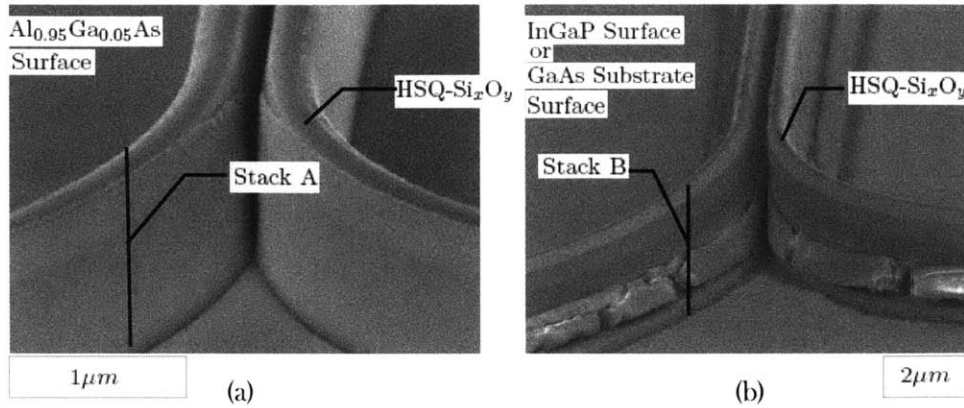
FIGURE 4.14: 45° tilted SEMS of two different heterostructure samples with ridge structures: (a) a sample after undergoing a 15*min* RIE process and (b) a sample after undergoing a 30min oxidation process.

Stack A		Stack B	
08	$< 450nm$ Attrited HSQ-Si$_x$O$_y$	08	$< 450nm$ Attrited HSQ-Si$_x$O$_y$
07	$10nm$ RF-sputtered SiO$_2$	07	$10nm$ RF-sputtered SiO$_2$
06	$280nm$ GaAs	06	$280nm$ GaAs
05	$500nm$ $Al_{0.85}Ga_{0.15}As$	05	$500nm$ $Ox - Al_xO_y(Al_{0.85}Ga_{0.15}As)$
04	Partially-Etched $Al_{0.90}Ga_{0.10}As$	04	$500nm$ $Ox - Al_xO_y(Al_{0.90}Ga_{0.10}As)$
		03	$1\mu m$ $Ox - Al_xO_y(Al_{0.95}Ga_{0.05}As)$
		02	$20nm$ $Ox - Al_xO_y(AlAs)$
		01	$100nm$ InGaP
		00	Partially-Etched GaAs Substrate

Prior to oxidation, a $5mm \times 5mm$-Wafer-A sample in Figure (4.14a) has just undergone a 15-*min* RIE (composite etch rate: $55nm/min$–$60nm/min$)[6]; the GaAs and Al$_{0.85}$Ga$_{0.15}$As layers are etched, the Al$_{0.90}$Ga$_{0.10}$As is partially etched. According to the reports in literature, the Al$_{0.90}$Ga$_{0.10}$As layer should have been oxidized in its entirety; the Al$_{0.85}$Ga$_{0.15}$As layer may not have been entirely oxidized.

---

[6]Note that there was a $\approx$ 10-*nm* thick HSQ-Si$_x$O$_y$-etch mask adhesion promotion layer, RF-Si$_x$O$_y$, on the sample's surface.

Figure (4.14b) is an SEM image of a different $5mm \times 5mm$-Wafer-A sample, after undergoing two consecutive oxidations. Prior to the oxidations, the sample in Figure (4.14b) has undergone an ≈ 20-min RIE (composite etch rate: $120nm/min$–$130nm/min$). Notably all six heterostructure layers (GaAs/ $Al_{0.85}Ga_{0.15}As$/ $Al_{0.90}Ga_{0.10}As$/$Al_{0.95}Ga_{0.05}As$/AlAs/InGaP) are observed to be etched.[7] Chamber conditioning is postulated as the chief cause in the etch rate discrepancy.

Pei-Cheng Ku and Connie J. Chang-Hasnain describes AlGaAs wet oxidation as a *"one-shot" deal*: a process that cannot be repeated to fine-tune the oxide depth since repeated oxidation leads to oxide film delamination [66]. Indeed, in Figure (4.14b), the lowest layers of oxide–the oxide layers that were created from the $Al_{0.95}Ga_{0.05}As$ and AlAs starting layers are compromised. In contrast, the oxides that were created from the $Al_{0.90}Ga_{0.10}As$ and $Al_{0.85}Ga_{0.15}As$ layers appear to not have been compromised. Comparing the mechanically integrity of each of the oxide layers suggests that oxide delamination that are created from multi-run oxidations can be mitigated by lowering the aluminum content of the starting layer.
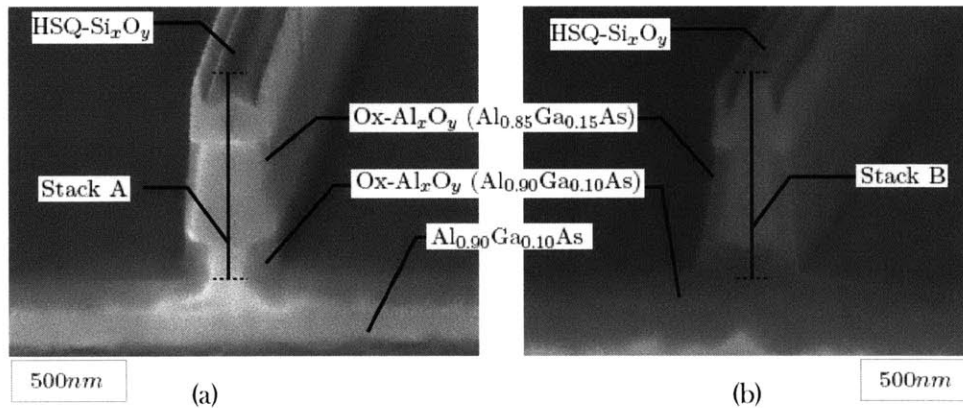
FIGURE 4.15: 45° tilted SEMS of two different cleaved Wafer A samples after undergoing the material conversion subprocess of $Al_{1-x}Ga_xAs$ alloy oxidation: (a) a $10min$ and (b) a $20min$ oxidation time.

---

[7]Visual inspection of Figure (4.14b) seems to indicate that the InGaP etch-stop material has been etched and the GaAs partially etched since all of the aluminum-rich layers are observed to be oxidized while the very bottom of the ridge is not oxidized. Either the very bottom is the InGaP layer or the GaAs wafer. The breach in the RIE-stop layer is speculated to be the result of unintentional RF sputtering with high-energy argon species used in the low-pressure RIE.

Stack A		Stack B	
04	Eroded HSQ	04	Eroded HSQ
03	RF-SiO$_2$	03	RF-SiO$_2$
02	GaAs	02	GaAs
01	500nm Al$_{0.85}$Ga$_{0.15}$As	01	500nm Ox-Al$_x$O$_y$ (Al$_{0.85}$Ga$_{0.15}$As)
00	Partially-Etched Al$_{0.90}$Ga$_{0.10}$As	00	Ox-Al$_x$O$_y$(Partially-Etched Al$_{0.90}$Ga$_{0.10}$As)

Further evidence of the effect of the alloy composition of the Al$_{1-x}$Ga$_x$As material on the oxidation rate is shown in the two SEMs of Figure (4.15). Particularly for the sample that is shown in Figure (4.15), the oxidation furnace was set to 400°C, the bubbler bath temperature was set to 90°C. Both the furnace and the bubbler bath were allowed to stabilized at those temperatures for at least 45min. After temperature stabilization, the quartz boat was extracted from the furnace (the quartz boat stayed inside the furnace during the temperature ramp). A sample having a submicron-width ridge was then place inside of the quartz boat which was again reintroduced into the furnace. The sample stayed inside the furnace for 10 minutes. Upon examination of the cross sections of the ridge structures, slight gradients of the $Al_{1-x}Ga_xAs$ alloys allow the oxidation fronts to proceed at vastly different rates. In these particular etches, the prior RIE process was able the reveal a heterostructure down to the $Al_{0.90}Ga_{0.10}As$ layer; the $Al_{0.90}Ga_{0.10}As$ layer is only etched partially. In Figure (4.15a) the two countervailing oxidation fronts in the $Al_{0.90}Ga_{0.10}As$ layer are yet to meet in the middle, while in Figure (4.15b), the oxidation fronts meet, thus forming a contiguous $O_x - Al_xO_y$ oxide. Incidentally, as indicated by Figure (4.15a), the oxidation front developed on the edge of the $Al_{0.90}Ga_{0.10}As$ ridge layer and on the $Al_{0.90}Ga_{0.10}As$ surface are seen to proceed at the same rate. The $Al_{0.85}Ga_{0.15}As$ layer experiences a markedly slower oxidation rate. Such a disparity in oxidation fronts highlights the importance of maintaining tight control over the alloy composition over an entire GaAs wafer during the Structural and Process Film Definition Process in order to make the gallium arsenide-on-insulator-technology-based electromechanical optical switches viable for manufacture. On the other hand, instead of being considered a liability, the alloy-dependant oxidation progression can be used to create symmetric ridge waveguides with customized cross-sections.

4.6 Sacrificial Etching

In general, either wet and dry isotropic etches can be used in order to micromachine freestanding semiconductor features. Wet sacrificial isotropic etching requires the use of an etchant-removal and a dry subprocess after the wet sacrificial etch in order to prevent fabrication stiction between the freestanding beam surfaces to the closely spaced rigid surfaces. Stiction is permanent and renders freestanding beams inoperable. Recent studies have identified solid bridging, liquid bridging, van der Waal forces, and electrostatic forces as the chief causes that leads to stiction [?]. Naturally, dry sacrificial etch processing only requires an etchant removal subprocess since there are no liquids used during the etch. A variety of wet sacrificial etch chemistries are available in order to selectively remove the bottom-most supportive process materials from underneath the to-be-released top-most functional materials. Particularly for the oxide bottom-most supportive material/semiconductor top-most material configuration, the most common wet sacrificial isotropic etch is hydrofluoric (HF) acid. Several rinse-and-dry methods are typically used in conjunction with the wet sacrificial isotropic etching: evaporation drying, sublimation drying, supercritical drying, and surface modification and evaporation drying [?]. Conversely, two dry sacrificial isotropic etch processes are available: low-pressure reactive ion etch- (RIE-) based processing [?], [?], [?], [?], [?] and vapor phase etch- (VPE-) based processing [?]. Particularly for the oxide bottom-most supportive material/semiconductor top-most material configuration, the newly developed HF VPE dry sacrificial isotropic etch has shown promising results. So much so that the newly developed HF VPE dry sacrificial isotropic etch has led to the development of commercially-available dedicated HF VPE apparatuses [?], [?].

Incidentally, SiO_2 can be etched under a wide range of HF VPE settings since the SiF_4 etch-product, having a boiling point temperature of $-86°C$, is easily desorbed whereas Al_2O_3 has been observed to be only etched at high reaction pressures since the AlF_3 etch product, having a sublimation temperature of $1291°C$, requires more energy for desorption [76].

Regardless of the shortcomings highlighted, the release process that was used in Process P1 and P2 becomes instructive as to how a liquid-based sacrificial etch affects the quality of the resultant submicron suspended beams. Specifically, the Suspended Structure Definition subprocess utilizes a nitric-acid wet etch which is preferentially selective to materials containing aluminum (i.e., $Al_{1-x}Ga_xAs$) over gallium arsenide (GaAs), photoresist (NR7-1000), and silicon dioxide (HSQ-Si_xO_y).
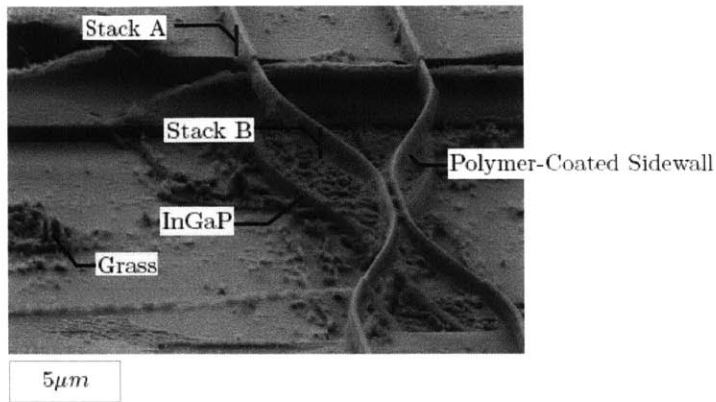
FIGURE 4.16: 45° tilted SEMS of a heterostructure sample after undergoing subprocess step 4 of Process P1

Several problems are readily identifiable upon examining Figures (4.16) and (4.17). One of the major problems is that the recession of the etchant under the mesa on which the ridge anchor (waveguide) sits atop. Clearly, the nitric acid has undercut the ridge anchor mesa and has not only etched the $Al_{0.95}Ga_{0.05}As$ layer but also etched the $Al_{0.90}Ga_{0.10}As$ layer.

Stack A		Stack B	
08	$450nm$ HSQ	08	$450nm$ Attrited HSQ
07	$10nm$ RF-SiO$_2$	07	$10nm$ RF-SiO$_2$
06	$280nm$ GaAs	06	$280nm$ GaAs
05	$500nm$ $(Al_{0.85}Ga_{0.15}As)$	05	Partially-Etched $(Al_{0.85}Ga_{0.15}As)$
04	Partially Etched $Al_{0.90}Ga_{0.10}As$	04	Partially Etched $Al_{0.90}Ga_{0.10}As$

The etched $Al_{0.95}Ga_{0.05}As$ layer creates a cantilevered mesa on top of which the ridge anchor structure resides. Moreover, the etched $Al_{0.95}Ga_{0.05}As$ layer is eroded which undoubtedly compromises the robustness of the ridge anchor structure. Less disastrous but equally as undesirable, the surface of the cantilevered mesa shows signs of photoresist debris. In the trench area, stalagmite-like material (i.e., grass) is seen cloistered around

the lower nitric acid-resistant InGaP layer which was originally apart of the ridge structure that was etched during the Sheathed Ridge, Ridge, and Mesa Definition subprocess. Incidentally, the InGaP layer was first exposed in the prior Sheathed Ridge, Ridge, and Mesa Definition subprocess (a second RIE process).

GaAs Surface

HSQ-Si_xO_y

Stack A

$5\mu m$
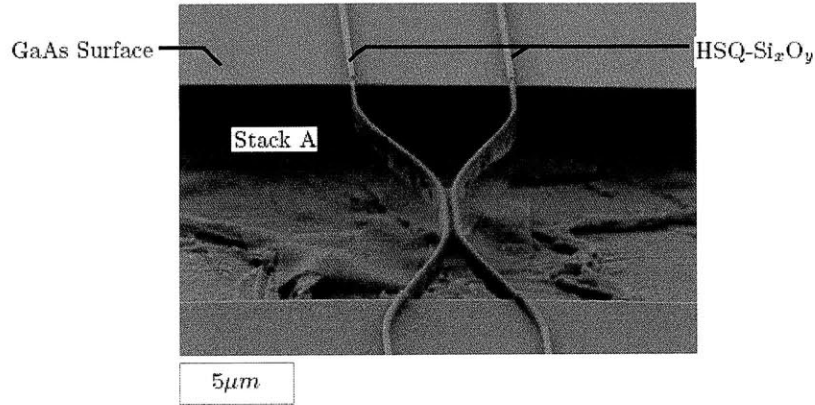
FIGURE 4.17: 45° tilted SEMS of a heterostructure sample after Al_xO_y undercutting.

Stack A	
08	$450nm$ Attrited HSQ
07	$10nm$ RF-SiO$_2$
06	$280nm$ GaAs
05	Partially-Etched/ Corroded $Al_{0.85}Ga_{0.15}As$
04	Partially Etched/ Corroded $Al_{0.90}Ga_{0.10}As$

Upon examination of Figure (4.17), Process P2 raises two important fabrication aspects. First, unlike the photoresist atop of the $Al_{1-x}Ga_xAs$ surface in Figure (4.16), the photoresist atop a GaAs surface is much easier to remove after undergoing a low-pressure RIE process. No discernible photoresist debris is present.

Such a result would seem to suggest that the NR7-1000 negative photoresist etch-mask has a stronger affinity to the previously etched $Al_{1-x}Ga_xAs$ surface than it does to the freshly-grown GSMBE GaAs surface. A reasonable assessment would state that during the Sheathed Ridge, Ridge and Mesa Structure Definition subprocess of Process P1–particularly during the RIE process–the exposed $Al_{1-x}Ga_xAs$ surface has a texture

and/or a chemical structure which allows the photoresist mask to strongly adhere to the $Al_{1-x}Ga_xAs$ surface. Following this logic, a surface that has not been etched would better prohibit a photoresist mask from adhering to that surface. Therefore, a freshly deposited/grown surface provides the best type of surface to avoid the difficulty in the removal of a photoresist etch-mask after a sample undergoes an RIE process. Indeed, the PECVD-SiO$_2$ that was deposited during the Sheathed Ridge Structure Definition subprocess (in the final process sequence) functions as a structural film as well as a process film. Should the PECVD-SiO$_2$ film undergo an RIE process, the PECVD-SiO$_2$ can be used as not only as the etch-mask to the underlying semiconductor films, but the PECVD-SiO$_2$ would make the top-most photoresist intermediate etch-mask easier to remove.

Again, as seen in Figure (4.16), the anchor ridge structures reside on not only a mesa but on a cantilevered mesa since the wet etchants attacked the $Al_{0.95}Ga_{0.05}As$ layer in the heterostructure mesa stack. This issue is remedied in the final process sequence as the $Al_{0.95}Ga_{0.05}As$ layer is first converted to Ox-Al$_x$O$_y$ before sacrificial etch processing commences. Essentially, while submicron width ridges will be completely oxidized, the *thicker-width* mesa structures will only be partially oxidized. As a result, the wet etchants that were used to release the submicron beams will only create a tractable submicron undercuts the partially-oxidized mesa.

4.6.1   Atomic Layer Deposition

Originally developed as a dielectric gate oxide for microelectronics, atomic layer deposited alumina (Al$_2$O$_3$) films have seen application as a protective coating [77], a creep-suppressant coating [?] and a wear-resistant coating [78]. Now, the optical switches that are presented in this thesis utilize atomic layer deposited Al$_2$O$_3$ coatings in an optical capacity.

In general, the atomic layer deposition (ALD) process allows users to deposit films with an angstrom level of accuracy. This angstrom level accuracy is made possible

due to the growth chemistry dynamics of the ALD process–a process that uses sequen-
tial, self-limiting surface reactions in order to build up films one layer at a time [?], [79].

A specified in [80], one popular method for depositing a conformal coating of Al_2O_3
around free-standing (and ridge) structures involves the injection of trimethylaluminum,
$Al(CH_3)_3$,(TMA) and water (H_2O)[?], delivered via nitrogen, carrier gas, into a heated
reaction chamber under vacuum conditions.

Specifically for depositing ALD-Al_2O_3 on GaAs surfaces, the GaAs surface is first hy-
droxylated. Hydroxylation (i.e., enriching the GaAs surface with OH radicals), as pro-
posed by Huang et al ([?], [?], can be accomplished by exposing GaAs to ammonia.
Once hydroxylated, the ALD-Al_2O_3 is formed by the two half-reactions:

$$GaAs - OH_{(s)} + Al(CH_3)_{3(g)} \rightarrow GaAs - O - Al(CH_3)_{2(s)} + CH_{4(g)} \qquad (4.12)$$

$$GaAs - O - Al(CH_3)_{2(s)} + H_2O \rightarrow GaAs - O - Al(CH_3)OH_{(s)} + CH_{4(g)} \qquad (4.13)$$
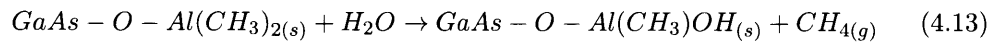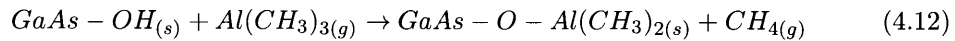
The growth cycle involves the reaction given in Equation (4.12): TMA $(Al(CH_3)_{3(g)})$
is carried via a nitrogen carrier gas into the reaction chamber in order for that gas to
interact with the hydroxylated GaAs surface $(GaAs - OH_{(s)})$. The interaction between
TMA and the GaAs surface is thermodynamically favorable, exothermic by $52.0 kcal/mol$
[?]. After the first growth cycle, the surface is now terminated with a $Al - CH_3$ group.
The first growth cycle is ended with an inert-gas chamber purge. For the second growth
cycle, water vapor infused nitrogen is then streamed into the reaction chamber in order
to interact with the $Al - CH_3$-rich surface, again enriching the surface with -OH [?].
The second growth cycle ends with an inert-gas chamber purge. The process starts again
with the TMA infused nitrogen delivered to the reaction chamber. A typical deposition
rate for ALD-Al_2O_3 is about $0.5 nm/min$ $(0.13 nm/cycle)$ at $175°C$ [?].

4.6.1.1 Atomic Layer Deposition of the Coat Cladding

Following the sacrificial release of the nanobeams, the nanobeam surfaces are to be cleared of native oxides and hydroxylated directly prior to being introduced into the ALD reaction chamber. Incidently, following the deposition of the coat cladding, the samples can remain in the reaction chamber in order to be treated with a nanometer-order self-assembled monolayer coating in order to improve upon wear resistance and stiction prevention should the ALD-Al_2O_3 coat cladding prove to be insufficient in those capabilities.

4.7 Summary

This chapter presented a flexible wafer process sequence which is catered to the creation of all seven electromechanical optical switches in the gallium arsenide-on-insulator material system. The process sequence begins with the Structural and Process Film Definition process: several epitaxially-grown film layers were specifically chosen to define the x-axis refractive-index distribution for the HIC waveguides. Incidentally, and to a major benefit to the fabrication of the electromechanical optical switches, the Structural and Process Film Definition process of epitaxial growth produces films with tractable interfacial stress. Following the Structural and Process Film Definition process, the ensuing processes are used to define the y-axis refractive index for both the anchored and suspended waveguides. The core inside the anchored and suspended waveguides and the lower cladding of the anchored waveguide is defined during the Ridge and Mesa Structure Definition process. The Sheathed Ridge Structure Definition process concludes the fabrication of the anchored waveguide while the Suspended Beam Definition process concludes the fabrication of the suspended waveguide.

The task of creating the suspended waveguide for electromechanical actuation occurs in two steps. The first step happens during the Electrical Pad and Wire Definition process which is used to reserve sections for electrical conduction on top of the freshly grown GaAs core material film surface. The second step, the Ridge and Mesa Structure Definition process step, etches reliefs into the GaAs surface, creating conductive pathways which includes connections to mesas serving as cathodes and the to-be-released ridges serving as anodes. Finally, the Suspended Beam Definition process concludes the fabrication of the suspended anode.

Chapter 5

Summary and Future Directions

5.1 Introduction

This thesis presented a compendium of seven electromechanical waveguide-based optical switches. These optical switches were strictly designed with high-index-contrast wave-guiding materials with square symmetric cross sections. A two-step design approach was employed: first, the switches were optimized for optical operation and then for electrome-chanical operation. Three different simulation methods were used in order to conduct optical operation optimizations: (1) three-dimensional Fast Fourier Transform beam propagation method (FFT-BPM) for polarization-dependent single-mode simulations, (2) three-dimensional wide-angle finite difference beam propagation method (WA FD-BPM) for polarization-dependent simulations, and (3) two-dimensional bi-directional eigenmode propagation method (BEPM) for forward and backward light propagation simulations. Two different simulation methods were used in order to conduct electrome-chanical operation optimizations: (1) three-dimensional finite element method (FEM) simulations for quasi-static switching studies, and (2) one-dimensional finite difference time domain implicit method (FDTD) simulations for dynamic switching studies. The simulation methods were described in Chapter 2. Chapter 4 discussed how the elec-tromechanical optical switches can be created in a gallium arsenide-on-insulator (GOI)

material system with preliminary fabrication results, providing qualitative evidence supporting the efficacy of a proposed fabrication sequence.

5.2   Comparative Analysis

What follows is a comparative analysis on all of the seven electromechanical optical switches.

5.2.1   Optical Transmission
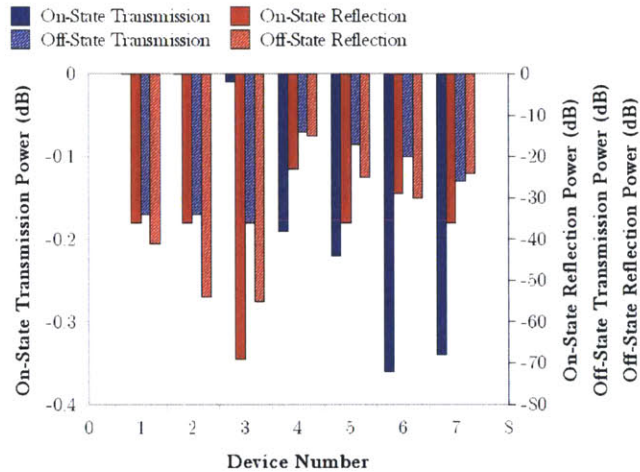
FIGURE 5.1: Optical performance comparison of all seven optical switches operated as on/off optical switches. On-state transmission (left axis), on-state reflection (right axis), off-state transmission (right axis) and off-state reflection (right axis) are compared. Only TE light transmission as modeled by two-dimensional eigenmode simulations is considered.

Devices 01, 02 and 03 are design specifically for on/off operation. Devices 04, 05, 06 and 07 were designed for 2×2 operation. As a result, Devices 04, 05, 06 and 07 can also be operated as on/off optical switches.

Consider the bar chart in Figure (5.1). On-state transmission and reflection as well as

off-state transmission and reflection for all seven optical switches are compared. Specifi-
cally, two-dimensional eigenmode simulated quasi-TE_0 light transmission and reflection
for the on- and off-states are compared. For Devices 04, 05, 06 and 07, the cross-state
light transmission serves as the on-state light transmission while the bar-state crosstalk
serves as the off-state light transmission.

The on/off optical switches (Device 01, 02 and 03) have extraordinarily low on-state
transmission loss as compared to the 2×2 optical switches (Devices 04, 05, 06 and 07)
which are made to function as on/off optical switches. The on/off optical switch Device
03 has the lowest on-state reflection even though Device 03 is based on the cantilevered-
waveguide optical switch design.

The on/off optical switches have lower off-state transmission as compared to the 2×2
optical switches. The off-state transmission (i.e., the bar-state crosstalk) for the 2×2 op-
tical switches can be improved by (a) increasing the waveguide-to-waveguide separation
in the bar-state configuration and/or (b) incorporating optically-absorptive structures
into the optical switch designs.

The on/off optical switches Device 02 and 03 have the lowest off-state transmission
of all of the optical switches. The low off-state transmission is the direct result of the
efficacy of the optical absorption structures that are used in both optical switch designs.
Recall that Device 02 is based on the anti-resonant reflection waveguide. In the off-state
configuration, both deflected suspended anti-resonant reflection waveguides are made to
intimately contact waveguide structures that form evanescent and butt coupling light-
paths with those deflected waveguides. Evidently, both evanescent and butt coupling
are require to achieve low off-state reflection since evanescent coupling alone (as imple-
mented by Device 01) does not yield the same level of off-state reflection.

Device 03, comprised of total internal reflection waveguides, is able to achieve the same low off-state reflection as Device 02 by relying on codirectional coupling optical power absorption.
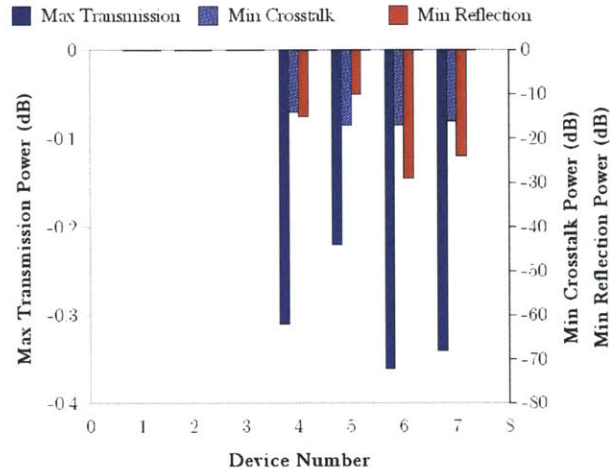
FIGURE 5.2: Optical performance comparison of four 2×2 optical switches. Considering both the bar- and cross-state lightpaths, the minimum transmission (left axis), the maximum crosstalk (right axis) and the maximum (reflection) are compared. Only TE light transmission as modeled by two-dimensional eigenmode simulations is considered.

5.2.2   MEMS Performance
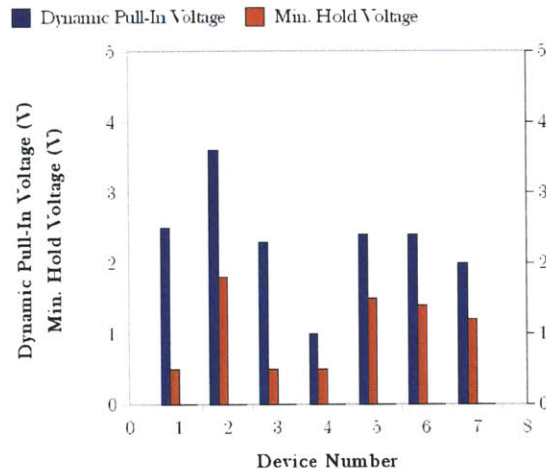
FIGURE 5.3: Electromechanical actuation voltage comparison of both the on/off and the 2×2 optical switches.

Each of the seven optical switches is designed to be operated with a 10-V actuation voltage. As shown in Figure (5.3), each switch can be operated with a voltage that is lower the 10V. Each switch can be actuated with approximately 2V with the notable exceptions being Device 02 ($V_{DPImin} \approx 3.5V$) and Device 04 ($V_{DPImin} \approx 1V$).

Device 05, the 2×2 optical switch that is based on tethered actuation has the lowest maximum transmission loss as compared to the other 2×2 optical switches. Considering these results, the T-junction (the contiguous intersection of the suspended waveguide and the tether beam) improves cross-state transmission.

All of the 2×2 optical switches appear to have roughly equivalent crosstalk figures. Note that the maximum crosstalk is attributed to the cross-state configuration. The cross-state crosstalk may be improved by incorporating other absorptive elements in each of the designs in order to prevent spurious power from unintentionally coupling into a waveguide that should have no exiting power.

Device 06 has the lowest reflection of all of the other 2×2 optical switches. The reflection loss of Device 04, 06 and 07 may be improved by waveguide redesign since all of the 2×2 optical switches are based on linear transitions–linear slanted waveguides and linear tapers (in the case of Device 07).
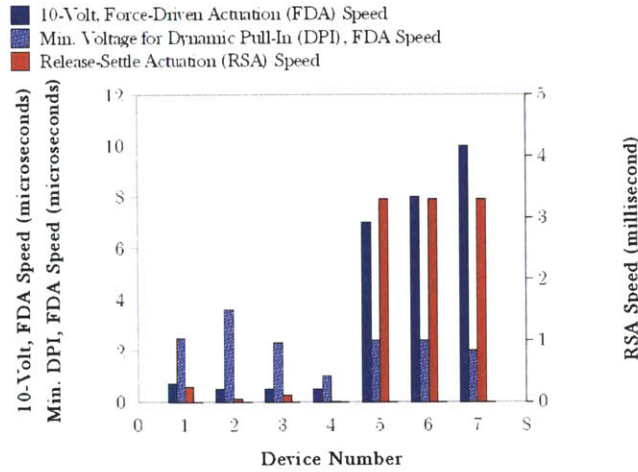
FIGURE 5.4: Electromechanical actuation speed comparison of both the on/off and 2×2 optical switches. The force-driven actuation speed for an 10-volt ($t_{FDA_{10V}}$) and a V_{DPImin} actuation voltage as well as the release-settle actuation speed (t_{RSA}) are compared.

For force-driven actuation under a $V_{DPI} = 10V$ actuation voltage, the optical switches that have waveguide-integrated parallel-plate MEMS actuators integrated have the fastest response time ($t_{FDA_{10V}}$); the optical switches that are controlled by remote parallel-plate MEMS actuators are slower. However, the slower $t_{FDA_{10V}}$ remote actuator-base optical switches are less sensitive to thin film stress as the parallel-plate actuators have folded-flexure suspensions.

For force-driven actuation under a $v_{DPI} = V_{DPImin}$ actuation voltage, the response time, $t_{FDA_{DPImin}}$ is 2 - 3 times higher than $t_{FDA_{10V}}$. As a result, the optical switches that have waveguide-integrated parallel-plate actuators will still have considerably faster switching speeds, on the order of a microsecond. In contrast, $t_{FDA_{DPImin}}$ of the optical switches that have remote parallel-plate actuators is about 15 times higher than their counterparts.

Most notably, all of the optical switches (except for Device 04) have considerably higher release-settle actuation switching speeds (t_{RSA}).

Ultimately, Device 04 has the best switching performance. Recall that Device 04 is the optical switch that is based on the waveguide-integrated parallel plate actuator and the fixed-fixed beam suspended waveguide suspension. Device 04 is an electromechanical optical switch that can be modulated on a $\approx 2\mu s$ time scale with a modulation voltage as low as $1.0V$.

5.2.3   Non-Ideal Considerations

Each of the optical switch designs is based on the assumption that all functional materials are homogeneous and the mechanical anchors are fixed. Moreover, only three types of forces were considered: damping force, electrostatic force and elastic force. Unfortunately, there are material, structural and force effects that must be considered in order to ascertain the viability of the proposed optical switches.

Thin-Film Stress. Thin-film stress is a condition that develops in layers that have material or dimensional irregularities. Fortunately, since thin-film stress in grown crystalline films is negligible, thin-film stress in the high-index core layer is not anticipated to be especially problematic for optical switches that are created in the AlGaAs material system.

Eccentric Beam Loading. Asymmetries along a suspended beam's length can generate axial eccentric loading which leads to beam deflection. Asymmetries arises from non-ideal boundary conditions and/or fabrication artifacts along the length of the beam. Beam deflections resulting from beam asymmetries undergo continuous nonlinear deflections prior to the discontinuous Euler buckling event that were observed in MEMS structures that only have thin-film stress gradients.

Carr and Wyborne have experimentally observed the asymmetric eccentric loading effects that were generated from post anchors of fixed-fixed beam suspended nanomechanical structures [?]. Incrementally larger beam deflections–from $200nm$ to $320nm$–were observed as the support material was sacrificially etched in eight discrete time intervals–the first interval lasted 85s; the total cumulative etch time was $140s$[?].[1]

Dispersion Forces. In addition to the damping, electrostatic and elastic forces, van der Waals and Casimir forces must also be considered. Typically, below several tens of

---

[1]Particular to their experiments, suspended fixed-fixed beams of thermally-grown SiO_2, with a 60-nm-width, 500-nm-thickness and a 7.2-μm-length, were supported by silicon posts[?].

nanometers, the van der Waals force is the dominate attractive force [?] [?] [?] [?]:

$$F_{vdW} = \frac{A_{HAM} w_{cA,B}}{6\pi \left(g_{NM} - \Delta g\right)^3}.$$ (5.1)

Above several tens of nanometers, the Casimir force is dominate [?] ,[?], [?], [?], [?], [?], [?], [?]:

$$F_{CMIR} = \frac{\pi^2 \hbar c w_{cA,B}}{240 \left(g_{NM} - \Delta g\right)^4}$$ (5.2)

van der Waals and Casimir forces become relevant for suspended, closely spaced nanostructures that have separations that are greater than their widths (e.g, $g_{NEM}/w_{cA,B} \geq 1$) [?], [?], [?] .

During actuation, all of the optical switches involve the establishment of intimate surface-to-surface contact of a deformable microstructure. As a result zero-gap adhesion forces must be considered. The zero-gap adhesion forces are generally caused by capillary, electrostatic, van der Waals and other kinds of 'chemical' forces [?] [81] [?]. The zero-gap adhesion forces leads to in-use stiction if the elastic restoration force of a deflected microstructure is not strong enough to counterbalance the zero-gap adhesion forces.

Mastrangelo and Hsu derived a dimensionless number, termed the peel number (N_{PEEL}), which is the ratio of elastic strain energy that is stored in a deformed microstructure to the work of adhesion of two intimately contacting surfaces [?] [?]. Ultimately, the condition of $N_{PEEL} > 1$ must be satisfied in order for the suspended microstructures to recover from the deformed configuration after the hold voltage is removed.

Recall that Devices 01, 02 and 03 are MEMS optical switches that are based on long slender cantilevered waveguides that are design to establish an s-shape profile in the mechanically-deflected configuration. For long slender S-shaped cantilever beams defined by a thickness of h_{cCORE}, an elastic modulus of E_{NM}, a surface-to-surface separation of g_c, the peel number is given as [?] [?]:

$$N_{PEEL_{cbeam}} = \frac{3 E_{NM} w_{cA,B}^3 g_c^2}{8 L_{CRACK}^4 W_{ADH}},$$ (5.3)

where L_{CRACK} is the crack length, and W_{ADH} is the work of adhesion between the two intimately contacting surfaces.

Also recall that Device 04, 05, 06 and 07 are MEMS optical switches that are based on fixed-fixed suspended waveguides. For a fixed-fixed beam that is defined by a composite width of $w_{cA,B}$, an elastic modulus of E_{NM}, a surface-to-surface separation of g_c, the peel number is given as [?] [?]:

$$N_{PEEL_{ffbeamd}} = \frac{128 E_{NM} w_{cA,B}^3 g_c^2}{5 L_{NM}^4 W_{ADH}} \left[1 + \frac{4 \sigma_R L_{NM}^2}{21 E_{NM} w_{cA,B}^2} + \frac{256}{2205} \left(\frac{g_c}{w_{cA,B}} \right)^2 \right], \quad (5.4)$$

where L_{NM} is the total length of the fixed-fixed beam suspended waveguide section and again W_{ADH} is the work of adhesion between two intimately-contacting surfaces.

Device 01. In the as-fabricated on-state configuration, Device 01, the optical switch that is based on cantilever beam waveguides with waveguide-integrated MEMS, requires that the two butt coupled waveguides be in axial alignment. The on-state transmission will be compromised if the deformable suspended cantilever waveguide undergoes angular-tilt, end-separation-offset and/or axial-offset misalignments. Thin-film stress is expected to contribute to those misalignments.

In the off-state, one of the cantilevered waveguide section is designed to make intimate contact with the top of the coated substrate surface over a distance $L_{CONTACT}$. As a result, the length of the deformable suspended waveguide section (L_{NM}) must be defined such that $N_{PEEL_{cbeam}} > 1$; a higher spring constant k_{NM} will be required. As a result, Device 01 will require a higher actuation voltage for deflection since the plate-to-plate separation is restricted to $g_{NEM} = 1.29 \mu m$, the separation that is required to maintain optical isolation between the anchored waveguides and the high-index substrate.

Device 02. In the as-fabricated on-state configuration, Device 02, the optical switch that is based on cantilever beam waveguides with waveguide-integrated MEMS, requires that the two butt coupled waveguides be in axial alignment. The on-state transmission will be compromised if the deformable suspended cantilever waveguide undergoes

angular-tilt, end-separation-offset and/or axial-offset misalignments. Thin-film stress is expected to contribute to those misalignments.

Device 03. In the as-fabricated on-state configuration, Device 03, the optical switch that is based on cantilevered waveguides that have waveguide-integrated MEMs, requires nanometer-order parallel waveguide alignment. While not as sensitive to misalignment as the butt-coupled-based optical switch, thin-film stress must be managed in order to ensure that the two waveguides maintain parallel alignment. As a result, the length of the cantilevered waveguides may have to be altered in order to prevent thin-film-stress misalignment. Also, a second consideration is the effects of dispersive forces. In the original design, the two cantilevered waveguides are required to maintain a surface-to-surface spacing of $g_{cON00_{AB}} = 10nm$. At a $g_{cON00_{AB}} = 10nm$ separation, Casimir forces can potentially pull the two waveguides into one another. As a result, the length L_{NM} of the cantilever waveguide sections may have to be shorten in order to increase the spring stiffness k_{NM} in order to counterbalance Casimir forces.

In the mechanically-deflected off-state configuration, the cantilevered waveguide section of both waveguides are designed to make intimate contact with in-plane waveguiding structures over a contact length of $L_{OPTIC_{AC,BD}}$. As a result, the length of the deformable suspended waveguide section L_{NM} must be defined such that $N_{PEEL_{cbeam}} > 1$ in order to ensure that the spring constant k_{NM} is stiff enough to counterbalance in-use adhesion forces. At the cost of on-state transmission, low-voltage operation may still be achieved by reducing the separation between the adjacent (waveguide) anodes. Note that optimizing for low-voltage operation against on-state transmission loss will also require the consideration of van der Waals forces since the surface-to-surface separation between the rigid and deformable waveguide sections, $g_{cON00_{AC,BD}}$, is on the order of 100s of nanometers.

Device 04. In the as-fabricated cross-state configuration, the two fixed-fixed beam suspended waveguide sections are required to maintain a surface-to-surface separation of $g_{cBAR00_{AB}} = 10nm$. As a result, the spring stiffness k_{NM} may have to be increased by decreasing L_{NM} in order to counterbalance the Casimir forces. Also, in order to

prevent out-of-plane beam sagging, L_{NM} may have to be adjusted in order to establish a spring stiffness (k_{NM}) that will counterbalance asymmetries that are created by the ridge anchors existing at both ends of the suspended waveguide section.

In the mechanically-deflected bar-state configuration, the two suspended waveguide sections are in intimate contact with two adjacent, discontinuous waveguides over a contact length of $L_{OPTIC_{AC,BD}}$. As a result, the length of the deformable suspended waveguide section L_{NM} must be defined such that $N_{PEEL_{ffbeam}} > 1$ in order to ensure that the spring constant k_{NM} has sufficient stiffness in order to counterbalance zero-gap adhesion forces. At the cost of increasing the cross-state loss (and possibly increased reflection), low-voltage operation may still be achieved by reducing the electrode separation of the parallel-plate actuator (g_{NEM}). Optimizing for low-voltage operation against the as-fabricated cross-state transmission loss will also require the consideration of van der Waals forces since the surface-to-surface separation between the rigid, discontinuous waveguides and the deformable, continuous waveguide sections ($g_{cCROSS00_{AC,BD}}$) is on the order of 100s of nanometers.

Device 05. In the as-fabricated cross-state configuration, the two fixed-fixed beam suspended waveguide sections are required to maintain a surface-to-surface separation of $g_{cCROSS00_{AB}} = 50nm$ (in the center region, Region 00). As a result, the spring stiffness k_{NM} may have to be increased by decreasing L_{NM} in order to counterbalance the Casimir forces. Alternatively, the $g_{cCROSS00_{AB}}$ could be increased in order to lessen the effect of the Casimir forces; in this case, Device 05 would have to be again optimized for maximized cross-state transmission, minimized crosstalk and minimized polarization dependence by adjusting the refractive index of the core and the coat cladding layers and/or the dimensions of the core and coat cladding layers. Also, in order to prevent out-of-plane beam sag due to eccentric loading that is created by asymmetries at the ridge anchor supports, L_{NM} may have to be adjusted in order to establish a sufficient spring stiffness (k_{NM}) that will counterbalance the eccentric loading.

Device 06. In the as-fabricated bar-state configuration, the two fixed-fixed beam suspended waveguide sections are required to maintain a minimum surface-to-surface

separation of $g_{cBAR00_{AB}} = 800nm$. van der Waals forces are the only dispersion forces that could possible alter $g_{cBAR00_{AB}}$.

In the mechanically-deflected configuration, the two suspended waveguide sections establish intimate contact over the length $L_{OPTIC00_{AB}} = 9.9\mu m$. As a result, the length of the deformable suspended waveguide section of both waveguides (L_{NM}) must be defined such that $N_{PEEL_{ffbeam}} > 1$ in order to ensure that the spring constant k_{NM} has sufficient stiffness in order to counterbalance adhesion forces. Fortunately, since the MEMS of Device 06 is defined independent of the suspended waveguide suspension, low-voltage operation can be maintained.

Device 07. In the as-fabricated bar-state configuration, the two fixed-fixed beam suspended waveguide sections are required to maintain a minimum surface-to-surface separation of $g_{cBAR_{AB}}$. van der Waals forces are the only dispersion forces that could possible alter $g_{cBAR_{AB}}$.

In the mechanically-deflected configuration, the two suspended waveguide sections establish intimate contact of the length $L_{CONTACT} = L_{02}+L_{01}+L_{00}+L_{10}+L_{20} = 34.2\mu m$. As a result, the spring constants k_{NM_A} and k_{NM_B} must have sufficient stiffness in order to counter balance adhesion forces; the total length of the deformable suspended waveguide section of Waveguide A (L_{NM_A}) and Waveguide B (L_{NM_B}) must be defined such that $N_{PEEL_{ffbeam}} > 1$. Similarly, the spring constant of the MEMS, k_{NEM}, must have sufficient stiffness in order to counter balance adhesion forces. However, since the MEMS is defined independent of the waveguiding structures, the parallel plates can be defined to have rough sidewalls in order to reduce the strength of adhesion forces. Moreover, since the MEMS is defined independent of the suspended-waveguide suspension, low-voltage operation can be maintained by increasing the force per volt of the MEMS.

5.2.4   Potential Applications

Photonic integrated circuit (PIC) technology is preferred over free space optical microsystems technology in order to fully implement low-cost, dynamic and miniature

optical communication systems [82]. Leveraging the years of technological development which was specifically catered to optical communication systems, PIC technology is now being developed for applications of environmental, biological and chemical sensing and detection [83], [84]. This section will cover the three areas of application uniquely served by (nano)electromechanical optical switch (NEM-OS) powered PIC technology: (a) optical communication, (b) optical sensing, and (c) optical component testing.

Optical Communications. One of the major and early driving application for PIC technology was the collective desire to replace bulky and expensive macroscopic optical systems with low-cost, mass-producible, easily-replaceable and smart miniaturized optical systems in order to better serve existing telecommunication networks. In order to clearly identify the role that PIC technology– more specifically, NEM-OS powered PIC technology–plays in increased network agility, the telecommunication network is briefly examined. Generally, telecommunication networks are partitioned into six hierarchical sub-system networks: (1) ultra-long-haul, (2) long-haul, (3) metro core, (4) access, (5) enterprise, and (6) residential networks. The six sub-system networks have a hierarchical arrangement of performance and price point. Performance has the highest priority for optical components in ultra-long-haul, and long-haul networks, while cost has the highest priority for optical components in access, enterprise and residential networks. Falling in the middle of the performance-price spectrum, optical components in metro core networks have equal prioritization of performance and price. For all levels of telecommunication networking, NEM-OS powered PICs can enhance the agility of those networks by providing bandwidth–on demand services and reducing the recovery time between data transmission interruptions. Moreover, NEM-OS powered PICs can be used for preventive maintenance of telecommunication networks by remotely monitoring and provisioning the networks. Essentially, NEM-OS powered PICs can potentially reduce the cost of operational and capital expenditures (OPEX and CAPEX) that are associated with network operation, administration, and maintenance.

Optical sensing. The general field of optical sensing is defined as encompassing the science of environmental, biological and chemical detection. In general, PIC technology is well suited for environmental, biological and chemical detection via optical telemetry

on a micro/nanoscopic level. Micron/submicron-order wavelength light guided along micron/submicron-order waveguides are especially sensitive to their ambient. A change in the ambient can be easily and accurately detected as a phase shift or an amplitude modulation in the affected light. Essentially, environmental, biological and chemical changes can be monitored on a micro/nanoscopic level in massively parallelized systems on a small and disposable chip. A wide range of optical sensing principles can be used for optical telemetry:

1. Light-Addressable Potentiometry Sensing (LAPS) [85],[86],[61],[87]

2. Surface Plasmon Resonance (SPR) [88], [82]

3. Light Interference [?], [89]

4. Evanescent Light Attenuation [90], [91], [92]

5. Reflectometric Inteference Spectroscopy (RIFS) [93], [94]

Generally, any of the optical sensing telemetry methods can be implemented with either a complete monolithic integrated PIC system or a heterogeneous system.

A fabric of on/off or 2 × 2 optical switches can be used to enhance the functionality of PIC systems that are dedicated to biological and chemical optical sensing. A variety of static PIC systems have already been demonstrated to streamline biological and chemical experiments with the miniaturization and parallelization of experiments on a massive level. By incorporating the electromechanical optical switches with the components of optical sensing PICs, biological and chemical interrogation experiments have the potential of being revolutionized. PICs featuring electromechanical optical switches can dynamically, accurately and precisely address localized microscale regions with multiple sources and detectors.

A switch fabric of either on/off or 2 × 2 optical switches can be used to extend the functionality of heterogeneous optical microsystems. For example, a PIC which integrates emitters, detectors, optical splitters and a fabric of electromechanical optical

switches can be connected to a bundle of commercially available germanium doped SMFs with integrated wavelength selective reflectors in order to perform multipoint detection of temperature or humidity changes in an environment [83]. Indeed, a fiber-based 18 optical switch fabric–consisting of a three-stage matrix of cascaded 1 × 2 electrome-chanical fiber switches-was used in a multipoint distributed temperature sensor system [95]. The 1 × 8 switch fabric was connected to discrete off-chip components: a light source, a circulator, and a spectrum analyzer. The indium phosphide-on-insulator (IOI) and the gallium arsenide- on-insulator (GOI) material systems are uniquely suit for the implementation of optical sensing systems. With these direct-band gap material sys-tems, light sources, circulators and possibly a spectrum analyzer can be integrated on the wafer level which as a result decreases manufacturing cost and increases reliability. Environmental analysis that once required an entire laboratory table to perform now can conceivably be done on a disposable microchip.

Optical component testing. A suite of optical characterization equipment is required to fully analyze a single optical device or a network of optical devices [device(s)-under-test (DUT)]. In general, optical DUTs are routinely tested and characterized with a set of optical devices which include optical spectrum analyzers (OSAs) [85], optical time domain reflectometers (OTDRs) [86], [61], Raman lasers [62], laser diodes (LDs) [96], optical power meters (OPMs), and polarization controllers. Manually connecting, dis-connecting, and reconnecting optical links between optical characterization equipment and DUTs not only is a time consuming task, but also compromises the integrity of the characterization and testing results. Using electromechanical optical switches both as an interface to the characterization equipment as well as in situ on-chip testing equipment could potentially streamline optical component characterizations.

5.3   Future Directions

5.3.1   Characterization and Testing

In order to generate predictive models for the electromechanical optical switches, the structural films of the electromechanical optical switches must be characterized before and after fabrication. In regards to the pre-processed thin-film layers, ellipsometry techniques can be used to accurately characterize and verify both the refractive index as well as the thickness of the atomic-layer-deposition (ALD) coat cladding films, the epitaxy core films, and the chemical-vapor-deposition (CVD) upper cladding films. Also, X-ray scattering techniques, such as X-ray diffraction and reflection, are other non-destructive techniques that can be used (in-situ or off-line) in order to investigate and characterize the effect that crystallographic structure and chemical composition has on the refractive index and the thin-film stress of the structural films. Contingent upon the size of the X-ray beam, X-ray reflectivity measurements can be used to analyze thickness, roughness and density of the grown core thickness of the anchored and suspended waveguides, the RIE core width of the anchored and suspended waveguides, ALD-deposited coat-cladding thickness of the suspended waveguides, and the upper cladding thickness of the anchor waveguides.

Similar to the single mode fiber, the photonic integrated circuit (PIC) based electromechanical optical switches are required to be characterized for operational integrity. Specifically, the electromechanical optical switches must be tested individually to characterize the amount of attenuation, the region of single-mode operation, the profile of the mode-field, the extent of chromatic dispersion and the amount of reflections[97]. However, unlike single mode fibers, the electromechanical optical switches must also be examined for polarization dependent loss (PDL).

Appendix A

Device Parameters

A.1 Device 01 Parameters

TABLE A.1: Device 01 Parameters: primary optical parameter (▲), (associated) optical parameter (△), primary MEMS parameter (■), (associated) MEMS parameter (□).

	Variable	Description	Value
▲	h_{Core}	The thickness of the core material.	$100nm$
▲	$wOptic_{01}$	The width of the suspended waveguides.	$100nm$
▲	n_{Core}	The refractive index of the core material.	3.0
	w_{Coat}	The width of the coat cladding layer.	$45nm$
	n_{Coat}	The refractive index of the coat cladding layer.	3.30
	$g_{cOptic_{01}}$	The surface-to-surface axial separation between the two suspended waveguides (Waveguides A and B) in the as-fabricated on-state configuration.	$10nm$
	$g_{cOFF00_{AB}}$	The center-to-center axial separation between the two suspended waveguides (Waveguides A and B) in the mechanically-deflected off-state configuration.	$1.2\mu m$
	$g_{cOptic_{02}}$	The surface-to-surface separation between Waveguide A and the substrate (Substrate C)–and Waveguide B and the substrate–in the as-fabricated on-state configuration.	$1.32\mu m$
	$g_{cOptic_{03}}$	The surface-to-surface separation between Waveguide A and the substrate (Substrate C) in the mechanically-deflected off-state configuration.	$0\mu m$
		Continued on Next Page...	

Table A.1 – Continued

Variable	Description	Value
$g_{cOptic_{04}}$	The surface-to-surface separation between Waveguide B and the substrate (Substrate C) in the mechanically-deflected off-state configuration.	$1.32\mu m$
$L_{Optic_{01}}$	The length over which Waveguide A forms an intimate contact with the substrate (Substrate C) in the mechanically-deflected off-state configuration.	$5\mu m$
g_{MEM}	The core-to-core separation between the anode and the cathode of the parallel plate actuator.	$1.29\mu m$
L_{MEM}	The overlap length between the anode and the cathode of the parallel plate actuator.	$17\mu m$
A_{MEM}	The electrode plate area of the parallel plate actuator.	$1.7\mu m^2$
$L_{NM_{01}}$	The length of the suspended section of Waveguide A.	$17\mu m$
k_{NM}	The lumped element spring constant of the two-material MEMS suspension.	$1.4 \cdot 10^{-3} N/m$
m_{NM}	The lumped element mass of the two-material suspended MEMS suspension.	$1.8 \cdot 10^{-4}$ ng
$c_{DAMP_{CD}}$	The damping constant for critically-damped conditions.	$1.0 \cdot 10^{-3} \mu N/m/s$
t_{MIN}	The minimum release-settle actuation time under critically-damped conditions.	$359ns$
c_{DAMP}	The damping constant.	$9.4 \cdot 10^{-6} \mu N/m/s$

TABLE A.2: Device 01 Optical Performance

As-Fabricated On-State Transmission

		$\lambda_0 - 50nm$	λ_0	$\lambda_0 + 50nm$
TE_{00}	Transmission	$-3.8 \cdot 10^{-4}dB$	$-3.3 \cdot 10^{-4}dB$	$-3.2 \cdot 10^{-4}dB$
	Reflection	$-35dB$	$-36dB$	$-37dB$
TM_{00}	Transmission	$-4.2 \cdot 10^{-2}dB$	$-2.0 \cdot 10^{-2}dB$	$-4.1 \cdot 10^{-2}dB$
	Reflection	$-24dB$	$-39dB$	$-29dB$

Mechanically-Deflected Off-State
Forward Transmission

		$\lambda_0 - 50nm$	λ_0	$\lambda_0 + 50nm$
TE_{00}	Transmission	$-40dB$	$-34dB$	$-30dB$
	Reflection	$-31dB$	$-41dB$	$-23dB$
TM_{00}	Transmission	$-12dB$	$-11dB$	$-10dB$
	Reflection	$-31dB$	$-13dB$	$-12dB$

Mechanically-Deflected Off-State
Backward Transmission

		$\lambda_0 - 50nm$	λ_0	$\lambda_0 + 50nm$
TE_{00}	Transmission	$-28dB$	$-28dB$	$-24dB$
	Reflection	$-31dB$	$-23dB$	$-7.9dB$
TM_{00}	Transmission	$-15dB$	$-14dB$	$-15dB$
	Reflection	$-19dB$	$-37dB$	$-25dB$

TABLE A.3: Device 01 MEMS Performance

Waveguide Actuator

Voltage	Speed
$V_{DPI} = 10V$	$t_{DPI} = 700ns$
$V_{DPI_{MIN}} = 2.5V$	$t_{DPI_{MIN}} = 2.1\mu s$
$V_{HOLD_{MIN}} = 0.5V$	N/A
$0V$	$t_{RSA} = 240\mu s$

A.2 Device 02 Parameters

TABLE A.4: Device 02 Parameters: primary optical parameter (▲), (associated) optical parameter (△), primary MEMS parameter (■), (associated) MEMS parameter (□).

Variable	Description	Value
h_{CORE}	The thickness of the core material.	$100nm$
$w_{A,B}$	The width of the suspended waveguide cores.	$100nm$
n_{CORE}	The refractive index of the core material.	3.0
w_{COAT}	The width of the coat cladding layer.	$45nm$
n_{COAT}	The refractive index of the coat cladding layer.	3.4
$g_{cON00_{AB}}$	The surface-to-surface axial separation between Waveguides A and B in the as-fabricated on-state configuration.	$10nm$
$g_{cOFF00_{AB}}$	The center-to-center separation between Waveguides A and B in the mechanically-deflected off-state configuration.	$800nm$
$g_{cON00_{AC,BD}}$	The surface-to-surface separation between Waveguides A and C–and Waveguides B and D–in the as-fabricated on-state configuration.	$400nm$
$g_{cOFF00_{AC,BD}}$	The surface-to-surface separation between Waveguides A and C–and Waveguides B and D–in the mechanically-deflected off-state configuration.	$0nm$
$L_{OPTIC_{AC,BD}}$	The overlap length between Waveguides A and C–and Waveguides B and D.	$5\mu m$
g_{NEM}	The core-to-core separation between the anode and the cathode of the parallel plate actuator.	$490nm$
L_{NEM}	The overlap length between the anode and the cathode of the parallel plate actuator.	$5\mu m$
A_{NEM}	The electrode plate area of the parallel plate actuator.	$0.5\mu m^2$
L_{NM}	The length of the suspended section of Waveguides A and B.	$14\mu m$
k_{NM}	The lumped element spring constant of the two-material MEMS suspension.	$3.0 \cdot 10^{-3}$ N/m
m_{NM}	The lumped element mass of the two-material MEMS suspension.	$1.8 \cdot 10^{-4}ng$
$c_{DAMP_{CD}}$	The damping constant for critically-damped conditions.	$1.5 \cdot 10^{-3}\mu N/m/s$
t_{MIN}	The minimum release-settle actuation time under critically-damped conditions.	$250ns$
c_{DAMP}	The damping constant.	$2.1 \cdot 10^{-5}\mu N/m/s$

TABLE A.5: Device 02 Optical Performance

As-Fabricated On-State

		$\lambda_0 - 50nm$	λ_0	$\lambda_0 + 50nm$
TE_{00}	Transmission	$-3.8 \cdot 10^{-4}dB$	$-3.3 \cdot 10^{-4}dB$	$-3.2 \cdot 10^{-4}dB$
	Reflection	$-35dB$	$-36dB$	$-37dB$
TM_{00}	Transmission	$-4.2 \cdot 10^{-2}dB$	$-2.0 \cdot 10^{-2}dB$	$-4.1 \cdot 10^{-2}dB$
	Reflection	$-24dB$	$-39dB$	$-29dB$

Mechanically-Deflected Off-State

		$\lambda_0 - 50nm$	λ_0	$\lambda_0 + 50nm$
TE_{00}	Transmission	$-37dB$	$-34dB$	$-31dB$
	Reflection	$-40dB$	$-54dB$	$-28dB$
TM_{00}	Transmission	$-22dB$	$-18dB$	$-22dB$
	Reflection	$-19dB$	$-16dB$	$-22dB$

TABLE A.6: Device 02 MEMS Performance

Waveguide Actuator

Voltage	Speed
$V_{DPI} = 10V$	$t_{FDA} = 500ns$
$V_{DPI_{MIN}} = 3.6V$	$t_{FDA} = 1.0\mu s$
$V_{HOLD_{MIN}} = 1.8V$	N/A
$0\ V$	$t_{RSA} = 46\mu s$

A.3   Device 03 Parameters and Performance

TABLE A.7: Device 03 Parameters: primary optical parameter ($\blacktriangle$), (associated) optical parameter ($\triangle$), primary MEMS parameter ($\blacksquare$), (associated) MEMS parameter ($\square$).

Variable	Description	Value
h_{CORE}	The thickness of the core material.	$300nm$
$w_{A,B}$	The width of the suspended waveguide cores.	$300nm$
$w_{C,D}$	The width of the suspended sections of Waveguides C and D.	$300nm$
n_{CORE}	The refractive index of the core material.	3.17
w_{COAT}	The width of the coat cladding layer.	$50nm$
n_{COAT}	The refractive index of the coat cladding layer.	1.50
$g_{cON00_{AB}}$	The surface-to-surface separation between Waveguides A and B in the as-fabricated on-state configuration.	$10nm$
$g_{cOFF00_{AB}}$	The surface-to-surface separation between Waveguides A and B in the mechanically-deflected off-state configuration.	$810nm$
$L_{OPTIC_{AB}}$	The overlap length between Waveguides A and B.	$6\mu m$
$g_{cON00_{AC,BD}}$	The surface-to-surface separation between Waveguides A and C–and Waveguides B and D–in the as-fabricated on-state configuration.	$400nm$
$g_{cOFF00_{AC,BD}}$	The surface-to-surface separation between Waveguides A and C and Waveguides B and D in the mechanically-deflected off-state configuration.	$0nm$
$L_{OPTIC_{AC,BD}}$	The overlap length between Waveguides A and C and Waveguides B and D.	$4\mu m$
g_{NEM}	The core-to-core separation between the anode and the cathode of the parallel plate actuator.	$400nm$
L_{NEM}	The overlap length between the anode and the cathode of the parallel plate actuator.	$4\mu m$
A_{NEM}	The electrode plate area of the parallel plate actuator.	$1.2\mu m^2$
L_{NM}	The length of the suspended section of Waveguides A and B.	$41\mu m$
k_{NM}	The lumped element spring constant of the two-material MEMS suspension.	$1.2 \cdot 10^{-3} N/m$
m_{NM}	The lumped element mass of the two-material MEMS suspension.	$6.3 \cdot 10^{-4} ng$
$c_{DAMP_{CD}}$	The damping constant for critically-damped conditions.	$1.7 \cdot 10^{-3} \mu N/m/s$
t_{MIN}	The minimum release-settle actuation time under critically-damped conditions.	$725ns$
	Continued on Next Page...	

Table A.7 – Continued

Variable		Description	Value
	c_{DAMP}	The damping constant.	$7.4 \cdot 10^{-5} \mu N/m/s$

TABLE A.8: Device 03 Optical Performance

As-Fabricated On-State

		$\lambda_0 - 50nm$	λ_0	$\lambda_0 + 50nm$
TE$_{00}$	Transmission	$-4.3 \cdot 10^{-2} dB$	$-9.0 \cdot 10^{-3} dB$	$-1.8 \cdot 10^{-2} dB$
	Reflection	$-57 dB$	$-69 dB$	$-79 dB$
TM$_{00}$	Transmission	$-5.5 \cdot 10^{-2} dB$	$-6.9 \cdot 10^{-1} dB$	$-2.3 dB$
	Reflection	$-46 dB$	$-24 dB$	$-23 dB$

Mechanically-Deflected Off-State

		$\lambda_0 - 50nm$	λ_0	$\lambda_0 + 50nm$
TE$_{00}$	Transmission	$-36 dB$	$-36 dB$	$-30 dB$
	Reflection	$-60 dB$	$-55 dB$	$-31 dB$
TM$_{00}$	Transmission	$-12 dB$	$-12 dB$	$-12 dB$
	Reflection	$-16 dB$	$-14 dB$	$-11 dB$

TABLE A.9: Device 03 MEMS Performance

Waveguide Actuator

Voltage	Speed
$V_{DPI} = 10V$	$t_{FDA} = 500ns$
$V_{DPI_{MIN}} = 2.3V$	$t_{FDA} = 1.5\mu s$
$V_{HOLD_{MIN}} = 0.5V$	N/A
$0V$	$t_{RSA} = 110\mu s$

A.4   Device 04 Parameters and Performance

TABLE A.10: Device 04 Parameters: primary optical parameter (▲), (associated) optical parameter (△), primary MEMS parameter (■), (associated) MEMS parameter (□).

Variable	Description	Value
h_{CORE}	The thickness of the core material.	$300nm$
$w_{A,B}$	The width of the suspended waveguide cores.	$350nm$
$w_{C,D}$	The width of the suspended sections of Waveguides C and D.	$200nm$
n_{CORE}	The refractive index of the core material.	3.15
w_{COAT}	The width of the coat cladding layer.	$30nm$
n_{COAT}	The refractive index of the coat cladding layer.	1.6
$g_{cBAR00_{AB}}$	The surface-to-surface separation between Waveguides A and B in the mechanically-deflected bar-state configuration.	$10nm$
$g_{cCROSS00_{AB}}$	The surface-to-surface separation between Waveguides A and B in the as-fabricated cross-state configuration.	$810nm$
$L_{OPTIC00_{AB}}$	The overlap length between Waveguides A and B in parallel central waveguide section (Section 00).	$6\mu m$
$g_{cBAR_{AC,BD}}$	The surface-to-surface separation between Waveguides A and C and Waveguides B and D in the mechanically-deflected bar-state configuration.	$0nm$
$g_{cCROSS_{AC,BD}}$	The surface-to-surface separation between Waveguides A and C and Waveguides B and D in the as-fabricated cross-state configuration.	$400nm$
$L_{OPTIC_{AC,BD}}$	The overlap length between Waveguides A and C and Waveguides B and D.	$42\mu m$
$\Theta_{ADB_{max}}$	The maximum angle over which the suspended waveguides are adiabatically transitioned between two straight waveguide sections with a slanted waveguide.	$18°$
Θ_{TRAN}	The angle over which the suspended waveguides are transitioned between two straight waveguide sections with a slanted waveguide.	$10°$
Δx_{TRAN}	The transitional waveguide offset.	$395nm$
L_{TRAN}	The transitional waveguide length.	$2.3\mu m$
g_{NEM}	The core-to-core separation between the anode and the cathode of the parallel plate actuator.	$500nm$
L_{NEM}	The overlap length between the anode and the cathode of the parallel plate actuator.	$42\mu m$
Continued on Next Page...		

Table A.10 – Continued

Variable	Description	Value
A_{NEM}	The electrode plate area of the parallel plate actuator.	$12.6\mu m^2$
L_{NM}	The length of the suspended section of Waveguides A and B.	$72\mu m$
k_{NM}	The lumped element spring constant of the two-material MEMS suspension.	$1.0 \cdot 10^{-2} N/m$
m_{NM}	The lumped element mass of the two-material MEMS suspension.	$1.4 \cdot 10^{-3} ng$
$c_{DAMP_{CD}}$	The damping constant for critically-damped conditions.	$7.5 \cdot 10^{-3} \mu N/m/s$
t_{MIN}	The minimum release-settle actuation time under critically-damped conditions.	$374 ns$
c_{DAMP}	The damping constant.	$7.8 \cdot 10^{-4} \mu N/m/s$

TABLE A.11: Device 04 Optical Performance

As-Fabricated Bar-State

		$\lambda_0 - 50nm$	λ_0	$\lambda_0 + 50nm$
TE_{00}	Transmission	$-0.33dB$	$-0.31dB$	$-0.68dB$
	Crosstalk	$-21dB$	$-14dB$	$-9.5dB$
	Reflection	$-19dB$	$-15dB$	$-17dB$
TM_{00}	Transmission	$-1.3dB$	$-3.2dB$	$-6.6dB$
	Crosstalk	$-11dB$	$-4.6dB$	$-2.1dB$
	Reflection	$-10dB$	$-12dB$	$-17dB$

Mechanically-Deflected Cross-State

		$\lambda_0 - 50nm$	λ_0	$\lambda_0 + 50nm$
TE_{00}	Transmission	$-0.40dB$	$-0.19dB$	$-0.49dB$
	Crosstalk	$-24dB$	$-20dB$	$-13dB$
	Reflection	$-25dB$	$-23dB$	$-19dB$
TM_{00}	Transmission	$-0.57dB$	$-0.59dB$	$-0.24dB$
	Crosstalk	$-22dB$	$-27dB$	$-23dB$
	Reflection	$-44dB$	$-32dB$	$-21dB$

TABLE A.12: Device 04 MEMS Performance

Waveguide Actuator

Voltage	Speed
$V_{DPI} = 10V$	$t_{FDA} = 500ns$
$V_{DPI_{MIN}} = 3.0V$	$t_{FDA} = 1.5\mu s$
$V_{HOLD_{MIN}} = 0.5V$	N/A
$0\ V$	$t_{RSA} = 2\mu s$

A.5 Device 05 Parameters

TABLE A.13: Device 05 Parameters: primary optical parameter (▲), (associated) optical parameter (△), primary MEMS parameter (■), (associated) MEMS parameter (□).

Variable	Description	Value
h_{CORE}	The thickness of the core material.	$300nm$
$w_{A,B}$	The width of the suspended waveguide cores.	$300nm$
n_{Core}	The refractive index of the core material.	3.17
w_{COAT}	The width of the coat cladding layer.	$100nm$
n_{COAT}	The refractive index of the coat cladding layer.	1.50
$g_{cBAR00_{AB}}$	The surface-to-surface separation between Waveguides A and B in the mechanically-deflected bar-state configuration.	$850nm$
$g_{cCROSS00_{AB}}$	The surface-to-surface separation between Waveguides A and B in the as-fabricated cross-state configuration.	$50nm$
$L_{OPTIC00_{AB}}$	The overlap length between Waveguides A and B in parallel central waveguide section (Section 00).	$5.5\mu m$
$\Theta_{ADB_{max}}$	The maximum angle over which the suspended waveguides are adiabatically transitioned between two straight waveguide sections with a slanted waveguide.	$18°$
Θ_{TRAN}	The angle over which the suspended waveguides are transitioned between two straight waveguide sections with a slanted waveguide.	$10°$
Δx_{TRAN}	The transitional waveguide offset.	$395nm$
L_{TRAN}	The transitional waveguide length.	$2.3\mu m$
w_{TETHER}	The core width of the tether beam connecting the suspended waveguides to the MEMS actuators.	$100nm$
g_{NEM}	The core-to-core separation between the anode and the cathode of the parallel plate actuator.	$400nm$
L_{NEM}	The overlap length between the anode and the cathode of the parallel plate actuator.	$20\mu m$
A_{NEM}	The electrode plate area of the parallel plate actuator.	$6\mu m^2$
L_{NM}	The length of the suspended section of Waveguides A and B.	$180\mu m$
k_{NM}	The lumped element spring constant of the two-material MEMS suspension.	$1.0 \cdot 10^{-2} N/m$
m_{NM}	The lumped element mass of the two-material MEMS suspension.	$1.1 \cdot 10^{-1} ng$
$c_{DAMP_{CD}}$	The damping constant for critically-damped conditions.	$6.6 \cdot 10^{-2} \mu N/m/s$
Continued on Next Page...		

Table A.13 – Continued

Variable		Description	Value
	t_{MIN}	The minimum release-settle actuation time under critically-damped conditions.	$3.3\mu s$
	c_{DAMP}	The damping constant.	$3.7 \cdot 10^{-4} \mu N/m/s$

TABLE A.14: Device 05 Optical Performance

As-Fabricated Bar-State

		$\lambda_0 - 50nm$	λ_0	$\lambda_0 + 50nm$
TE$_{00}$	Transmission	$-2.8 \cdot 10^{-1}dB$	$-1.8 \cdot 10^{-1}dB$	$-2.6 \cdot 10^{-1}dB$
	Crosstalk	$-15dB$	$-17dB$	$-18dB$
	Reflection	$-22dB$	$-10dB$	$-29dB$
TM$_{00}$	Transmission	$-6.1 \cdot 10^{-1}dB$	$-2.0dB$	$-4.0dB$
	Crosstalk	$-18dB$	$-9.1dB$	$-20dB$
	Reflection	$-16dB$	$-23dB$	$-23dB$

Mechanically-Deflected Cross-State

		$\lambda_0 - 50nm$	λ_0	$\lambda_0 + 50nm$
TE$_{00}$	Transmission	$-1.0 \cdot 10^{-1}dB$	$-2.2 \cdot 10^{-1}dB$	$-3.4 \cdot 10^{-1}dB$
	Crosstalk	$-21dB$	$-19dB$	$-16dB$
	Reflection	$-24dB$	$-36dB$	$-24dB$
TM$_{00}$	Transmission	$-7.7 \cdot 10^{-1}dB$	$-8.9 \cdot 10^{-1}dB$	$-9.6 \cdot 10^{-1}dB$
	Crosstalk	$-26dB$	$-27dB$	$-27dB$
	Reflection	$-31dB$	$-21dB$	$-17dB$

TABLE A.15: Device 05 MEMS Performance

Waveguide Actuator

Voltage	Speed
$V_{DPI} = 10V$	$t_{FDA} = 7\mu s$
$V_{DPI_{MIN}} = 2.4V$	$t_{FDA} = 20\mu s$
$V_{HOLD_{MIN}} = 1.5V$	N/A
$0V$	$t_{RSA} = 3.3ms$

Latch Actuator

Voltage	Speed
$V_{DPI} = 20V$	$t_{FDA} = 7.0\mu s$
$V_{DPI_{MIN}} = 3.3V$	$t_{FDA} = 17\mu s$
$V_{HOLD_{MIN}} = 2.0V$	
	$t_{RSA} = 2.5ms$

A.6 Device 06 Parameters and Performance

TABLE A.16: Device 06 Parameters: primary optical parameter (▲), (associated) optical parameter (△), primary MEMS parameter (■), (associated) MEMS parameter (□).

Variable	Description	Value
h_{CORE}	The thickness of the core material.	$300nm$
$w_{A,B}$	The width of the suspended waveguide cores.	$300nm$
n_{CORE}	The refractive index of the core material.	3.17
w_{COAT}	The width of the coat cladding layer.	$50nm$
n_{COAT}	The refractive index of the coat cladding layer.	1.6
$g_{cBAR00_{AB}}$	The surface-to-surface separation between Waveguides A and B in the as-fabricated bar-state configuration.	$800nm$
$g_{cCROSS00_{AB}}$	The surface-to-surface separation between Waveguides A and B in the mechanically-deflected cross-state configuration.	$0nm$
$L_{OPTIC00_{AB}}$	The overlap length between Waveguides A and B in parallel central waveguide section (Section 00).	$8.9\mu m$
$g_{cBAR00_{AC,BD}}$	The surface-to-surface separation between Waveguide A and and the bumper beam (Waveguide C) and Waveguide B and bumper beam (Waveguide D) in the as-fabricated bar-state configuration.	$10nm$
$g_{cCROSS00_{AC,BD}}$	The surface-to-surface separation between Waveguide A and bumper beam (Waveguide C) and Waveguide B and the bumper beam (Waveguide D) in the mechanically-deflected cross-state configuration.	$0nm$
$\Theta_{ADB_{max}}$	The maximum angle over which the suspended waveguides are adiabatically transitioned between two straight waveguide sections with a slanted waveguide.	$18°$
Θ_{TRAN}	The angle over which the suspended waveguides are transitioned between two straight waveguide sections with a slanted waveguide.	$10°$
Δx_{TRAN}	The transitional waveguide offset.	$395nm$
L_{TRAN}	The transitional waveguide length.	$2.3\mu m$
w_{BUMP}	The core width of the bumper beam waveguides.	$100nm$
g_{NEM}	The core-to-core separation between the anode and the cathode of the parallel plate actuator.	$410nm$
L_{NEM}	The overlap length between the anode and the cathode of the parallel plate actuator.	$20\mu m$
Continued on Next Page...		

Table A.16 – Continued

Variable	Description	Value
A_{NEM}	The electrode plate area of the parallel plate actuator.	$6\mu m^2$
L_{NM}	The length of the suspended section of Waveguides A and B.	$180\mu m$
k_{NM}	The lumped element spring constant of the two-material MEMS suspension.	$6.3 \cdot 10^{-2} N/m$
m_{NM}	The lumped element mass of the two-material MEMS suspension.	$1.1 \cdot 10^{-1} ng$
$c_{DAMP_{CD}}$	The damping constant for critically-damped conditions.	$5.3 \cdot 10^{-2} \mu N/m/s$
t_{MIN}	The minimum release-settle actuation time under critically-damped conditions.	$4.2\mu s$
c_{DAMP}	The damping constant.	$3.7 \cdot 10^{-4} \mu N/m/s$

TABLE A.17: Device 06 Optical Performance

As-Fabricated Bar-State

		$\lambda_0 - 50nm$	λ_0	$\lambda_0 + 50nm$
TE_{00}	Transmission	$-0.25dB$	$-0.14dB$	$-0.03dB$
	Crosstalk	$-14dB$	$-20dB$	$-26dB$
	Reflection	$-13dB$	$-30dB$	$-24dB$
TM_{00}	Transmission	$-0.92dB$	$-0.95dB$	$-0.14dB$
	Crosstalk	$-35dB$	$-24dB$	$-25dB$
	Reflection	$-30dB$	$-35dB$	$-21dB$

Mechanically-Deflected Cross-State

		$\lambda_0 - 50nm$	λ_0	$\lambda_0 + 50nm$
TE_{00}	Transmission	$-0.47dB$	$-0.36dB$	$-0.47dB$
	Crosstalk	$-12dB$	$-17dB$	$-21dB$
	Reflection	$-29dB$	$-29dB$	$-49dB$
TM_{00}	Transmission	$-4.0dB$	$-7.4dB$	dB
	Crosstalk	$-6.8dB$	$-3.7dB$	$-2.1dB$
	Reflection	$-39dB$	$-31dB$	$-37dB$

TABLE A.18: Device 06 MEMS Performance

Waveguide Actuator

Voltage	Speed
$V_{DPI} = 10V$	$t_{FDA} = 8\mu s$
$V_{DPI_{MIN}} = 2.4V$	$t_{FDA} = 23\mu s$
$V_{HOLD_{MIN}} = 1.4V$	N/A
$0V$	$t_{RSA} = 3.3ms$

Latch Actuator

Voltage	Speed
$V_{DPI} = 20V$	$t_{FDA} = 7.0\mu s$
$V_{DPI_{MIN}} = 3.3V$	$t_{FDA} = 17\mu s$
$V_{HOLD_{MIN}} = 2.0V$	N/A
$0V$	$t_{RSA} = 3.2ms$

A.7   Device 07 Parameters and Performance

TABLE A.19: Device 01 Parameters: primary optical parameter (▲), (associated) optical parameter (△), primary MEMS parameter (■), (associated) MEMS parameter (□).

Variable	Description	Value
h_{CORE}	The thickness of the core material.	$300nm$
n_{CORE}	The refractive index of the core material.	3.32
w_{COAT}	The width of the coat cladding layer.	$60nm$
n_{COAT}	The refractive index of the coat cladding layer.	1.82
$\Theta_{ADB_{max}}$	The maximum angle over which the suspended waveguides are adiabatically transitioned between two straight waveguide sections with a slanted waveguide.	$18°$
Θ_{TRAN}	The angle over which the suspended waveguides are transitioned between two straight waveguide sections with a slanted waveguide.	$10°$
Δx_{TRAN}	The transitional waveguide offset.	$395nm$
L_{TRAN}	The transitional waveguide length.	$2.3\mu m$
w_{BUMP}	The core width of the bumper beam waveguides (Waveguides C and D).	$100nm$
g_{NEM}	The core-to-core separation between the anode and the cathode of the parallel plate actuator.	$520nm$
L_{NEM}	The overlap length between the anode and the cathode of the parallel plate actuator.	$20\mu m$
A_{NEM}	The electrode plate area of the parallel plate actuator.	$6\mu m^2$
L_{NM}	The length of the suspended section of Waveguides A and B.	$200\mu m$
k_{NM}	The lumped element spring constant of the two-material MEMS suspension.	$5.8 \cdot 10^{-3} N/m$
m_{NM}	The lumped element mass of the two-material MEMS suspension.	$1.4 \cdot 10^{-1} ng$
$c_{DAMP_{CD}}$	The damping constant for critically-damped conditions.	$5.7 \cdot 10^{-2} \mu N/m/s$
t_{MIN}	The minimum release-settle actuation time under critically-damped conditions.	$4.9\mu s$
c_{DAMP}	The damping constant.	$4.1 \cdot 10^{-4} \mu N/m/s$

TABLE A.20: Device 07 Optical Performance

As-Fabricated Bar-State

		$\lambda_0 - 50nm$	λ_0	$\lambda_0 + 50nm$
TE_{00}	Transmission	$-0.31dB$	$-0.30dB$	$-0.32dB$
	Crosstalk	$-23dB$	$-26dB$	$-27dB$
	Reflection	$-21dB$	$-24dB$	$-24dB$
TM_{00}	Transmission	$-3.6dB$	$-4.5dB$	$-2.4dB$
	Crosstalk	$-13dB$	$-8.0dB$	$-15dB$
	Reflection	$-27dB$	$-21dB$	$-31dB$

Mechanically-Deflected Cross-State

		$\lambda_0 - 50nm$	λ_0	$\lambda_0 + 50nm$
TE_{00}	Transmission	$-0.90dB$	$-0.34dB$	$-0.29dB$
	Crosstalk	$-8.7dB$	$-16dB$	$-17dB$
	Reflection	$-25dB$	$-36dB$	$-30dB$
TM_{00}	Transmission	$-1.1dB$	$-1.9dB$	$-2.6dB$
	Crosstalk	$-10dB$	$-8.0dB$	$-12dB$
	Reflection	$-39dB$	$-31dB$	$-37dB$

TABLE A.21: Device 07 MEMS Performance

Waveguide Actuator

Voltage	Speed
$V_{DPI} = 10V$	$t_{FDA} = 10\mu s$
$V_{DPI_{MIN}} = 2.0V$	$t_{FDA} = 20\mu s$
$V_{HOLD_{MIN}} = 1.2V$	N/A
$0V$	$t_{RSA} = 3.3ms$

Latch Actuator

Voltage	Speed
$V_{DPI} = 20V$	$t_{FDA} = 1.6\mu s$
$V_{DPI_{MIN}} = 5.5V$	$t_{FDA} = 3.0\mu s$
$V_{HOLD_{MIN}} = 3.3V$	N/A
$0V$	$t_{RSA} = 510\mu s$

Bibliography

[1] N. Holonyak and S. F. Bevacqua, "Coherent (visible) light emission fromGaAsP junctions," Appl. Phys. Let, vol. 1, p. 82, 1962.

[2] R. N. Hall, G. E. Fenner, J. D. Kingsley, T. J. Soltys, and R. O. Carlson, "Coherent light emission from GaAs junctions," Physical Review Letters, vol. 9, no. 9, pp. 366–368, 1962.

[3] M. I. Nathan, W. P. Dumke, G. Burns, F. H. Dill, and G. Lasher, "STIMULATED EMISSION OF RADIATION FROM GaAs p-n JUNCTIONS," Applied Physics Letters, vol. 1, no. 3, p. 6264, 1962.

[4] M. I. Nathan and G. Burns, "Recombination radiation in GaAs by optical and electrical injection," Applied Physics Letters, vol. 1, p. 8990, 1962.

[5] T. M. Quist, R. H. Rediker, R. J. Keyes, W. E. Krag, B. Lax, A. L. McWhorter, and H. J. Zeigler, "Semiconductor maser of GaAs," Applied Physics Letters, vol. 1, p. 91, 1962.

[6] F. P. Kapron, D. B. Keck, and R. D. Maurer, "RADIATION LOSSES IN GLASS OPTICAL WAVEGUIDES," Applied Physics Letters, vol. 17, pp. 423–425, Nov. 1970.

[7] T. Li, "Advances in optical fiber communications: An historical perspective," Selected Areas in Communications, IEEE Journal on, vol. 1, no. 3, pp. 356–372, 1983.

[8] T. H. Wu and S. F. Habiby, "Strategies and technologies for planning a cost-effectivesurvivable fiber network architecture using optical switches," Lightwave Technology, Journal of, vol. 8, no. 2, pp. 152–159, 1990.

[9] L. Berthelon, B. Miller, G. Capitolo, and J. P. Faure, "The benefits of reconfigurable photonic networks," Alcatel Telecommunications Review, no. 3, pp. 197–203, 2005.

[10] L. Eldada, "Advances in telecom and datacom optical components," OPTICAL ENGINEERING, vol. 40, pp. 1165–1178, July 2001.

[11] L. Pavesi, D. J. Lockwood, and Lorenzo, Silicon Photonics. Springer, 2004.

[12] V. Ghergia, "New materials for optoelectronic devices," Ceramics International, vol. 19, no. 3, pp. 181–190, 1993.

[13] L. Eldada, "Optical communication components," Review of Scientific Instruments, vol. 75, no. 3, pp. 575–593, 2004.

[14] R. Fehse, I. Marko, and A. Adams, "Long wavelength lasers on GaAs substrates," IEE Proceedings: Circuits, Devices and Systems, vol. 150, no. 6, pp. 521–528, 2003.

[15] K. Inoue, Y. Sugimoto, N. Ikeda, Y. Tanaka, K. Asakawa, T. Maruyama, K. Miyashita, K. Ishida, and Y. Watanabe, "Ultra-Small GaAs-Photonic-Crystal-Slab-Waveguide-Based Near-Infrared components: Fabrication, Guided-Mode identification, and estimation of Low-Loss and Broad-Band-Width in Straight-Waveguides, 60-Bends and Y-Splitters," Japanese Journal of Applied Physics, vol. 43, no. no. 9 a, pp. 6112–6124, 2004.

[16] S. G. Johnson, C. Manolatou, S. Fan, P. R. Villeneuve, J. D. Joannopoulos, and H. A. Haus, "Elimination of cross talk in waveguide intersections," Optics Letters, vol. 23, no. 23, pp. 1855–1857, 1998.

[17] H. Han, R. A. Boudreau, T. Bowen, S. Tan, and M. L. Reed, "Micromachined structures for optoelectronics packaging (invited)," vol. 1 of Conference Proceedings - Lasers and Electro-Optics Society Annual Meeting-LEOS, (San Francisco, CA, USA), pp. 232–233, IEEE, Piscataway, NJ, USA, 1995.

[18] M. Soljacic, M. Ibanescu, S. G. Johnson, Y. Fink, and J. D. Joannopoulos, "Optimal bistable switching in nonlinear photonic crystals," Physical Review E, vol. 66, no. 5, p. 55601, 2002.

[19] S. Bank, H. Bae, H. Yuen, L. Goddard, M. Wistey, T. Sarmiento, and J. H. Jr., "Low-threshold CW 1.55-m GaAs-based lasers," vol. 2006 of 2006 Optical Fiber Communication Conference, and the 2006 National Fiber Optic Engineers Conference, (Anaheim, CA, United States), p. 1636802, Institute of Electrical and Electronics Engineers Computer Society, Piscataway, NJ 08855-1331, United States, 2006.

[20] X. Yang, J. B. Hroux, L. F. Mei, and W. I. Wang, "InGaAsNSb/GaAs quantum wells for 1.55 m lasers grown by molecular-beam epitaxy," Applied Physics Letters, vol. 78, p. 4068, 2001.

[21] M. Razeghi, J. Ramdani, H. Verriele, D. Decoster, M. Constant, and J. Vanbremeersch, "Planar monolithic integrated photoreceiver for 1.31.55 m wavelength applications using GaInAs-GaAs heteroepitaxies," Applied Physics Letters, vol. 49, p. 215, 1986.

[22] A. Guzman, J. Miguel-Sanchez, E. Luna, and E. Munoz, "InGaAsN-and GaAsN-based quantum well lasers and detectors for optical sensing in 1.3 and 1.55 m," Proceedings of SPIE, vol. 5502, p. 414, 2004.

[23] G. Christenson, G. Christenson, A. Tran, A. Tran, Z. Zhu, and Y. Lo, "Surface micromachined long wavelength LED/photodetector with a continuous tuning range of 75 nm," in Micro Electro Mechanical Systems, 1997. MEMS '97, Proceedings, IEEE., Tenth Annual International Workshop on, pp. 61–65, 1997.

[24] R. Deri, R. Deri, E. Kapon, and E. Kapon, "Low-loss III-V semiconductor optical waveguides," Quantum Electronics, IEEE Journal of, vol. 27, no. 3, pp. 626–640, 1991.

[25] M. K. Chin, C. W. Lee, S. Y. Lee, and S. Darmawan, "High-index-contrast waveguides and devices," Applied Optics, vol. 44, no. 15, pp. 3077–3086, 2005.

[26] S. Suzuki and M. Kawachi, "Planar lightwave circuits based on silica waveguides on silicon," Electronics & Communications in Japan, Part II: Electronics (English translation of Denshi Tsushin Gakkai Ronbunshi), vol. 77, no. 11, pp. 25–36, 1994.

[27] S. Hosain, J. Meunier, E. Bourillot, F. de Fornel, and J. Goudonnet, "Review of the basic methods for characterizing integrated-optic waveguides," Fiber and Integrated Optics, vol. 14, no. 1, pp. 89–107, 1995.

[28] K. Okamoto, "Planar waveguide devices for WDM communications," in Proceedings of the 1999 Pacific Rim Conference on Lasers and Electro-Optcis (CLEO/PACIFIC Rim '99), Aug 30-Sep 3 1999, vol. 1 of Pacific Rim Conference on Lasers and Electro-Optics, CLEO - Technical Digest, (Seoul, South Korea), pp. 112–113, IEEE, Piscataway, NJ, USA, 1999.

[29] D. Rauch, "Manufacturing of planar lightwave circuits," Lightwave, vol. 18, no. 12 SPECIAL EDITI, pp. 23–25, 2001.

[30] E. Lee, S. Lee, B. H. O, S. Park, and S. Kim, "Micro/Nano-scale integrated photonic devices and circuits: Issues and challenges," vol. 4905 of Proceedings of SPIE - The International Society for Optical Engineering, (Shanghai, China), pp. 170–182, The International Society for Optical Engineering, 2002.

[31] J. E. Goell, "A circular-harmonic computer analysis of rectangular dielectric waveguides(Rectangular dielectric waveguide propagation modes, describing computer analysis based on electromagnetic field expansion in circular harmonics series terms)," Bell System Technical Journal, vol. 48, p. 21332160, 1969.

[32] P. Bienstman, H. Derudder, R. Baets, F. Olyslager, and D. D. Zutter, "Analysis of cylindrical waveguide discontinuities using vectorialeigenmodes and perfectly matched layers," Microwave Theory and Techniques, IEEE Transactions on, vol. 49, no. 2, pp. 349–354, 2001.

[33] I. RSoft, "BeamPROP users guide RSoft," Ossining, NY, 2001.

[34] M. D. Feit and J. A. Fleck, "Calculation of dispersion in graded-index multimode fibers by a propagating-beam method," Applied Optics, vol. 18, no. 16, pp. 2843–51, 1979.

[35] G. R. Hadley, "Wide-angle beam propagation using pade approximant operators," Opt. Lett, vol. 17, no. 20, pp. 1426–1428, 1992.

[36] Z. Huan, R. Scarmozzino, G. Nagy, J. Steel, and R. Osgood, "Realization of a compact and single-mode optical passive polarization converter," Photonics Technology Letters, IEEE, vol. 12, no. 3, pp. 317–319, 2000.

[37] J. van der Tol, F. Hakimzadeh, J. Pedersen, D. Li, and H. van Brug, "A new short and low-loss passive polarization converter on InP," Photonics Technology Letters, IEEE, vol. 7, no. 1, pp. 32–34, 1995.

[38] M. Kotlyar, L. Bolla, M. Midrio, L. O'Faolain, and T. Krauss, "Compact polarization converter in InP-based material," Opt. Express, vol. 13, no. 13, pp. 5040–5045, 2005.

[39] T. Koster and P. Lambeck, "Passive polarization converter in SiON technology," Lightwave Technology, Journal of, vol. 19, no. 6, pp. 876–883, 2001.

[40] M. FEIT and J. FLECK, "Computation of mode properties in optical fiber waveguides by a propagating beam method," Applied Optics, vol. 19, no. 7, pp. 1154–1164, 1980.

[41] G. Sztefka, G. Sztefka, H. Nolting, and H. Nolting, "Bidirectional eigenmode propagation for large refractive index steps," Photonics Technology Letters, IEEE, vol. 5, no. 5, pp. 554–557, 1993.

[42] M. Hammer, "Quadridirectional eigenmode expansion scheme for 2-D modeling of wave propagation in integrated optics," Optics Communications, vol. 235, pp. 285–303, May 2004.

[43] P. Bienstman and R. Baets, "Optical modelling of photonic crystals and VCSELs using eigenmode expansion and perfectly matched layers," Optical and Quantum Electronics, vol. 33, no. 4, pp. 327–341, 2001.

[44] P. Bienstman and R. Baets, "Advanced boundary conditions for eigenmode expansion models," Optical and Quantum Electronics, vol. 34, no. 5, pp. 523–540, 2002.

[45] H. Derudder, D. D. Zutter, and F. Olyslager, "Analysis of waveguide discontinuities using perfectly matchedlayers," Electronics Letters, vol. 34, no. 22, pp. 2138–2140, 1998.

[46] S. D. Senturia, Microsystem Design. Springer, 1st ed. 2000. corr. 2nd printing ed., Dec. 2004.

[47] S. HAN, H. BENAROYA, and T. Wei, "DYNAMICS OF TRANSVERSELY VIBRATING BEAMS USING FOUR ENGINEERING THEORIES," Journal of Sound and Vibration, vol. 225, no. 5, pp. 935–988, 1999.

[48] R. B. Bhat and R. V. Dukkipati, Advanced dynamics. CRC Press, Nov. 2001.

[49] B. J. Torby, Advanced dynamics for engineers. Holt, Rinehart, and Winston, 1984.

[50] G. L. Downey and G. M. Smith, Advanced dynamics for engineers. International Textbook Co., 1960.

[51] D. Elata and V. Leus, "Switching time, impact velocity and release response, of voltage and charge driven electrostatic switches," MEMS, NANO and Smart Systems, 2005. Proceedings. 2005 International Conference on, pp. 331–334, 2005.

[52] P. M. Osterberg, Electrostatically actuated microelectromechanical test structures for material property measurement. PhD thesis, Massachusetts Institute of Technology, Dept. of Electrical Engineering and Computer Science, 1995.

[53] E. K. Chan and R. W. Dutton, "Effects of capacitors, resistors and residual change on the static and dynamic performance of electrostatically actuated devices," Proc. of SPIE, vol. 3680, pp. 120–130, 1999.

[54] C. Goldsmith, J. Ehmke, A. Malczewski, B. Pillans, S. Eshelman, Z. Yao, J. Brank, and M. Eberly, "Lifetime characterization of capacitive RF MEMS switches," IEEE MTT S INT MICROWAVE SYMP DIG, vol. 3, pp. 227–230, 2001.

[55] C. F. Herrmann, F. W. DelRio, D. C. Miller, S. M. George, V. M. Bright, J. L. Ebel, R. E. Strawser, R. Cortez, and K. D. Leedy, "Alternative dielectric films for rf MEMS capacitive switches deposited using atomic layer deposited Al2O3/ZnO alloys," Sensors and Actuators A: Physical, vol. 135, pp. 262–272, Mar. 2007.

[56] S. Melle, F. Flourens, D. Dubuc, K. Grenier, P. Pons, F. Pressecq, J. Kuchenbecker, J. Muraro, L. Bary, and R. A. P. Plana, "Reliability behavior of RF MEMS," vol. 1, p. 26 Vol. 1, 2003.

[57] C. P. Yuan and T. N. Trick, "A simple formula for the estimation of the capacitance of two-dimensional interconnects in VLSI circuits," Electron Device Letters, IEEE, vol. 3, no. 12, pp. 391–393, 1982.

[58] S. Chu, "Simulation and analysis of waveguide based optical integrated circuits," Computer Physics Communications, vol. 68, no. 1, pp. 451–484, 1991.

[59] M. Kaniewska and K. Klima, "Investigations of surface defects of GaAs grown by molecular beam epitaxy," Materials Science and Engineering B, vol. 91-92, pp. 512–515, Apr. 2002.

[60] S. H. Davis and MyiLibrary, Theory of solidification. Cambridge University Press New York, 2001.

[61] U. Glombitza and E. Brinkmeyer, "Coherent frequency-domain reflectometry for characterization of single-mode integrated-optical waveguides," Lightwave Technology, Journal of, vol. 11, no. 8, pp. 1377–1384, 1993.

[62] R. A. Modavis and W. F. Love, "MULTIPLE-WAVELENGTH SYSTEM FOR CHARACTERIZING DISPERSION IN SINGLE-MODE OPTICAL FIBERS.," in Technical Digest - Symposium on Optical Fiber Measurements, 1984., National Bureau of Standards, Special Publication, (Boulder, CO, USA), pp. 115–118, NBS, Washington, DC, USA, 1984.

[63] S. Assefa, "The development of novel passive and active photonic-crystal devices," 2004.

[64] K. Choquette, K. Geib, C. Ashby, R. Twesten, O. Blum, H. Hou, D. Follstaedt, B. Hammons, D. Mathes, and R. Hull, "Advances in selective wet oxidation of AlGaAs alloys," Selected Topics in Quantum Electronics, IEEE Journal of, vol. 3, no. 3, pp. 916–926, 1997.

[65] K. Y. Lim, "Design and fabrication of one-dimensional and two-dimensional photonic bandgap devices," Thesis (PhD). MASSACHUSETTS INSTITUTE OF TECHNOLOGY, Source DAI-B 60/09, p. 4687, Mar 2000, pages., 1999.

[66] P. Ku, P. Ku, C. Chang-Hasnain, and C. Chang-Hasnain, "Thermal oxidation of AlGaAs: modeling and process control," Quantum Electronics, IEEE Journal of, vol. 39, no. 4, pp. 577–585, 2003.

[67] H. Nickel, "Detailed experimental study of the wet oxidation kinetics of AlxGa1-xAs layers," Journal of Applied Physics, vol. 78, no. 8, p. 5201, 1995.

[68] Y. Suematsu and K. Furuya, "Propagation mode and scattering loss of a Two-Dimensional dielectric waveguide with gradual distribution of refractive index," Microwave Theory and Techniques, IEEE Transactions on, vol. 20, no. 8, pp. 524–531, 1972.

[69] E. H. Snow, A. S. Grove, B. E. Deal, and C. T. Sah, "Ion transport phenomena in insulating films," Journal of Applied Physics, vol. 36, pp. 1664–1673, May 1965.

[70] A. Mahajan, L. Patil, and D. Gautam, "Influence of process parameters on the properties of TEOS-PECVD-grown SiO2 films," Surface and Coatings Technology, vol. 188-189, no. 1-3 SPECISS, pp. 314–318, 2004.

[71] C. I. H. Ashby, J. P. Sullivan, K. D. Choquette, K. M. Geib, and H. Q. Hou, "Wet oxidation of AlGaAs: the role of hydrogen," Journal of Applied Physics, vol. 82, no. 6, pp. 3134–3136, 1997.

[72] C. I. H. Ashby, M. M. Bridges, A. A. Allerman, B. E. Hammons, and H. Q. Hou, "Origin of the time dependence of wet oxidation of AlGaAs," Applied Physics Letters, vol. 75, pp. 73–75, July 1999.

[73] P. V. Zant, Microchip Fabrication. 2004.

[74] P. Legay, P. Petit, J. Debray, A. Khl, G. Patriarche, G. L. Roux, M. Juhel, and M. Quillec, "Wet thermal oxidation of AlInAs and AlAsSb alloys lattice-matched to InP," in Indium Phosphide and Related Materials, 1997., International Conference on, pp. 586–589, 1997.

[75] D. Liang and D. C. Hall, "Reduction of etched AlGaAs sidewall roughness by oxygen-enhanced wet thermal oxidation," Applied Physics Letters, vol. 91, no. 6, pp. 061110–3, 2007.

[76] W. S. Yang and S. W. Kang, "Comparative study on chemical stability of dielectric oxide films under HF wet and vapor etching for radiofrequency microelectrome-chanical system application," Thin Solid Films, vol. 500, pp. 231–236, Apr. 2006.

[77] N. D. Hoivik, J. W. Elam, R. J. Linderman, V. M. Bright, S. M. George, and Y. Lee, "Atomic layer deposited protective coatings for micro-electromechanical systems," Sensors and Actuators, A: Physical, vol. 103, no. 1-2, pp. 100–108, 2003.

[78] T. M. Mayer, J. W. Elam, S. M. George, P. G. Kotula, and R. S. Goeke, "Atomic-layer deposition of wear-resistant coatings for microelectromechanical devices," Applied Physics Letters, vol. 82, pp. 2883–2885, Apr. 2003.

[79] M. Ritala and M. Leskelae, "Atomic layer epitaxy-a valuable tool for nanotechnology?," NANOTECHNOLOGY, vol. 10, pp. 19–24, 1999.

[80] M. K. Tripp, C. Stampfer, D. C. Miller, T. Helbling, C. F. Herrmann, C. Hierold, K. Gall, S. M. George, and V. M. Bright, "The mechanical properties of atomic layer deposited alumina for use in micro- and nano-electromechanical systems," Sensors and Actuators A: Physical, vol. 130-131, pp. 419–429, Aug. 2006.

[81] R. Maboudian and R. T. Howe, "Critical review: Adhesion in surface microme-chanical structures," Journal of Vacuum Science & Technology B: Microelectronics and Nanometer Structures, vol. 15, pp. 1–20, Jan. 1997.

[82] J. Dostalek, J. Ctyroky, J. Homola, E. Brynda, M. Skalsk, P. Nekvindov, J. Spirkov, J. Skvor, and J. Schrfel, "Surface plasmon resonance biosensor based on integrated optical waveguide," Sensors and Actuators B: Chemical, vol. 76, pp. 8–12, June 2001.

[83] W. W. Morey, J. R. Dunphy, G. Meltz, A. D. Kersey, and J. P. Dakin, "Multiplexing fiber bragg grating sensors," in Distributed and Multiplexed Fiber Optic Sensors, vol. 1586, (Boston, MA, USA), pp. 216–224, SPIE, Jan. 1992.

[84] S. Nagaoka, "Compact latching type Single-Mode fiber switches and their applications in subscriber loop networks," IEICE TRANSACTIONS on Electronics, vol. 80, no. 1, pp. 149–153, 1997.

[85] V. Torres-Company, J. Lancis, P. Andres, and M. Muriel, "Real-time optical spectrum analyzers operating with spectrally incoherent broadband continuous-wave light source," Optics Communications, vol. 273, no. 2, pp. 320–323, 2007.

[86] W. Rutzen, W. Stcklein, and C. Unger, "Calibration of optical time domain reflectometers," Optics Communications, vol. 127, pp. 343–352, June 1996.

[87] J. Kloock, L. Moreno, A. Bratov, S. Huachupoma, J. Xu, T. Wagner, T. Yoshinobu, Y. Ermolenko, Y. Vlasov, and M. Schning, "PLD-prepared cadmium sensors based on chalcogenide glasses-ISFET, LAPS and ISE semiconductor structures," Sensors and Actuators, B: Chemical, vol. 118, no. 1-2, pp. 149–155, 2006.

[88] J. Homola, H. B. Lu, G. G. Nenninger, J. Dostlek, and S. S. Yee, "A novel multi-channel surface plasmon resonance biosensor," Sensors and Actuators B: Chemical, vol. 76, pp. 403–410, June 2001.

[89] R. Tominaga, M. Sivakumar, M. Tanaka, and T. Kinoshita, "Design of novel sensing device based on thin-film interference," in 54th SPSJ Symposium on Macromolecules, Sep 20-22 2005, vol. 54 of Polymer Preprints, Japan, (Tokyo, 104-0042, Japan), pp. 3891–3892, Society of Polymer Science, 2005.

[90] G. T. Dobbs and B. Mizaikoff, "Shining new light on old principles: Localization of evanescent field interactions at infrared-attenuated total reflection sensing interfaces," Applied Spectroscopy, vol. 60, no. 6, pp. 573–583, 2006.

[91] F. Rehouma, W. Elflein, D. Persegol, A. Kevorkian, G. Clauss, P. Benech, and R. Rimet, "Improved structures for evanescent wave sensors," Applied Physics Letters, vol. 66, no. 12, pp. 1461–1462, 1995.

[92] G. de Graaf, W. der Vlist, and R. Wolffenbuttel, "Design and fabrication steps for a MEMS-based infrared spectrometer using evanescent wave sensing," Sensors and Actuators, A: Physical, vol. 142, no. 1, pp. 211–216, 2008.

[93] D. Reichl, R. Krage, C. Krummel, and G. Gauglitz, "Sensing of volatile organic compounds using a simplified reflectometric interference spectroscopy setup," Applied Spectroscopy, vol. 54, no. 4, pp. 583–586, 2000.

[94] J. Seemann, G. Kraus, and G. Gauglitz, "Performance and limitations of reflectometric fibre optical sensors for VOC sensing applications," in Proceedings of the 1995 8th International Conference on Solid-State Sensors and Actuators, and Eurosensors IX. Part 2 (of 2), Jun 25-29 1995, vol. 2 of International Conference on Solid-State Sensors and Actuators, Proceedings, (Piscataway, NJ, USA), pp. 801–803, IEEE, 1995.

[95] S. Nagaoka and Y. Suzuki, "Compact optomechanical switches and their applications in optical communication and testing systems," in Micro Electro Mechanical Systems, 1997. MEMS '97, Proceedings, IEEE., Tenth Annual International Workshop on, pp. 366–371, 1997.

[96] W. Hatton and M. Nishimura, "New method for measuring the chromatic dispersion of installed single-mode fibers utilizing wavelength division multiplexing techniques," Lightwave Technology, Journal of, vol. 4, no. 8, pp. 1116–1119, 1986.

[97] H. Sunak, "Single-mode fiber measurements," Instrumentation and Measurement, IEEE Transactions on, vol. 37, no. 4, pp. 557–560, 1988.